AXIAL HEAT TRANSFER IN PACKED BEDS

by D.P. HAUGHEY M.E

Meat Industry Research Institute of New Zealand Research Fellow

Thesis presented for the degree of

Doctor of Philosophy

University of Edinburgh

August 1966

CONTENTS

1.1. TECHNOLOGICAL APPLICATIONS OF PACKED BED SYSTEMS

Packed beds of solids have a central place as a processing tool in chemical engineering operations. Their inherent characteristics of extended fluid interfacial area and good fluid mixing have led to application in a wide variety of physical and chemical processes. These include chemical reactors, drying, filtration, distillation, gas absorbtion, adsorbtion, leaching, ion exchange and regenerators. Many of these involve the transfer of heat between the bed material and the fluid in the bed. Modified forms of the packed bed also form the basis of many other systems of chemical engineering concern (Fig.1.1). Expansion of the bed leads to a fluidised bed and fluidised transport, whereas consolidation gives a porous solid. Utilization of packed beds in continuous processes involving physico-chemical changes in the bed material is made possible by the use of moving beds.

One particular application where both static and moving beds are used is in non-catalytic gas-solid reactions. In this case the reacting solid comprises the bed of particles through which the reactant gas is passed. Typical examples of such systems are the oxidation of zinc sulphide as a stage in the manufacture of zinc, combustion of solid fuels such as coal and coke, reduction of iron ore in a blast furnace, limestone calcination and sintering operations. An interesting application of a different type is the pebble bed nuclear reactor where the nuclear fuel is in the form of pellets which liberate

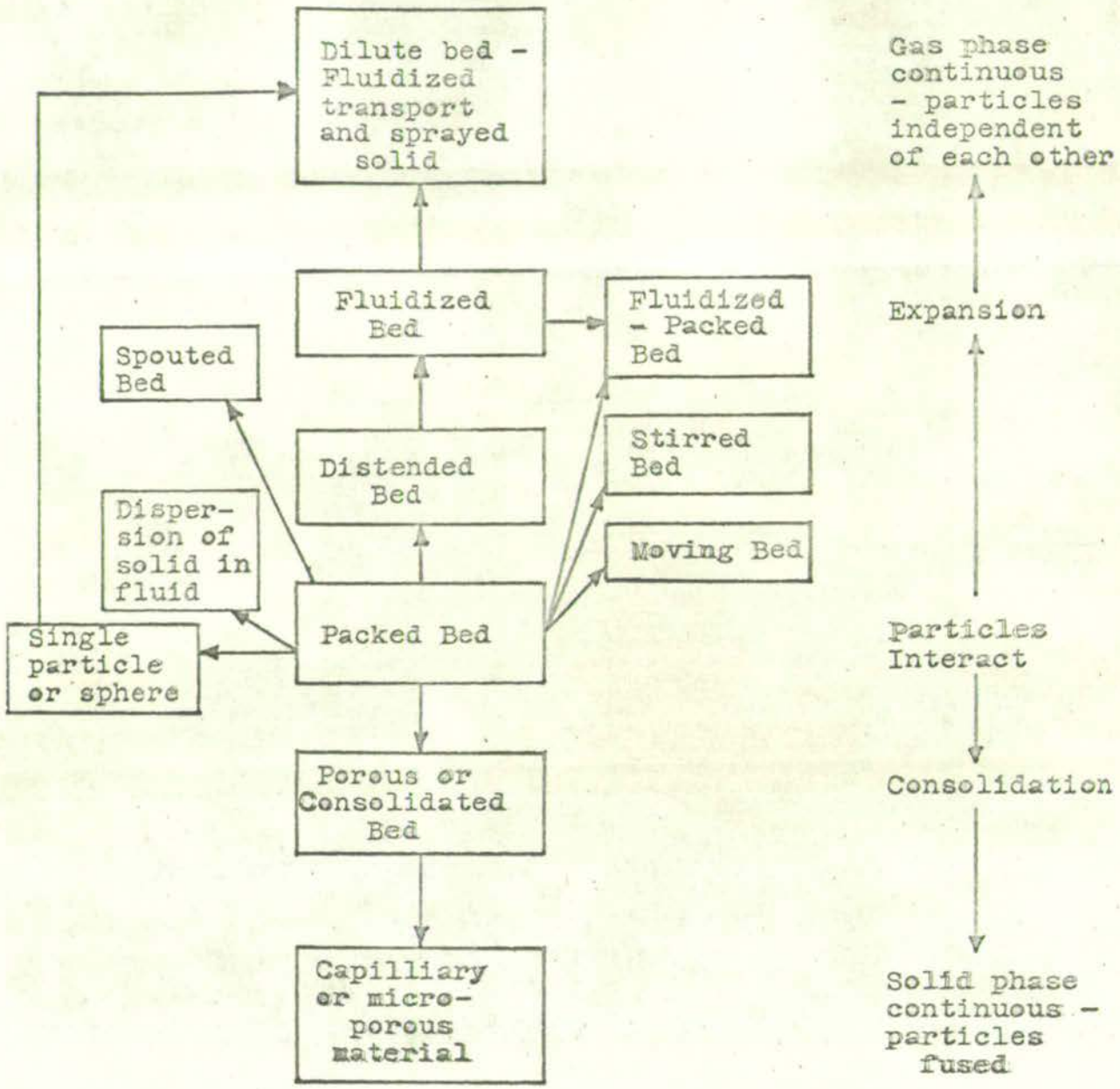

FIG. 1.1 THE RELATIONSHIP BETWEEN PACKED BEDS AND OTHER GAS-SOLID SYSTEMS.

heat to a gas flowing through the bed.[1]

1.2. HEAT TRANSFER IN REACTING GAS-SOLID PACKED BED SYSTEMS

In the most common type of reacting gas-solid system the solid is ignited at one end of the bed. This initiates chemical reaction (usually exothermic) between the gas and the solid. The heat liberated is transferred further into the unreacted portion of the bed by various mechanisms of conduction, convection and radiation heat transfer, thus raising the unreacted solid to ignition temperature. In this way the reaction zone is propagated through the bed of solid. Thus reaction kinetics, heat transfer and mass transfer (diffusion of reactants to and products away from the surface of reaction, evaporation of moisture in the solid) are all involved in a series of sequential steps in such a system. But the overall rate of a process controlled by such steps in series is limited by the rate of the slowest step. It has been found both theoretically and experimentally[2] that under most conditions the rate of propagation of the reaction zone is controlled by heat transfer considerations rather than by kinetics or mass transfer. Thus the process design of such systems requires a knowledge of the heat transfer characteristics of the bed at the process temperatures and flow rates. This work originated with the aim of elucidating the mechanisms of heat transfer involved and providing such information in the form of suitable mathematical models.

---

1. Schulten et al (1959a,b), Prushek (1963), Anon. (1965)
2. Voice and Wild, (1956), Beveridge (1960)

The conditions characterising heat transfer in such moving zone systems are:

(a) Axial heat flow - since the beds are usually of large diameter and radial heat loss is negligible away from the perimeter of the bed.

(b) The direction of gas flow is countercurrent to the direction of heat flow through the solid in one section of the bed and co-current in the other section (Fig. 1.2).

(c) High temperatures and temperature gradients are present in the bed. In zinc sulphide oxidation, for example, a peak temperature of 1500°C is reached in the reaction zone.

(d) Significant temperature differences between gas and solid temperatures are present.

(e) Pseudo steady state conditions obtain for heat transfer.

1.3. AIMS AND APPROACH OF THE RESEARCH

It was considered necessary, at least initially, to study heat transfer under the above conditions independently of any effects from reaction kinetics or mass transfer. Thus it was decided to simulate these conditions in a non-reactive packed bed. This approach also has considerable experimental advantages:

(a) The bed does not need repacking with new solid reactant for each run.

(b) The achievement of purely axial heat flow is easier in a steady state non-reactive bed than in a moving zone reacting bed.

(c) Temperatures can be controlled at any desired level.

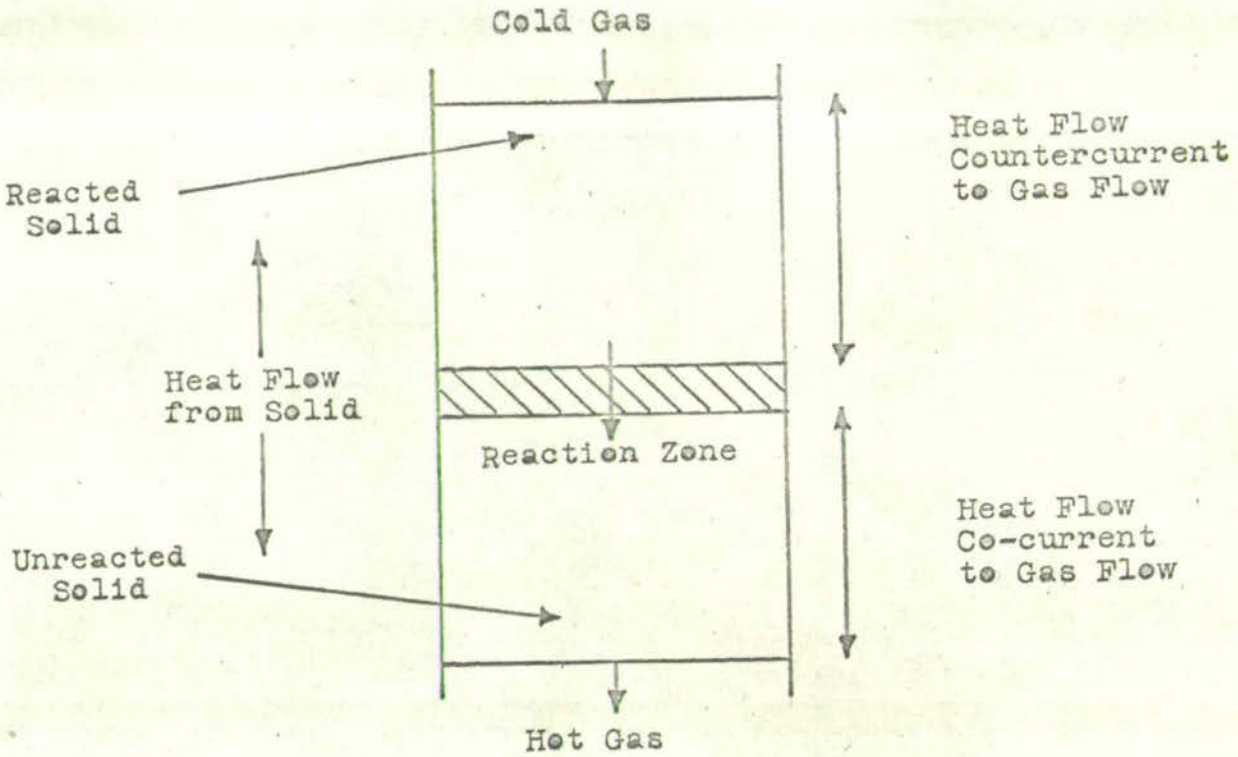

FIG. 1.2 DIRECTIONS OF GAS FLOW AND HEAT MOVEMENT IN A REACTING GAS-SOLID BED (EXOTHERMIC REACTION).

(d) Theoretical analysis and hence interpretation of experimental results is simplified. There is also the advantage that with this approach the work is more generally applicable to other packed bed heat transfer systems, for example, packed heat exchangers, catalytic packed beds, regenerators, porous cooling systems and thermal methods of petroleum recovery.

The literature on heat transfer in packed beds is voluminous but contains virtually no information for the combination of relevant conditions given above. Even at low temperatures the contributions of the various mechanisms are not fully understood and the theoretical models proposed are not adequately proven. Experimental elucidation is complicated by the fact that it is not possible to study the various heat transfer mechanisms independently of each other. It is however, possible to carry out experiments such that one type of mechanism predominates. For example, stagnant gas[1] conditions eliminate forced convection and at high temperatures radiation predominates compared with conduction, whereas at low temperatures the situation is reversed.

There are many factors which affect heat transfer in packed beds. These include gas velocity, gas temperatures, solid temperatures, relative directions of gas and heat flow, fluid properties, particle sizes and shapes, solid thermal conductivity and emissivity, the bed voidage and geometric packing characteristics. In the experimental work described

---

1. Non-flowing gas

here, attention has been concentrated on gas velocity and temperature level as variables. The theoretical models proposed in this work seek to account for the effect of the other factors as well.

Thus the object of the research is to study from both experimental and theoretical approaches, axial heat transfer in packed beds under conditions pertinent to moving zone, reacting, gas-solid systems with the aim of understanding the various heat transfer mechanisms involved and proposing adequate models.

1.4. STRUCTURE OF THE THESIS

Fig. 1.3 indicates the structure and inter-relation of the various sections of the thesis. Chapter two discusses the structure and fluid mechanics of packed beds in order to define the geometry and flow properties of the system on which all the heat transfer considerations are based. This leads to some new ideas on local voidage variations in random packed beds of equal-sized spheres. Chapter three investigates the literature on heat transfer in packed beds which has relevance to the present problem, and summarizes what is known about the effect of variables, the concept of effective thermal conductivity, the local mechanisms of conduction, convection and radiation, and theoretical models proposed to account for these.

Chapter four develops the theoretical models used in this work. This is done for mechanisms of conduction alone, conduction-radiation, conduction-convection, and finally conduction-convection-radiation.

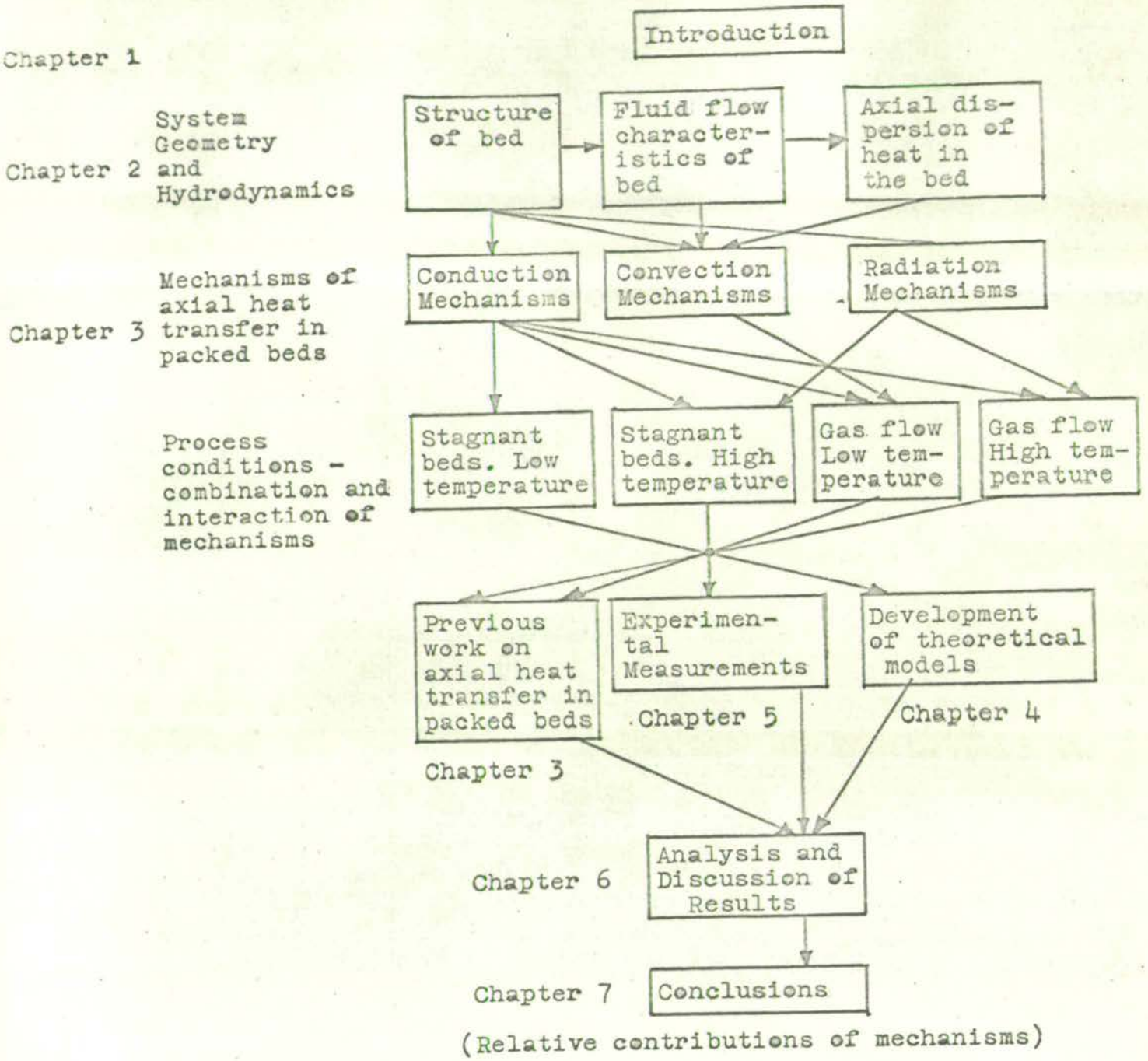

FIG. 1.3. STRUCTURE OF THE THESIS

Chapter five describes the experimental work, and gives the reasons for the choice of the experimental system, descriptions of the equipment, experimental method and procedure. Chapter six discusses the results and the comparison of these and the results of other workers with the theoretical models. Conclusions and suggestions for further work are given in Chapter seven.

2.1 STRUCTURE AND PROPERTIES OF A PACKED BED

2.1.1 Definition and Scope of a Packed Bed

A packed bed consists of an aggregate of individual particles of any size or shape which remain in contact with each other and are constrained to lie within a container of any size or shape. It follows that the structural nature of a packed bed has application beyond the diverse chemical engineering uses (1.1) to such varied fields of study as the structure of liquids, crystals and geological formations. This discussion is primarily concerned with elucidating the structure of random packed beds of equal sized spheres which is the geometry of the present experimental system.

In order to define both bulk and local geometric properties, a packed bed is considered to consist of an assembly of unit cells which are the smallest portions of the bed giving complete representation of the manner of packing and the distribution of voids throughout the bed. The non-solid or void space contained within a unit cell is called a unit void. It is assumed that the particles are non-porous and that no capilliary effects are present.

2.1.2 The Distinction Between Regular and Random Packed Beds

In a regular packing each particle is situated in a position which is fixed relative to the positions of each other particle in the bed and can vary only in orientation with respect to some fixed axis. Thus the various geometric properties of a regular packed bed are uniquely determined

Table 2.1. Structure and Geometric Properties of Regular Packings of Equal-sized Spheres.

* as used by Martin (1951)

Packing group	Packing name*	Packing order	Repeating packing layer patterns (Fig.A.1, A.2)	Layer Form	Unit cell volume $/D_p^3$	Unit void volume $/D_p^3$	Bulk mean voidage	Surface area/unit volume x D_p	Layer spacing $/D_p$	Coordination number n	Fractional Free area		no.spheres /per unit volume x D_p^3
											max.	min.	
Cubic	cubic no. 1	1	1	square	1.0	.467	.4764	3.13	1.0	6	1.0	.215	1.0
Ortho-rhombic	orthorhombic no.2. clear passage	2	1.2, 1.3	square	.867	.343	.3954	3.52	.866	8	.635	.215	1.15
	orthorhombic no.2.blocked passage	3	2.1.3	square									
	orthorhombic no.4.	1	1	triangular					1.0		1.0	.093	
Tetrag-onal sphenoidal	tetragonal sphenoidal no.5.clear passage	2	1.2, 1.3, or 1.4	triangular	.75	.226	.3019	4.19	.866	10	.580	.093	1.33
	tetragonal sphenoidal no.5.blocked passage	3	2.1.3, 2.1.4, or 3.1.4.	triangular									
Rhombo-hedral	rhombohedral no.3 (pyramidal)	2	1.4	square	.708	.184	.2595	4.44	1707	12	.349	.214	1.41
	rhombohedral no.6.clear passage(close packed hexagonal) (tetrahedral)	2	1.5 or 1.6	triangular					.816		.455	.093	
	rhombohedral no.6.blocked passage(face centred cubic)	3	5.1.6	triangular									

(Table 2.1). Similarly the extension of a regular packing is governed by deterministic rules since there are only a finite number of well specified sites to which one can add new particles. (Fig.A.1., A.2.)

In contrast, for a random packing the position of each particle relative to other particles is described by probability considerations limited by geometric constraints. The geometric properties of a random packed bed take the form of stochastic parameters which have probability distributions. Apart from stability considerations, the sites available for the extension of a random packing are limited only by the criterion that two particles cannot overlap.

Local variations in voidage are present in both regular and random packed beds (Fig. 2.1). In a cubic packing, for example, the local voidage,[1] ε', relative to a reference plane between sphere layers shows variations between unity and 0.41 even although the bulk mean voidage, ε, remains constant at .476. Appendix 2 outlines the structure of regular packings of equal sized spheres.

In a random packed bed, due to the stochastic nature of the packing, probability distributions are obtained for the local mean voidage relative to some reference point (2.1.4). Bridging or arching of particles can lead to large voids in random packing (e.g. Brown and Hawksley (1945, 1954)) particularly for irregular particles, and when a bed of

---

1. Definitions of the various voidage terms and the other properties of packed beds are given in Appendix 1.

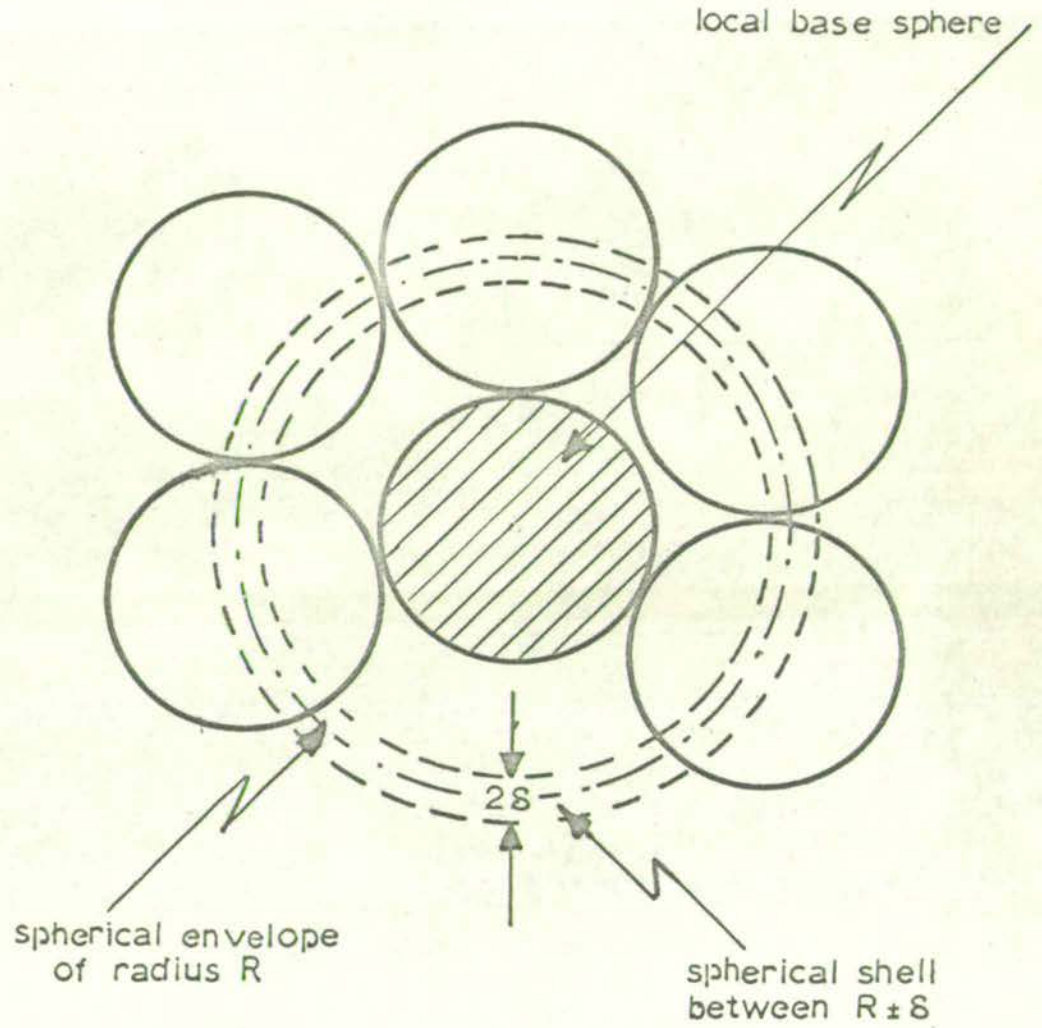

FIG. 2.1 LOCAL STRUCTURE OF RANDOM PACKED BED

granular material commences to flow through an opening (e.g. Wohlbier and Reisner (1962)). The opposite effect of clustering of particles can produce regions of regular packing with low voidages (Barker (1965)). Wadsworth (1960) has shown that random packings tend towards a rhombohedral arrangement particularly near the bottom of a container. Shearing of a random packing also tends to promote the growth of "crystals" of regular packing (e.g. Bernal et al (1964)).

A random packing is produced by placing particles haphazardly into a container, for example, by pouring, or by reducing the velocity of a fluidised bed below the minimum fluidisation velocity. In contrast to regular packings in which unit cells are identical throughout the bed, the structure of unit cells for random packings varies throughout the bed and must be described by some form of stochastic model.

2.1.3 Models for Random Packings

(i) polyhedra models

Bernal (1959, 1960, 1963, 1964) interpreted a random packing of equal sized spheres in terms of the neighbour polyhedra formed around each sphere in the bed. The points of the polyhedra were obtained by bisecting the lines joining a sphere centre to the centres of neighbouring spheres which may or may not have touched the base sphere. Bernal examined the frequency of occurrence of the possible polyhedral arrangements and found a predominance of pentagonal faces. Wise (1952, 1960) and Hogendijk (1963) interpreted these

polyhedra in terms of component tetrahedra. Levine and Chernick (1965) used a unit cell based on the polyhedron formed by a base sphere and touching neighbours only.

(ii) coupled sphere model

A unit cell in which an integral number of touching spheres were coupled to form a cohesive unit was used by Blum and Wilhelm (1965).

(iii) local sphere shells models

Models in which shells of spheres were centred at certain fixed distances from a base sphere were used by Haughey and Beveridge (1966). A triangular close packed model and a triangular equispaced model were used to describe the limits of the local stochastic packing for possible values of the base sphere coordination number, n. The construction of these models is given in Appendix 3.

(iv) Monte Carlo models

In the simplest Monte Carlo models spheres were placed at random in a container and any position which did not satisfy the non-overlap position was rejected (Bernal (1960, 1964)). This method was applied by Griffith (1962) and Smalley (1962) to the packing of one-dimensional O-spheres, i.e. line intervals along a straight line. However, this process is computationally wasteful since a large number of trials are necessary to find a non-overlapping position when the packing is almost complete (Fluendy and Smith (1962)).

In a two-dimensional application, Round and Newton (1963) avoided this problem by displacing any overlapping spheres to accommodate a new sphere. An alternative solution was used by Levine and Chernick (1965) for packing around a local base sphere, by stopping the calculation when the number of trials necessary became large and then arbitrarily filling any holes which would accommodate another sphere.

Another approach which has often been applied to the equation of state for hard sphere molecules is to start with the spheres in a regular packing lattice in a unit container. Spheres selected at random are then given attempted random displacements. An effectively infinite packing is simulated by the application of periodic boundary conditions which are equivalent to the unit container being surrounded by identical containers. This method has been applied in two dimensions (Alder, Frankel, Lewinson (1955)) and to the three-dimensional packing of equal sized spheres[1] and unequal sized spheres (Smith and Lea (1960), Rotenburg (1965)).

(v) void models

For the estimation of flow properties in packed beds (for example, pressure drop and fluid dispersion), models of the void structure of the bed are required. Scheidegger (1953, 1954, 1960) reviewed the straight and serial types of capilliary models. Random networks of different sized capilliarieshave also been used (e.g. Fatt (1956), Saffman (1960)).

---

1. Metropolis, Rosenbluth and Teller (1953); Rosenbluth and Rosenbluth (1954); Alder and Wainwright (1957); Wood and Jacobsen (1957); Wood and Parker (1957); Bernal (1960,1964).

Harris (1965) used the rows and columns of a Latin Square to simulate the pore size distribution, while Lamb and Wilhelm (1963) used a size distribution of interconnected spherical holes. Turner (1958, 1959) proposed a model consisting of tubes with recessed pockets in which the fluid would be stagnant.

The mixing cell model, in which the voids are considered equivalent to interconnected mixing tanks, is discussed in 4.3. The packed bed voids may also be considered as fluid envelopes which have the average properties of the fluid in the bed and which surround each sphere.[1]

2.1.4 Properties of Random Packings[2]

Bulk Properties

(i) overall voidage, ε_0, and bulk mean voidage, ε

The methods available for the measurement of voidage have been discussed by Scheidegger (1960) and Denton (1957). These include volumetric displacement of a fluid, bulk density measurement by weighing, and a gas expansion method.

The range of voidage values obtained for the random packing of equal sized spheres, enables four modes of packing to be distinguished. (Table 2.2).

a) very loose random packing: The loosest possible random packing is obtained by slowly reducing the fluid velocity in a fluidised bed of spheres to below the minimum

---

1. Ranz (1952); Pfeffer (1964); Pfeffer and Happel (1964); Happel and Brenner (1965).
2. Definitions of the bed properties are given in Appendix 1.

Table 2.2. Voidage and co-ordination numbers for types of random equal-sized sphere packings.

Type of Packing	Bulk mean Voidage, ε	Co-ordination number, n close	near	total	References*
Very loose random	0.44				1
Loose random	0.40-0.41	5 - 6		7 - 8	2,4,5,6,
	0.40	(mean 5.5)		(mean 7.1) ..	3
Poured random	0.375-0.391				7,8,9
	0.375			8	
Close random	0.359-0.375	6 - 7		8 - 9	10,5,6,4
	0.36	(mean	1 - 2	(mean	
	0.38	6.4)		8.5) ..	3
Random packing with wall effects					11,8,9

*1. Lamb and Wilhelm(1963).
2. Smith, Foote, Busang(1929); Oman and Watson(1944); Rice(1944); Happel(1944); Scott, Charlesworth, Mak(1964); Epstein and Young(1962).
3. Bernal and Mason(1960).
4. Scott(1960).
5. MacCrae(1961) and Gray(1961).
6. Rutgers(1962).
7. Westman and Hugill(1930); Wadsworth(1960).
8. Carman(1937).
9. McGeary(1961)
10. Denton(1957); Scott(1962); Bernal, Mason and Knight(1962).
11. Sullivan and Herdel(1940); Zhavoronkov(1944); Verman and Banerjee(1946); Brown and Hawksley(1946); Leva and Grummer(1947); Aerov(1951); Mott(1951); Sonntag(1960); Jeschar(1964).

fluidisation velocity when the spheres settle to a mean voidage of about 0.44.[1]

b) loose random packing: Values around 0.40[1] are obtained by packing the spheres so that they roll into place over similarly placed spheres, by individual random hand packing, by dropping the spheres into the container as a complete loose mass, or by rapid inversion of a container of particles. The model of Levine and Chernick (1965) gave a voidage of 0.391. The Monte Carlo models usually produce bulk mean voidage values representative of loose packings since no shaking down is accounted for.

c) poured random packing: When spheres are poured together into a container as is often the case in packing an industrial bed, values around 0.38[1] are obtained. The coupled sphere model of Blum and Wilhelm (1965) gives a value of 0.388 for three sphere coupling.

d) close random packing: The minimum voidage values of around 0.36[1] are obtained when the bed is vibrated or shaken down vigorously.

Successive repacking of a bed by the same packing method gives voidage values which have a normal distribution around the most probable value. For random packing of equal sized spheres Denton (1957) obtained a range of .009 and a standard deviation of .0016 for a most probable voidage of 0.391.

The effect of a rigid container wall enclosing a packing is to increase the overall voidage due to the increase in local

---

1. Higher values for the overall voidage, ε_0, will be obtained if the wall effect is significant.

voidage in the region near the wall. The effect of the ratio of the particle diameter to container diameter has been examined experimentally for spherical, cylindrical, and irregular particles and Raschig rings (references are given in Table 2.2). It is generally concluded that the effect of the container wall is negligible (i.e. $\varepsilon_0 = \varepsilon$) for D_T/D_P greater than about 10 with a somewhat higher limit for irregular particles. Verman and Banerjee (1946) used the relationship.

$$1-\varepsilon_0 = C_1^3(1-\varepsilon) + (1-C_2^3)(\varepsilon_W - \varepsilon) \quad \ldots.(2.1)$$

where $C_1 = 1-D_P/D_T$, $C_2 = 1-2\delta_W \cdot D_P/D_T$ and δ_W and ε_W are respectively the width (in particle diameters) and voidage of the wall layer. Aerov (1951) applied this equation to sphere packings and obtained $1-\varepsilon_0 = C_1^2(.61 + .288(1/C_1^2 - C_3^2))$ .... (2.2) where C_1 and C_2 are as above and $C_3 = (D_T/D_P-2)/(D_T/D_P-1)$. The data of Sonntag (1961) and Jeschar (1964) for spherical packings give the equation $\varepsilon_0 = \varepsilon + 0.34\, D_P/D_T$ ....(2.3) where $\varepsilon = .36$ for close random packing and $\varepsilon = .39$ for loose random packing.

Many workers (e.g. Westman and Hugill (1930); McGeary (1961); Yerazunis, Cornell and Winter (1965)) have made experimental studies of the voidage obtained with mixtures of two or more particle sizes. When smaller particles are mixed into a bed of larger particles there are two opposing effects which produce an optimum component composition giving the minimum voidage. The smaller particles tend to increase the voidage by forcing the larger particles apart and tend to decrease the voidage by filling the voids formed by the larger particles.

In a theoretical calculation Horsfield (1934) showed that filling the voids by five successive diminishing sphere diameters would give a theoretical minimum voidage of 0.1481. Other theoretical studies have been made by Hudson (1949) and Wise (1952,1960).

Oman and Watson (1944) measured dense and loose random packing voidages for various particle shapes. The voidage increased in the order cylinders, spheres, granules, Raschig rings, Berl saddles. For irregular particles, overall voidage values vary widely (e.g. Wadell(1935)).

(ii) solid surface area, S

For equal sized spheres the solid surface area, S is given by (equation A.2) $S=6(1-\varepsilon)/D_p$ ....(2.4)
This equation is also applicable to other shaped particles by replacing D_p by ψD_{pe} where ψ is a shape factor (e.g. Gamson (1951), Brown et al (1952)) and D_{pe} is an equivalent spherical diameter (e.g. Chechetkin (1957), Oman and Watson (1944)). Solid surface areas for irregular particles have been given by Carman (1956), Jones and Mills (1961) and others.

(iii) layer spacing, βD_p

Since the regular packing form to which random packed beds of equal sized spheres tend is rhombohedral (Wadsworth (1960)), the simplest way of evaluating the layer spacing, βD_p is on the basis of a rhombohedral unit cell in which the spheres are moved equally apart to give the bulk, mean voidage, ε, corresponding to the random packing. It may thus be proved (Smith (1931)) that $\beta = \sqrt{\frac{2}{3}}\left[\frac{\pi}{3\sqrt{2}(1-\varepsilon)}\right]^{\frac{1}{3}}$ .... (2.5)

This relationship was used for heat transfer in packed beds by Hill and Wilhelm (1959).

(iv) tortuosity, χ

The true estimation and definition of tortuosity are open to doubt. (Scheidegger (1960)). Discussion is more often in terms of χ^2 which is the proportionality factor for the laminar flow velocity (Carman (1956)). Bartell and Osterhof (1928) used $\chi^2 = \pi/2$ which is the ratio of the circumference to the diameter of a circle. Carman (1937) used $\chi^2=2$ based on the observation that dye streamlines adopt an average angle of 45° to the flow direction. Assuming that the fluid always flows in a direction parallel to the surface nearest it, Fowler and Hertel (1940) obtained $\chi^2=1.5$.

Ionic conductivity measurements have also been used to evaluate tortuosity which is slightly dependent on voidage, ε. From conductivity measurements for random packed glass spheres (ε =.388-.435) Klinkenberg (1951) and Cornell and Katz (1954) obtained χ^2=1.41-1.43. This value is based on the somewhat doubtful (Carman (1956)) assumption that the effective molecular diffusivity in a packed bed is the fluid molecular diffusivity multiplied by χ^2.

Local Properties

(v) distribution of inter-particle distance, RD_p

Measurement of the coordinates of each sphere centre in a random packed bed enables the radial distribution of sphere centres relative to a base sphere centre to be calculated. This has been done for close random packing by Scott (1962)

and Bernal, Mason and Knight (1962) and for loose random packing by Scott, Charlesworth and Mak (1964). Curve A of Fig. 2.2 (Scott (1962)) shows the damped wave nature of the distribution. At any given value of R there is a distribution of $\frac{N_{AV}}{4\pi R^2}$ about the mean value shown on the curve. Using much more closely spaced radial intervals, Mason and Clark (1965) obtained more detail in the range R=1.0-1.35. The radial distributions calculated from the various Monte Carlo models generally show a similar result to Fig. 2.2, but the local Monte Carlo model of Levine and Chernick (1965) shows marked differences.

Fig. 2.2 also shows the radial variation of the total number of spheres cut per unit area by a spherical envelope of radius RD_P. This was calculated from the data of Scott (1962) by summing over the five shells centred at $(R + \beta^*)D_P$ for $\beta^* = \pm.4, \pm.2, 0$ giving

$$\frac{N_T}{4\pi R^2} = \frac{1}{4\pi R^2} \sum_{\beta^*} 4\pi (R+\beta^*)^2 \frac{N_{AV}}{4\pi (R+\beta^*)^2} \quad \ldots\ldots(2.6)$$

From the coordination number data of Bernal and Mason (1960) the value of $(N_T/4\pi R^2)_{R=\frac{1}{2}}$ can be found to be $8.5/\pi$. It is not possible to obtain the standard deviation from Scott's work since the standard deviations of adjacent shells are not independent.

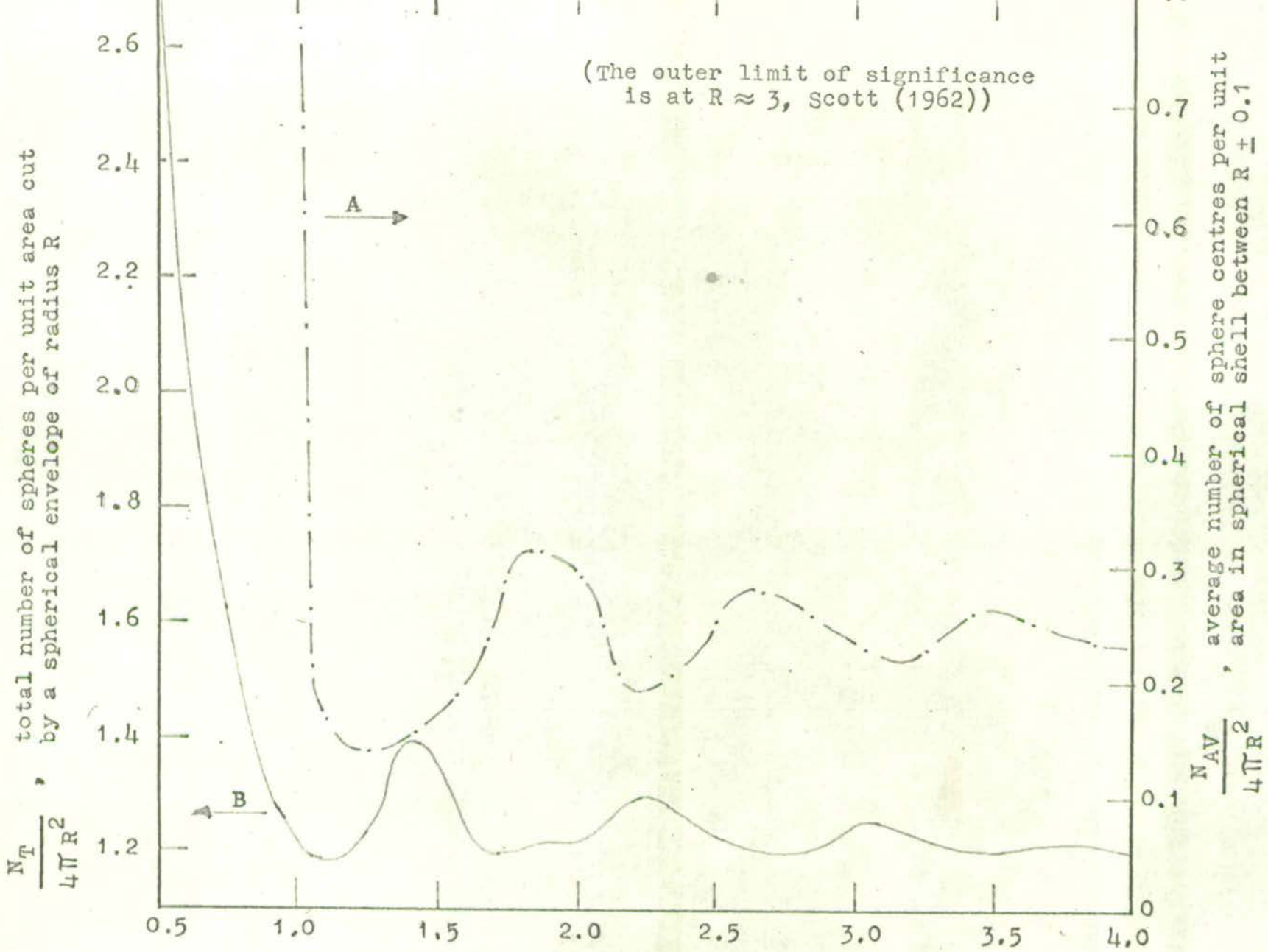

FIG. 2.2 THE RADIAL DISTRIBUTIONS OF SPHERES RELATIVE TO A BASE SPHERE

(vi) distribution of coordination numbers

The earliest measurements of the coordination numbers of spheres in random packings were made by Smith, Foote and Busang (1929), but these are open to criticism since lead spheres were used which are liable to deformation with heavy tamping and the overall voidage values are apparently incorrect (Wadsworth (1960)). Bernal and Mason (1960) obtained coordination numbers free from wall effects for the closest and loosest random packings of equal sized steel spheres. They distinguished between close contacts, where the spheres actually touched the base sphere, and near contacts where the spheres almost touched (Table 2.2). The distributions are approximately normal about the mean values (Fig. 2.3). Wadsworth (1960) using the same paint marking technique found little effect of container size on the distribution for poured random packings. He did not distinguish between the two types of contact and the distribution obtained (Fig. 2.3) lay between the total contact distributions of Bernal and Mason. Bennett and Brown (1940) made similar measurements for irregular particles.

Fig. 2.4 shows the average coordination number for random packings plotted against the overall voidage. The model of Haughey and Beveridge (1966) (Appendix 3) gives $n = 22.47 - 39.39\varepsilon$ - and this fits the experimental data better than the model of Levine and Chernick (1965) or the relationships of Smith, Foote, Busang (1929) and Kunii and Smith (1960) derived from consideration of regular packings.

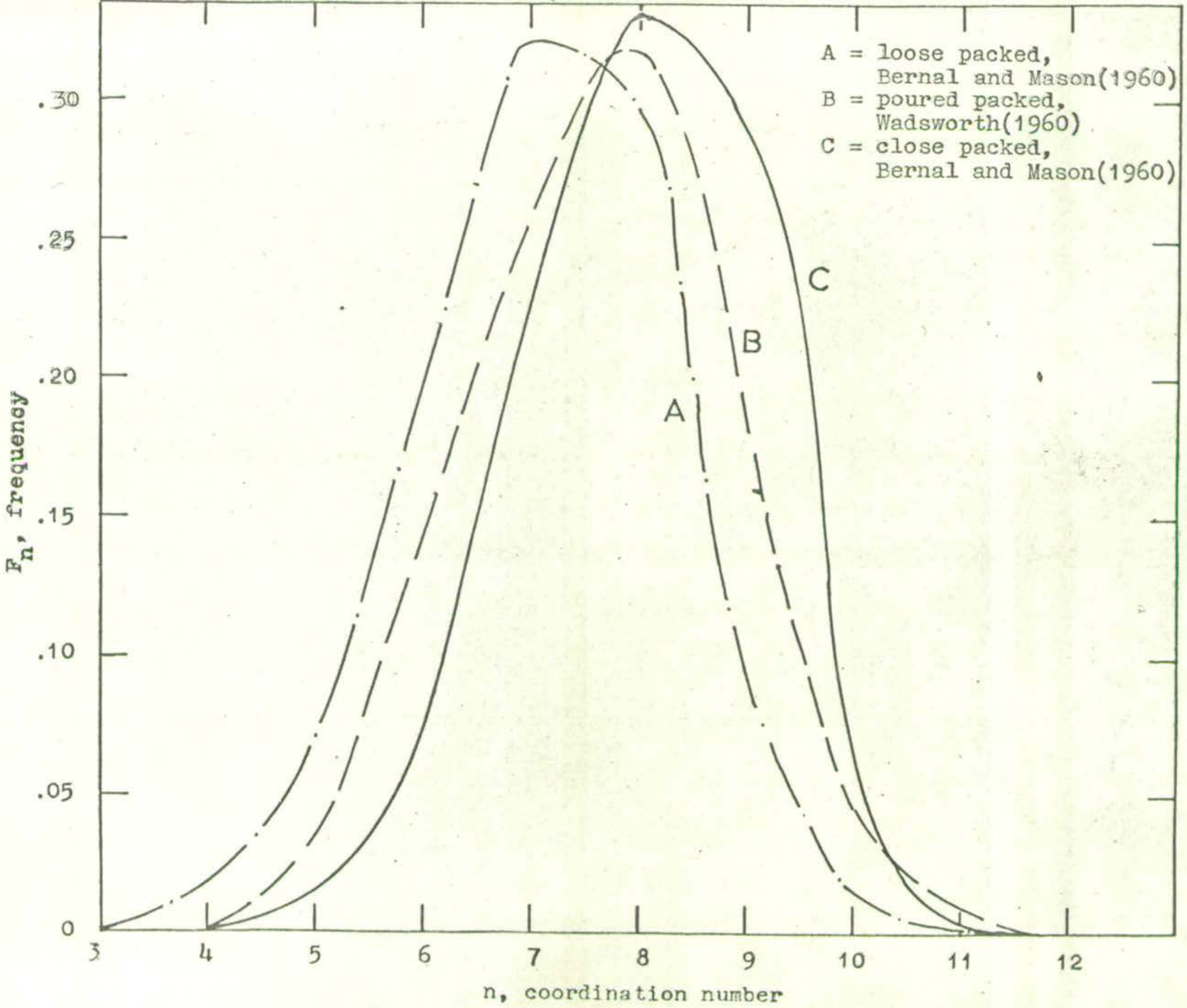

FIG. 2.3 EXPERIMENTAL COORDINATION NUMBER FREQUENCY DISTRIBUTIONS FOR A RANDOM PACKED BED

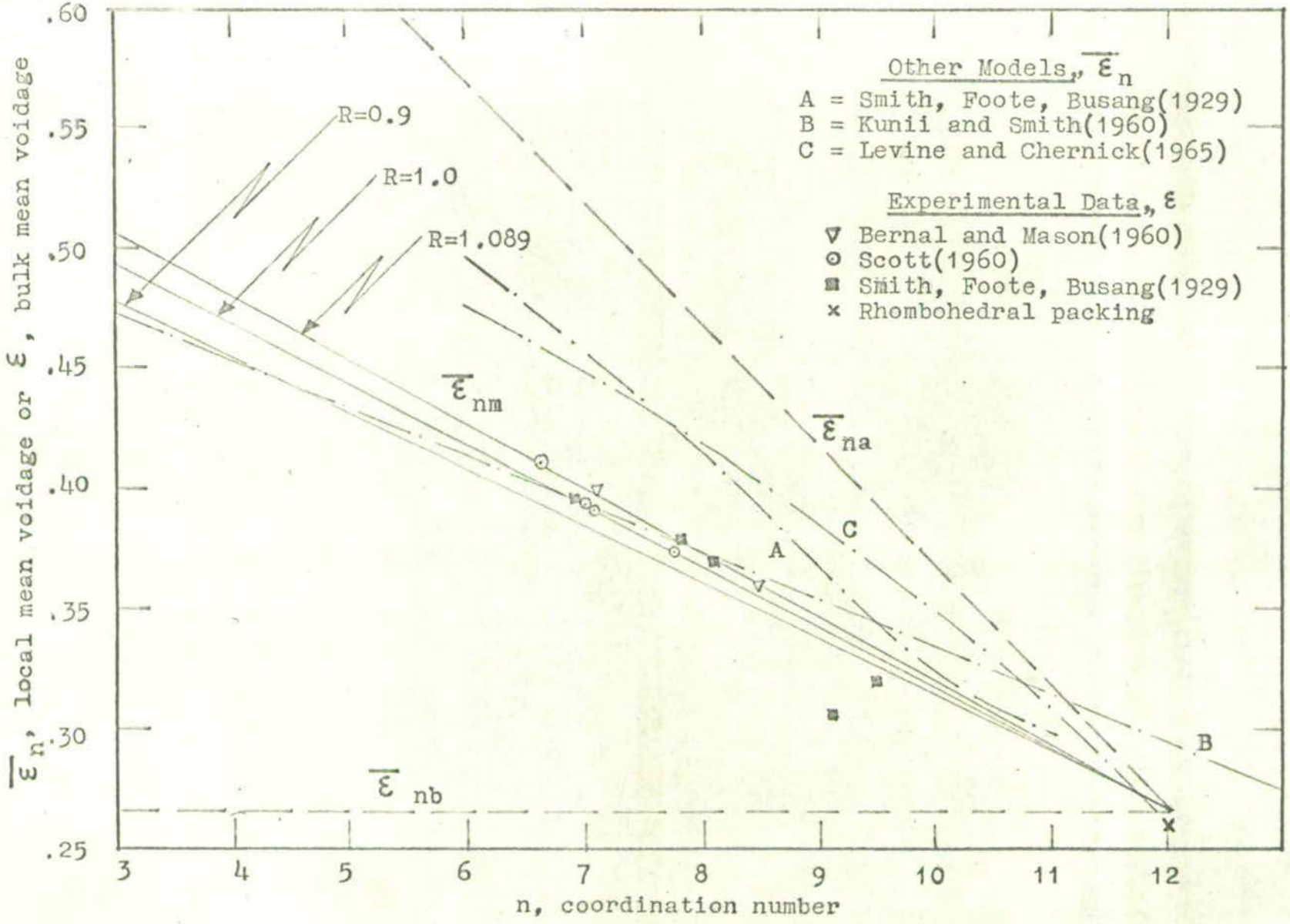

FIG.2.4. COMPARISON OF MEAN VALUES OF THE LOCAL MEAN VOIDAGE, $\overline{\varepsilon}_n$

Marvin (1939) applied axial compression to a random packing of lead shot. A moderate compression gave an average coordination number of 8.41 which compares well with the total coordination number measurement of 8.5 obtained by Bernal and Mason (1960) for close random packing. When the compression applied was such that all voids were eliminated the average coordination number was 14.16. This indicates that the total number of nearest neighbours enclosing a sphere is about 14. Matzke (1939) made similar measurements for a mixture of two sizes of lead shot.

The coordination number distribution calculated from the theoretical model of Levine and Chernick (1965) does not agree particularly well with the experimental distributions. Blum (1964) obtained a theoretical distribution for a two dimensional random packing of circular discs based on the coupled sphere model.

(vii) angular distribution of contact points available

The only experimental data for the angular distribution of contact points were obtained by Scott and Mader (1964), and showed a significant amount of angular structure (Fig.2.5). The distribution given by the theoretical model of Levine and Chernick (1965) shows qualitative agreement (Fig.2.5).

(viii) distribution of local mean voidage

As a basis for calculating local transport property variations, Haughey and Beveridge (1966) determined the variation in local mean voidage, $\bar{\varepsilon}$, in a randomly packed bed of equal sized spheres (Fig. 2.6). The triangular close packed and triangular equispaced shell models were used to determine the maximum

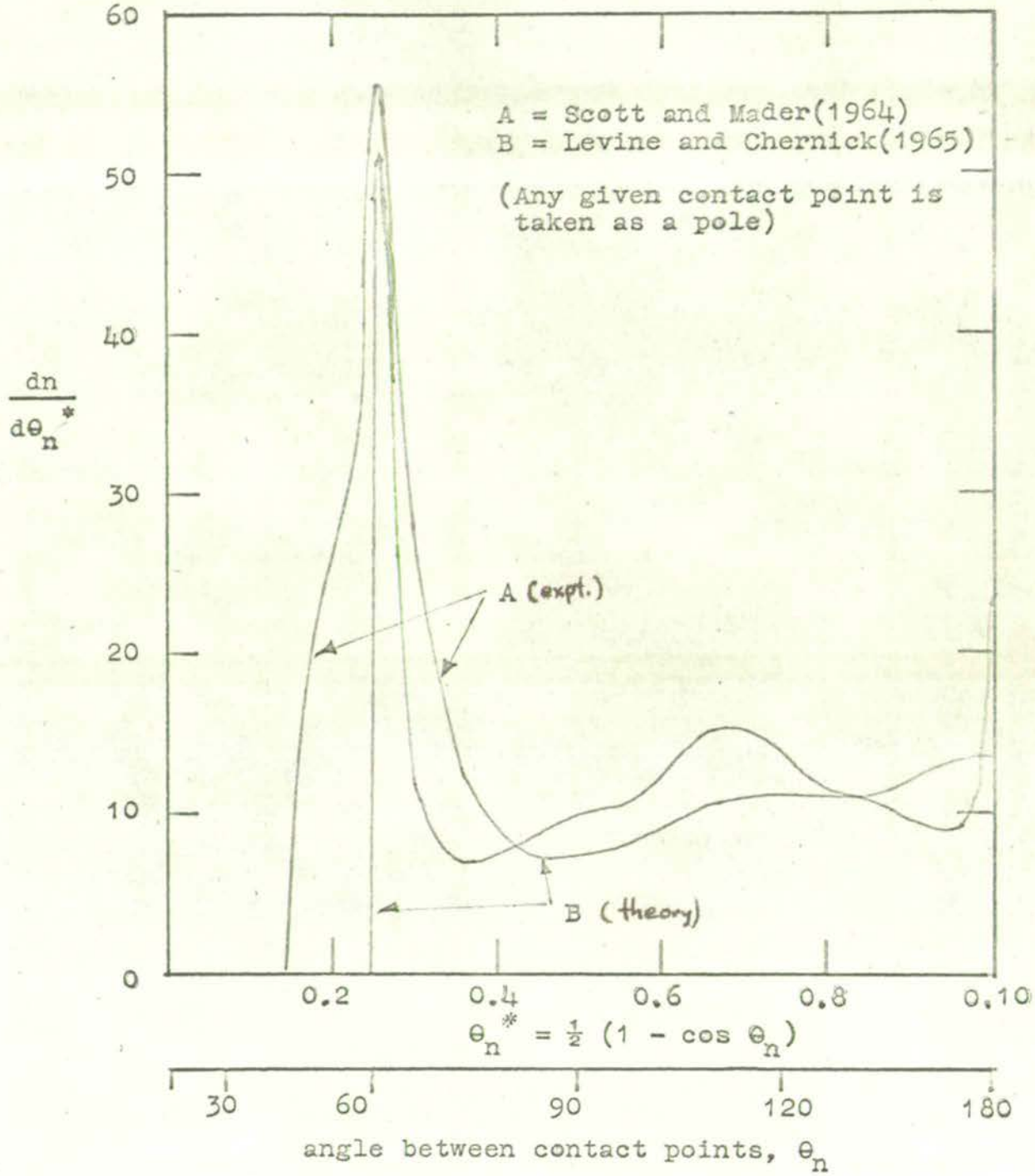

FIG. 2.5 ANGULAR DISTRIBUTION OF CONTACTING SPHERES AROUND A SPHERE IN A RANDOM PACKED BED

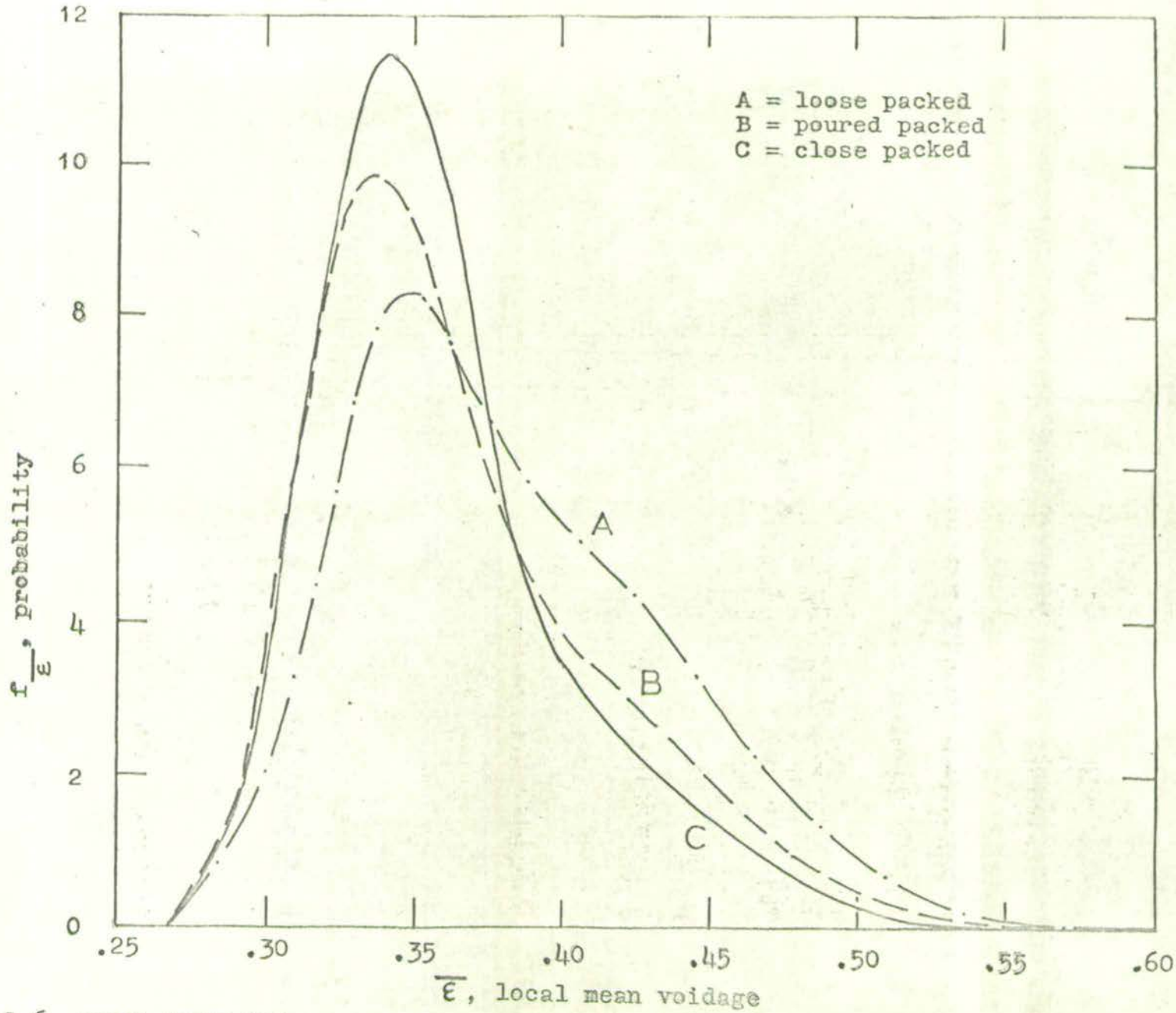

FIG. 2.6 LOCAL MEAN VOIDAGE PROBABILITY DISTRIBUTION, $f_{\bar{\varepsilon}}$, FOR RANDOM PACKING

and minimum local mean voidages, $\bar{\varepsilon}_{na}$, $\bar{\varepsilon}_{nb}$ for a given coordination number, n. A normal distribution between these limits was then assumed on the basis of the measurements of Denton (1957). The distributions for each n were then combined with an experimental coordination number frequency distribution to obtain the local mean voidage distribution. The method is fully explained in Appendix 3.

The distributions obtained in this way were skewed and resembled beta distributions. This is due to the existence of a definite lower limit for the local mean voidage dictated by the closest possible local packing, while the upper limit varies for each coordination number. Over a region of two sphere diameters (R=1.0) around any sphere the standard deviation in the local mean voidage is 12 - 14% of the mean value, compared with a standard deviation about the mean value of .41% for the bulk mean voidage (Denton (1957)).

To define the unit cell it was assumed that R=1.0 and this choice was confirmed by the fair correspondence of the average local mean voidage values with bulk mean voidage values both for each value of the coordination number (Fig.2.4) and for the complete distribution (Table A.2). Exact correspondence with the bulk mean voidage may be obtained by adjustment of the position of the mean value of the local mean voidage between the limiting values (Appendix 3.5). This was done in Fig. A.9 for a voidage of 0.40 which corresponds to the present experimental system.

Haughey and Beveridge (1966) also calculated the variation

of the local mean voidage with distance from the reference point (Fig.2.7), both using the local sphere shells models and using Scott's (1960) inter-particle distance data. For packing against a cylindrical wall, this variation has been measured by Roblee, Baird and Tierney (1958) and Benenati and Brosilow (1962) (Fig.2.7).

(iv) distribution of local surface areas

This may be obtained from the distribution of local mean voidage and equation 2.4 which relates the surface area to the voidage. (Appendix 4)

(x) distributions of local hole size and volume

Direct experimental methods of measuring pore size distribution are discussed by Carman (1956) and Scheidegger (1957). The effect of grain size on pore size for irregular particles has been reviewed by Scheidegger (1957). The distributions of local sizes and volumes may be obtained from equations A.6 and A.7 which relate these quantities to the voidage. The first moment of the hole size distribution is given by equation A.10.

(xi) distributions of local area and volume fractions

Thoenes (1957) and Greenaway (1959) obtained local area fraction data for a plane cut through random packings of spheres and Raschig rings respectively. The two dimensional equivalent channel diameter distribution of Thoenes (1957) and the three dimensional local mean voidage distribution of Haughey and Beveridge (1966) show qualitative agreement.

Brown and Hawksley (1945) measured local volume fractions for a two dimensional packing of spheres (one layer thick).

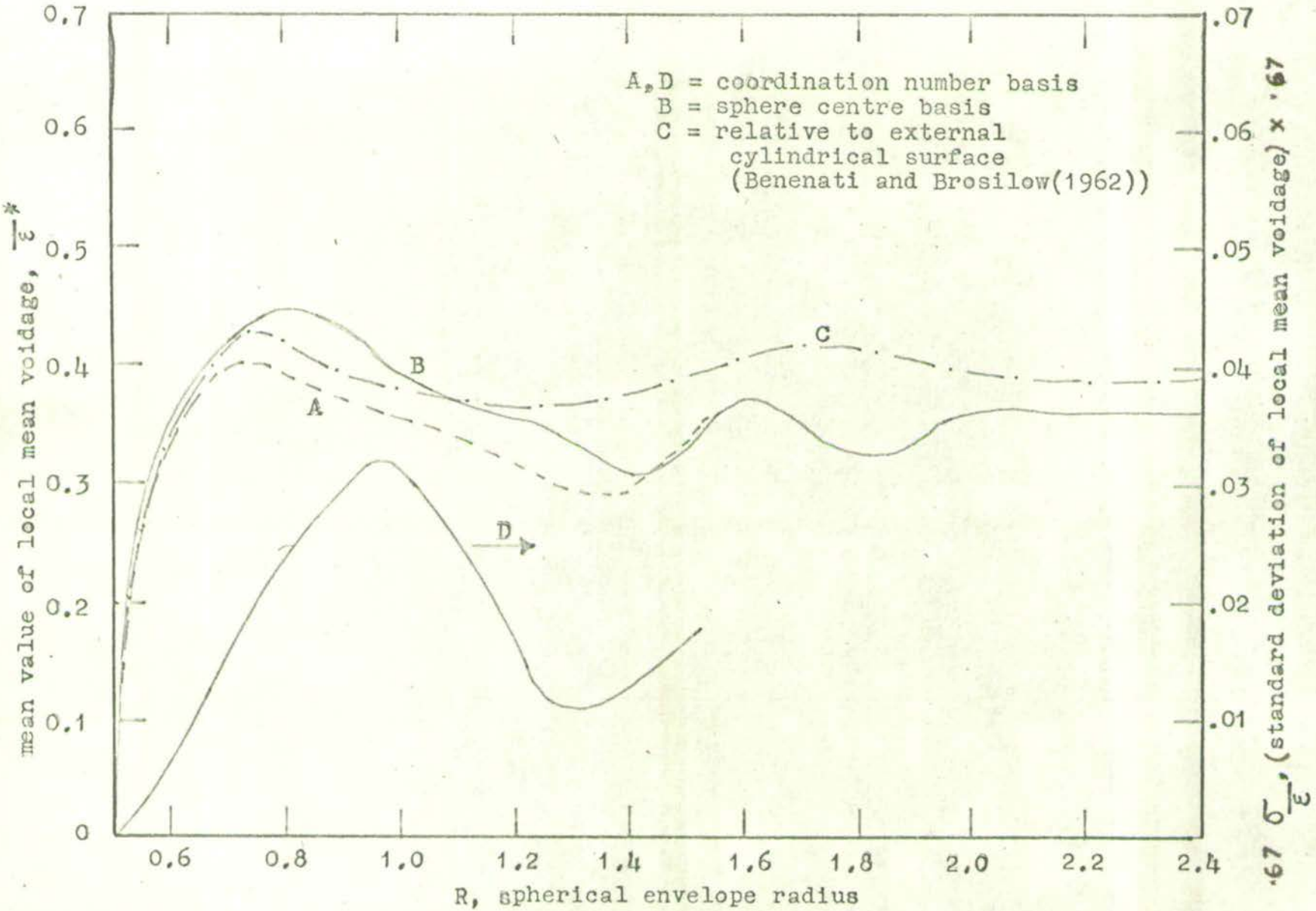

FIG. 2.7 EFFECT OF ENVELOPE RADIUS, R, ON MEAN VALUE AND STANDARD DEVIATION OF LOCAL MEAN VOIDAGE, $\overline{\varepsilon}$

Local volume fraction measurements in three dimensional beds have been made in a finite bed by Thadani and Peebles (1966) and for packing against a cylindrical wall by several workers[1] who obtained a damped cyclic variation (Fig. 2.8). Based on the sphere centre data of Scott (1960), Haughey and Beveridge (1966) (see Appendix 3) obtained similar variations for the local voidage in shells around a base sphere (Fig. 2.8).

For a slice through a random packing, the area fraction, ε'_A, is equal to the bulk mean voidage (Reid (1955) ; Coulson and Richardson (1959), Blum and Wilhelm (1965)). The area fraction may be related to the average number of spheres cut per unit area, N_T/A, by a cross-sectional slice. Blum and Wilhelm (1965) showed that

$$1 - \varepsilon'_A = \pi/6 \left(\frac{N_T}{A}\right)^3 \qquad \ldots\ldots (2.7)$$

and obtained values for the mean and variance of N_T for two and three coupled sphere units.

The size distribution of a mixture of sphere sizes may be determined from the size distribution of circles for a slice through the packing (e.g. Fromm (1948); Lenz (1954)).

(xii) <u>distribution of local layer spacings</u>

This may be obtained from the distribution of local mean voidage and equation 2.5 which relates the layer spacing to the voidage. (Appendix 4)

---

1. Speck (1955); Kimura and Kaeda (1955); Roblee, Baird, Tierney (1958); Sonntag (1960); Benenati and Brosilow (1962); Chiam (1962).

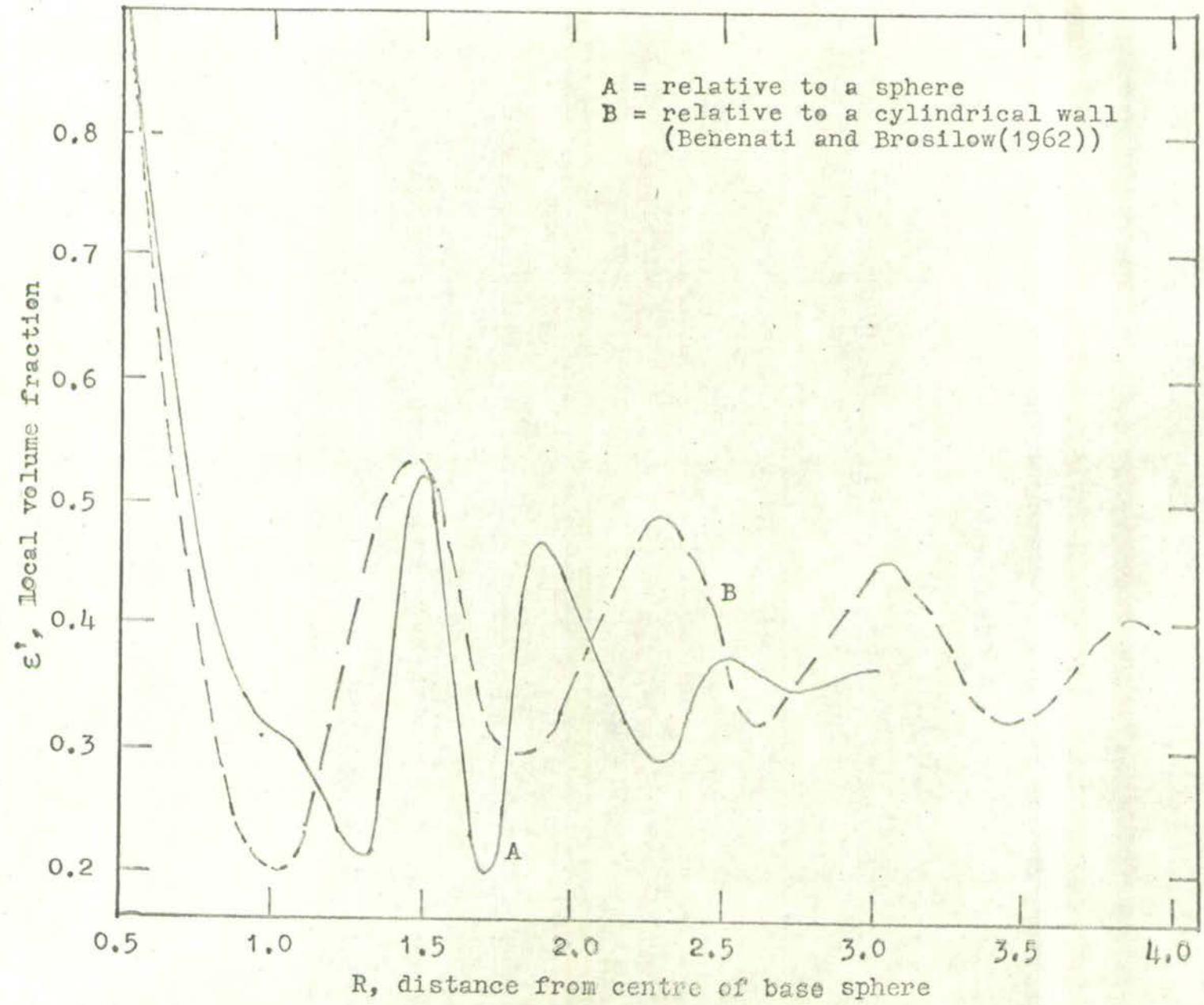

FIG. 2.8 VARIATION OF LOCAL VOLUME FRACTION WITH RADIUS R

2.2.1. Nature of the Fluid Flow

In packed beds there is no sharp transition from laminar to turbulent flow as in open tubes. This is shown most clearly from pressure drop measurements which indicate a broad transition zone over an approximate range of interstitial Reynolds numbers, $Re^* = 10 - 1000$ for spherical particles (e.g. Perkins and Johnston (1963)).

The method of packing can have a marked effect on the nature of the fluid flow since the various regular packings of equal sized spheres (Table 2.1) show considerable differences in pressure drop and friction factor values.[1] Many experimental investigations have been made for random packings over a large range of particle sizes, shapes and fluid flow rates.[2] Probably the most widely accepted correlation is that of Ergun (1952) who obtained

$$\frac{\Delta P}{L} = 150 \frac{(1-\varepsilon)^2}{\varepsilon^3} \left(\frac{\mu v_0}{D_P^2}\right) + 1.75 \left(\frac{1-\varepsilon}{\varepsilon^3}\right) \frac{G v_0}{D_P} \qquad \ldots.(2.7)$$

where the first term accounts for viscous energy loss and the second term for kinetic loss. Brinkman (1947) made a theoretical estimation of the viscous loss. More recently Aerov (1963) obtained

$$\frac{\Delta P}{L} = \frac{v_0^2 \rho}{2g} \left(\frac{S}{\varepsilon^3}\right) \left[\frac{8C_1}{Re'} + C_2\right] \quad (Re' > 6) \qquad \ldots.(2.8)$$

and

$$\frac{\Delta P}{L} = v_0 S^2 C_1/\varepsilon^3 \quad (Re' < 6) \qquad \ldots.(2.9)$$

where $Re' = \frac{4 v_0 \rho}{S \mu}$ and C_1 and C_2 are structural constants.

---

1. Martin (1951); Galloway, Komarnicky and Epstein (1957); Chiam (1962); Wentz and Thodos (1963).
2. Reviews are given by Carman (1937, 1956); Scheidegger (1960); Zenz and Othmer (1960); Chiam (1962); Chechetkin (1957).

The pressure drop in a packed bed may also be interpreted as equivalent to the pressure drop produced by flow through a rough pipe (Gay and Alcorn (1962); Lebedev and Petrov-Denisov (1964)) or by flow around a single sphere (Ranz (1952)) or bank of tubes.

.2.2. Velocity Profiles in Packed Beds

(i) downstream velocity profiles

Because of the difficulty of making velocity measurements within the voids of a packed bed, most investigations have measured velocity profiles downstream of the packing. A variety of experimental methods have been used, including:

a) flow rate measurement in individual annuli placed at the outlet to the bed (Arthur et al(1950); King (1965)).

b) analysis of chemical reaction products or gas adsorption in different annuli of the bed (Arthur et al(1950)).

c) pitot tube measurements of point velocities (Saunders and Ford (1940)).

d) hot wire anenometer measurements of point velocities (Schwartz and Smith (1953); Rhoades (1964); Mickley, Smith, Korchak (1965)).

e) circular hot wire anenometer measurement of the average velocity at a given radial position (Morales, Spin and Smith (1951); Calderbank and Pogorski (1957)).

f) thermal conductivity probes (Prausnitz and Wilhelm (1957); Cairns and Prausnitz (1959); Lamb and Wilhelm (1963)) or electrode probes (Akehata and Sato (1958)).

These methods have been used to measure velocity profiles for both gas[1] and liquid[2] flow in beds of spherical, cylindrical and irregular particles.

The measurements show that there are marked local velocity variations over a distance of 1 - 2 particle diameters due to the jet effect of the fluid leaving a void. Coberly and Marshall (1951) obtained variations as great as 100% just above the packing surface. The jet effect decreases markedly with the distance between the velocity probe and the packing surface (Morales, Spin, Smith (1951)) and can also show angular variations due to local voidage variations caused by the local packing arrangement.

There may also be marked velocity variations across the bed diameter. These variations are greatly dependent on the bed inlet and outlet conditions. Any variations in flow resistance over different parts of the bed at the fluid outlet are reflected in the velocity distribution across the bed and the greater the variation in inlet velocity, the greater the variation in the fluid distribution downstream from the bed. For the parabolic velocity profile characteristic of well developed streamline flow the velocity rises from zero at the wall to a maximum at slightly greater than one particle diameter from the wall. This maximum may be up to 100% greater than the average velocity. The velocity falls to a minimum in the centre of the bed. This velocity variation across the bed is greater with increased flow rate, increased packing size or smaller tube diameter. Schwartz and

---

1. Kinney(1929); Saunders and Ford(1940); Arthur et al(1950); Morales, Spin and Smith(1951); Schwartz and Smith(1953); Calderbank and Pogorski(1957); Coberly and Marshall(1951); Collins(1957); Mickley, Smith and Korchak(1965).
2. Akehata and Sato(1958); Cairns and Prausnitz(1959); King(1965).

Smith (1953) obtained a maximum deviation of less than 20% for $D_T/D_P > 30$. Skin friction causes the decrease in velocity at the wall. The maximum near the wall is usually explained as being due to a combination of the greater voidage and the less tortuous flow path near the wall. For flat velocity profiles at the entrance to the bed, Cairns and Prausnitz (1959) and Coberly and Marshall (1951) obtained virtually flat mean velocity profiles just downstream from the bed. The profile measurements of the present work (Fig.52)confirm this.

(ii) velocity profiles within the bed in the wall region

Chiam (1962) measured the velocity distribution within a region of one particle diameter from the wall by measuring the effect of fluid flow rate on the bed pressure drop for the application of successive wax annuli. For both liquids and gases he obtained a maximum of one third of the average velocity at $\sim 0.4\ D_P$. For gas flow with $D_T/D_P = 5.4$, 52% of the flow was within an annulus of $0.5\ D_P$ from the wall. For water with $D_T/D_P = 2.7$ - there was 83% of the flow in this region. Chiam found the velocity profile near the wall was similar to the radial voidage variation in this region.

From kinetic studies of the catalytic transfer of deuterium, Palmer (1960) estimated that for a catalyst bed with $D_T/D_P = 27$, the gas flow through this peripheral wall zone was 24% of the total and for $D_T/D_P = 7$ it was 64%.

(iii) velocity profiles within packing voids

Mickley, Smith and Korchak (1965) made hot wire anenometer measurements in the voids of a cubic packing at

particle Reynolds numbers of 4780 and 7010. Velocity peaks were obtained on either side of the void due to flow around the particles. A wall effect was found to exist even if split particles were used at the wall of the bed to give a constant voidage. The mean velocity in the wall voids was 10% higher than for voids in the centre of the packing. It was concluded that the wall itself decreases the total resistance to flow in the wall region so that for a given pressure drop more fluid will flow through this region. There was little correlation with the velocity distribution downstream from the packing. From velocity measurements in the voids of a cubic packing at a particle Reynolds number of 266, Nield and Ross (1966) showed that 80% of the gas flows through a void area equivalent to the unobstructed free area.

Hirai (1954) and Akehata and Sato (1958) inserted electrode probes inside a packing and determined the velocity from a diffusion controlled electrode reaction.

(iv) theoretical approaches

Schwartz and Smith (1953) combined a mixing length theory based on an assumed mixing length of $D_p/2$ with pressure drop equations to give a predicted velocity at a given radial position R^* in the form $v = \Psi(\varepsilon_R'^*, D_p, R^*, L)$ ....(2.10)

King (1965) and Rhoades(1964) made similar theoretical approaches.

Synder and Stewart (1966) made a theoretical study of the velocity and pressure profiles for creeping flow in a cubic packing.

2.2.3. Turbulent Intensities in Packed Beds

From their measurements of downstream concentration fluctuations for liquid flow at Reynolds numbers of 216 - 566, Prausnitz and Wilhelm (1957) deduced a turbulent intensity of about 50%. For measurements in the voids of a cubic packing Mickley, Smith and Korchak (1965) obtained a similar figure in the void centre, but obtained values down to 15% in the constricted region between two spheres. The turbulent intensity relative to the local mean velocity increased slightly with greater Reynolds numbers.

Nield and Ross (1966) found that the regions of greatest turbulent intensity in a packing void are where the fluid flow enters a rapidly widening area region from a narrow area region downstream.

2.3. AXIAL DISPERSION AND MIXING IN PACKED BEDS

When heat or mass transfer takes place during fluid flow through a packed bed, dispersion and diffusional mixing occur. This is the transport of heat or mass through the fluid in the bed under the influence of a temperature or concentration gradient by whatever mechanism this transport occurs. For uniform radial overall temperature and velocity profiles as in the present experimental system there can only be nett dispersion in the axial direction, although radial dispersion can still occur on a local scale.

2.3.1. Mechanisms of Axial Dispersion

Axial dispersion may occur by any combination of the following mechanisms:

a) Molecular diffusion may occur due to either mass diffusion or themal conduction in the presence of a transport flux gradient.

b) The packing particles cause a random displacement or sidestepping of the fluid streams impinging upon them. Partial recombination of the streams occurs in the next void.

c) There is a mixing effect due to fluid flow through alternately converging and diverging void passages.

d) The radial velocity profiles within individual voids may produce lateral diffusion within a void.

e) Variations in average void velocities due to local voidage variations may produce lateral diffusion on a local scale.

f) Convective movement of the fluid may occur at low flow rates due to temperature or concentration inequalities.

g) Turbulent eddies may be generated by the onset of turbulence in the fluid flow.

h) Eddies may be shed from the wake on the downstream side of a particle.

i) The finite heat or mass transfer rate between a particle and the surrounding fluid may produce dispersion particularly for large transfer flux gradients.

The turbulence measurements of Mickley, Smith and Korchak (1965) indicate that (h) does not contribute substantially to the dispersion in a packed bed. The experiments of Hiby (1965) showed that the dispersion mechanisms in a packed

bed do not produce a significant amount of backmixing by diffusive backflow against the mainstream over a distance greater than the length of a mixing stage. This would seem to indicate that there is no real physical basis for the diffusion model (4.3) although in fact this model tends to the mixing cell model for long beds.

2.3.2. Characterisation and Measurement of Axial Dispersion

The amount of axial dispersion in a packed bed is most commonly characterised and measured in terms of an axial or longitudinal Peclet number. This may be based on either the particle diameter, D_p or the bed length L. Thus

$$Pe = \frac{v_0 D_p}{\varepsilon E_z} \quad , \quad Pe_L = \frac{v_0 L}{\varepsilon E_z} \qquad \ldots.(2.10)$$

where v_0 is the bulk velocity based on the empty bed container cross-sectional area and E_z is the axial eddy diffusivity characterising the dispersion. Thus the Peclet number represents the ratio of characteristic times for flow and dispersion.

Axial dispersion of heat or mass is measured experimentally by transient methods based on either dispersion of a tracer step input, attenuation of a tracer pulse input or damping and phase lag of a tracer sinusoidal input. Evaluation of the eddy diffusivity or Peclet number from the experiments is usually based on the diffusion model (4.3). For axial mass transfer the diffusion model equations (4.3) reduce to

$$E_z \frac{\partial^2 C^*}{\partial z^2} - v_z \frac{\partial C^*}{\partial z} = \frac{\partial C^*}{\partial \tau} \qquad \ldots.(2.11)$$

This equation is then solved for the boundary and initial conditions relevant to the experimental bed and tracer input system. Levenspiel (1962a) and Bischoff and Levenspiel (1962) summarise and generalise dispersion models based on solutions of the diffusion equation.

Several dispersion models[1] account for the presence of stagnant fluid regions in the bed which is particularly important in the case of liquid flow. Various forms of a capilliary network model for dispersion have been used by Scheidegger (1953,1954,1960) and Saffman (1959,1960).

2.3.3. Effect of System Variables on Axial Dispersion of Gas

(i) fluid flow rate

Fig. 2.9 and Fig. 2.10 illustrate the effect of Reynolds number and molecular diffusion on the Peclet number. At low Reynolds numbers only molecular diffusion causes dispersion and the Peclet number increases in proportion to the Reynolds number. At higher Reynolds numbers dispersion by molecular diffusion is negligible in comparison with the other dispersion mechanisms and the Peclet number is approximately constant. Between these two regions, dispersion is affected by both molecular diffusion and turbulent mixing mechanisms.

(ii) nature of the mixing transfer

Most packed bed dispersion measurements have been made for the dispersion of mass. No heat dispersion measurements

---

1. Turner (1958, 1959); Aris (1959); Deans and Lapidus (1960); Gottschlich (1963); Deans (1963).

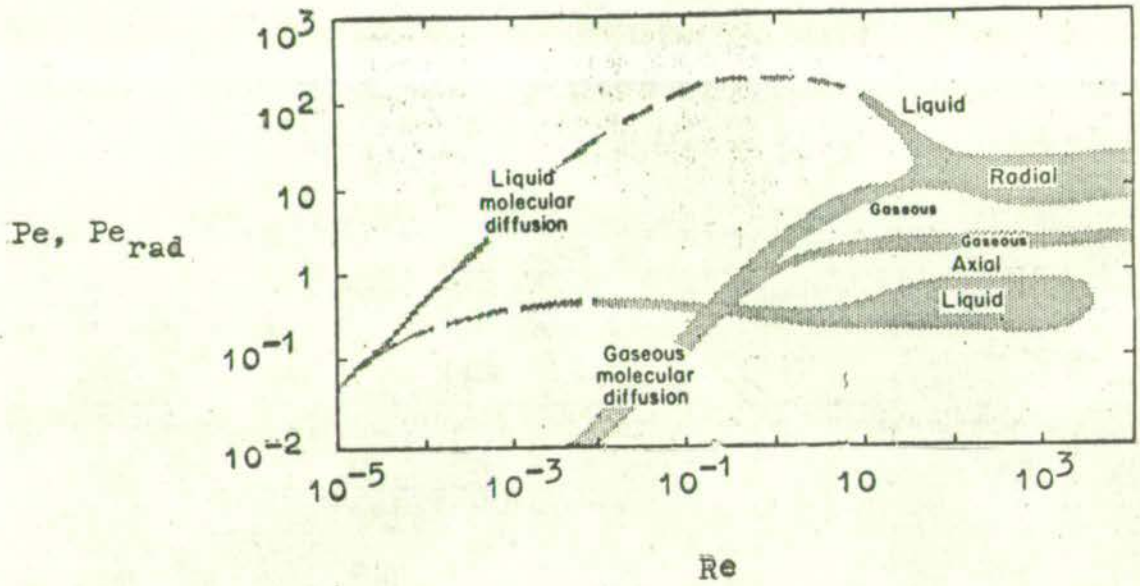

FIG. 2.9 RADIAL AND AXIAL PECLET NUMBERS AS FUNCTIONS OF REYNOLDS NUMBERS

(Adapted from Wilhelm (1962)

Shaded areas represent range of experimental results)

FIG.2.10 LITERATURE EXPERIMENTAL RESULTS FOR AXIAL DISPERSION OF GASES

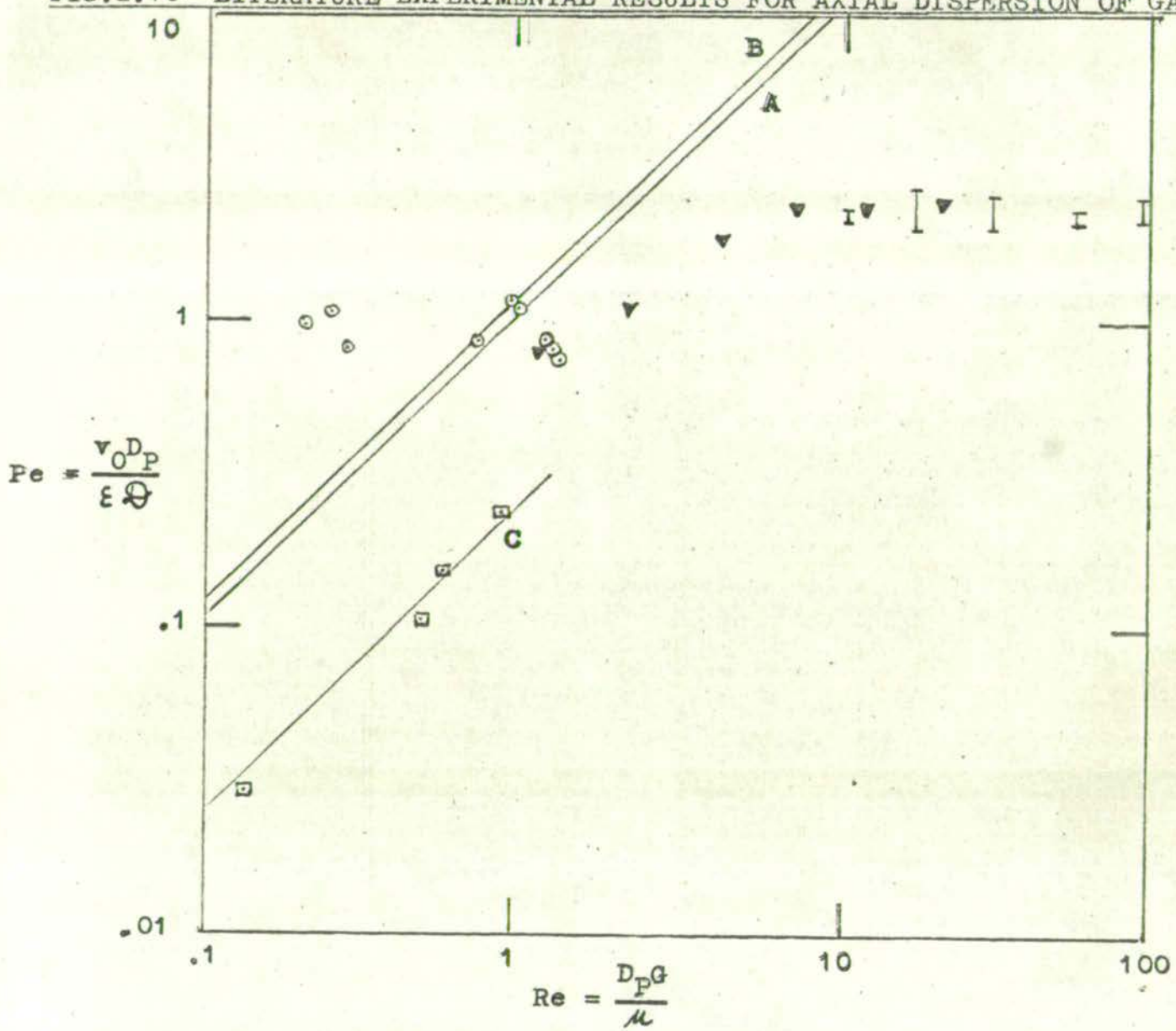

I McHenry and Wilhelm(1957); H_2 - N_2, glass spheres D_p=.127in., ε=.388

▼ Sinclair and Potter(1965); Hg-air, glass ballotini D_p=.0551,.0172in.

⊡ Carberry and Bretton(1958); He-air, glass spheres D_p=.5-5.0 mm., ε=.365

⊙ Chao and Hoelscher(1966); C_2H_4-He, glass chips, ε=.425

— Molecular diffusivity lines:
A = H_2-N_2, B = Hg-air, C = He-air.

appear to have been made for gases but Kimura (1961) and Green, Perry and Babcock (1964) have made measurements of the longitudinal dispersion of heat by liquids. The results obtained agreed with the literature mass dispersion results. The radial heat transfer Peclet numbers obtained from radial thermal conductivity measurements by Baddour and Yoon (1960) and Singer and Wilhelm (1950) also agree with the corresponding mass transfer values. This evidence indicates that mass transfer dispersion data for packed beds may be applied equally well to heat transfer in packed beds.

(iii) presence of interphase transfer

The only data on dispersion in the presence of transfer between the solid particles and the fluid are given in the recent study of Chao and Hoelscher (1966) on gas adsorption. The longitudinal Peclet number values obtained during the adsorption process were substantially lower than those obtained for dispersive mixing alone.

(iv) nature of the fluid or Schmidt number value

Axial dispersion Peclet numbers for liquids are lower than those for gases at Reynolds numbers where molecular diffusion is unimportant. This is the case for $Re > \frac{1000\varepsilon}{Sc}$ (Hiby (1962)) for which the Peclet number is solely a function of the Schmidt number. This is generally attributed (e.g. Gottschlich (1963)) to the presence of stagnant liquid regions in the bed. Wilhelm (1962) also suggests that an increased Taylor axial diffusion mechanism for liquids as compared with

gases contributes to this effect.

(v) wall and end effects

Peclet number values based on mixing across the complete bed cross section are decreased in the presence of a significant wall effect ($D_P/D_T < 0.1$). This has been shown for axial dispersion in laminar flow by Hiby (1962) and Perkins and Johnston (1963) and for axial dispersion in turbulent flow by Latinen (1951), Singer and Wilhelm (1950) and Fahien and Smith (1955). The dependence of Peclet number on D_T/D_P disappears if it is based on the hydraulic diameter of the voids. Hiby (1962) used the relationship

$$D_h = \frac{2}{3}\left(\frac{\varepsilon}{1-\varepsilon}\right) D_P \qquad \ldots.(2.12)$$

Other workers[1] use $D_h = \varepsilon D_T / \left[\frac{3}{2}\left(D_T/D_P\right)\left(1-\varepsilon\right) + 1\right]$ ....(2.13)

which correctly gives $D_h = D_T$ when $\varepsilon = 1$ for an empty tube.

More detailed information on the effect of the velocity profile across the bed on axial dispersion was given by Converse (1960), Bonifaz (1962) and Fesenmeier (1965).

The influence of bed end effects on axial dispersion measurements is discussed by Liles and Geankoplis (1960) and Hiby (1962). Hiby found the Peclet number increased with increasing values of D_T/L for axial dispersion in laminar liquid flow.

---

1. Mott (1951); Wilhelm (1953); Cairns and Prausnitz (1960); Levenspiel and Bischoff (1962).

(vi) particle and packing characteristics

Non-spherical particles generally give greater dispersion than spherical particles[1] as do wide particle size distributions (Perkins and Johnston (1963)).

Most axial dispersion measurements have been made for random packings but Jacques and Vermuelen (1957) and Hiby (1962) also used regular packings. Hiby found that the Peclet numbers for liquid flow through random packings of spheres were generally intermediate between the values for cubic and rhombohedral packings. Huyten, van Beersum and Rijnders (1960) found that the method of filling and consolidating random packings affected the dispersion characteristics of the bed. With very fine particles bridging can increase dispersion (Perkins and Johnston (1963)).

2.3.4. Axial Dispersion in the Experimental System

For the present experimental system, information is required on the axial dispersion of heat by a gas flowing through a random packed bed over a range Re = 0.3 - 5.0. At these Reynolds numbers both molecular diffusion and the eddy mixing type of mechanism can affect the dispersion. No direct experimental data is available for these conditions. Fig. 2.10 shows the available experimental data for mass dispersion by mixing mechanisms during gas flow through random packed beds. These data indicate that at sufficiently

---

1. Bernard and Wilhelm (1950); Carberry (1958); Ebach and White (1958); Hiby (1962).

low Reynolds numbers only molecular diffusion controls while for Re > 10 the dispersion corresponds to perfect stage mixing (4.3). For the present experimental system these two limits are given by (Fig. 2.11).

$$\text{Pe (molecular)} = \frac{D_p v_o}{\varepsilon \mathcal{D}} = .69\ \text{Re} \qquad \ldots.(2.14)$$

$$\text{Pe (perfect stage mixing)} = \frac{D_p v_o}{E\,\varepsilon} = \frac{2}{\beta} = 2.42 \qquad \ldots.(2.15)$$

Between these two limits the Peclet number values were taken from the interpolated values of Wilhelm (1962) (Fig.2.9). Over the lower part of the transition region these agree with the prediction of the generalised dispersion model of Bischoff and Levenspiel (1962). However the latter gives a lower upper limit than the perfect stage mixing obtained experimentally by McHenry and Wilhelm (1957) and Sinclair and Potter (1965).

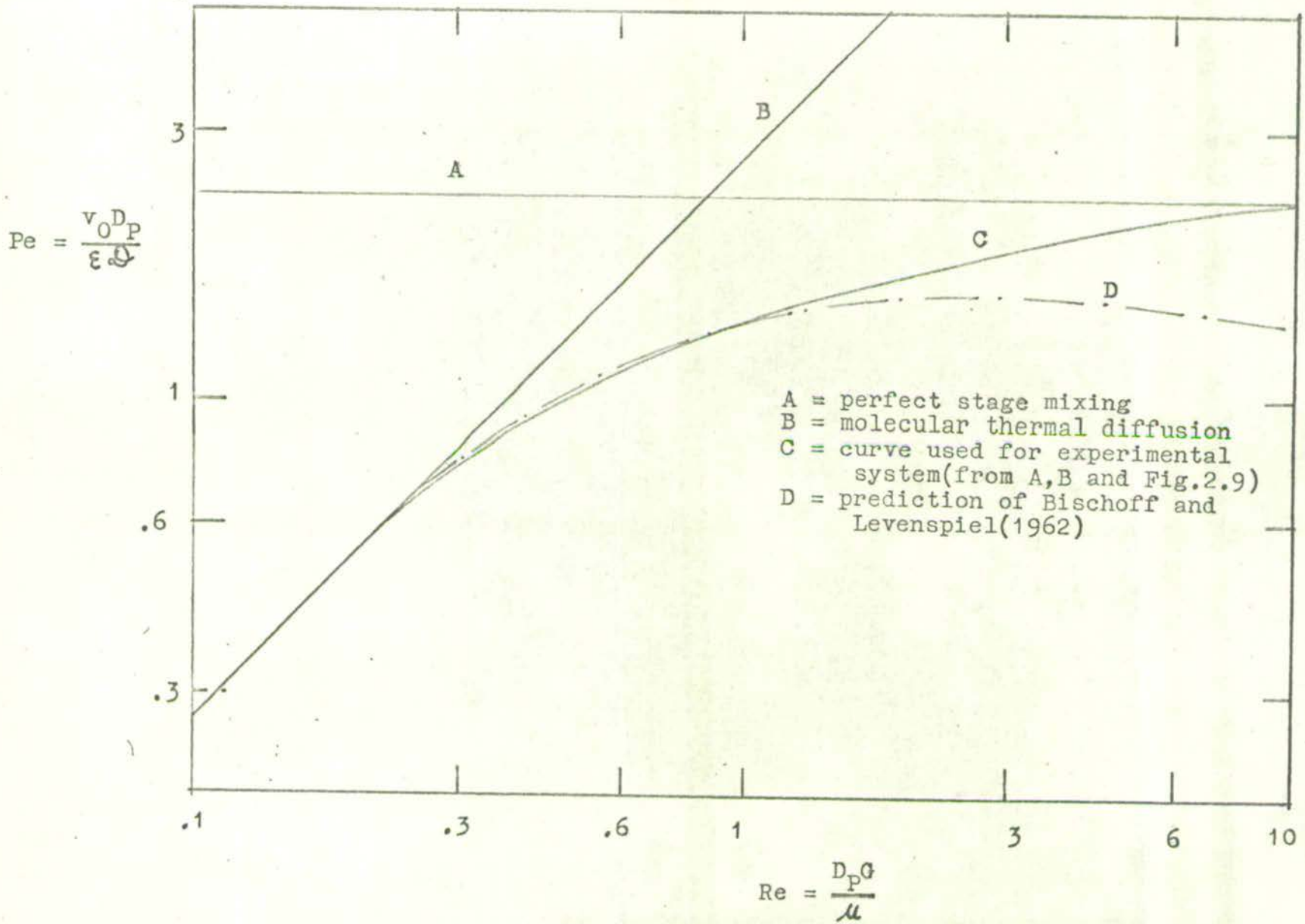

FIG. 2.11 AXIAL DISPERSION IN THE EXPERIMENTAL SYSTEM

CHAPTER 3 MECHANISMS OF AXIAL HEAT TRANSFER IN PACKED BEDS

3.1. IDENTIFICATION OF THE MECHANISMS

There are three basic modes of heat transfer - conduction, convection and radiation. For a stagnant gas in the bed, conduction and radiation are the contributing modes.[1] When the gas flows through the bed all three modes contribute to the heat transfer in the form of various mechanisms which interact by a number of series and parallel paths.[2]

The following possible mechanisms have been identified (Fig. 3.1):

conduction mechanisms

1. conduction through the solid particles.
2. conduction across the stagnant gas in the voids.
3. conduction across the stagnant gas surrounding the points of contact of particles.
4. conduction through the points of contact of particles.

radiation mechanisms

5. radiation between adjacent particle surfaces.
6. radiation between particle surfaces seen through more than one void space.
7. radiation absorption by the gas.

convection mechanisms

8. natural convection in the gas.
9. forced convection solid-gas heat transfer.

---

1. Argo and Smith (1953); Kunii and Smith (1960); Schotte (1960); Glaser (1961).
2. Leva and Grummer (1948); Singer and Wilhelm (1950); Schuler, Stallings and Smith (1952); Yagi and Kunii (1957); Baddour and Yoon (1960).

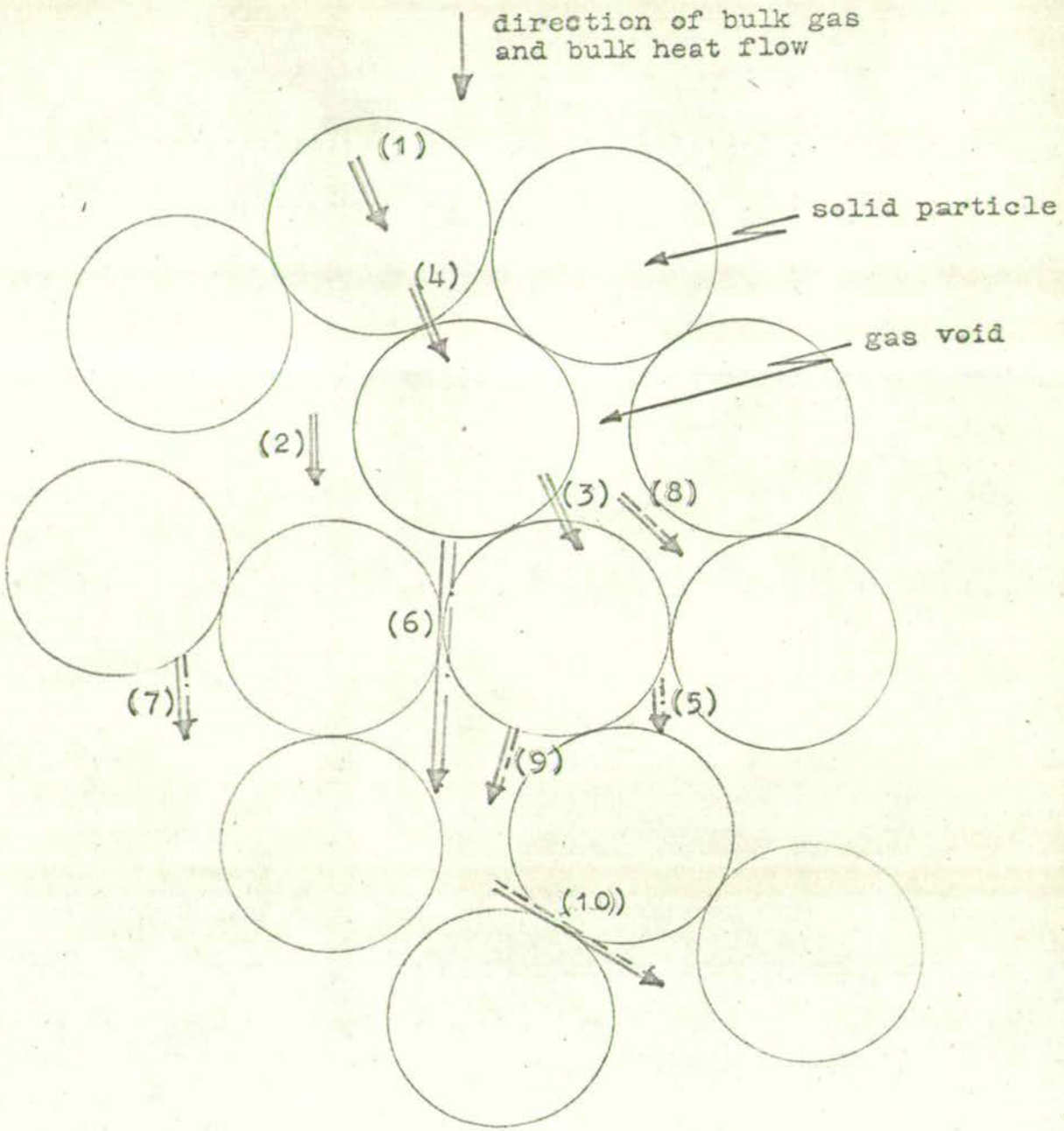

FIG. 3.1 AXIAL HEAT TRANSFER MECHANISMS IN A PACKED BED

conduction mechanisms (1 - 4)

convection mechanisms (8 - 10)

radiation mechanisms (5 - 7)

(see 3.1 for key to mechanism numbers)

10. forced convection due to bulk flow, turbulent diffusion or mixing of the gas.

3.2. EFFECTIVE THERMAL CONDUCTIVITY

Heat transfer in heterogeneous two phase systems is most commonly characterised by the concept of an effective thermal conductivity. This concept treats the system as homogeneous with respect to heat transfer through it and thus enables the Fourier equation to be applied to give

$$Q = - k_e A (dT/dz) \qquad ....(3.1)$$

$$Y = k_e/k_g = (Q/A)/k_g (- dT/dz) \qquad ....(3.2)$$

In the following descriptions of models which have been proposed to predict the effective thermal conductivities of such systems emphasis is placed on application to packed beds of spheres which is the present experimental system. In the majority of cases (and unless otherwise stated) the basic assumption inherent in the models is that there is no bending of the flux lines so that the heat flow is one dimensional.

3.3. CONDUCTION MECHANISMS

Only the conduction mechanisms need to be considered under conditions of no gas flow through the bed (eliminates forced convection), sufficiently small particles (negligible natural convection) and sufficiently low temperatures (negligible radiation).

For the conduction mechanisms, the effective thermal conductivity ratio, Y_c, is primarily dependent on (a) the effective thermal conductivities of the solid and gas phases

(k_s, k_g) (b) the bulk mean voidage, ε, which is a measure of the volume concentration of the phases (c) the structure of the system as represented by the shape and arrangement of the phases and contact points.

3.3.1. Conduction through Solid and Gas Phases (mechanisms 1,2,3.)

This section describes models which account for the closely related mechanisms 1, 2 and 3, but which do not specifically account for mechanism 4. Some of the models do not distinguish between the two gas conduction mechanisms 2 and 3.

(i) pseudo-regular models

This type of model considers a random heterogeneous system as a regular arrangement of phase elements for the purpose of conduction heat transfer evaluation. In some cases the voidage of the model is adjusted to correspond with the random system voidage.

For a cubic packing of equal sized spheres, Deissler and Eian (1952) and Baddour and Yoon (1960) showed that

$$Y_C = \frac{\pi}{2}\left(\frac{X}{X-1}\right)^2\left[\ln X - \left(\frac{X-1}{X}\right)\right] + \left(1 - \frac{\pi}{4}\right) \qquad \ldots.(3.3)$$

where $X = k_s/k_g$.

A model of a cubic array of spherical voids in an expanded solid was considered by Topper (1955). For an orthorhombic packing Shimokawa (1962) replaced $\frac{\pi}{2}$ by $\frac{\pi}{\sqrt{3}}$ in equation (3.3) and this expression may be generalised for $1 - \varepsilon \leq \pi/3\sqrt{3}$ (Godbee and Ziegler (1966)). Baddour and Yoon (1960) gave the variation of Y_C with X for a close packed tetrahedral packing of solid spheres. Rayleigh (1892) gave a general

series relationship for any regular packing of equal sized spheres[1]

$$Y_C = 1 - 3(1 - \varepsilon)/\left[\left(\frac{2 + X}{1 - X}\right) + (1 - \varepsilon) - \left(\frac{1 - X}{4/3 + X}\right) C(1 - \varepsilon)^{\frac{10}{3}} + \ldots\right] \quad \ldots.(3.4)$$

A different expression was obtained by Webb (1956) and Woodside (1958) using the assumption that $k_s = \infty$ perpendicular to the heat flow

$$1/Y_C = 1 - \left[\frac{6(1 - \varepsilon)^{\frac{1}{3}}}{\pi}\right]\left[1 - \left(\frac{C^2 - 1}{C}\right)\right] \ln\left(\frac{C + 1}{C - 1}\right)\Bigg] \quad \ldots.(3.5)$$

where $$C = \left\{1 + 4/\left[\pi (X - 1)\left\{\frac{6(1 - \varepsilon)^{\frac{2}{3}}}{\pi}\right\}\right]\right\}^{\frac{1}{2}}$$

Fig. 3.2 shows effective thermal conductivities for conduction in regular packings of equal sized spheres.

For a random packing of voidage, ε, Deissler and Eian (1952) interpolated between the effective thermal conductivity values for regular packings of fixed voidage. A unit cell of close packed tetrahedral spheres was used by Dul'nev and Sigalova (1965). It was assumed that $k_s = \infty$ and that the random bed voidage was attained by a spherical gas envelope completely surrounding each sphere. In this case for $\varepsilon < .75$

$$Y_C = \frac{\sqrt{2}}{C}\left[\pi C \ln\left(\frac{C}{C - 1} - 1\right) + 2\pi\left(\sqrt{2}C - 1\right)\right] \quad \ldots. (3.6)$$

---

1. De Vries (1952) gives the following values for C: simple cubic, 1.31; body centred cubic, .129; face centred cubic, .0752.

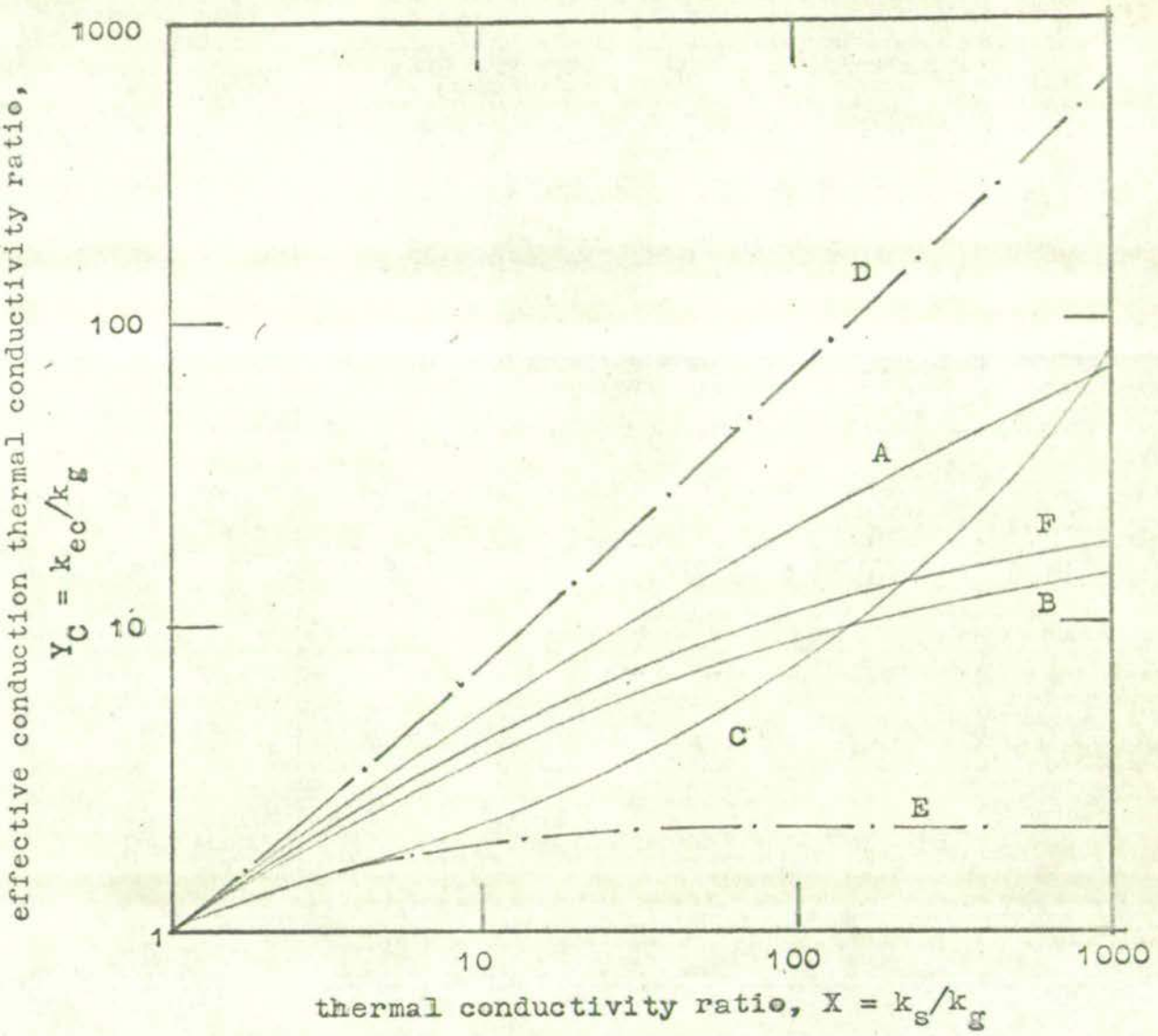

FIG. 3.2 EFFECTIVE THERMAL CONDUCTIVITIES FOR CONDUCTION IN REGULAR PACKINGS OF EQUAL-SIZED SPHERES

Cubic Packing:

A = Deissler and Eian(1952), Baddour and Yoon(1960), equation(3.3)
B = relaxation solution, Deissler and Boegli(1958)
C = Webb(1956), Woodside(1958), equation(3.5)
D = maximum parallel limit, equation(3.6a)
E = minimum series limit, equation(3.7a)

Tetrahedral Packing:

F = Baddour and Yoon(1960)

An unorthodox mathematical treatment was used by Schumann and Voss (1934) for cylinders with a hyperbolic surface to give

$$Y_C = \frac{X}{1 - C(X - 1)} \left\{ 1 - \frac{C(1 + C)(X - 1)}{1 - C(X - 1)} \ln \left(\frac{1 + C}{CX} \right) \right\} \quad \ldots.(3.7)$$

where $\varepsilon = C(1 + C) \ln [(1 + C)/C] - C$. Gorring and Churchill (1961) used a constant C obtained through a volume balance of the phases to define the amount of contact area perpendicular to the heat flow direction in a model of a cubic array of particles bounded by parabaloids of revalution. For $X > 50$ the result was

$$Y_C = 1.92 \, (X/C^2)^{\frac{1}{3}} \quad \ldots.(3.8)$$

Pseudo-regular models have also been based on cubical and cylindrical packing elements.[1]

The assumption of no bending of the flux lines has been tested by the application of relaxation techniques[2] and found to be poor in some cases. Fig. 3.3 shows that the isothermal lines and hence flux lines are crowded together near the points of contact indicating that most of the heat flow takes place there. This effect is accentuated as X increases (Fig.3.3) The relaxation solutions give higher values for the effective thermal conductivity than solutions based on the no flux line

---

1. Rayleigh (1892); Lichtenecker (1924); Russell (1935); Topper (1955); Deissler and Eian (1952).
2. Deissler and Eian (1952); Deissler and Boegli (1958); Stephenson and Woodside (1958).

Variation of ratio of local heat flux (per unit area) to average heat flux across plane A-A for various values of k_s/k_g

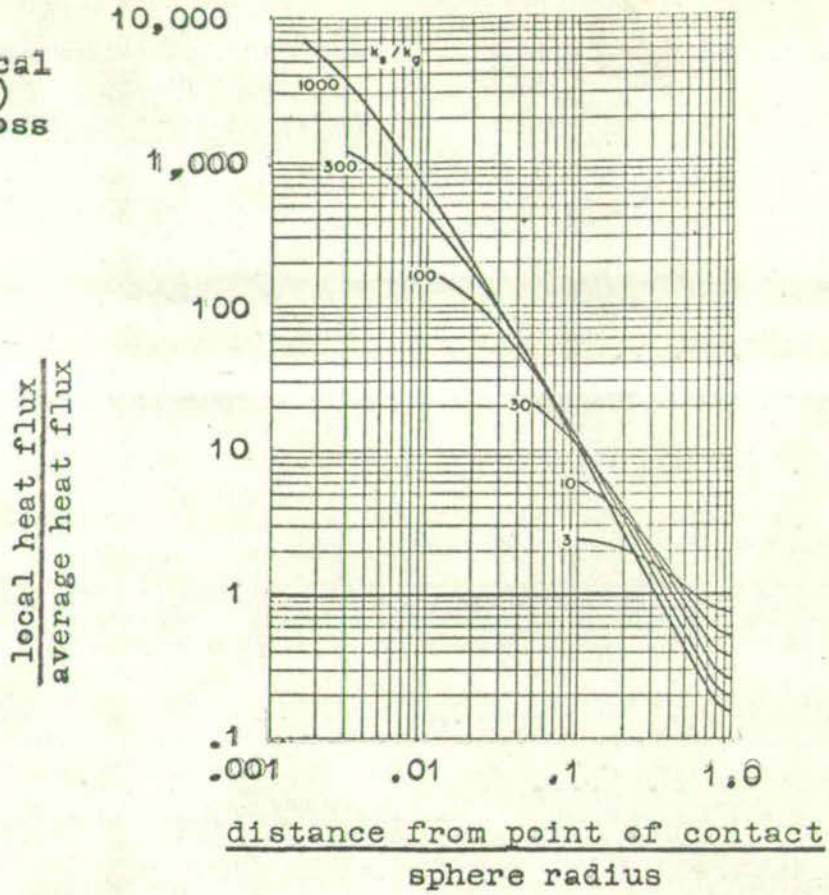

Constant temperature lines in representative sample spheres in cubical array as obtained by relaxation solution (k_s/k_g = 30)

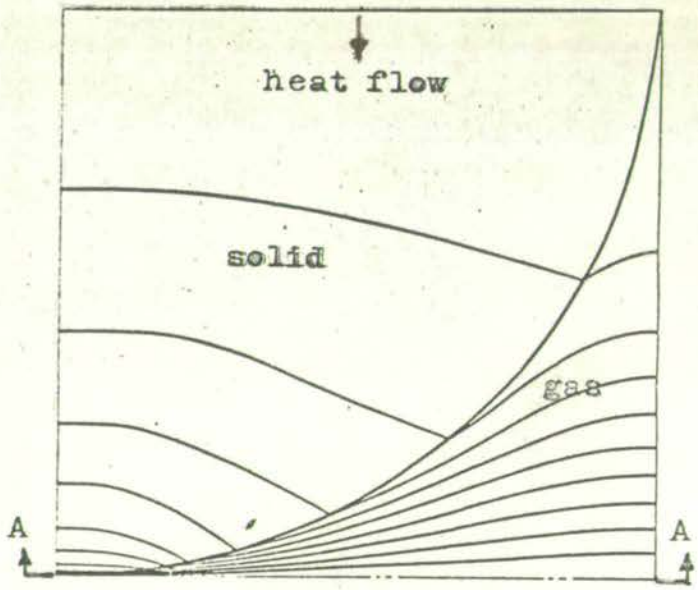

FIG. 3.3 RELAXATION SOLUTION FOR CONDUCTION IN A CUBIC PACKING OF EQUAL SIZED SPHERES (DEISSLER AND BOEGLI(1958))

bending assumption. For example, at X = 40 the relaxation solution for a cubic packing of spheres gives Y = 5.0 while the simplified solution gives Y = 3.6.

(ii) models based on means of the phase contributions

Since mechanism 1 acts over the solid volume, $1 - \varepsilon$, and mechanisms 2 and 3 act over the gas volume, ε, the effective thermal conductivity of the system may be predicted from a mean of the two phase contributions. (e.g. Deissler and Boegli (1958)). The form of the mean depends on the arrangement of the two phases.

The maximum value of Y_C is given by the arithmetic mean corresponding to a parallel arrangement of the phases for which

$$Y_C = \varepsilon + (1 - \varepsilon)X \qquad \ldots.(3.6a)$$

Conversely the minimum value is given by the harmonic mean corresponding to a series arrangement of the phases for which

$$Y_C = X / [\varepsilon X + (1 - \varepsilon)] \qquad \ldots.(3.7a)$$

Fig. 3.5 shows that for the values of ε and X relevant to packed beds of spheres, the arrangement of the phases has considerable significance.

Since in most heterogeneous materials the two phases are arranged with some degree of randomness, the effective thermal conductivity ratio lies between the above limits. Thus a geometric mean formula has been proposed[1] which has the form

$$Y_C = X^{1 - \varepsilon} \qquad \ldots.(3.8a)$$

---

1. Lichtenecker (1926); Asaad (1955); Somerton (1958); Woodside and Messmer (1961).

(iii) probabilistic models

Maxwell (1892) derived an equation for the electrical conductivity of a random distribution of solid spheres in a continuous medium based on the assumption that the spheres were far enough apart not to mutually interact. This has often been applied to the effective thermal conductivity of heterogeneous materials in the form[1]

$$Y_C = \frac{2\varepsilon + (3 - 2\varepsilon)X}{(3 - \varepsilon) + X} \qquad \ldots.(3.9)$$

The limitation of no interaction between the particles was avoided by Strickler (1954) who applied two empirical constants (functions of surface area and solid thermal conductivity) to equation 3.9.

Tsao (1961) used the limiting parallel and series equations (3.6, 3.7) to derive a probability model which required two experimentally determined statistical parameters. The mathematical basis of this model was criticised by Warren and Messmer (1962).

(iv) geometric models

Models based on idealised geometric arrangements of the solid and gas phases have often been used. The various models proposed are basically similar and consider the packed bed to be represented by a gaseous conduction path (mechanism 2)

---

1. Extensions of this treatment have been made to account for more than two dispersed phases (Eucken(1932); Brailsford Major (1964)), non-sperical particles (Burgers (1919); Fricke (1924); De Vries (1952); Sehr (1958); Hamilton and Crosser (1962)) and a size distribution of particles (Bruggeman (1935)).

in parallel with a combined solid-gas series path (mechanisms 1 and 3). The basic assumption of uni-directional heat flow again applies.

In most models[1] the two heat transfer paths are insulated from each other. Fig. 3.4 shows a unit cell for this case where summation of the parallel and series heat transfer resistances gives

$$Y_C = \varepsilon_{A1} + \frac{(1 - \varepsilon_{A1})}{\alpha + (1 - \alpha)/X} \qquad \ldots.(3.10)$$

where $\alpha = \phi/\beta$ and since the total gas volume per unit volume must be ε, it follows that $\varepsilon_{A1} = (\varepsilon - \alpha)/(1 - \alpha)$. The various models differ in their evaluations of the parameter β and ϕ (or α) and ε_{A1} which are in some cases based on erroneous or inconsistent assumptions.[2]

Godbee and Ziegler (1966) assumed an isothermal line completely across the unit cell at the solid-gas interface in the series path which gives

$$Y_C = 1/\left[\alpha + \frac{1 - \alpha}{\varepsilon_{A1} + X(1 - \varepsilon_{A1})}\right] \qquad \ldots.(3.11)$$

The value of α was obtained from the relationship

$$1 - \alpha = \left[\frac{1 - \varepsilon}{\psi}\right]^{\frac{1}{3}}$$

where ψ is a shape factor.

Kessler (1962) used a set of series solid-gas layers in series with a set of parallel solid-gas layers.

---

1. Van Loon (1952); Yagi and Kunii (1957); Kunii and Smith (1960); Willhite, Kunii and Smith (1962); Masamune and Smith (1963).

2. The contribution of the parallel gaseous conduction path

(continued p. 44)

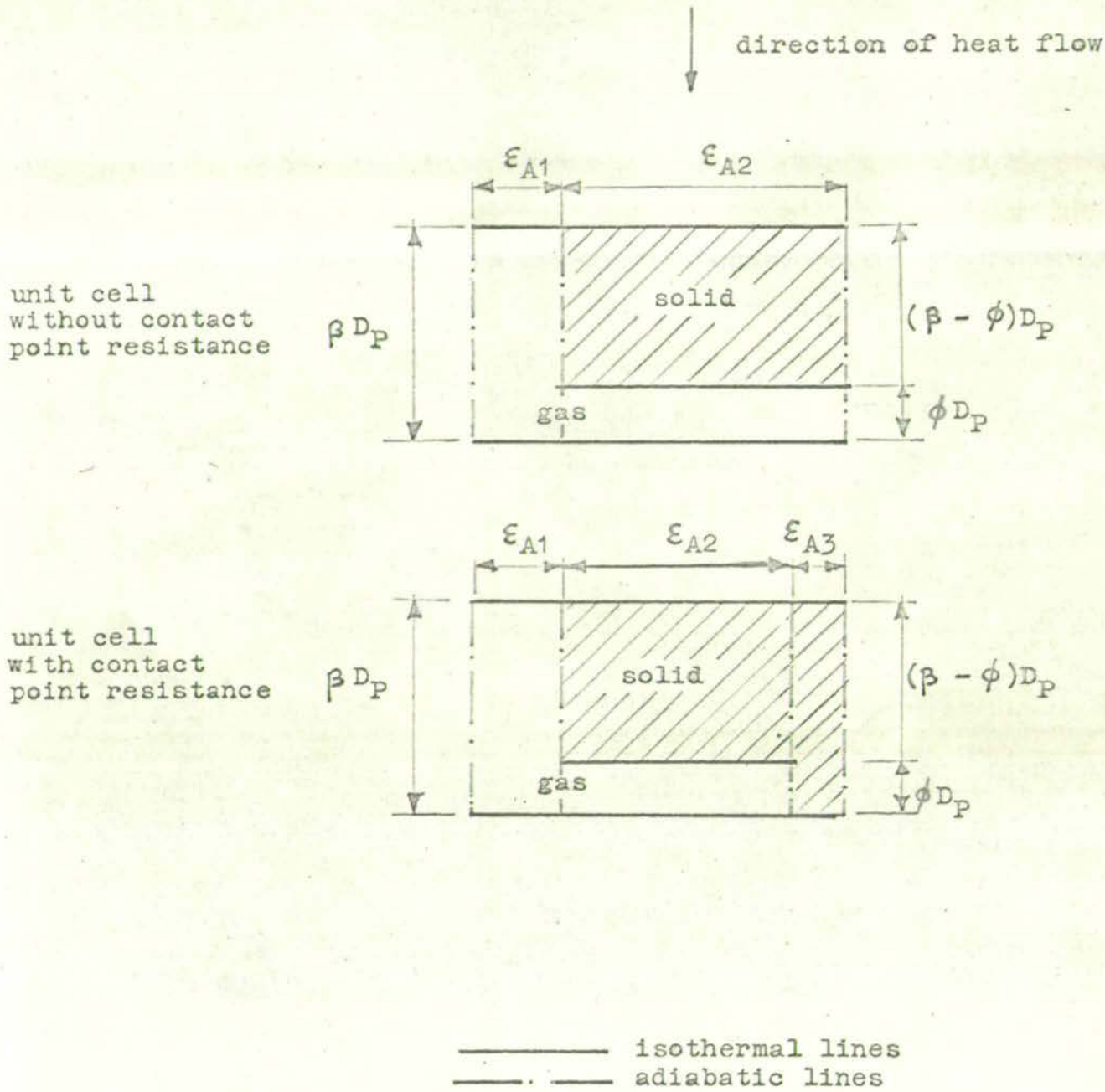

FIG. 3.4 PREVIOUS GEOMETRIC MODELS FOR THE CONDUCTION MECHANISMS

(Footnote 2 continued) (mechanism 2) was neglected completely by Yagi and Kunii (1957). The parameter α was obtained by assuming $\beta = 1$ and fitting the experimental data to get ϕ (for air, $\varepsilon = .4$, $\alpha = .034$).

Kunii and Smith (1960) incorectly assumed $\varepsilon_{A1} = \varepsilon$, derived maximum and minimum limits for β of 1.0 and .895 respectively and assumed that the solid path length is the length of a cylinder having the same volume as a spherical particle to obtain $\beta - \phi = \frac{2}{3}$. But they also determined ϕ from the heat flow through a cubic packing of spheres (equation 3.3) by assuming that $1/n$ of the total heat flux passed through the fluid film near one contact point. The value of the coordination number, n was obtained from empirical considerations of closest and loosest packing arrangements. But this approach gave ϕ as a function of X and ε which is incompatible with the previous assumption of a constant value of ϕ ($= \frac{1}{3}$ if $\beta = 1$).

The latter approach to determine ϕ was also used by Willhite, Kunii, Smith (1962) except that n was determined from the equation of Smith, Foote and Busang (1929). Low conductivity spherical particle systems were correlated using the assumption $\beta - \phi = \frac{2}{3}$, while for non-spherical or high conductivity spherical systems the value $\beta - \phi = \frac{1}{2}$ was used. It was pointed out that ε_{A1} must be positive. This condition is given by $\alpha < \varepsilon$ which requires $\phi < \frac{1}{3}$ for $\varepsilon = .4$ and $\beta - \phi = \frac{1}{2}$. But the above values imply that $\beta < .834$ which is less than the minimum value for β given by Kunii and Smith (1960).

Masamune and Smith (1963) based the determination of ε_{A1} on the erroneous equation $\varepsilon = \varepsilon_{A1} + \varepsilon_{A2}$. The assumption of equal area and volume fractions cannot be made for a unit cell of definite geometric configuration and only applies to the bulk mean voidage over a large region of random packing. The determination of α was based on the assumption that the complete surface area of each particle was in contact with gas in pendular rings (Fig.4.2) which compose the gas phase part of the series path. But the intersection of a pendular ring and a sphere is a circle and thus the surface cannot be completely covered by such rings without overlapping of the rings. It is also incorrect to base the determination of α on the number of rings around one sphere instead of the number of rings in the unit cell volume.

Fig. 3.5 shows the effective thermal concudtivities for random packings of voidage 0.40 predicted by some of the above models.

3.3.2. Conduction through the Points of Contact of Particles (mechanism 4)

Several approaches have been made to include mechanism 4 in conduction models.

(i) equivalent conductivity

Wilhelm et al (1948) used an empirical equivalent conductivity correction, k_p, to correlate experimental effective thermal conductivity measurements with the model of Schumann and Voss (1934). Thus

$$Y_C = Y_C(\text{equation 3.7}) + k_p/k_g \qquad \ldots.(3.12)$$

where $$\log_{10} k_p = - .678 + .00107 (k_s/\varepsilon) \qquad \ldots.(3.13)$$

But this approach incorrectly implies that mechanism 4 is in parallel with the combination of mechanisms 1, 2, 3, and does not account for the effects of particle loading, deformation and surface characteristics.

(ii) equivalent heat transfer coefficient

Kunii and Smith (1960) accounted for mechanism 4 by postulating an equivalent heat transfer coefficient h_p which is a characteristic of the solid material and type of consolidation. The coefficient was regarded as providing heat transfer resistance in parallel with the gas phase portion of the series path of the geometric model so that

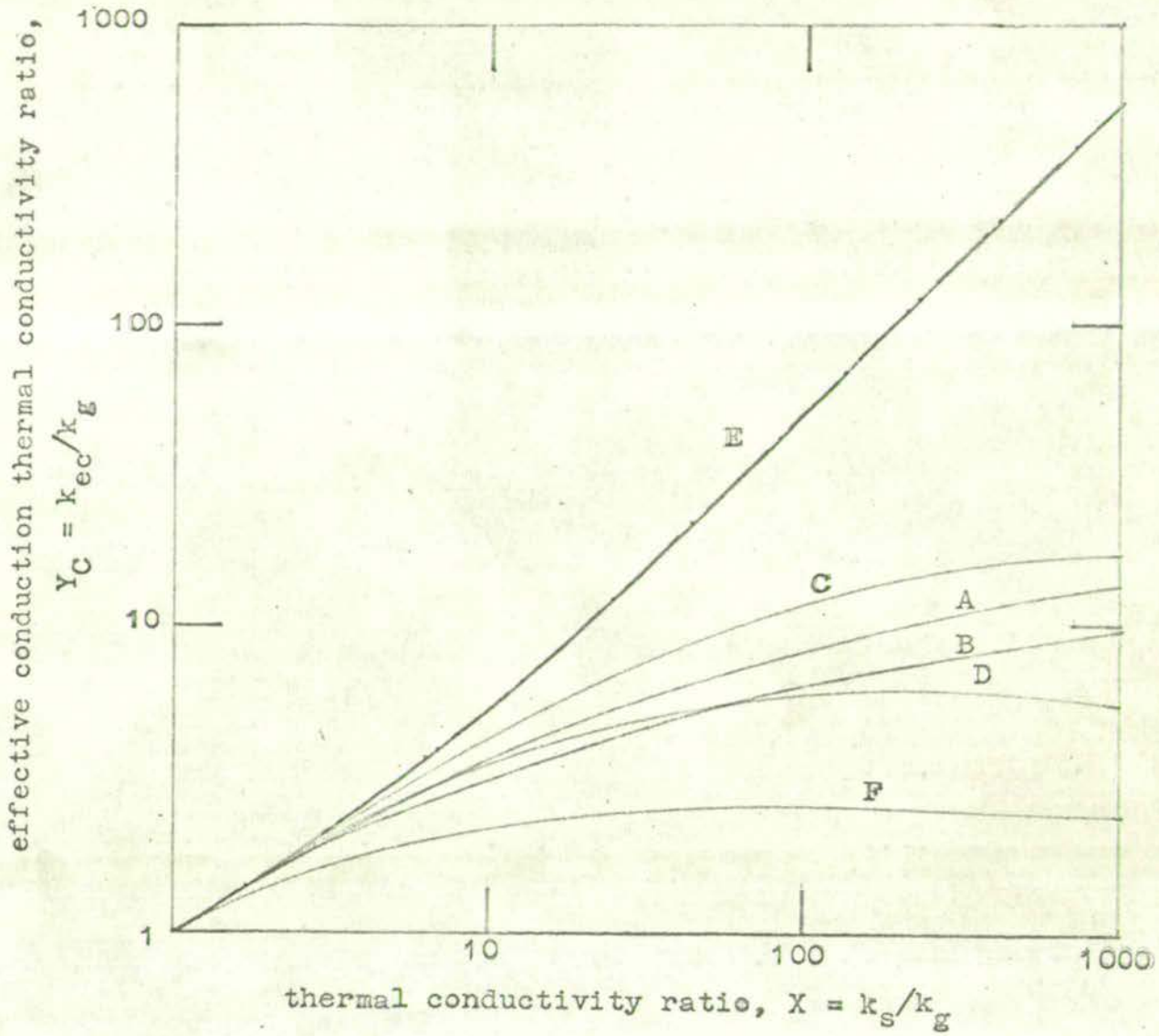

FIG. 3.5 EFFECTIVE THERMAL CONDUCTIVITIES FOR RANDOM PACKINGS OF VOIDAGE 0.40

Model Predictions:

A = Deissler and Eian(1952)
B = Schuman and Voss(1934), equation(3.7)
C = Yagi and Kunii(1957)
D = Maxwell(1892), equation (3.9)
E = Maximum parallel limit, equation(3.6a)
F = Minimum series limit, equation(3.7a)

$$Y_C = \varepsilon_{A1} + (1 - \varepsilon_{A1}) / \left[1 / \left\{ \frac{1}{\alpha} + \frac{h_p D_p}{k_g} \right\} + \frac{1 - \alpha}{X} \right] \quad \ldots.(3.14)$$

However Kunii and Smith incorrectly assumed that $h_p = 0$ for unconsolidated particles.

(iii) equivalent contact area

This approach assumes a finite area of perfect solid contact between particles which gives a heat transfer rate equivalent to mechanism 4.

Riemann (1919) used the model of a cubic packing of truncated spheres which made contact over a circle of diameter CD_p where C was determined from the voidage mass balance. The assumptions of $k_g = 0$ and $C \ll 1$ implied that only mechanisms 1 and 4 contributed to the heat transfer and gave the relationship $Y_C = X(C + \frac{1}{\pi} \ln 2C)^{-1}$ ....(3.15)
Takeoka and Nishimura (1963) analysed the heat transfer through the contact points of a soldered packed bed.

To include mechanism 4 in the geometric models a parallel path of solid conduction is added to the unit cell (Fig.3.4). It is usually erroneously assumed that there is no heat transfer at right angles to this solid path[1] which gives

$$Y_C = \varepsilon_{A1} + \varepsilon_{A2} / \left[\alpha + \frac{1 - \alpha}{X} \right] + \varepsilon_{A3} \cdot X \quad \ldots.(3.16)$$

Van Loon (1952) and Yagi and Kunii (1957) incorrectly assumed $\varepsilon_{A3} = 0$ in quantitative calculations.

---

1. Van Loon (1952); Yagi and Kunii (1957); Woodside and Messmer (1961); Masamune and Smith (1963).

Masamune and Smith (1963) determined ε_{A3} from vacuum thermal conductivity measurements. From equation 3.16

$$\varepsilon_{A3} = Y_C^*/X \quad \text{but the assumption of no} \quad \ldots.(3.17)$$

bending of the flux lines is very poor under vacuum conditions. They also incorrectly related ε_{A3} to a contact angle based on one point of contact instead of the number of contact points in the unit cell. Harper and El Sahrigi (1964) allowed for interaction between the parallel paths at atmospheric pressure but used equation 3.17 for vacuum conditions.

Dul'nev and Sigalova (1965) made a semi-empirical analysis of the loading and deformation of a unit cell contact point in their pseudo-regular model (3.3.1) and estimated the heat transfer resistance of the gas and solid contact areas. Considerable work has recently been done on the thermal conductance of contacting flat metal surfaces (e.g. Fenech and Rosenhow (1963); Vidoni (1965)).

3.3.3. Effect of System Variables on Conduction Mechanisms

Table 3.1 indicates which system variables influence heat transfer due to a particular conduction mechanism.

(i) phase variables

All the models indicate that the effective thermal conductivity increases with both gas and solid thermal conductivities, but the gas conductivity has a greater effect. A large amount of experimental data confirms this and may be correlated by equations of the form $Y = C_1 X^{C_2}$ (e.g. Verschoor and Schuit (1952), Kunii and Smith (1960)).

Table 3.1. System Variables affecting Heat Transfer Mechanisms in Packed Beds. (x indicates that a variable has an effect)

	Variable		Mechanism (as in 3.1)		
			Conduction	Radiation	Convection
			1 2 3 4	5 6 7	8 9 10
Phase Variables	solid thermal conductivity	k_s	x x	x x x	
	solid emissivity	e		x x	
	gas thermal conductivity	k_g	x x		
	gas emissivity	e_g		x	
	gas density				x x x
	gas specific heat	C_P			x x
	gas viscosity	μ			x x x
	gas volumetric expansion coefficient	η			x
Structural Variables	Voidage	ε	x x x x	x x x	x x x
	packing method		x x x x	x x	x x x
	packing orientation*		x x x x	x x	
	particle size**	D_P		x x	x
	particle shape	ψ	x x x x	x x	
	particle surface area	S			x
	particle surface roughness		x		x
Operational Variables	temperature	T, T_A	x x x	x x x	x x x
	temperature gradient	dT/dz			x x
	gas pressure	P	x x	x	x
	gas flow rate	G	x x		x x x
	direction of gas flow				x
	direction of heat flow				x
	direction of transfer flux				x
	applied loading		x x x		

* For regular packings.
** For equal-sized packings.

(ii) structural variables

The models predict that the effective thermal conductivity decreases with increased voidage and the decrease is more marked for high values of X. For example at X = 30 Deissler and Eian (1952) predicted a 12% decrease in Y for a voidage change of .35 to .40. The range of bulk mean voidages in random packed beds is relatively small, and experimental investigations of this variable are more often concerned with consolidated systems (e.g. Woodside and Messmer (1961)), partially sintered systems (e.g. Grootenhius, Mackworth and Saunders (1951)) and powders (e.g. Godbee and Ziegler (1966)).

The models do not distinguish between a regular packing of voidage, ε, and a random packing of the same voidage. However a change in the method of packing normally gives rise to a change in voidage and coordination number and thus affects the conduction mechanisms. Bretsnajder and Ziolkowski (1959) examined the effect of repacking a random packed bed of aluminium cylinders on the effective thermal conductivity and also compared the results with measurements on regular packings.[1]

For regular packings the packing orientation with respect to the direction of heat flow affects the conduction mechanisms.

---

1. For ε = .360 - .415 the range of Y_o values was - 17.2% to + 4.1% about the mean value. For two repackings having the same voidage (ε = .36) the values of Y_o differed by 2.6% compared with an error of .8% in the individual values. A triangular array of the cylinders (heat flow perpendicular to axes, ε = .096) gave a 19.6% increase in Y_o compared with 41.2% for a square array (heat flow parallel to axes, ε = .25).

For relaxation solutions of a square array of cylinders, Deissler and Eian (1952) obtained a 7% increase in Y_C (for X = 30) when the heat flow was at 45° to the line joining two cylinder centres compared with heat flow parallel to this line. The increase was greater for larger values of X.

For equal sized particles both models and experimental results (e.g. Masamune and Smith (1963)) show that the magnitude of the particle size has no effect on the effective thermal conductivity. For a range of particle sizes, a change in the size of one component will change the voidage and thus affect the conduction mechanisms.

Hamilton and Crosser (1962) measured the effective thermal conductivity of balsa wood and aluminium particles of various shapes embedded in rubber and found a decrease with increased sphericity of the particles.

Differing solid surface characteristics can have a considerable effect on mechanism 4 (Masamune and Smith (1963)).

(iii) operational variables

For pressures less than atmospheric the graph of effective thermal conductivity versus log P is an S-shaped curve (e.g. Masamune and Smith (1963)). This is due to a reduction in the gas thermal conductivity when the path length for gaseous conduction is of the same order as the mean free path of the gas molecules.[1] At very low pressures gaseous conduction becomes negligible and the thermal conductivity tends to a constant value indicating that heat transfer through

---

1. As predicted by the kinetic theory of gases (Kennard (1938)).

the contact points is the controlling mechanism. Experimental thermal conductivity measurements at low pressures have been made for a variety of heterogeneous two phase systems.[1] At high pressures the effective thermal conductivity increases slightly but tends to an asymptotic value (e.g. Deissler and Eian (1952)).

When gas flows through a packed bed, mechanism 1 is unchanged, but mechanisms 2 and 3 are dependent on the amount of mixing of the gas in the void spaces.

Increased temperature increases conduction heat transfer in a packed bed, due mainly to the increased gas thermal conductivity, but temperature gradient has no effect on the effective conduction thermal conductivity.

An applied load on the bed increases the effective thermal conductivity due to a decrease in the contact point resistance (Woodside and Messmer (1961)). If the solid material is compressible there will also be a decrease in voidage, thus affecting mechanisms 2 and 3 (Kistler and Caldwell (1934)).

---

1. Equal-sized spheres e.g. Schumann and Voss (1934); Woodside and Messmer (1961); Kessler (1962); Masamune and Smith (1963); Dul'nev and Sigalova (1965); powders e.g. Godbee and Ziegler (1966); freeze dried material e.g. Harper and El Sahrigi (1964); consolidated rocks e.g. Woodside and Messmer (1961).

3.4. RADIATION MECHANISMS AND THEIR INTERACTION WITH CONDUCTION MECHANISMS

3.4.1. Application of the Laws of Radiative Transfer to Packed Bed Systems

There are three types of radiative transfer - absorption-emission, transmission, and reflection or scattering. All of these processes can occur in packed bed systems. If f^*_A, f^*_T, f^*_S, are the fractions of the total radiant flux accounted for by the above processes, it follows that

$$f^*_A + f^*_T + f^*_S = 1 \qquad \ldots.(3.18)$$

(i) absorption-emission

Kirchoff's Law states that at thermal equilibrium the ratio of the emissive power of a surface (i.e. the radiant flux density I) to its absorptivity, f^*_A, is the same for all bodies. But for a blackbody (of emissive power, I_B), $f^*_A = 1$. Thus

$$I/f^*_A = I_B/1 \qquad \ldots.(3.19)$$

and since the emissivity $e = I/I_B$ it follows that at thermal equilibrium $e = f^*_A$.

The Stefan-Boltzmann law states that the emissive power of a blackbody depends only on temperature. Thus

$$I_B = C_{SB}\, T_A^4 \qquad \ldots.(3.20)$$

and $$I = f^*_A\, C_{SB}\, T_A^4 = e\ C_{SB}\ T_A^4 \qquad \ldots.(3.21)$$

at thermal equilibrium.

Both emissivity and absorptivity are functions of temperature and surface roughness. Emissivity is also a function of direction but an integrated total emissivity is

normally used. The absorptivity is also a function of the spectral energy distribution. The relationship between the monochromatic emissive power of a black body at wavelength λ, $I_{B\lambda}$, and the absolute temperature, T_A is given by Planck's law which has the form

$$I_{B\lambda}/T_A = \Psi(\lambda T_A) \qquad \ldots.(3.22)$$

A gray surface is one for which the total absorptivity, f^*_A, does not depend on the spectral energy distribution. For each wavelength the intensity of radiation will be smaller than that for a black body by a fixed ratio. Thus for a source of material 1 and a sink of material 2

$$f^*_{A1,2} = f^*_{A1,1} = e_1 \qquad \ldots.(3.23)$$

It follows that for a gray surface the emissivity, e, may be used in substitution for the absorptivity, f^*_A, even although the source and sink temperatures are not equal. From equations 3.21 and 3.23 the nett radiant energy transfer between two gray surfaces of the same material is given by

$$Q = e\, C_{SB} F^*_{12} (A_1 T_{A1}^4 - A_2 T_{A2}^4) \qquad \ldots.(3.24)$$

where F^*_{12} is a view factor defined as the fraction of radiation leaving a gray surface 1 which is intercepted by a gray surface 2.

For packed bed systems the assumption of gray surfaces is normally a good approximation. Packed beds may also be assumed to emit radiation diffusely (i.e. give an equal distribution of radiant flux density in all directions).

For very smooth particle surfaces unsymmetrical specular reflections may invalidate this assumption (Baddour and Yoon (1960)).

(ii) transmission

Transmission of radiation through the solid particle material need only be considered when the material is not opaque to radiation as is the case for glass (e.g. Chen and Churchill (1963)).

(iii) scattering

Scattering occurs when electro-magnetic waves encounter a discontinuity in refractive index. Thus an assumption of no scattering assumes a refractive index of unity. Scattering of backward radiation flux in the forward direction increases heat transfer and occurs when radiation hits a particle with dimensions smaller than the radiation wavelength (Glaser (1961)). The laws of scattering for small particles are given by Jenkins and White (1957). Scattering can be a significant process of radiation transfer in packed bed systems (Chen and Churchill (1963); Viskanta (1964)).

3.4.2. Radiation between particle surfaces (mechansims 5 and 6)

The only difference between mechanisms 5 and 6 is the path length over which radiation occurs. For mechanism 5, radiation takes place across a single void space, while for mechanism 6 radiation takes place across more than one void.

(i) geometric models

The simplest geometric model considers a packed bed

as containing radiating planes a distance D_P apart. The nett radiation heat transfer between two infinite, gray planes is given by (McAdams (1954))

$$Q_r/A = C_{SB} (T_{A1}^4 - T_{A2}^4) / (\frac{1}{e_1} + \frac{1}{e_2} - 1) \quad \ldots.(3.25)$$

An equivalent radiation thermal conductivity, k_r, or equivalent radiation heat transfer coefficient, h_r may be defined by

$$Q_r/A = - k_r \, dT/dz = h_r (T_2 - T_1) \quad \ldots.(3.26)$$

Thus taking $e_1 = e_2 = e$ and using the approximations for small values of

$T_2 - T_1$ that $dT/dz = (T_2 - T_1) / D_P$ and $T_{2A} \approx T_{1A} = T_A$, it follows from equations 3.25 and 3.26 that

$$k_r = h_r D_P = 4 C_{SB} (\frac{e}{2 - e}) D_P T_A^3 \quad \ldots.(3.27)$$

Damkohler (1937) replaced the emissivity factor $(\frac{e}{2 - e})$ by the factor ϵe and Dul'nev and Sigalova (1965) by the factor $e^2/2$. Godbee and Ziegler (1966) use the factor

$$\omega^2 e (\frac{1}{1 - \epsilon} - 1)$$

where ω is the refactive index of the gaseous media. This model does not allow for interaction between conduction and radiation mechanisms, and does not distinguish between mechanisms 5 and 6.

Schotte (1960) uses an analysis similar to that of Argo and Smith (1953) to distinguish between these mechanisms by considering the radiation between two planes located on

either side of a particle. The result may be expressed as

$$Y_r = \frac{1 - \varepsilon}{1/X + 1/X_{rs}} + \varepsilon X_{rg} \qquad \ldots.(3.28)$$

where

$$X_{rs} = X_{rg}{}^{1} = h_r D_P / k_g = 4\, C_{SB} e T_A{}^3 / k_g$$

It is then assumed that $Y_0 = Y_C + Y_r$ but due to the interaction implied in equation 3.28 these quantities are not additive.

A more satisfactory approach is to apply effective radiation coefficients to the surfaces of a geometric conduction model (Van Loon (1952); Yagi and Kunii (1957)[2]; Kunii and Smith (1960)). Thus equation 3.16 becomes

$$Y_0 = \varepsilon_{A1}(1 + X_{rg}) + \varepsilon_{A2} / \left[\alpha / (1 + \alpha X_{rs}) + \frac{1 - \alpha}{X} \right] + \varepsilon_{A3} X \qquad \ldots.(3.29)$$

(ii) pseudo-homogeneous models

In pseudo-homogeneous models the bed and gas are considered as a single homogeneous medium. This converts the problem to heat transfer in a radiating fluid which may be described by either differential or integro-differential equations. Considerable attention has recently been paid[3] to the numerical solution of such equations for conduction and

---

1. X_{rs} refers to mechanism 5 and X_{rg} to mechanism 6
2. Yagi and Kunii used the expressions $h_{rs} = 4C_{SB}\left(\frac{e}{2 - e}\right) T_A{}^3$ and $h_{rg} = 4C_{SB} / \left[1 + \varepsilon e/2\,(1 - \varepsilon)(1 - e)\right] T_A{}^3$
3. Usiskin and Sparrow(1960); Viskanta and Grosh(1961,1962a, 1962b,1964); Viskanta(1964); Heaslet and Warming(1965); Howell(1965). Radiation was considered as a diffusive process by Traugott and Wang(1964) and Hottel(1962).

radiation in absorbing and scattering materials. The addition of a radiation term to the Fourier equation was used by Van der Held (1953) to obtain

$$Y_r = \frac{16\, C_{SB}\, \omega^2\, T_A^3}{3\, k_g\, (a + b)} \qquad \ldots.(3.30)$$

where a and b are absorption and scattering cross sections per unit volume of packing.

Hamaker (1947) applied the two flux model of Schuster (1905) for the transmission and reflection of light in scattering material to the present radiation - conduction problem. This approach is one dimensional and represents the radiation intensity as a forward flux, i, and a backward flux, j, (Fig. 3.6). In passing through a differential layer dz a fraction, aidz, of the incident flux will be absorbed and a fraction, bjdz, lost by scattering. The forward flux is increased by scattering of the backward flux into the forward direction and by radiant emission from the solid. The basic differential equations are thus[1]

$$di/dz = -(a + b)\, i + bj + a\, C_{SB}\, T_A^4 \qquad \ldots.(3.31)$$

$$-dj/dz = -(a + b)\, j + bi + a\, C_{SB}\, T_A^4 \qquad \ldots.(3.32)$$

---

1. Scattering sideways has been disregarded and it is supposed that any loss of radiant energy in a sideward direction is compensated by an equal contribution from the neighbouring parts of the layer. Thus the area of the layer must be large compared with the thickness. The equations are only applicable to diffuse radiation.

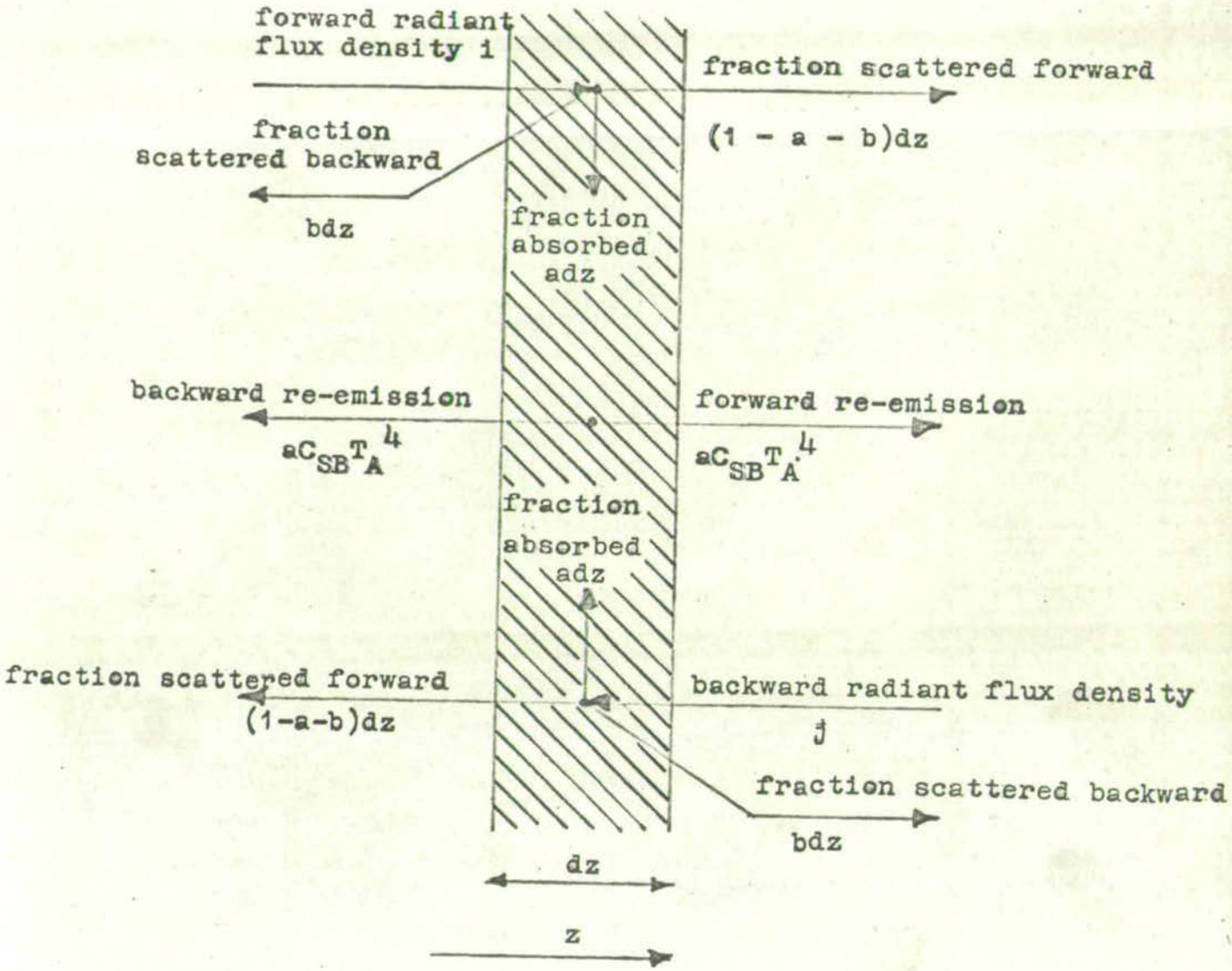

FIG. 3.6 TWO-FLUX PSEUDO-HOMOGENEOUS RADIATION MODEL
e.g. Larkin and Churchill (1959)

and an energy balance gives

$$k_s \, d^2T/dz^2 + a\,(i + j) - 2a\, C_{SB}\, T_A^4 = 0 \qquad \ldots.(3.33)$$

Solutions to the equations based on various approximations have been obtained by Hamaker (1947), Larkin and Churchill (1959) and Chen and Churchill(1963). Sufficiently far from the boundaries of an optically thick bed Chen and Churchill obtained the result[1]

$$Y_r = \frac{8\, C_{SB} T_A^3}{k_g(a + 2b)} \qquad \ldots.(3.34)$$

(iii) finite difference transmission model

Hill and Wilhelm (1959) used a model combining the characteristics of both a geometric model and Hamaker's approach to diffuse energy transfer. A general finite difference method was used to derive both overall and local radiation thermal conductivities. For axial one dimensional heat transfer the local conductivity was given by

$$Y_r = \frac{4\, C_{SB}}{k_g} \left[\frac{1 - f_S^* + f_T^*}{1 + f_S^* - f_T^*} \right] \beta D_P \qquad \ldots.(3.35)$$

(iv) random walk model

By taking the mean free path for photon diffusion equal to D_P in Rosseland's (1936) random walk interpretation

---

1. Based on the boundary conditions

$T = T_1$, $i = e_1\, C_{SB}\, T_{A1}^4 + (1 - e_1)j$, at $z = 0$

and $T = T_2$, $j = e_2\, C_{SB}\, T_{A2}^4 + (1 - e_2)j$, at $z = L$

of radiant energy transfer Bosworth (1952) obtained

$$Y_r = 4D_P T_A^3/3k_g \qquad \ldots.(3.36)$$

3.4.3. Radiation Absorption by the Gas (mechanism 7)

Absorption of radiation by the gas in the bed has to be considered for heteropolar gases such as carbon dioxide, water vapour and sulphur dioxide.

In this case $I_{\lambda,z} = I_{\lambda,o} \exp^{-C_\lambda z}$ ....(3.37)

and $f^*_{A\,\lambda,z} = 1 - \exp^{-C_\lambda z}$ ....(3.38)

where for a gray gas the absorption constant, C_λ , is independent of temperature and distance into the absorbing medium.

Air may be considered non-absorbing and thus mechanism 7 may be neglected for the present experimental system.

3.4.4. Effect of System Variables on the Radiation Mechanisms

Experimental thermal conductivity measurements under radiation conditions have been made on a variety of heterogeneous two phase materials.[1] The radiation contribution has been obtained either by subtraction of the conduction contribution e.g. Hill and Wilhelm (1959) or by direct measurement of the attenuation of radiation transmission through the material e.g. Chen and Churchill (1963). The magnitude of the

---

1. Packed beds:- Yagi and Kunii (1957); Hill and Wilhelm (1959); Baddour and Yoon (1960); Chen and Churchill (1963).
Foamed insulations e.g. Larkin and Churchill (1959).
Fibrous insulations e.g. Verschoor and Greebler (1952).
Ceramic materials e.g. Kingery, Klein and McQuarrie (1958).
Powders e.g. Godbee and Ziegler (1966).

radiation contribution (Table 3.2) is determined by a number of system variables (Table 3.1).

(i) phase variables

The solid thermal conductivity affects the interaction of the radiation and conduction mechanisms. The experimental results of Baddour and Yoon (1960) show that a greater solid thermal conductivity increases the radiation contribution.

The solid emissivity affects the value of the radiation heat transfer coefficients, h_{rs} and h_{rg}, and thus influences mechanisms 5 and 6. For metals the emissivity is low and approximately proportional to the absolute temperature, while for non-metals the emissivity is much greater and generally decreases with increasing temperature.

The gas emissivity which controls mechanism 7 depends on the gas temperature, pressure and molecular structure.

(ii) structural variables

The structural variables of voidage, packing method, packing orientation (for regular packings), particle size and shape affect the radiation view factors and path lengths and thus affect mechanisms 5 and 6. For example, the results of Yagi and Kunii (1957) and Baddour and Yoon (1960) showed increased radiation effects with increased particle size. Radiation increases with a more open structure. For example, in a cubic packing of spheres some points on a particle can see completely through the bed compared with a close-packed tetrahedral packing in which no point on a

Table 3.2. Radiation Contribution to Radiation-Conduction Heat Transfer in Packed Beds.

Reference	Material	Particle size D_P	Temperature T	Y_r/Y_o
Yagi and Kunii(1957) (analysed by Schotte) - (1960))	Iron, cement firebricks	1 - 10 mm.	840°C	.80
Hill and Wilhelm (1959)	Alumina spheres	3 - 8 mm.	100°C 1000°C	.10 .55
Chen and Churchill (1963)	Glass spheres, irregular Silicon Carbide grains	3 - 5 mm. 1 - 7 mm.	2000°F 2000°F	.85 .35
Larkin and Churchill (1959)	Foamed insulation		80-200°F	.05-.20

particle can see further than the next void space.

(iii) operational variables

All models and experimental results (e.g. Table 3.2) show a strong dependence on temperature level. This arises from the temperature dependence of h_{rs}, h_{rg} ($\propto T_A^3$), emissivities and the solid thermal conductivity. Below about 200°C the radiation contribution to the effective thermal conductivity is generally less than 10% and is often neglected.

Large temperature gradients might be expected to increase the interaction of radiation and conduction mechanisms. However, the results of Hill and Wilhelm (1959) and Baddour and Yoon (1960) show no significant effect of temperature gradient (< 500°F/in.).

The gas pressure influences mechanism 7.

3.5. CONVECTION MECHANISMS

3.5.1. Natural Convection in the Gas (mechanism 8)

No direct investigations of natural convection in the voids of porous media appear to have been made. When a gas layer between two parallel plates is heated from below, natural convection commences at a critical value of the Rayleigh number given by (Thompson and Sogin (1966))

$$Ra = Gr.Pr = \left[\frac{\rho^2 \eta g c_p}{\mu k_g}\right] L^3 \Delta T = 1793 \pm 80 \quad ....(3.39)$$

and for $8000 < Ra < 300{,}000$ (Bosworth (1952))

$$Nu = hL/k_g = .208\ Ra^{\frac{1}{2}} \quad ....(3.40)$$

Indirect evidence[1] indicates that natural convection within the voids may be neglected in heterogeneous two-phase systems for the particle sizes and temperature gradients normally encountered.

Horton and Rogers (1945) studied natural convection through porous media and found a critical temperature difference given by

$$\Delta T = \frac{4\pi^2}{p^* L}\left[\frac{\mu k_g}{\rho^2 \eta g c_p}\right] \qquad \ldots.(3.40a)$$

where p^* is the permeability of the bed and L the length of the bed. Bosworth (1952) pointed out that this expression is equivalent to stating that the criterion for the onset of convection is εRa. Further studies have been made by Morrison (1947); Morrison, Rogers and Horton (1949) and Rogers and Morrison (1950). Gopalaratham et al (1961) included an empirical natural convection term in the model of Yagi and Kunii(1957).

3.5.2. Forced Convection Solid-Gas Heat Transfer (mechanism 9)

Mechanism 9 occurs in packed beds whenever there is a temperature difference between the surface of a solid particle in the bed and a gas flowing through the surrounding voids. Thus for an element of solid surface area dA,

$$dQ = hdA\,(T - t) \qquad \ldots.(3.41)$$

where h is the solid-gas heat transfer coefficient.

---

1. Pollack (1948); Verschoor and Greebler (1952); Deissler and Eian (1952); Hill and Wilhelm (1959).

The coefficient, h, varies locally around a particle in the bed, approaching zero at the contact points and reaching a maximum value at points furthest away from the contact points on the upstream side of the particle.[1] For a sphere in a cubic packing the variations in h over most of the surface are in the range 80 - 150% of the average value (Denton (1951)). Since the local variations are very dependent on local structural and hydrodynamic factors it is better to describe mechanism 9 in terms of an average value of h which is much less dependent on such factors.

Values of h may be determined from heat, mass or simultaneous heat and mass transfer considerations, since the two processes are closely analagous in packed bed systems.

(i) theoretical models for the solid-gas transfer coefficient, h

Ranz (1952) and Weisman (1955) related packed bed coefficients to those for single spheres and staggered tube banks respectively by considering equivalent Reynolds numbers for the different geometries.

A boundary layer model was used by Carberry (1960) by considering transient molecular diffusion into a boundary layer which alternately developed and collapsed over a distance of one particle diameter.

---

1. Denton (1951); Aerov et al (1960); Ozisik, Korsmeyer and Rhoden (1961); Rhodes and Peebles (1965); Nawaz (1966).

The result was

$$J = \left(\frac{h}{c_p G}\right) Pr^{\frac{2}{3}} = 1.15 \, (Re\,\varepsilon)^{-\frac{1}{2}} \quad \left(1/\varepsilon < Re < \frac{1000}{\varepsilon}\right) \quad \ldots.(3.42)$$

Pfeffer (1964) combined a free surface model with a thin boundary layer solution of the diffusion equation. A unit cell in the bed was represented as a solid sphere surrounded by a spherical envelope of fluid (giving a cell voidage ε) which had a frictionless or free outer surface with the temperature or concentration of the forward moving fluid. The solution is applicable for low Reynolds numbers and high Peclet numbers and has the result

$$J = 1.26 \left\{ \left[\frac{1 - (1 - \varepsilon)^{\frac{5}{3}}}{C_1} \right]^{-\frac{1}{2}} Re \right\}^{\frac{2}{3}} \quad \ldots.(3.43)$$

where $C_1 = 2 - C_2 + 3C_2^5 + 2C_2^6$ and $\varepsilon = 1 - C_2^3$

A similar approach was taken by Kitaura and Tanaka (1964). Kolar (1962) applied the penetration theory.

(ii) <u>experimental determination and correlation of the solid-gas transfer coefficient, h</u>

Numerous experimental derivations of h have been made but the wide range of results indicates that the data obtained must be considered in relation to the particular experimental technique used and the limitations thereof.

a) <u>sublimation of solid into gas</u>. The mass transfer from a sublimable material in the form of a solid or coated particle is measured under steady state conditions (e.g. Rowe and Claxton (1965)). Napthalene-air is the most common system and measurements have been made in the range Re = .2 - 20,000.

Most determinations have not corrected for axial mixing of the gas (Bradshaw and Bennett(1961)).

b) dissolution of solid in liquid. The mass transfer of a soluble material in the form of a solid or coated particle is measured under steady state conditions (e.g. Williamson, Bazaire and Geankoplis (1963)). Benzoic acid-water is the most common system. Errors due to natural convection may occur at low Reynolds numbers.

c) steady state heat transfer. Such methods have included internally heated spheres placed in the centre of the bed (e.g. Glaser (1962)), induction heating throughout the bed (e.g. Baumeister and Bennett(1958)) and axial heat transfer through the bed (e.g. Kunii and Smith (1961)).

d) unsteady state heat transfer. This method obtains the coefficient h from an analysis of the temperature-time graph of the outlet gas temperature for either a step change (e.g. Saunders and Ford (1940)) or a cyclic variation (e.g. Meek (1962)) in the inlet gas temperature.

e) evaporation of a liquid from a porous solid. The bed particles consist of porous particles saturated with liquid which is evaporated under constant rate conditions (e.g. Kramers and Thoenes (1958); Gupta and Thodos (1963)). These workers also discuss the errors present in this method.

f) heterogeneous gas-solid reactions. The transfer coefficient may be obtained from the temperature or concentration profiles in a reacting (Chukanov (1963)) or catalytic (Satterfield and Resnick (1954)) bed of solids.

Experimental data are usually correlated in terms of J factors as a function of some form of Reynolds number or in terms of Nusselt numbers as a function of Reynolds and either Prandtl or Schmidt numbers.

Yeh (1961) gave a generalised correlation which included fluidised bed data.

$$J_h \, Re = Nu/Pr^{\frac{1}{3}} = .85 \, Re^{.65} \qquad ....(3.44)$$

$$J_d \, Re = Nu/Sc^{\frac{1}{3}} = .80 \, Re^{.60} \qquad ....(3.45)$$

Yoshida, Ramaswami and Hougen (1962) gave the generalised correlations

$$J_h = 0.91 \, Re''^{-.51} \qquad (Re'' < 50) \qquad ....(3.46)$$

$$J_d = 0.85 \, Re''^{-.51} \qquad (Re'' < 50) \qquad ....(3.47)$$

$$J_h = 0.61 \, Re''^{-.41} \qquad (Re'' < 50) \qquad ....(3.48)$$

where $Re'' = G/(S \mu \psi)$.

For low Reynolds numbers the most accurate data appear to be those obtained using a solid dissolution method by Williamson, Bazaire and Geankoplis (1963) for which

$$J_d = 2.50 \, Re^{-.66} \qquad (.035 < Re < 55) \qquad ....(3.49)$$

Further recent work by Wilson and Geankoplis (1966) confirmed and extended this data. In the absence of any available solid-gas transfer coefficient measurements at low Reynolds numbers equation 3.49 is used for the analysis of the present experimental data.

3.5.3. Forced Convection due to Bulk Flow and Mixing of the Gas (mechanism 10)

Mechanism 10 makes a considerable contribution to the heat transfer when gas flows through the bed. Since the bulk flow of the gas is dependent on the Reynolds number and the void mixing of the gas is dependent on the Peclet number (2.3), this mechanism is accounted for directly in the diffusion and mixing cell models (4.3).

3.5.4. Effect of System Variables on Convection Mechanisms

Table 3.1 indicates the system variables which affect the convection mechanisms.

(i) phase variables

The fluid properties of density, viscosity, specific heat, volumetric expansion coefficient and thermal conductivity affect one or more of the convection mechanisms. (equation 3.39 - 49).

(ii) structural variables

An increase in bed voidage gives a decreased transfer coefficient, h. This is often accounted for by using a Reynolds number based on the interstitial velocity, v_o/ε. For regular packings of spheres Galloway, Komarnicky and Epstein (1957) found some dependence on the method of packing.

Most investigations have found no effect of particle size on mechanism 9, but it does affect mechanism 8 (equations 3.39 - 40). The effect of surface roughness of

the particles does not appear to have been investigated, but it may well be a factor accounting for some of the wide range of results obtained for transfer coefficients.

(iii) operational variables

Since temperature affects the fluid properties it has a small effect on all the convection mechanisms. Temperature gradient is a controlling factor for mechanism 8 and also affects the solid-gas temperature difference for mechanism 9. Increased gas flow rate tends to eliminate mechanism 8 and substantially increase heat transfer by the forced convection mechanisms 9 and 10.

Any differences in heat transfer between upward and downward fluid flow or heat flow are due to natural convection effects. Different results have sometimes been obtained for solid-gas and gas-solid heat transfer, but this was probably due to conduction and radiation effects in the experimental system. Slightly higher values have usually been obtained for heat transfer J factors compared with mass transfer J factors. e.g. $J_h/J_d = 1.076$ (Gupta and Thodos (1963)). However this effect may be due to heat losses since by taking special precautions McConnachie and Thodos (1963), obtained $J_h = J_d$.

3.6. SIMULTANEOUS CONDUCTION, CONVECTION, AND RADIATION MECHANISMS

The only previous experimental investigations of axial heat transfer with a flowing fluid in packed bed systems (Table 3.3) have been for heat flow countercurrent to the fluid flow and for low bed temperatures ($< 300^{\circ}C$) where radiation effects are small and have been neglected. All the investigators have expressed their results in terms of an overall effective thermal conductivity, k_e, which does not distinguish between the conduction and convection mechanisms and assumes equal solid and fluid temperatures. Axial heat transfer was found to increase with the solid thermal conductivity, fluid flow rate and fluid Prandtl number and more efficient void mixing of the fluid represented by the constant C in correlations of the form

$$Y' = Y_0 + C\,RePr \qquad ....(3.50)$$

However, Bischoff (1962) showed that the overall axial effective thermal conductivity could not be separated into a stagnant contribution and a flowing contribution as is implied in such correlations.

Bischoff (1962) estimated axial conductivities from data on radial conductivities[1] by comparing second moments of temperature distributions assuming equal solid and fluid temperatures, to obtain

---

1. heat flow perpendicular to fluid flow.

Table 3.3. Experimental Measurements of Axial Heat Transfer for Gas Flow through Random Packed Beds.

Reference	Fluid	Packing	ε	D_P	D_T	L	T	Re	Correlation
Yagi, Kunii, Wakao (1960)	air	glass beads, steel balls, lead shot, broken lime-stone pieces	.40-.69	0.91-9.0 mm.	50,68 mm.	11.5 cm.	90-140°C	.79-52.3	$Y = Y_0 + (0.7 - 0.8)RePr$
Kunii and Smith (1961)	air, helium, nitrogen, carbon dioxide, water	glass beads, sand	.37, .43	.00043 -.0402 mm.			293-565°F	10^{-3} -1.0	
Kimura (1961)	glass, celluloid and steel spheres, Raschig rings, quartz sand	water	.392-.439	2.82-12.2 mm.	10.6 cm.	16.2-52.7 cm.		5.08-208*	
Adivarahan, Kunii, Smith (1962)	nitrogen, carbon dioxide, helium, 10% NaCl soln.	consolidated sandstone	.177-.298	(2.14-5.61)x 10^{-5} ft.**	2.0 in.	3.75 in.	70-300°F	5 x 10^{-4} -1.0*	$Y = Y_0(1 - \varepsilon) + \varepsilon(1 + 4 \times 10^3 RePr)$
Ikeda, Nishimura, Kubota (1964)	air	glass, steel, brass spheres		9.6-10.1 mm.			40°C	10-75	$Y = Y_0 + .14Y_0^{.6}RePr$
Green, Perry, Babcock (1964)	distilled water, 30%, 60% glycerol soln. ethyl alcohol	glass spheres	.355	.0038 -.118 ins.			70-180°F		$Y = Y_0 + 115(RePr)^{1.25} + C\,Re^{1.5}Pr^{1.67}$ ***

* interstitial Reynolds number. ** pore radius. *** $C = \dfrac{.085/\varepsilon}{\left[\sqrt{\dfrac{1-\varepsilon}{\varepsilon}} + \dfrac{\rho c_P}{\rho_S c_S}\sqrt{\dfrac{\varepsilon}{1-\varepsilon}}\right]^2}$

$$Y = Y_{rad} + \frac{C_1 (D_T/D_P)^2 Re^2 Pr^2}{4\, Y_{rad}} \qquad \ldots.(3.51)$$

where $Y_{rad} = Y_0 + C_2\, RePr$ and C_1 and C_2 are radial dispersion constants. Huang and Smith (1963) related the axial and radial conductivities through Peclet number values for mass transfer by the relationship

$$(Y' - Y_0)/(Y_{rad} - Y_0) = Pe_{rad}/Pe_z \qquad \ldots.(3.52)$$

where $$Pe_{rad} = \frac{v_0 D_P}{\varepsilon E_r}$$

Weiner and Edwards (1963) made a theoretical study of one dimensional heat transfer by conduction, convection and radiation in an absorbing bed. The bed was assumed semi-infinite, gray and non-scattering and to be in thermal equilibrium with a constant property transparent fluid flowing through it.

CHAPTER 4 THEORETICAL MODELS

4.1. CONDUCTION MODEL

4.1.1. Nature of the Model

The model developed here for the conduction mechanisms is a geometric type of model in which the thermal conductivity of a random packed bed of spheres is calculated from an idealised arrangement of the gas and solid phases. This type of model has been chosen since it is a simple one-dimensional representation and is thus well suited for axial heat transfer as in the present experimental system. It may also be extended to include the radiation mechanisms as in 4.2.

The geometric models developed by previous workers were discussed in 3.3.1 where various errors, inconsistencies and poor assumptions were pointed out. In the model developed here it is intended to avoid these faults and to base the evaluation of model parameters on fundamental rather than semi-empirical considerations.

4.1.2. Unit Cell of the Model

The packing of the bed consists of a random (or regular) arrangement of equal-sized spheres. To apply a conduction model the bed is considered to consist of an assembly of unit cells (defined in 2.1.1) built up from parallel rows of unit cells placed on top of each other in the direction of axial heat flow. The axial positions of unit cells in successive rows are randomly displaced with respect to each other (Fig. 4.1) so that a cross-sectional slice across the bed has

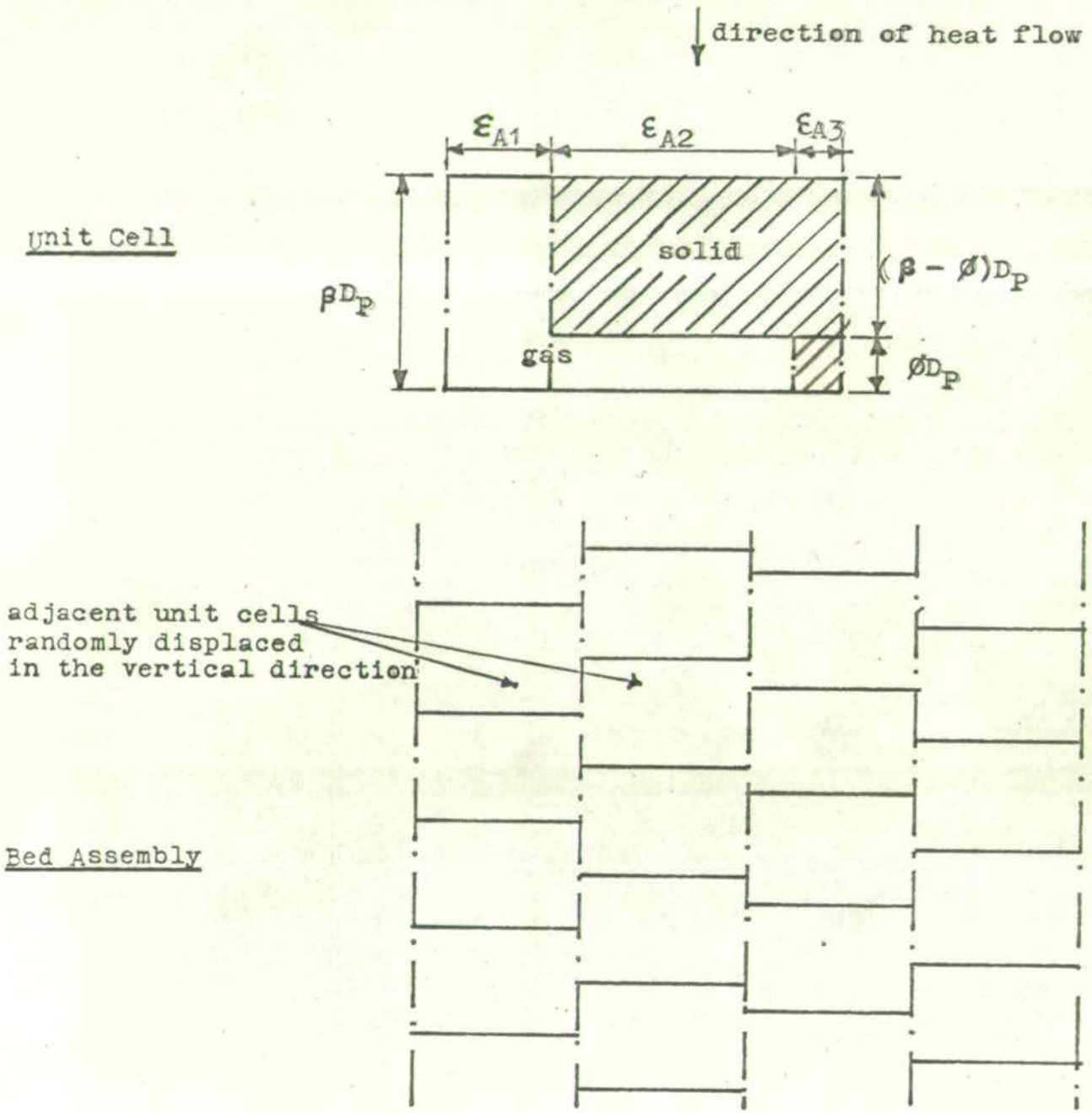

FIG. 4.1 CONDUCTION MODEL

—·— adiabatic lines

——— isothermal lines

an area gas fraction equal to the bulk mean voidage of the bed (2.1.4).

The unit cell is a rectangular slab (Fig. 4.1) of unit cross-sectional area and thickness equal to the average layer spacing, βD_p. The cell consists of a fractional volume $(1 - \varepsilon)$ of solid material of thermal conductivity k_s and a fractional volume ε of stagnant gas of thermal conductivity k_g.

The unit cross sectional area is divided into three parallel paths of areas ε_{A1}, ε_{A2} and ε_{A3} (Fig. 4.1) to account for the following conduction mechanisms. Conduction across the gas in the bulk of the voids (mechanism 2) is represented by the heat transfer through the area ε_{A1} across a gas layer of thickness βD_p. Conduction through the solid (mechanism 1) is represented by heat transfer through an area $\varepsilon_{A2} + \varepsilon_{A3}$ across a solid layer of thickness $(\beta - \phi)D_p$ in series with

a) a gas layer of thickness βD_p and area ε_{A2} accounting for the series path conduction across the stagnant gas surrounding the points of contact (mechanism 3) and

b) a solid layer of thickness βD_p and area ε_{A3} accounting for the conduction through the points of contact of particles (mechanism 4).

The major difference from previous geometric models (3.3.1) is that the contact point path of area ε_{A3} is not insulated adiabatically from the series solid path of area ε_{A2} (compare Fig. 3.4 and Fig. 4.1). The bending of the isothermal lines in Fig. 3.3 shows that heat transfer does take place across the

boundary between these paths. Under vacuum conditions the previous models with an adiabatic line only gave heat transfer through the solid in the contact point path. But in fact heat transfer takes place throughout the solid particles and the greater the number of contact points the more uniformly is the flux distributed through the particles. The present model under vacuum conditions allows for this by giving heat flow through the solid area $\varepsilon_{A2} + \varepsilon_{A3}$ over the length $(\beta - \phi)D_p$ and then out into the next cell through the contact area ε_{A3}.

The side boundaries of the unit cell are considered adiabatic. This implies that any sideways heat outflow from one part of the cell is compensated by sideways heat inflow into another part, which is a reasonable assumption for nett axial heat flow. The end boundaries of the unit cell, the solid-gas interface in the series path and the line extending the interface into the contact area path are all considered isothermal (Fig. 4.1).

4.1.3. Effective Thermal Conductivity of the Model

Consider the assembly of unit cells shown in Fig. 4.1. Let $\overline{R}_o$ be the heat transfer resistance of a unit cell, $\overline{R}_1$, $\overline{R}_2$ ..... $\overline{R}_m$ the resistances of m parallel cell paths, and $\overline{R}$ the resistance of a complete bed assembly m cells long. Since a unit cell has unit cross sectional area

$$\overline{R}_o = \beta D_p / k_{ec}(\text{cell}) \qquad \ldots.(4.1)$$

and

$$\overline{R} = \beta D_p / k_{ec}(\text{bed}) \qquad \ldots.(4.2)$$

Since in each parallel path there are m cells in series

$$\bar{R}_1 = \bar{R}_2 = \cdots = \bar{R}_m = m\bar{R}_o \qquad \ldots.(4.3)$$

and since there are m parallel paths

$$\frac{1}{\bar{R}} = \sum_{1}^{m} \frac{1}{\bar{R}_r} = \frac{m}{\bar{R}_1} = \frac{1}{\bar{R}_o} \qquad \ldots.(4.4)$$

therefore $\bar{R} = \bar{R}_o$ $\ldots.(4.5)$

From equations 4.1, 4.2, and 4.5 it follows that

$$k_{ec}(\text{bed}) = k_{ec}(\text{cell}) \qquad \ldots.(4.6)$$

Thus the thermal conductivity of the bed may be evaluated from the thermal conductivity of a unit cell.

Applying the Fourier equation to the gas parallel path gives

$$Q\,\varepsilon_{A1} = k_g\ \varepsilon_{A1}\ \Delta T/\beta D_P \qquad \ldots.(4.7)$$

Applying the Fourier equation to the solid-gas series and contact area paths gives the temperature drops ΔT_1 and ΔT_2 across the lengths $(\beta - \phi)D_P$ and ϕD_P as

$$\Delta T_1 = \frac{Q\,(\varepsilon_{A2} + \varepsilon_{A3})(\beta - \phi)D_P}{k_s\,(\varepsilon_{A2} + \varepsilon_{A3})} \qquad \ldots.(4.8)$$

and $$\Delta T_2 = \frac{Q\,(\varepsilon_{A2} + \varepsilon_{A3})\phi D_P}{k_g\,\varepsilon_{A2} + k_s\,\varepsilon_{A3}} \qquad \ldots.(4.9)$$

since the gas and solid paths of area ε_{A2} and ε_{A3} are in parallel over the length ϕD_P.

Since the axial temperature drop across the unit cell, ΔT, is given by $\Delta T = \Delta T_1 + \Delta T_2$ ....(4.10)

equations 4.8, 4.9, 4.10 give

$$Q(\varepsilon_{A2} + \varepsilon_{A3}) = \frac{1}{\frac{\beta - \phi}{k_s(\varepsilon_{A2} + \varepsilon_{A3})} + \frac{\phi}{k_g \varepsilon_{A2} + k_s \varepsilon_{A3}}} \left(\frac{\Delta T}{D_P}\right) \quad \ldots.(4.11)$$

Since the continuous gas and gas-solid-contact area paths are in parallel

$$Q = \frac{k_{ec} \Delta T}{\beta D_P} = Q \varepsilon_{A1} + Q(\varepsilon_{A2} + \varepsilon_{A3}) \quad \ldots.(4.12)$$

From equations 4.7, 4.11 and 4.12 it follows that

$$k_{ec} = \varepsilon_{A1} k_g + \frac{\beta}{\frac{\beta - \phi}{k_s(\varepsilon_{A2} + \varepsilon_{A3})} + \frac{\phi}{k_g \varepsilon_{A2} + k_s \varepsilon_{A3}}} \quad \ldots(4.13)$$

$$\text{therefore } Y_C = \varepsilon_{A1} + \frac{1}{\frac{1 - \alpha}{X(1 - \varepsilon_{A1})} + \frac{\alpha}{\varepsilon_{A2} + X \varepsilon_{A3}}} \quad \ldots(4.14)$$

where $Y_C = k_{ec}/k_g$, $X = k_s/k_g$ and $\alpha = \phi/\beta$

Under vacuum conditions the contributions from the gas phase resistances disappear giving

$$Y_C^* = \frac{X}{\frac{1 - \alpha}{1 - \varepsilon_{A1}} + \frac{\alpha}{\varepsilon_{A3}}} \quad \ldots.(4.15)$$

4.1.4. Evaluation of Model Parameters

(i) assumptions

It is assumed that the volume of the gas layer in the series conduction path is equal to the volume of pendular gas rings surrounding each contact point between particles in the unit cell (Fig. 4.2). It is further assumed that these pendular rings cover the maximum possible surface area of each particle. This condition is obtained when the contact points on each particle are equispaced from each other and the pendular rings of adjacent contact points touch each other on the particle surface.

(ii) pendular ring angle, Θ_{PR}

The pendular ring angle, Θ_{PR} is half the angle subtended at the centre of a particle by the circumference of a pendular ring which touches the particle surface (Fig.4.2). For the assumption of equispaced contact points given above it follows from equations A.46 and A.47 that

$$\Theta_{PR} = \frac{1}{2} \cos^{-1} \left\{ \frac{\cos[\pi n/3(n-2)]}{1 - \cos[\pi n/3(n-2)]} \right\} \quad \ldots\ldots(4.16)$$

(iii) coordination number n

It was shown in 2.1.4 that a suitable relationship between the coordination number, n and the voidage ε is the equation of Haughey and Beveridge (1966),

$$n = 22.47 - 39.39\varepsilon \quad \ldots\ldots(4.17)$$

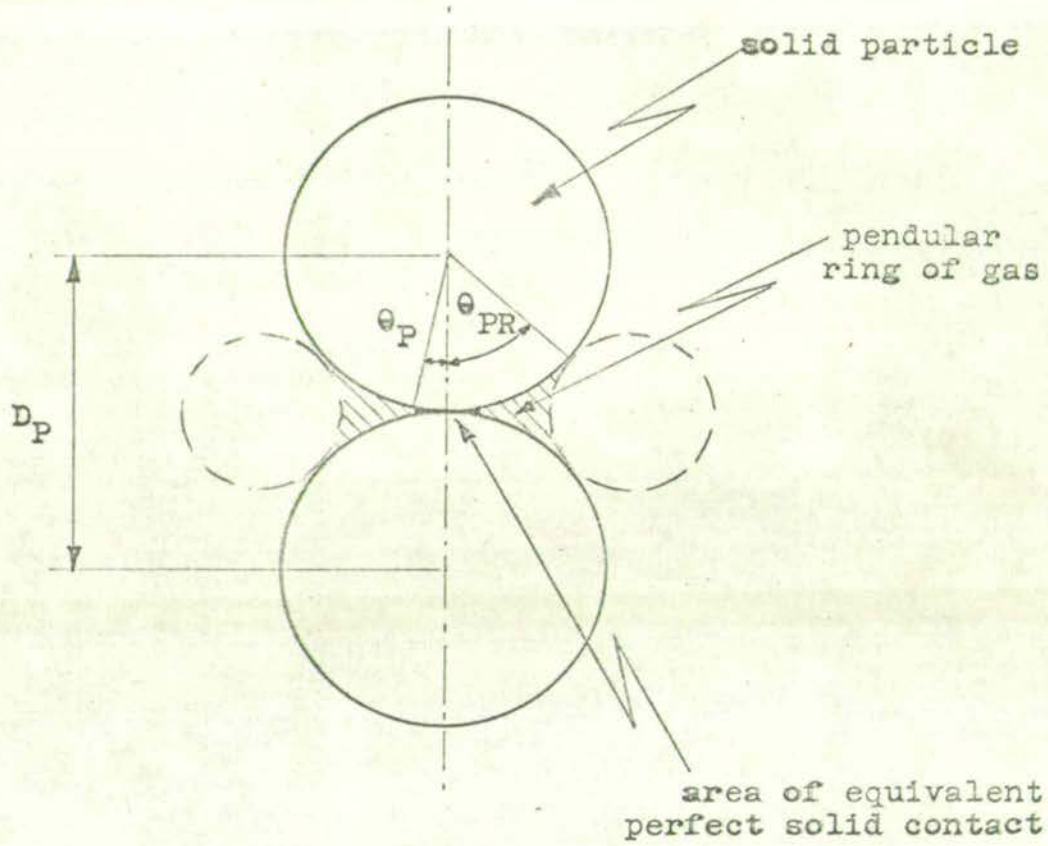

FIG. 4.2 GAS PENDULAR RING AND SOLID CONTACT AREA BETWEEN TWO PARTICLES

(iv) fractional series gas layer thickness,

Since the unit cell volume is βD_P, the fractional volume of solid is $1 - \varepsilon$, the volume of one sphere is $\pi D_P^3/6$ and each of the n contact points on a sphere is associated with two spheres, the total number of contact points and hence the total number of pendular rings in a unit cell is given by

$$N_{PR} = N_n = \frac{3(1 - \varepsilon)\beta n}{\pi D_P^2} \qquad \ldots.(4.18)$$

Fisher (1926) and Rose (1958) showed that the volume of a pendular ring is given by

$$V_{PR} = \frac{\pi D_P^3}{4} (\text{Sec}\ \theta_{PR} - 1)^2 \left[1 - (\frac{\pi}{2} - \theta_{PR}) \tan \theta_{PR} \right] \qquad \ldots(4.19)$$

From the assumptions given above, the gas volume in the series path is

$$N_{PR}\, V_{PR} = \emptyset\, D_P\, \varepsilon_{A2} \qquad \ldots.(4.20)$$

therefore

$$\alpha = \frac{N_{PR}\, V_{PR}}{D_P\, \varepsilon_{A2}\, \beta} \qquad \ldots.(4.21)$$

From equations 4.18, 4.19 and 4.21

$$\alpha = \frac{3}{4} \frac{(1 - \varepsilon)}{\varepsilon_{A2}} n\, (\sec \theta_{PR} - 1)^2 \left[1 - (\frac{\pi}{2} - \theta_{PR}) \tan \theta_{PR} \right] \qquad \ldots.(4.22)$$

It is convenient to define a parameter α^* by

$$\alpha^* = \alpha \varepsilon_{A2} = \frac{3}{4} (1 - \varepsilon)\, n\, (\sec \theta_{PR} - 1)^2 \left[1 - (\frac{\pi}{2} - \theta_{PR}) \tan \theta_{PR} \right] \qquad \ldots.(4.23)$$

(v) area fractions ε_{A1}, ε_{A2}

Since the cell is of unit cross-sectional area we have

$$\varepsilon_{A1} + \varepsilon_{A2} + \varepsilon_{A3} = 1 \qquad \ldots.(4.24)$$

and since the total gas volume in the cell is $\varepsilon \beta D_P$ we have

$$\varepsilon_{A1}\, \beta D_P + \varepsilon_{A2}\, \emptyset\, D_P = \varepsilon \beta D_P \qquad \ldots.(4.25)$$

Thus since $\alpha = \phi/\beta$ it follows that

$$\varepsilon_{A1} + \alpha \varepsilon_{A2} = \varepsilon \qquad \ldots.(4.26)$$

From equations 4.24 and 4.26

$$\varepsilon_{A1} = \frac{\varepsilon - \alpha(1 - \varepsilon_{A3})}{1 - \alpha} \qquad \ldots.(4.27)$$

$$\varepsilon_{A2} = \frac{1 - \varepsilon - \varepsilon_{A3}}{1 - \alpha} \qquad \ldots.(4.28)$$

Substituting $\alpha = \alpha^* / \varepsilon_{A2}$ into equations 4.28 and 4.27

gives $\varepsilon_{A2} = 1 - \varepsilon - \varepsilon_{A3} + \alpha^* \qquad \ldots.(4.29)$

and $\varepsilon_{A1} = 1 - \alpha^* \qquad \ldots.(4.30)$

(vi) <u>area fraction, ε_{A3}</u>

Since the contact point area fraction, ε_{A3}, is a function of particle surface characteristics, solid elasticity and particle loading, it cannot be evaluated solely from the bed geometry, but must be obtained from an experimental effective thermal conductivity measurement under the required particle surface and loading conditions. The experimental measurement used may be made either under vacuum or at atmospheric pressure at a temperature such that radiation effects are insignificant.

For a vacuum effective thermal conductivity measurement substituting equations 4.29 and 4.30 into 4.15 and solving gives

$$\varepsilon_{A3} = -\left[\frac{C_2 + \sqrt{C_2^2 - 4C_1C_3}}{2C_1}\right] \qquad \ldots.(4.31)$$

where $$C_1 = (1 - \varepsilon + \alpha^*) \frac{X}{Y_C^*} - 1$$

$$C_2 = (1 - \varepsilon) - (1 - \varepsilon + \alpha^*) \frac{X}{Y_C^*}$$

$$C_3 = \alpha^*(1 - \varepsilon + \alpha^*)$$

For an atmospheric effective thermal conductivity measurement, substituting equations 4.29 and 4.30 into 4.14 and solving gives

$$\varepsilon_{A3} = \frac{C_2 + \sqrt{C_2^2 - 4C_1C_3}}{2C_1} \qquad \ldots.(4.32)$$

where $$C_1 = (X - 1)\left[\frac{1}{X(1 - \varepsilon + \alpha^*)} - \frac{1}{(Y - \varepsilon + \alpha^*)}\right]$$

$$C_2 = (1 - \varepsilon + \alpha^*)\left[\frac{1}{X(1 - \varepsilon + \alpha^*)} - \frac{1}{(Y - \varepsilon + \alpha^*)}\right] +$$

$$(X - 1)\left[\left(\frac{1 - \varepsilon + \alpha^*}{Y - \varepsilon + \alpha^*}\right) - \frac{1}{X}\left(\frac{1 - \varepsilon}{1 - \varepsilon + \alpha^*}\right)\right]$$

$$C_3 = (1 - \varepsilon + \alpha^*)\left[\left(\frac{1 - \varepsilon + \alpha^*}{Y - \varepsilon + \alpha^*}\right) - \frac{1}{X}\left(\frac{1 - \varepsilon}{1 - \varepsilon + \alpha^*}\right)\right]$$

(vii) <u>contact point area angle,</u> θ_P

If the contact area ε_{A3} is assumed to be composed of a circular area of contact at each contact point within the unit cell, then a contact area angle θ_P may be evaluated.

This angle is defined as half the angle subtended at a sphere centre by the circumference of the contact area at each contact point (Fig. 4.2). Thus it follows that

$$N_n \pi \left(\frac{D_P}{2} \sin\theta_P\right)^2 = \varepsilon_{A3} \qquad \ldots.(4.33)$$

and from equation 4.18

$$\theta_P = \sin^{-1}\left[\frac{4\ \varepsilon_{A3}}{3(1-\varepsilon)\beta n}\right] \qquad \ldots.(4.34)$$

4.1.5. Solution of the Model

The effective condution thermal conductivity ratio, Y_C is given by equations 4.14, 4.16, 4.17, 4.23 and either 4.31 or 4.32. These equations show that the conduction effective thermal conductivity ratio is a function solely of the bulk mean voidage ε and the contact area ε_{A3}. The contact area, ε_{A3} must be determined by an experimental measurement and may be related to a contact area angle θ_P (equation 4.34).

If the model is applied at conditions between atmospheric and vacuum then the effect of pressure on the thermal conductivity of the gas in the series path should be evaluated from kinetic theory of gases (e.g. Kennard (1938)) (see 3.3.3).

4.1.6. Effect of Model Parameters

Using the above equations, Fig. 4.3 and 4.4 show the effect of the solid and gas thermal conductivities and the bulk mean voidage on the conduction effective thermal conductivity and the conduction vacuum conductivity respectively. The thermal conductivities increase with the ratio of solid

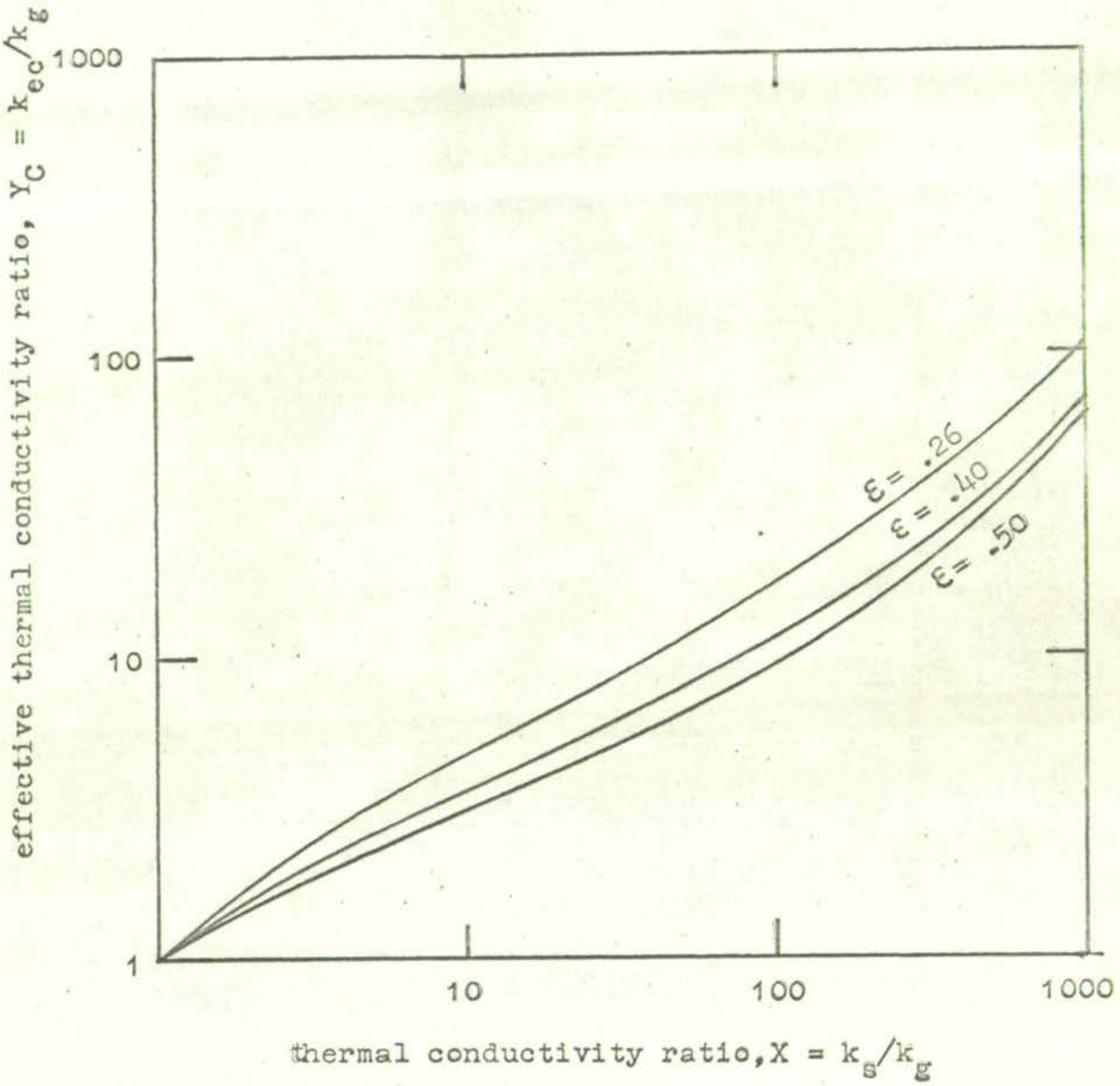

FIG. 4.3 EFFECT OF PHASE CONDUCTIVITIES AND BED VOIDAGE ON THE CONDUCTION MODEL EFFECTIVE THERMAL CONDUCTIVITY

($\varepsilon_{AS} = .01$)

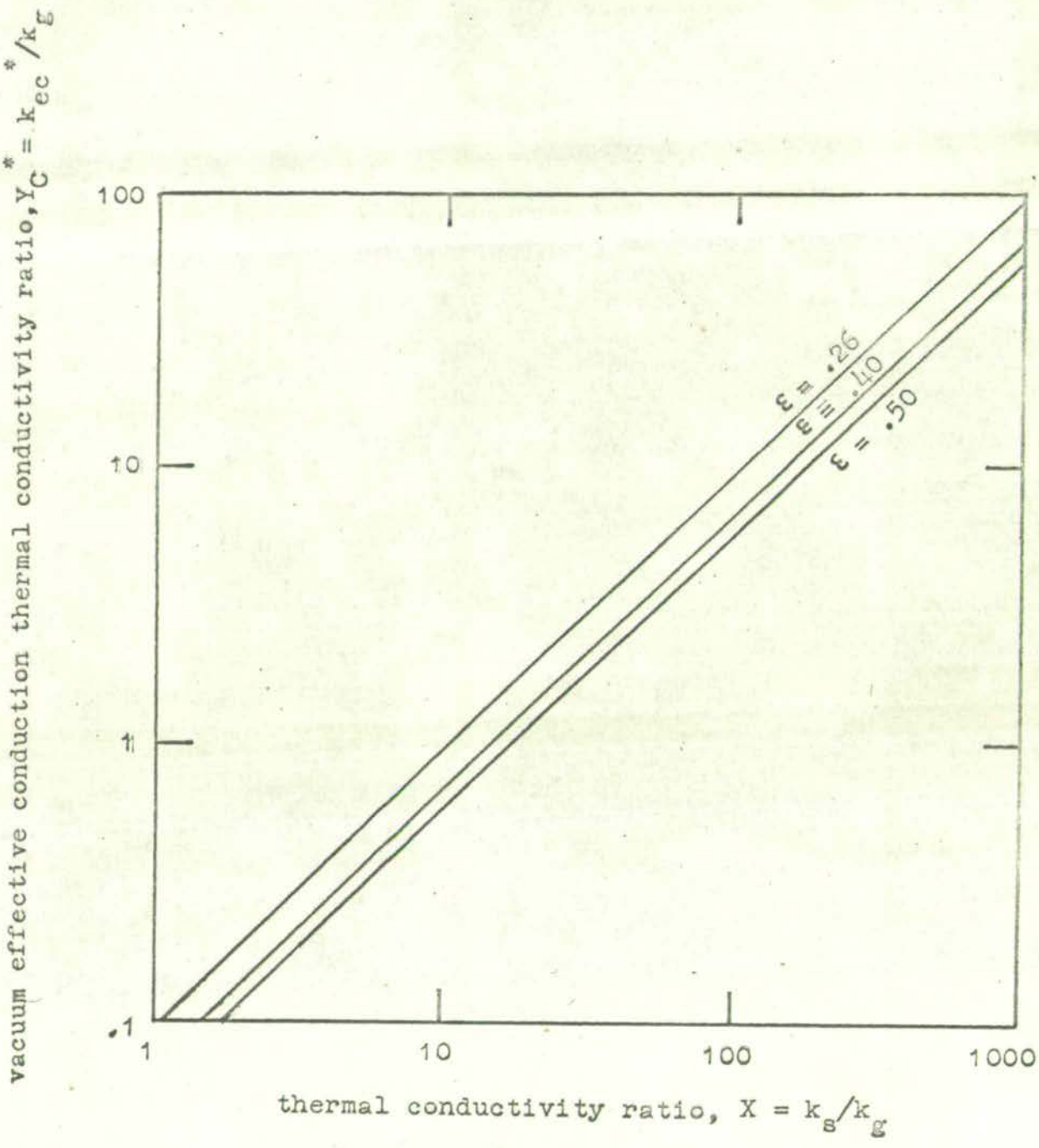

FIG. 4.4 EFFECT OF PHASE CONDUCTIVITIES AND BED VOIDAGE ON THE CONDUCTION MODEL EFFECTIVE THERMAL CONDUCTIVITY UNDER VACUUM

($\varepsilon_{AB} = .01$)

to gas thermal conductivity, linearly in the case of the vacuum conductivity. The effective thermal conductivities decrease linearly over the voidage range .26 - .45 corresponding to packed beds of spheres.

The effect of the contact point area ε_{A3} is shown in Fig. 4.5. Both the effective thermal conductivity and vacuum conductivity increase with ε_{A3} but the effect is very much greater on the vacuum conductivity.

4.2. CONDUCTION-RADIATION MODEL

4.2.1. Inclusion of Radiation Mechanisms

The radiation mechanisms 5 and 6 may be incorporated by an extension of the conduction model. Radiation between adjacent particle surfaces (mechanism 5) is accounted for by the application of a radiation heat transfer coefficient, h_{rs}, over the area ε_{A2} of the solid-gas interface in the series path. Radiation between particle surfaces seen through more than one void (mechanism 6) is accounted for by the application of the radiation heat transfer coefficient, h_{rg}, over the area ε_{A1} of the gas parallel path. To produce this radiation mechanism physically, successive unit cells placed on top of each other in the bed assembly (Fig. 4.1) may be regarded as being rotated through 180° with respect to each other. Both radiation paths are in parallel with the respective gas conduction paths.

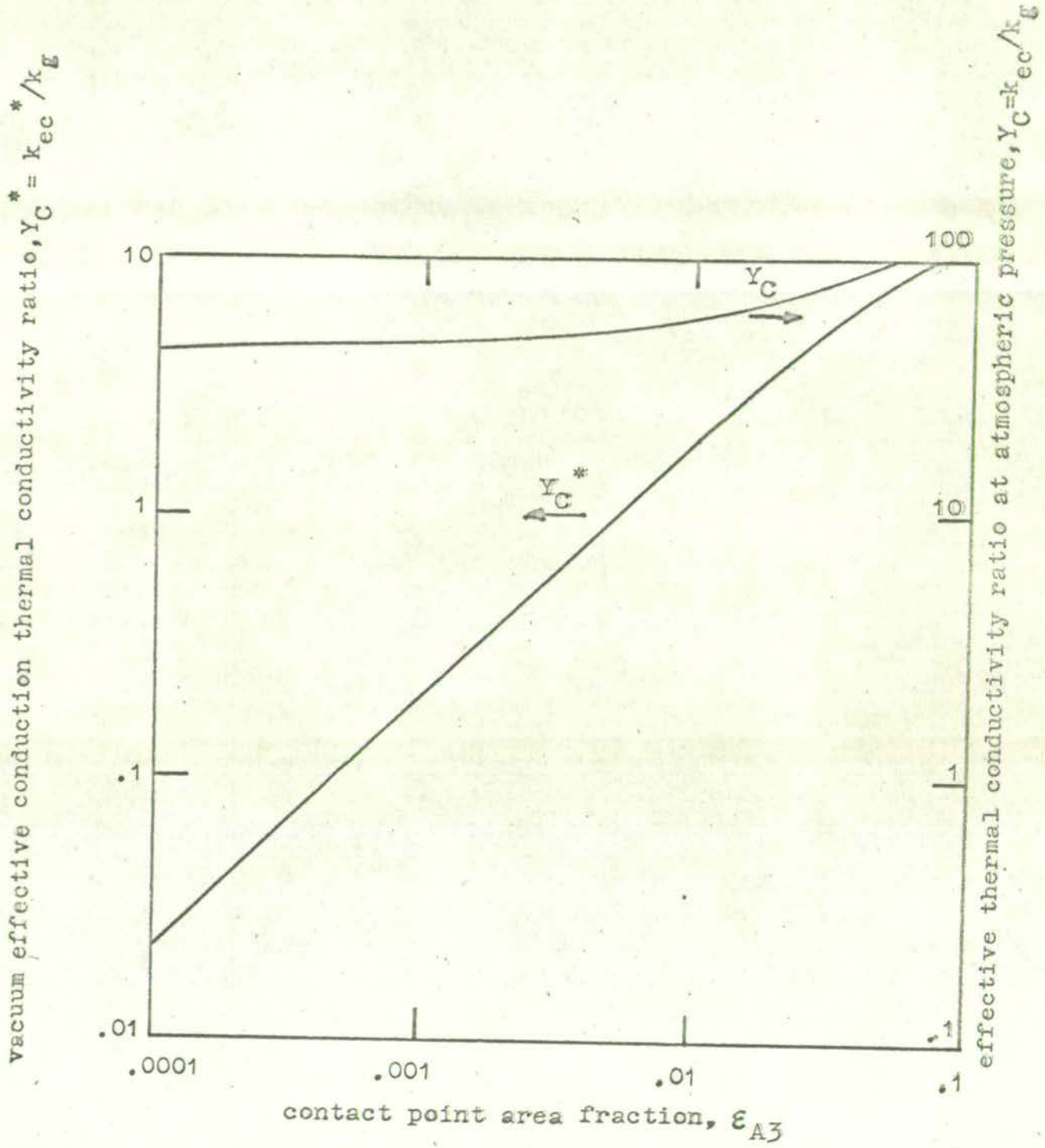

FIG. 4.5 EFFECT OF CONTACT POINT AREA ON THE CONDUCTION MODEL EFFECTIVE VACUUM AND ATMOSPHERIC PRESSURE THERMAL CONDUCTIVITIES

bulk mean voidage, ε = .40; thermal conductivity ratio, X = 30

4.2.2. Effective Thermal Conductivity of the Model

With the inclusion of radiation, equation 4.7 becomes

$$Q\,\varepsilon_{A1} = \left(\frac{k_g}{\beta D_P} + h_{rg}\right)\varepsilon_{A1}\,\Delta T \qquad \ldots.(4.35)$$

and equation 4.9 becomes

$$\Delta T_2 = \frac{Q(\varepsilon_{A2} + \varepsilon_{A3})}{\frac{k_g\,\varepsilon_{A2} + k_s\,\varepsilon_{A3}}{\phi\, D_P} + h_{rs}\,\varepsilon_{A2}} \qquad \ldots.(4.36)$$

Equations 4.8, 4.10 and 4.36 give

$$Q(\varepsilon_{A2} + \varepsilon_{A3}) = \frac{\Delta T}{\frac{(\beta - \phi)D_P}{k_s(\varepsilon_{A2} + \varepsilon_{A3})} + \frac{\phi D_P}{\varepsilon_{A2}(k_g + \phi D_P h_{rs}) + k_s \varepsilon_{A3}}} \qquad \ldots.(4.37)$$

From equations 4.7, 4.37 and 4.12 it follows that

$$k_{eo} = \varepsilon_{A1} k_g(1 + \beta h_{rg} D_P) + \frac{\beta}{\frac{\beta - \phi}{k_s(\varepsilon_{A2} + \varepsilon_{A3})} + \frac{\phi}{\varepsilon_{A2}(k_g + \phi D_P h_{rs}) + k_s \varepsilon_{A3}}} \qquad \ldots.(4.38)$$

therefore

$$Y_0 = \varepsilon_{A1}(k_g + H_{rg}) + \frac{1}{\frac{1 - \alpha}{X(1 - \varepsilon_{A1})} + \frac{\alpha}{\varepsilon_{A2}(1 + \alpha H_{rs}) + X\varepsilon_{A3}}} \qquad \ldots.(4.39)$$

where $H_{rg} = \frac{\beta h_{rg} D_P}{k_g}$ and $H_{rs} = \frac{\beta h_{rs} D_P}{k_g}$

Since in practice the value of the fractional series gas layer thickness α is small and of the order 0.1 it is good approximation to assume $h_{rg} = h_{rs} = h_r$ and hence $H_{rg} = H_{rs} = H_r$. Thus equation 4.39 becomes

$$Y_0 = \varepsilon_{A1}(1 + H_r) + \frac{1}{\frac{1 - \alpha}{X(1 - \varepsilon_{A1})} + \frac{\alpha}{\varepsilon_{A2}(1 + \alpha H_r) + X \varepsilon_{A3}}} \quad \ldots.(4.40)$$

4.2.3. Evaluation of Model Parameters

The area fractions ε_{A1}, ε_{A2}, ε_{A3} are evaluated from the model for conduction alone (4.1.4).

Due to unknown view factors, emissivity factors, temperature factors, and radiation scattering factors it does not appear possible to evaluate the radiation parameter H_r solely from the geometry of the model and it must be obtained by fitting the model to experimental thermal conductivity measurements made at temperatures such that radiation is significant. Solving equation 4.40 for H_r gives

$$H_r = \frac{- C_2 + \sqrt{C_2^2 - 4C_1 C_2}}{2C_1} \quad \ldots.(4.41)$$

where $$C_1 = \frac{-\alpha(1-\alpha)\varepsilon_{A1}\varepsilon_{A2}}{X(1-\varepsilon_{A1})}$$

$$C_2 = \frac{1-\alpha}{X(1-\varepsilon_{A1})}\left[\alpha\varepsilon_{A2}(Y-\varepsilon_{A1}) - \varepsilon_{A1}(\varepsilon_{A2}+X\varepsilon_{A3}) - \alpha(\varepsilon_{A1}+\varepsilon_{A2})\right]$$

$$C_3 = \left[\frac{(1-\alpha)(Y-\varepsilon_{A1})}{X(1-\varepsilon_{A1})} - 1\right](\varepsilon_{A2}+X\varepsilon_{A3}) + (Y-\varepsilon_{A1})$$

4.2.4. Effect of model parameters

The effects of phase conductivities, voidage and contact area on the effective thermal conductivity are similar to the effects on the conduction model. Fig. 4.6 shows how the effective thermal conductivity increases with the radiation parameter H_r, and that the effect is much greater at higher values of H_r corresponding to higher temperatures.

4.3. CONDUCTION-CONVECTION MODELS

A. Diffusion Model

4.3.1. General Description of the Model

The diffusion model applies differential equations to a homogeneous medium. For a packed bed this may be done in two ways. The first method allows for different gas and solid temperatures and treats the gas and solid phases as separate, continuous, homogeneous media. The second method assumes equal solid and gas temperatures throughout the bed and treats the solid-gas system as one continuous homogeneous media. Thus the validity of the diffusion model for an actual packed bed depends on the degree of heterogeneity of the bed being much smaller than the length of the bed (i.e. $D_p \ll L$).

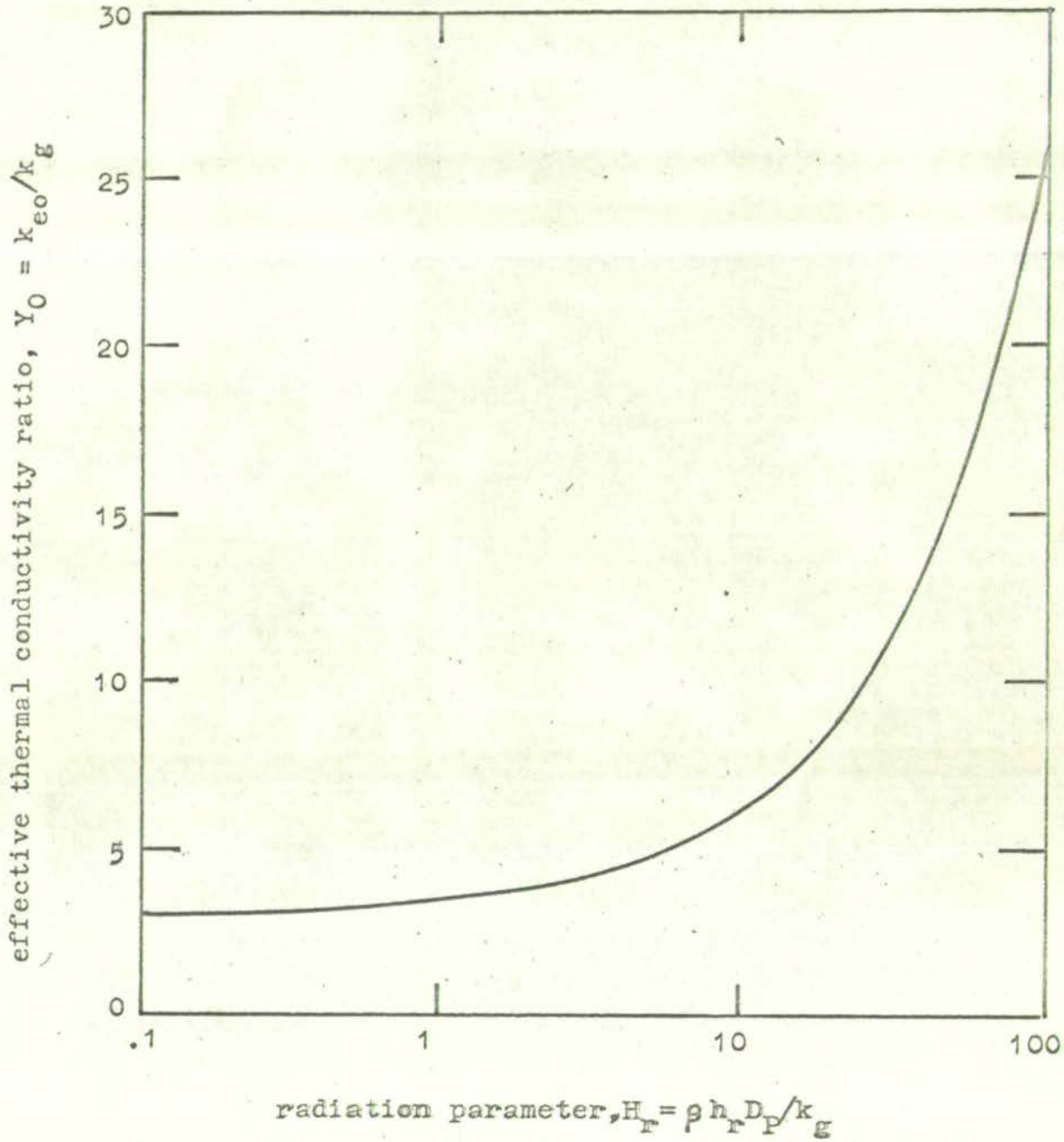

FIG.4.6 EFFECT OF THE RADIATION PARAMETER H_r ON THE EFFECTIVE THERMAL CONDUCTIVITY RATIO GIVEN BY THE CONDUCTION-RADIATION MODEL

bulk mean voidage, $\varepsilon = .40$
thermal conductivity ratio, $X = 30$
contact point area fraction $\varepsilon_{A3} = .01$

4.3.2. General Equations of the Model

For heat transfer including chemical reaction the general equations for the diffusion model of a packed bed have been discussed by Singer and Wilhelm (1950), Baddour and Yoon (1960) and Beveridge (1960, 1962, 1963).

For heat transfer in a packed bed with no chemical reaction, a similar consideration of a differential element of bed volume leads to the following basic differential heat balance equations. For the gaseous phase

$$- \text{div}\left[- c_p \rho E \, \text{grad}\,(t)\right] - \text{div}\,(G c_p t) + h_v S\,(T - t) = \varepsilon c_p \rho \left(\partial t / \partial \tau\right) \qquad \ldots\ldots(4.42)$$

where successive terms represent axial dispersion, bulk flow, interphase transfer and heat accumulation. The diffusivity, E, is the sum of an effective gas molecular thermal diffusivity and the turbulent eddy diffusivity. Thus for a tortuosity χ (2.1.4),

$$E = \frac{\varepsilon}{\chi}\left(\frac{k_g}{c_p \rho}\right) + E_t \qquad \ldots\ldots(4.43)$$

For the solid phase

$$- \text{div}\left[- k_{es}\,(1 - \varepsilon)\,\text{grad}\,(T)\right] - h_v S\,(T - t) = (1 - \varepsilon)\,\rho_s c_s \left(\partial T / \partial \tau\right) \qquad \ldots\ldots(4.44)$$

where successive terms represent conduction through the solid phase and contact points, interphase transfer and heat accumulation.

With the assumption of equal gas and solid temperatures equations 4.42 and 4.44 become

$$- \text{div}\left[- c_p \rho E \, \text{grad}(T)\right] - \text{div}\,(Gc_pT) - \text{div}\left[- k_{es}(1 - \varepsilon)\text{grad}(T)\right]$$

$$= \rho_s c_s \left(\partial T / \partial \tau \right) \qquad \ldots.(4.45)$$

4.3.3. One Dimensional Steady State Model Equations

For gas flow in the direction of positive z and steady state heat flow cocurrent or countercurrent to the gas flow direction, equations 4.42, 4.44 and 4.45 become respectively

$$c_p \rho E_z \frac{d^2t}{dz^2} - Gc_p \frac{dt}{dz} + h_v S (T - t) = 0 \qquad \ldots..(4.46)$$

$$k_{es} (1 - \varepsilon) \frac{d^2T}{dz^2} - h_v (T - t) = 0 \qquad \ldots..(4.47)$$

$$c_p \rho E_z \frac{d^2T}{dz^2} - Gc_p \frac{dT}{dz} + k_{es} (1 - \varepsilon) \frac{d^2T}{dz^2} = 0 \qquad \ldots.(4.48)$$

These equations may be written in dimensionless form by using the transformations

$$t^* = \frac{t - T_m}{T_o - T_m} \quad , \quad T^* = \frac{T - T_m}{T_o - T_m} \quad ,$$

$Z = z/L$ where T_o, T_m, are the solid temperatures at the bed inlet and outlet respectively. Thus equations 4.46, 4.47 and 4.48 become respectively

$$\frac{1}{Pe_L}\frac{d^2t^*}{dZ^2} - \frac{dt^*}{dZ} + H_L(T^* - t^*) = 0 \quad \ldots.(4.49)$$

$$K_L\frac{d^2T^*}{dZ^2} - H_L(T^* - t^*) = 0 \quad \ldots.(4.50)$$

$$\left(K_L + \frac{1}{Pe_L}\right)\frac{d^2T^*}{dZ^2} - \frac{dT^*}{dZ} = 0 \quad \ldots.(4.51)$$

where

$$K_L = \frac{k'_{es}}{Gc_pL} = \frac{k_{es}(1-\varepsilon)}{Gc_pL} = \frac{(k_{es}/k_g)(1-\varepsilon)}{(L/D_p)(RePr)} = \frac{Y(1-\varepsilon)}{RePr}\left(\frac{D_p}{L}\right)$$

$\ldots.(4.51a)$

and

$$H_L = \frac{hSL}{Gc_p} = \frac{NuSL}{RePr} = \frac{J_hSL}{Pr^{2/3}} \quad \ldots.(4.51b)$$

4.3.4. Boundary Conditions for the Gas Phase

(i) gas phase equations at boundaries

Fig. 4.7 shows a packed bed with unpacked inlet and outlet diffusion sections at opposite ends of the bed (Wehner and Wilhelm (1956)). For the packed section (2) equation 4.49 applies directly. For the end sections (1) and (2), the last term of equation 4.49 disappears. The three sections may in general have different Peclet number values. Thus the gas phase equations for the three sections are as follows

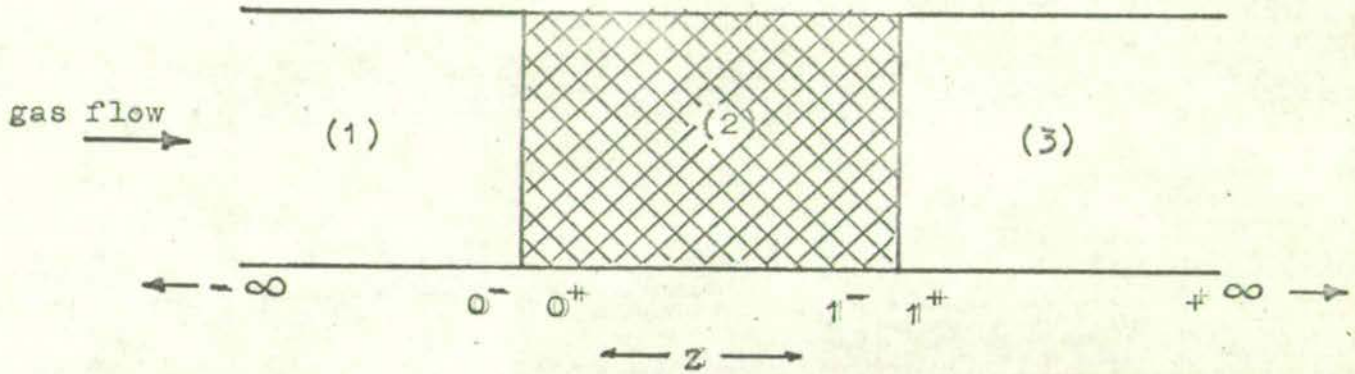

FIG. 4.7 PACKED BED BOUNDARY CONDITIONS FOR THE DIFFUSION MODEL (Wehner and Wilhelm (1956))

section (1): $(Z \leq 0)$ $$\left(\frac{1}{Pe_{L1}}\right) \frac{d^2 t_1^*}{dZ^2} - \frac{dt_1^*}{dZ} = 0 \qquad \ldots.(4.52)$$

section (2): $(0 \leq Z \leq 1)$ $$\left(\frac{1}{Pe_{L2}}\right) \frac{d^2 t_2^*}{dZ^2} - \frac{dt_2^*}{dZ} + H_L(T_2^* - t_2^*) = 0 \qquad \ldots.(4.53)$$

section (3): $(Z \leq 1)$ $$\left(\frac{1}{Pe_{L3}}\right) \frac{d^2 t_3^*}{dZ^2} - \frac{dt_3^*}{dZ} = 0 \qquad \ldots.(4.54)$$

(ii) general boundary conditions

The following general boundary conditions apply to the above equations

(a) $$t_1^*(-\infty) = t_o^* \text{ (by definition)} \qquad \ldots.(4.55)$$

(b) For a continuous gas temperature profile at Z = 0,

$$t_1^*(0^-) = t_2^*(0^+) \qquad \ldots.(4.56)$$

(c) For a constant gas specific heat, c_p, a heat balance at Z=0 gives

$$t_1^*(0^-) - \frac{1}{Pe_{L1}} \frac{dt_1^*(0^-)}{dZ} = t_2^*(0^+) - \frac{1}{Pe_{L2}} \frac{dt_2^*(0^+)}{dZ} \qquad \ldots.(4.57)$$

(d) For a continuous gas temperature profile at Z = 1,

$$t_2^*(1^-) = t_3^*(1^+) \qquad \ldots.(4.58)$$

(e) For a constant gas specific heat, c_p, a heat balance at Z = 1 gives

$$t_2^*(1^-) - \frac{1}{Pe_{L2}} \frac{dt_2^*(1^-)}{dZ} = t_3^*(1^+) - \frac{1}{Pe_{L3}} \frac{dt_3^*}{dZ}(1^+) \quad \ldots(4.59)$$

(f) Since $t_3^*(+\infty)$ cannot be infinite it is a necessary condition that

$$t_3^*(+\infty) = \text{finite} \quad \ldots.(4.60)$$

(iii) simplified boundary conditions

A simplification in the boundary conditions given above is possible. This allows solutions to the bed section (2) to be obtained independently of the inlet and outlet sections.

The general solutions of equations 4.52 and 4.54 are respectively

$$t_1^* = C_1 + C_2 e^{Pe_L Z} \quad \ldots.(4.61)$$

and

$$t_3^* = C_3 + C_4 e^{Pe_L Z} \quad \ldots.(4.62)$$

From equations 4.55 and 4.60 respectively it follows that

$$C_1 = t_o^* \quad \ldots.(4.63)$$

$$C_4 = 0 \quad \ldots.(4.64)$$

Substituting equation 4.63 into equation 4.61 gives

$$t_1^*(0^-) = t_o^* + C_2 \quad \ldots.(4.65)$$

and

$$\frac{dt_1^*(0^-)}{dZ} = Pe_L C_2 \quad \ldots.(4.66)$$

Substituting equations 4.65 and 4.66 into equation 4.57 gives

$$t_o^* = t_2(0^+) - \left(\frac{1}{Pe_{L2}}\right) \frac{dt_z^*}{dZ} \quad (0^+) \qquad \ldots.(4.67)$$

From equations 4.64 and 4.62 it follows that

$$\frac{dt_3^*(1^+)}{dZ} = 0 \qquad \ldots.(4.68)$$

Substituting equations 4.68 and 4.58 into equation 4.59 gives

$$\frac{dt_2^*(1^-)}{dZ} = 0 \qquad \ldots.(4.69)$$

Equations 4.67 and 4.69 represent the simplified boundary conditions at Z = 0 and Z = L respectively. These are often called the Danckwerts boundary conditions and have frequently been applied to tubular flow reactors.[1] They apply under all steady state conditions for any order of reaction (Bischoff (1961)) but under unsteady state conditions are only true if there is no diffusion in the end sections (i.e. $Pe_{L1} = Pe_{L2} = \infty$) (Van Cauwenberghe (1966)).

If there is plug flow in section (1) so that $Pe_{L1} = \infty$ it follows that

$$t_1^*(0^-) = t_o^* \qquad \ldots.(4.70)$$

and there is then a discontinuity in gas temperature at Z = 0.

---

1. e.g. Danckwerts(1953); Kramers and Alberda(1953); Wehner and Wilhelm(1956); Fan and Bailie(1960); Levenspiel and Bischoff(1959); Pearson(1959); Fan and Ahn(1962).

(iv) approximate boundary conditions

To obtain simpler solutions to equation 4.53 approximate boundary conditions have sometimes been applied. Hulbert (1944) neglected the diffusion in the entrance section (1) and used a boundary condition equivalent to

$$t_2^*(0^+) = t_o^*, \qquad \text{at } Z = 0 \qquad \ldots.(4.70a)$$

in conjunction with equation 4.69. Levenspiel and Smith (1957) and Otake and Kunugita (1958) used the approximate boundary condition given by equation 4.70a in conjunction with the approximation that a reactor or packed bed of finite length is equivalent to one of infinite length so that

$$t_2^* = 0, \qquad \text{at } Z = \infty \qquad \ldots.(4.71)$$

Fan and Ahn (1962) made a quantitative comparison of the solutions using the approximate boundary conditions of equations 4.70_a and 4.71 and the exact boundary conditions of equations 4.67 and 4.69 for first and greater order reactions in a tubular flow reactor. They obtained the domains for which the approximate boundary conditions gave conversions inconsistent with the limit of a stirred tank reactor ($Pe_2 = 0$) and showed that the approximate boundary condition set of equations 4.70_a and 4.71 gave both simpler and more accurate solutions than the approximate boundary condition set of equations 4.70_a and 4.69.

4.3.5. Boundary Conditions for the Solid Phase

From the dimensionless solid temperature definition of $T^* = \frac{T - T_m}{T_o - T_m}$ it is evident that the following solid phase boundary conditions must always apply;

at Z = 0 (gas inlet), $T^* = 1$ ....(4.72)

and

at Z = 1 (gas outlet), $T^* = 0$ ....(4.73)

If semi-infinite boundary conditions are employed by the use of equation 4.71, the latter condition becomes

at $Z = \infty$, $T^* = t^* = 0$ ....(4.74)

Yagi, Kunii and Wakao (1960) and Ikeda, Nishimura, and Kubota (1964) used the condition that the heat supplied to the solid particles at one end of the bed is equal to the enthalpy change of the gas through the bed so that

at Z = 0 (cocurrent gas and heat flow)

or Z = 1 (countercurrent gas and heat flow)

it follows that

$$\frac{k_{es}}{L} \frac{dT^*}{dZ} + c_p G (t_m^* - t_o^*) = 0 \quad ....(4.75)$$

or $$K \frac{dT^*}{dZ} + (t_m^* - t_o^*) = 0 \quad ....(4.76)$$

or $$\frac{dT^*}{dZ} = C_1 \quad ....(4.77)$$

4.3.6. Boundary Conditions for Equal Gas and Solid Temperatures

Equations 4.72, 4.73 and 4.74 are the applicable boundary conditions for the case of equal gas and solid temperatures.

4.3.7. Relative Directions of Gas and Heat Flow

The above diffusion model equations and boundary conditions are applicable to conditions of both cocurrent and countercurrent gas and heat flows, provided the convention of Z = 0 at the gas inlet is observed.

For countercurrent gas and heat flow, it is usually more convenient to define Z = 0 at the gas outlet. In this case the diffusion model solutions are the mirror images of the cocurrent case solutions given here (e.g. see Fig. 4.8).

4.3.8. Model Solution for Unequal Gas and Solid Temperatures using the Exact Boundary Conditions

The general solutions to equations 4.49 and 4.50 for unequal gas and solid temperatures are respectively

$$T^* = C_1 e^{\Lambda_1 Z} + C_2 e^{\Lambda_2 Z} + C_3 e^{\Lambda_3 Z} + C_4 \qquad ....(4.78)$$

$$t^* = C_1 (\Lambda_1^2 - K_L/H_L)\, e^{\Lambda_1 Z} + C_2 (\Lambda_2^2 - K_L/H_L)\, e^{\Lambda_2 Z}$$

$$+ C_3 (\Lambda_3^2 - K_L/H_L)\, e^{\Lambda_3 Z} + C_4 \qquad ....(4.79)$$

where Λ_1, Λ_2, and Λ_3 are the roots of

$$\Lambda^3 - Pe_L \Lambda^2 - \frac{H_L}{K_L}(1 + K_L Pe_L)\Lambda + \frac{Pe_L H}{K} = 0 \qquad ....(4.80)$$

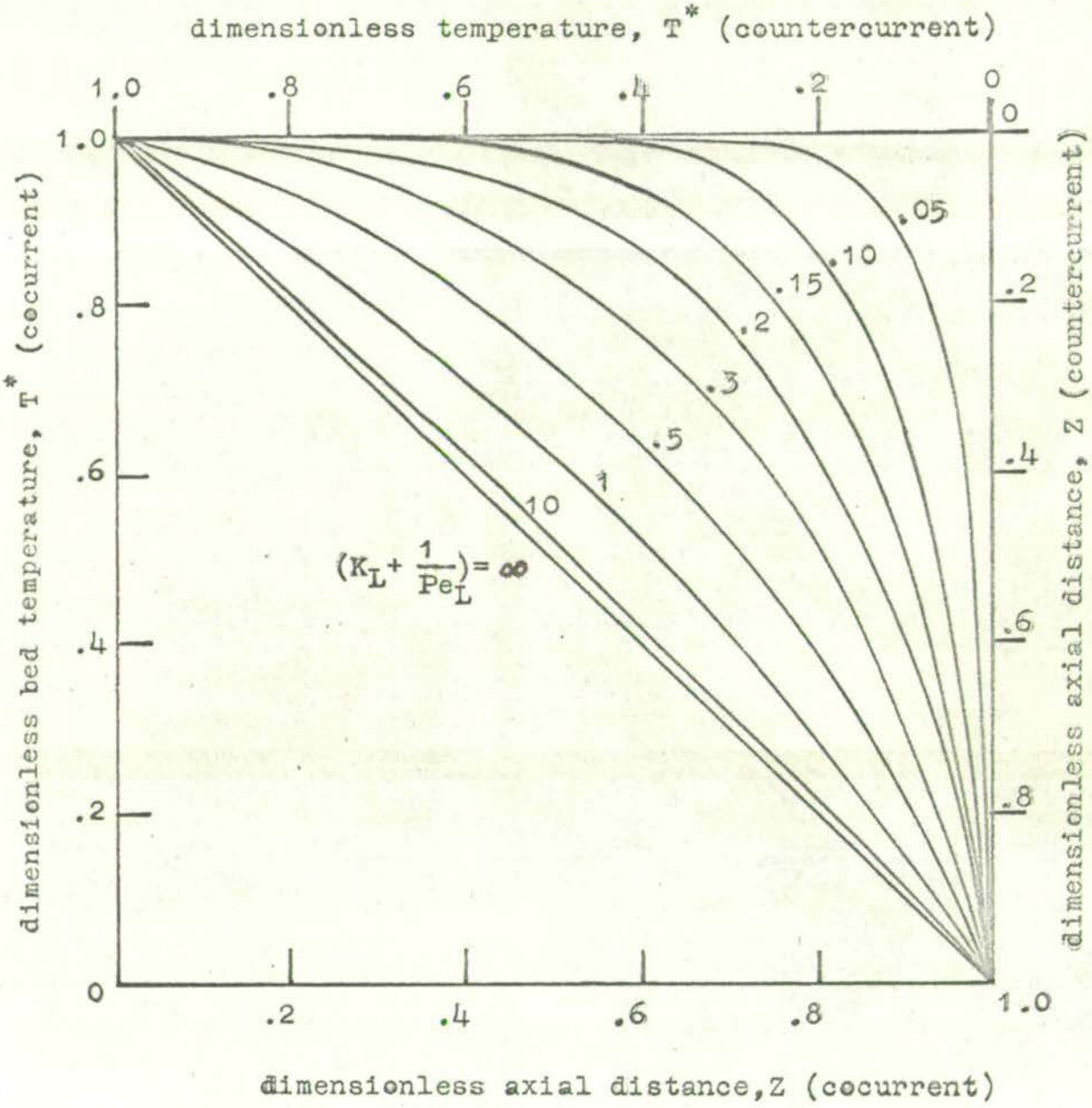

FIG. 4.8 DIFFUSION MODEL SOLUTION FOR EQUAL GAS AND SOLID TEMPERATURES

(for both cocurrent and countercurrent gas and heat flows)

Application of the boundary conditions given by equations 4.67, 4.69, 4.72 and 4.73 gives the values of the constants C_1, C_2, C_3 and C_4 as

$$\begin{bmatrix} \Lambda_1(\Lambda_1^2 - K_L/H_L)e^{\Lambda_1} & \Lambda_2(\Lambda_2^2 - K_L/H_L)e^{\Lambda_2} & \Lambda_3(\Lambda_3^2 - K_L/H_L)e^{\Lambda_3} & 0 \\ e^{\Lambda_1} & e^{\Lambda_2} & e^{\Lambda_3} & 1 \\ \Lambda_1 & \Lambda_2 & \Lambda_3 & 1/K_L \\ 1 & 1 & 1 & 1 \end{bmatrix} \begin{bmatrix} C_1 \\ C_2 \\ C_3 \\ C_4 \end{bmatrix}$$

$$= \begin{bmatrix} 0 \\ 0 \\ -t_o^*/K_L \\ 0 \end{bmatrix} \qquad \ldots.(4.81)$$

4.3.9. Other Model Solutions

Table 4.1 gives the diffusion model solutions for both non-equal and equal gas and solid temperatures for various system conditions. These include plug flow ($Pe = \infty$), finite Peclet number, infinite bed length and finite bed length.

Stewart (1965) proposed the application of a diffusion model which does not allow propagation of heat or mass in the upstream direction. This was called the wave model because of similarities to the wave equations of optics and acoustics. The advantage of the model is that the equations may be solved by moving sequentially along the length of the bed as is possible in the mixing cell model.

TABLE 4.1 DIFFUSION MODEL SOLUTIONS FOR AXIAL HEAT TRANSFER IN PACKED BEDS

System Conditions			Diffusion model equation	Boundary Conditions				Solution	Used by
				Z = 0		Z = 1	Z = ∞		
Equal gas and solid temperatures (t = T)	Plug flow (Pe = ∞)	Infinite bed length (Z = ∞)	$K\frac{d^2T^*}{dZ^2} - \frac{dT^*}{dZ} = 0$	$T^*=1$			$T^*=0$	$1-T^* = e^{-(1-Z/K)}$	Yagi, Kunii, Wakao (1960)
		Finite bed length Z				$T^*=0$		$T^* = \frac{e^{Z/K} - e^{1/K}}{1 - e^{1/K}}$	Kunii and Smith (1960); Adivarahan, Kunii, Smith (1962)
	Finite Peclet number Pe	Z = ∞	$(K+\frac{1}{Pe_L})\frac{d^2T^*}{dZ^2} - \frac{dT^*}{dZ} = 0$				$T^*=0$	$1-T^* = e^{1-Z/(K+Pe_L)}$	This work
		Z				$T^*=0$		$T^* = \frac{e^{Pe_L Z/(KPe_L+1)} - e^{Pe_L/(KPe_L+1)}}{1 - e^{Pe_L/(KPe_L+1)}}$	This work
Unequal gas and solid temperatures t and T	Plug flow (Pe=∞)	Z = ∞	$-\frac{dt^*}{dZ} + H(T^*-t^*)=0$	$T^*=1$	$t(0^+) = t_o$		$T^*=t^*=0$	$T^* = e^{\Lambda Z}$ where Λ is the negative root of $\Lambda^2 + H\Lambda - H/K = 0$	This work
		Z	$K\frac{d^2T^*}{dZ^2} - H(T^*-t^*)=0$			$T^*=0$, $\frac{dt^*}{dZ}=0$		Appendix 6	This work
	Finite Peclet number Pe	Z= ∞	$\frac{1}{Pe_L}\left(\frac{d^2t^*}{dZ^2}\right) - \frac{dt^*}{dZ} + H(T^*-t^*) = 0$		$\frac{dT}{dZ} = C$		$t^*=T^*=0$, $\frac{dt^*}{dZ}=0$	Appendix 6	Yagi, Kunii Wakao (1960) Ikeda, Nishimura, Kubota (1964)
		Z	$K\frac{d^2T^*}{dZ^2} - H(T^*-t^*)=0$		$t_o = t(0^+) - \frac{1}{Pe_L}\left(\frac{dt^*}{dZ}\right)_0$	$T^*=0$, $\frac{dt^*}{dZ}=0$		Equations 4.78 - 4.81	This work

4.3.10. Effect of Model Parameters

Fig. 4.8 shows that decreasing values of the effective thermal conductivity parameter, $(K_L + 1/Pe_L)$, (or K_L in the case of $Pe_L = \infty$) increase the departure of the dimensionless temperature profile from linearity. These curves are based on the assumption of equal solid and gas temperatures (Table 4.1).

For the non-equal solid and gas temperature solution (equations 4.78 - 81), Fig. 4.9 shows the effect of Peclet number. For Peclet numbers in the range .5 - 2 there is little change in the dimensionless temperature profile and the effect of Peclet number decreases further for longer beds. The effects of the convection and conduction parameters H_L and K_L are similar to the effects of the mixing cell model parameters H and K (Figs. 4.16 and 4.15).

B. Mixing Cell Model

.3.11. General Description of the Model

The mixing cell model of a packed bed considers gas flow through the bed to be equivalent to gas flow through an array of perfectly mixed tanks or cells. For a one-dimensional model the cells are arranged in series as a cascade. The number of cells equivalent to the bed length is chosen to give the correct amount of axial dispersion. For a two-dimensional model the inlet and outlet gas streams for each cell branch to two cells at different radial positions. This arrangement accounts for radial dispersion.

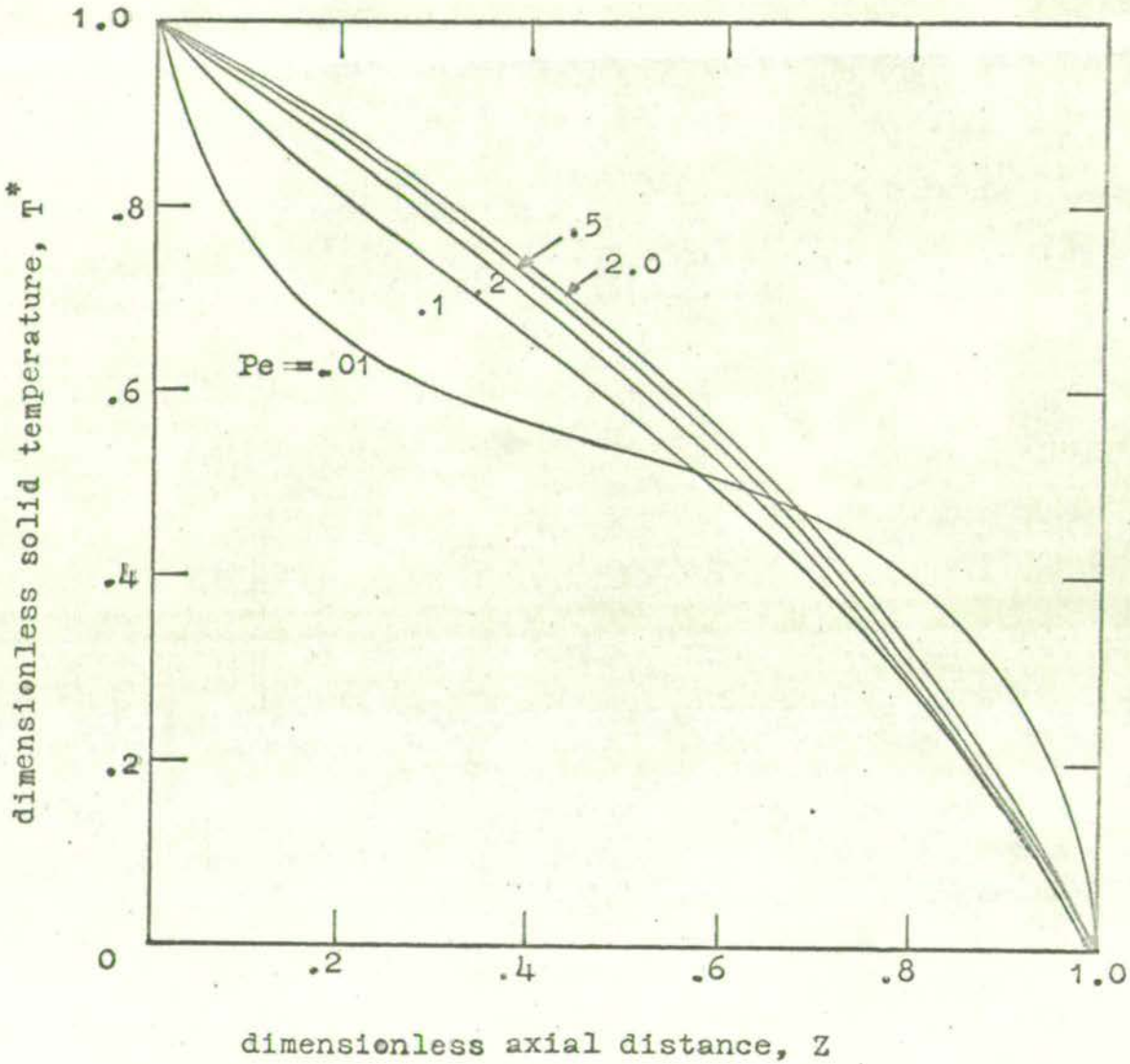

FIG. 4.9 EXACT DIFFUSION MODEL SOLUTION - EFFECT OF PECLET NUMBER

$t_o^* = 1.0$, $K_L = .75$, $H_L = 100$, $Pe_L = 10\ Pe$

Thus heat (and mass) transfer processes in the bed are considered in a sequence of finite stages. This characteristic gives the mixing cell model the following advantages compared with the diffusion model.

(i) It is suitable for straightforward stepwise computer computation.

(ii) Continuous stagewise adjustment of the model parameters along the length of the bed is possible.

(iii) It is more suitable for the inclusion of the discrete process of radiation heat transfer than the diffusion model.

(iv) Heat transfer resistance at particle contact points may be placed at a point in the cell instead of merely being included in an effective solid path thermal conductivity throughout the cell.

4.3.12. Number of Mixing Cells along the Bed Length, m

The number of mixing cells, m, along the bed length L directly determines the mixing cell stage length, l, if this is assumed constant for each cell, since $l = L/m$.

(i) ideal bed

For an idealised bed each void in the bed corresponds to a mixing cell in the model. In this case the stage length l is the equivalent void length on layer spacing βD_P and the number of cells in the bed length is given by

$$m = L/\beta D_P \qquad \ldots.(4.82)$$

It may be shown (Aris and Amundson (1957)) that this

corresponds to an axial Peclet number given by

$$Pe = 2/\beta \qquad \ldots.(4.83)$$

so that for a stage length of one particle diameter Pe = 2 and the closer the packing the greater the Peclet number and the lower the axial dispersion. For regular packings of equal-sized spheres, β is given in Table 2.1 and for random packings by equation 2.5.

(ii) actual bed

The value of m for an actual bed may be found in two ways

(a) directly from the residence time distribution

For m perfectly mixed cells in series the variance of the output tracer curve (the C curve) obtained from the response to a pulse tracer input is related to m by the equation (Levenspiel (1962))

$$m = 1/\frac{\sigma}{\tau_C}^2 \qquad \ldots.(4.84)$$

(b) from axial dispersion data interpreted on the basis of the diffusion model

The axial dispersion data discussed in 2.3 from which a Peclet number based on the diffusion model has been derived may also be used to calculate m. This may be done by equating a variety of parameters for both the mixing cell and diffusion models (Levenspiel (1962c)) and the various equations for m are given in Table 4.2. For relatively long beds with $Pe_L > 10$ and $m > 5$ all the formula tend to the simplest

TABLE 4.2 METHODS FOR THE DETERMINATION OF THE NUMBER OF MIXING CELLS, m, FROM THE AXIAL PECLET NUMBER.

Reference	Parameters equated		Equation for m	Validity of equation for limiting conditions	
	Mixing cell model	Diffusion model		Plug flow limit $Pe_L = \infty$, $m = \infty$	Complete mixing limit $Pe_L = 0$, $m = 1$
Aris and Amundson(1957)	variance of C curve	approximate variance of C curve for all bed end conditions	$m = Pe_L/2$	valid	not valid
McHenry and Wilhelm(1957)	approximate inlet/outlet amplitude ratio for sinusoidal tracer input	approximate inlet/outlet amplitude ratio for sinusoidal tracer input	$m = Pe_L/2$	valid	not valid
Carberry(1958)	mean residence time for one mixing cell	Einstein equation diffusion time constant for bed length l	$m = Pe_L/2$	valid	not valid
Kramers and Alberda(1953)	variance of C curve	corrected approximate variance of C curve for all bed end conditions	$m = Pe_L/2 + 1$	valid	valid
Van der Laan (1958)	variance of C curve	variance of C curve for closed bed end conditions	$m = 1/\left[\frac{2}{Pe_L} - \frac{2}{Pe_L^2}(1-e^{-Pe_L})\right]$	valid	valid
Trambouze(1960)	maxima of C curve	maxima of C curve	$\frac{m(m-1)(4m-1)}{(2m-1)^2} = Pe_L$	valid	valid
Trambouze(1960)	ordinate of C curve at mean residence time	ordinate of C curve at mean residence time	$\frac{2m}{(1+\frac{1}{12m})^2} = (Pe_L^2 + Pe_L - \frac{3}{4})^2$	valid	not valid

equation which is

$$m = \frac{Lv}{2E} = \frac{Pe_L}{2} = \frac{Pe}{2}\left(\frac{L}{D_P}\right) \qquad ....(4.85)$$

Hence
$$l = \frac{L}{m} = \frac{2D_P}{Pe} \qquad ....(4.86)$$

For a random packed bed at a given Reynolds number the Peclet number given by Figs. 2.9, 2.10, 2.11, may be used in equation 4.85 to give the value of m.

Thus l[1] and m are measures of the mixing efficiency of an actual bed which may be defined from equations 4.82 and 4.85 as (Carberry (1958))

$$\text{bed mixing efficiency} = \frac{m\ (\text{actual})}{m\ (\text{ideal})} = \frac{\beta\, Pe}{2} \qquad ....(4.87)$$

4.3.13. Previous Mixing Cell Models

Epstein (1958) gives the solution of a mixing cell model for the simple case of constant solid temperature throughout the bed (as in constant rate drying for example). In this case there is no axial conduction in the solid and assuming no gaseous conduction the solution is

$$\frac{t_o - T}{t_m - T} = (1 + H_L)^m \qquad ....(4.88)$$

---

1. The stage length l is sometimes called the height of a mixing unit, H.M.U.

Deans and Lapidus (1960) used a two-dimensional mixing cell model for numerical steady and unsteady state solutions under conditions of non-isothermal and non-ideal flow in a packed bed with and without chemical reactions. Crider and Foss (1965) used a similar form of one and two-dimensional models. In contrast to Deans and Lapidus solid and fluid temperatures were not assumed equal at each stage. Neither the Deans and Lapidus' nor the Crider and Foss' models accounted for axial conduction.

4.3.14. A One-Dimensional Mixing Cell Model for Conduction and Convection in a Packed Bed with Non-equal Gas and Solid Temperatures

(i) description and assumptions of the model

The model is shown in diagramatic form in Fig.4.11. The packed bed is considered to consist of non-reactive particles and have a bulk mean voidage, ε, a length L and unit cross-sectional area. Gas flows through the voids of the bed under conditions of steady state heat transfer. The gas and solid temperatures at the gas inlet to the bed are t_o and T_o respectively, and at the gas outlet from the bed t_m and T_m respectively. It is assumed that the nett heat flow is one-dimensional so that there is no heat transfer across the bed container walls in a direction perpendicular to the axial flow direction. This implies that either the container walls are perfectly insulated or that the bed is large and effectively infinite in diameter, but the container walls may be of any geometrical shape.

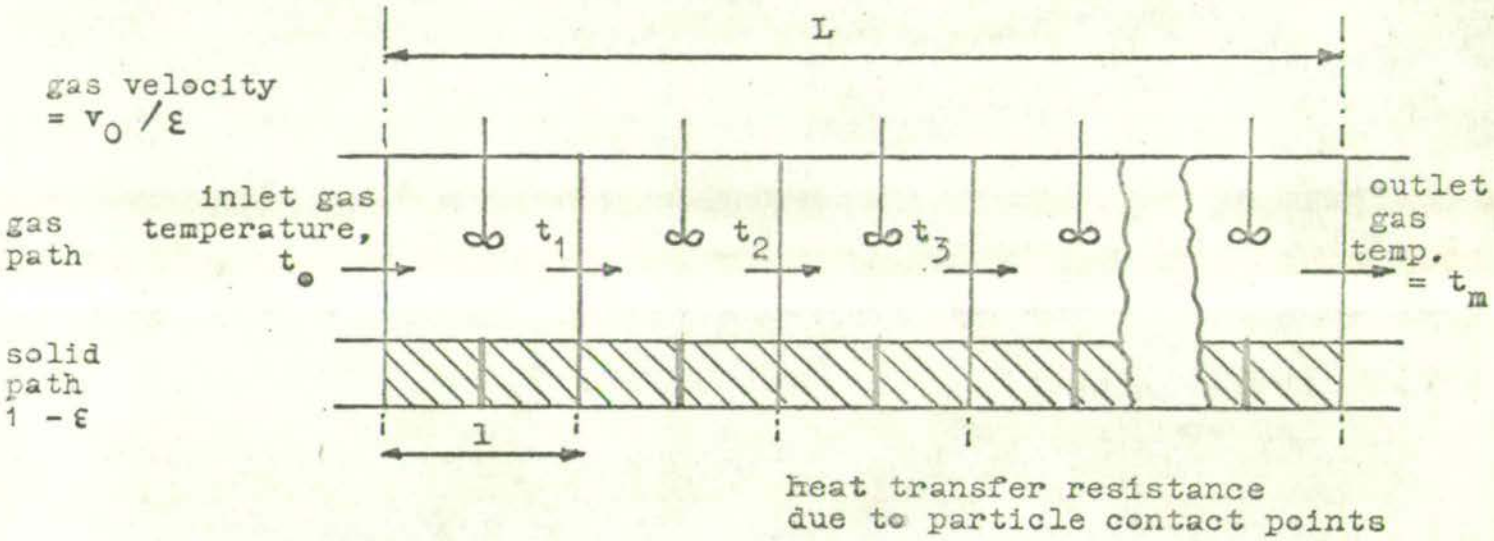

FIG.4.11 ONE-DIMENSIONAL MIXING CELL MODEL FOR CONDUCTION AND CONVECTION IN A PACKED BED WITH NON-EQUAL GAS AND SOLID TEMPERATURES

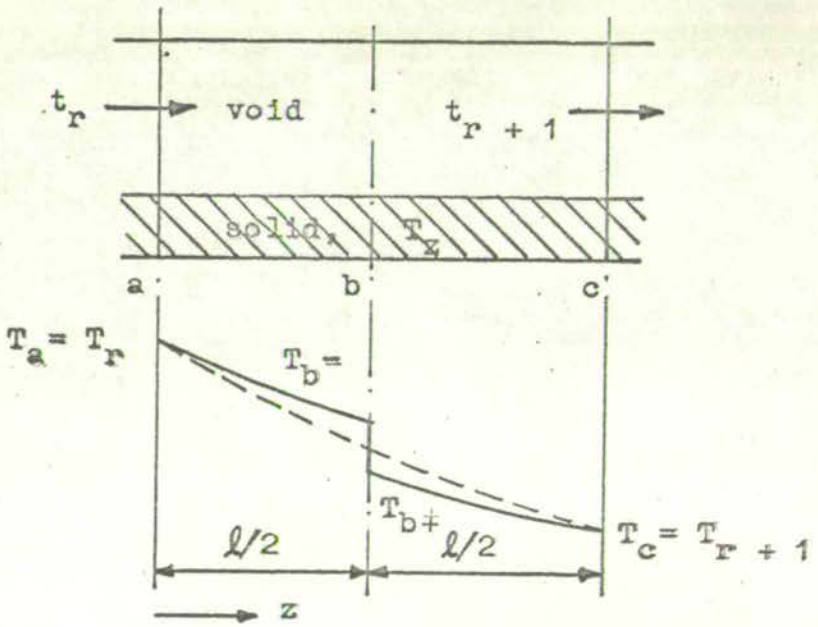

FIG. 4.12 BOUNDARY CONDITIONS AND TEMPERATURE PROFILES IN A UNIT CELL OF THE MIXING CELL MODEL

——— solid temperature profile for finite contact point resistance N_P^*

— — → solid temperature profile for $N_P^* = 0$

The flow of gas through the voids is considered as flow through a series of m perfectly mixed stages each of cross sectional area ε and length l. This arrangement accounts for the heat transfer by bulk flow and axial mixing or dispersion of the gas (mechanism 10). The gas flow velocity through each stage is the interstitial velocity $\frac{v_o}{\varepsilon}$.

In contact with the perfectly mixed gas in each cell, there is a solid section which represents the solid particles as a finite rod which has any arbitrary shape, a cross-sectional area $1 - \varepsilon$ and a surface area equal to the particle surface area per cell, Sl. The rod is assumed to have an infinite thermal conductivity in a direction perpendicular to the bed axis and thus has a constant temperature in this direction. Axial conduction in the rod is accounted for by an effective solid thermal conductivity k_{es} in the axial direction. The direction of heat flow in the solid rod may be either cocurrent or countercurrent to the direction of the gas flow. The effective solid thermal conductivity k_{es} represents the heat transfer resistance of the solid material (mechanism 1). The heat transfer resistance at the contact points of the particles (mechanisms 3 and 4) is represented by a heat transfer coefficient h_p (dimensionless parameter N_p^*) applied at the mid point of the solid path of each mixing cell. Solid-gas convection at the rod surface (mechanism 9) is accounted for by applying a convection coefficient h at this surface.

The stage length l may either be kept constant or varied

from stage to stage. The model heat transfer parameters (H, K, N_p^*) representing the above mechanisms may be similarly varied between stages but are assumed to be constant within each stage.

(ii) unit cell equations

Fig. 4.12 gives the boundary conditions for the $r+1$ th mixing cell. The temperature at any distance Z along a finite rod of length l in which heat transfer takes place both by axial conduction and by transfer at the rod surface to a gas of temperature t_{r+1} is given by the following equation (Carslaw and Jaegar (1948))

$$T_z - t_{r+1} = C_1 e^{\sqrt{\frac{H}{K}}\left(\frac{z}{l}\right)} + C_2 e^{-\sqrt{\frac{H}{K}}\left(\frac{z}{l}\right)} \qquad \ldots.(4.89)$$

A heat balance on the solid at $z = b$ gives (i.e. at the interface)

$$-k_{es}(1-\varepsilon)\left(\frac{\partial T}{\partial z}\right)_{b-} = h_p(1-\varepsilon)(T_{b-} - T_{b+}) = k_{es}(1-\varepsilon)\left(\frac{\partial T}{\partial z}\right)_{b+} \qquad \ldots.(4.90)$$

Hence
$$l\left(\frac{\partial T}{\partial z}\right)_{b+} = l\left(\frac{\partial T}{\partial z}\right)_{b-} \qquad \ldots.(4.91)$$

and
$$T_{b-} - T_{b+} = N_p^* \, l\left(\frac{\partial T}{\partial z}\right)_{b+} \qquad \ldots.(4.92)$$

From equations 4.89, 4.91, 4.92 the solid temperature and temperature gradient at any position z in the cell may be derived from the cell gas temperature t_{r+1} and the boundary conditions at the inlet to the cell at $z = a$ which are

$$T = T_a = T_r, \quad \frac{\partial T}{\partial z} = \left(\frac{\partial T}{\partial z}\right)_a = \left(\frac{\partial T}{\partial z}\right)_r$$

The complete unit cell equations are given in Appendix 7.

(iii) model stage equations

From the above discussion it follows that the solid temperature at the cell outlet ($z = c$) is given by equations (A.92) (A.93) which have the forms

$$T_{r+1} = \Psi_1\left\{t_{r+1}, T_r, \left(\frac{\partial T}{\partial z}\right)_r, H, K, N_P^*, 1\right\} \quad \ldots\ldots(4.93)$$

$$(\partial T/\partial z)_{r+1} = \Psi_2\{ \quad " \quad " \quad " \quad " \quad " \quad \} \quad \vdots$$

A heat balance at each end of the cell gives

$$Q^* = Gc_P t_r - k_{es}(1-\varepsilon)\left(\frac{\partial T}{\partial z}\right)_r$$

$$= Gc_P t_{r+1} - k_{es}(1-\varepsilon)\left(\frac{\partial T}{\partial z}\right)_{r+1} \quad \ldots\ldots(4.94)$$

Hence $$\left(\frac{Q^*}{Gc_P}\right) = t_r - Kl\left(\frac{\partial T}{\partial z}\right)_r \quad \ldots\ldots(4.95)$$

$$= t_{r+1} - Kl\left(\frac{\partial T}{\partial z}\right)_{r+1} \quad \ldots\ldots(4.96)$$

Thus starting from the bed inlet temperatures T_o, t_o, equations 4.93, 4.96, 4.95 enable a stepwise solution to be made for the temperatures T_r, t_r at each successive stage along the bed. For constant values of the model parameters throughout the bed an analytical solution may be obtained as described below.

(iv) <u>difference equations for constant parameter values</u>

Eliminating $\left(\frac{\partial T}{\partial z}\right)_r$ and $\left(\frac{\partial T}{\partial z}\right)_{r+1}$ between equations 4.93, 4.95 and 4.96 enables a second order difference equation to be obtained for the gas temperature. This has the form

$$C_1\, t_{r+2} + C_2\, t_{r+1} + C_3\, t_r + C_4 = 0 \qquad \ldots.(4.97)$$

where the constants C_1, C_2, C_3 and C_4 are functions of the model parameters H, K, N_P^* and $\left(\frac{Q^*}{GC_P}\right)$.

The complementary function and particular integral for this equation give a solution of the form

$$t_r = C_5\, B^r + C_6\, D^r + C_7 \qquad \ldots.(4.98)$$

Substituting equation 4.98 into equations 4.93, 4.96 and 4.95 gives a solution for the solid temperature of the form

$$T_r = C_8\, B^r + C_9\, D^r + C_7 \qquad \ldots.(4.99)$$

The constant C_7 which is the only constant involving the heat flow parameter $\left(\frac{Q^*}{GC_P}\right)$ is eliminated by writing equations 4.98 and 4.99 in dimensionless form to give

$$t_r^* = \frac{t_r - T_m}{T_o - T_m} = C_{10}\, B^r + C_{11}\, D^r \qquad \ldots.(4.100)$$

and

$$T_r^* = \frac{T_r - T_m}{T_o - T_m} = C_{12}\, B^r + C_{13}\, D^r \qquad \ldots.(4.101)$$

Apart from the model parameters H, K and N_p^*, only one independent constant is involved in the constants C_{10}, C_{11}, C_{12} and C_{13} and this is evaluated from either the gas inlet temperature t_o^* or the gas outlet temperature t_m^*.

(v) model solution for constant parameters

In terms of the basic model parameters the solutions given by equations 4.100 and 4.101 are

$$T_r^* = \frac{(B+1)(D-1)(B^r - D^m) + W(B-1)(D+1)(D^r - D^m)}{(B+1)(D-1)(1-B^m) + W(B-1)(D+1)(1-D^m)} \quad \ldots(4.102)$$

and

$$t_r^* = \frac{[2B^r(BD-1) - B^m(B+1)(D-1)] + W[2D^r(BD-1) - \ldots D^m(B-1)(D+1)]}{(B+1)(D-1)(1-B^m) + W(B-1)(D+1)(1-D^m)} \quad \ldots(4.103)$$

where

$$W = -\left\{\frac{(B+1)(D-1)\left[B^m + t_o^*(1-B^m)\right] - 2(BD-1)}{(B-1)(D+1)\left[D^m + t_o^*(1-D^m)\right] - 2(BD-1)}\right\} \quad \ldots(4.104)$$

$$= -\left\{\frac{(B+1)(D-1)\left[B^m - t_m^*(1-B^m)\right] - 2B^m(BD-1)}{(B-1)(D+1)\left[D^m - t_m^*(1-D^m)\right] - 2D^m(BD-1)}\right\} \quad \ldots(4.105)$$

$$B = -\overline{U}/\overline{O}\left[1 + \sqrt{1 - 4\,\overline{O}/\,\overline{U}^2}\right] \quad \ldots(4.106)$$

$$D = -\overline{U}/\,\overline{O}\left[1 - \sqrt{1 - 4\overline{O}/\,\overline{U}^2}\right] \quad \ldots(4.107)$$

$$\overline{O} = \sqrt{HK}\sinh\sqrt{\frac{H}{K}} + \frac{HN_P^*}{2}\left(\cosh\sqrt{\frac{H}{K}} - 1\right) + 1 \qquad \ldots.(4.108)$$

$$\overline{U} = -\left[\left(\sqrt{HK} + N_P^*\sqrt{\frac{H}{K}}\right)\sinh\sqrt{\frac{H}{K}} + \cosh\sqrt{\frac{H}{K}}\left(\frac{HN_P^*}{2} + 2\right) - \frac{HN_P^*}{2}\right]$$

$\ldots.(4.109)$

(vi) <u>model solution for $N_P^* = 0$</u>

If $N_P^* = 0$ any contact point resistance (mechanisms 3 and 4) is included in the conduction parameter K and the derived parameters $\overline{O}$ and $\overline{U}$ simplify to

$$O = \sqrt{HK}\sinh\sqrt{\frac{H}{K}} + 1 \qquad \ldots.(4.109a)$$

$$\overline{U} = -\left[\sqrt{HK}\sinh\sqrt{\frac{H}{K}} + 2\cosh\sqrt{\frac{H}{K}}\right] \qquad \ldots.(4.109b)$$

4.3.15. <u>Evaluation of Model Parameters</u>

From equations 4.102 - 109 it is seen that the dimensionless gas and solid temperatures t_Z^* and T_Z^* respectively at any dimensionless distance $Z = \frac{z}{L} = \frac{r}{m}$ along the bed[1] are determined by three heat transfer parameters (H, K, N_P^*), an

---

1. To be strictly correct r must be an integer so that equations 4.102 - 109 only determine the solid temperatures at either end of a cell. To determine t_Z^* and T_Z^* where Z and m do not give an integer value for r so that Z lies within a cell, equations 4.102 - 4.109 may still be applied to give values corresponding to smooth profiles passing through the temperatures at the end of the cell. Alternatively the true temperatures corresponding to the temperature profiles within a cell as given by the model may be obtained by using the next integer value higher than r in equation 4.103 for t_Z^* and equations A.83 and A.89 for T_Z^*.

axial mixing parameter m and a gas boundary temperature (either t_o^* or t_m^*). These parameters arise from the basic model equations (Appendix 7) and may be written in various forms.

(i) conduction parameter, K

This is in effect a conduction Stanton number and gives the heat transfer by effective solid conduction, (mechanisms 1, 3, and 4) relative to theheat transfer by bulk flow of gas (mechanisms10)

$$K = \frac{k_{es}(1-\varepsilon)}{Gc_P l} = \frac{(k_{es}/k_g)(1-\varepsilon)}{(\frac{l}{D_P})\,RePr} = \frac{Y(1-\varepsilon)}{RePr}\,(\frac{D_P}{l}) \quad \ldots(4.110)$$

(ii) convection parameter, H

This represents the solid-gas convection coefficient (Mechanism 9) relative to an effective heat transfer coefficient for bulk flow of the gas in the form of a convection Stanton number

$$H = \frac{h\,Sl}{Gc_P} = \frac{Nu\,Sl}{RePr} = \frac{J_h\,Sl}{Pr^{2/3}} \quad \ldots\ldots(4.111)$$

(iii) contact point parameter, N_P^*

This represents the heat transfer resistance at the contact points (Mechanisms 3 and 4) relative to the effective solid conduction resistance (Mechanism 1) in the form of an inverse Nusselt number

$$N_P^* = 1/(\frac{h_P l}{k_{es}}) \quad \ldots\ldots(4.112)$$

Thus for no contact point resistance $N_P^* = 0$.

(iv) number of mixing cells, m

This determines the stage length since $l = L/m$ ...(4.113) and is evaluated from the axial mixing and dispersion characteristics of the bed as described in 2.3.

(v) total heat flow parameter, N_Q^*

The total axial heat flow parameter N_Q^* may be determined from the basic model parameters. The defining equation may be obtained by substituting equations 4.102, and 4.103 into equations 4.94 - 4.96 written in dimensionless form to give

$$N_Q^* = \frac{1}{T_o - T_m}\left[\frac{1}{RePr}\left(\frac{Q^* D_P}{k_g}\right) - T_o\right] \quad ....(4.114)$$

$$= \frac{(B+1)(D-1) + W(B-1)(D-1)}{(B+1)(D-1)(1-B^m) + W(B-1)(D+1)(1-D^m)} \quad ...(4.115)$$

(vi) relative heat flow parameters, Φ_A, Φ_B

From equation 4.95 written in dimensionless form, the ratio of the axial heat flow through the solid phase (mechanisms 1, 3, and 4) to the heat flow in the gas (mechanism 10) at any dimensionless distance $Z(= \frac{z}{L} = \frac{r}{m})$ along the length of the bed is given by

$$\Phi_A = \frac{-Kl\left(\frac{\partial T}{\partial z}\right)_r}{t_r^*} = \frac{N_Q^* + 1}{t_r^*} - 1 \quad ....(4.116)$$

The enthalpy change in the gas, during flow through the bed, relative to the total axial heat flow rate Q^* is a measure of the importance of the gas-solid convection mechanism (mechanism 9). This ratio is given by

$$\Phi_B = \frac{Gc_P}{Q^*} (t_o - t_m) \qquad \ldots.(4.116a)$$

or from equation 4.114

$$\Phi_B = \frac{t_o^* - t_m^*}{N_Q^* + 1/(1 - \frac{T_m}{T_o})} \qquad \ldots.(4.116b)$$

4.3.16. Sophistication of Model Mixing Characteristics

The model is capable of greater sophistication to account more closely for local void mixing characteristics such as a stagnant or by-passing fluid regions. This may be done by the use of mixed models consisting of various interconnected arrangements of perfectly mixed regions, stagnant regions and plug flow regions. This approach has been used to account for incomplete mixing in an actual mixing vessel. (Cholette and Cloutier (1959), Levenspiel (1962a,c), Cholette and Blanchet (1961)).

4.3.17. Evaluation of the Contact Point Parameter N_P^* from the Stagnant Gas Conduction Model

Since the stagnant gas conduction model (4.1) specifically accounts for the contact point mechanisms 3 and 4, the contact point parameter N_P^* for the mixing cell model may be estimated

by equating the conduction resistance over the bed length L for the two models. Thus regarding the parallel gas paths in the two models as perfectly mixed within each unit cell and hence not contributing to the conduction resistance gives

$$\frac{1 + N_P^*}{X(1 - \varepsilon)} = \frac{1 - \alpha}{X(1 - \varepsilon_{A1})} + \frac{\alpha}{\varepsilon_{A2} + X\,\varepsilon_{A3}} \quad \ldots(4.117)$$

Since for the mixing cell model (Fig. 4.11)

$$\frac{1}{k_{es}} = \frac{1}{k_s(1 - \varepsilon)} + \frac{1}{h_p(1 - \varepsilon)} \quad \ldots.(4.118)$$

If the gas in the series path is also perfectly mixed, equation 4.117 becomes

$$\frac{1 + N_P^*}{1 - \varepsilon} = \frac{1 - \alpha}{1 - \varepsilon_{A1}} + \frac{\alpha}{\varepsilon_{A3}} \quad \ldots.(4.119)$$

If the value of N_P^* obtained from either equation 4.118 or 4.119 is used in the mixing cell model, the effective conduction parameter, K will still include the radiation effects but not the contact point resistance.

.3.18. Effect of Model Parameters

Figs. 4.13 - 18 and Table 4.3 show the effect of the mixing cell model parameters on the dimensionless solid temperature profile by varying one parameter at a time. Table 4.3 also shows the effect of the parameters on the

TABLE 4.3 EFFECT OF MIXING CELL MODEL PARAMETER VALUES ON MODEL VARIABLES

+, - indicate increased and decreased parameter or variable values respectively.

Mixing cell model parameter +	Mixing cell model variable			
	T_r^*	t_r^*	$t_r^* - T_r^*$	N_Q^*
inlet gas temperature t_o^*	+	+	+	+
number of mixing cells, m	+	+	-	-
conduction parameter, K	-	-	-	+
convection parameter, H	+, -	-	-	-, +
contact point parameter N_P^*	+	+	+	-
Reynolds number Re	+	+	+	-

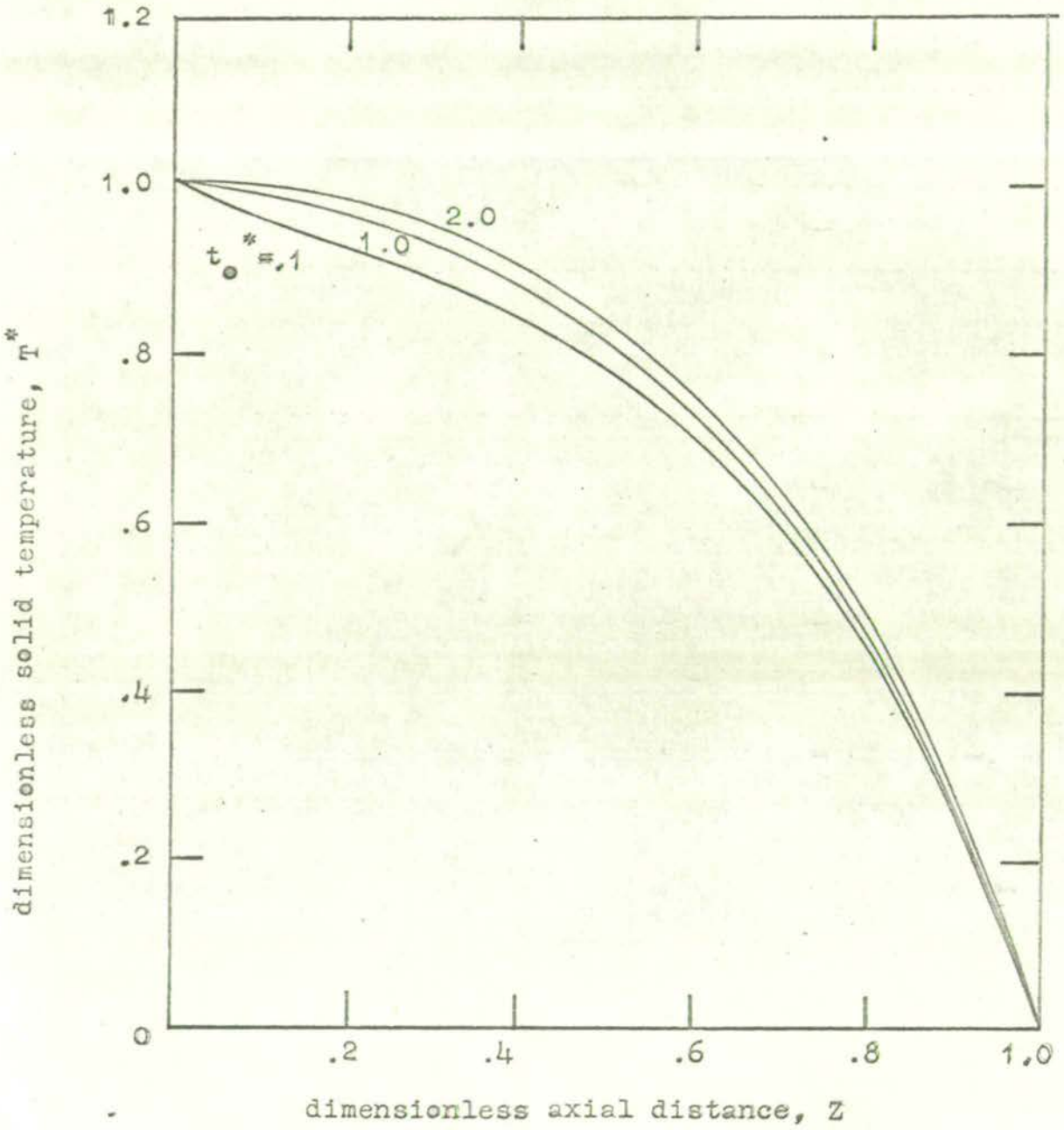

FIG. 4.13 EFFECT OF THE INLET GAS TEMPERATURE, t_o^*, ON THE MIXING CELL MODEL SOLID TEMPERATURE PROFILE

model parameter values: K = 17.5, H = 10, $N_p^* = 0$, m = 55.

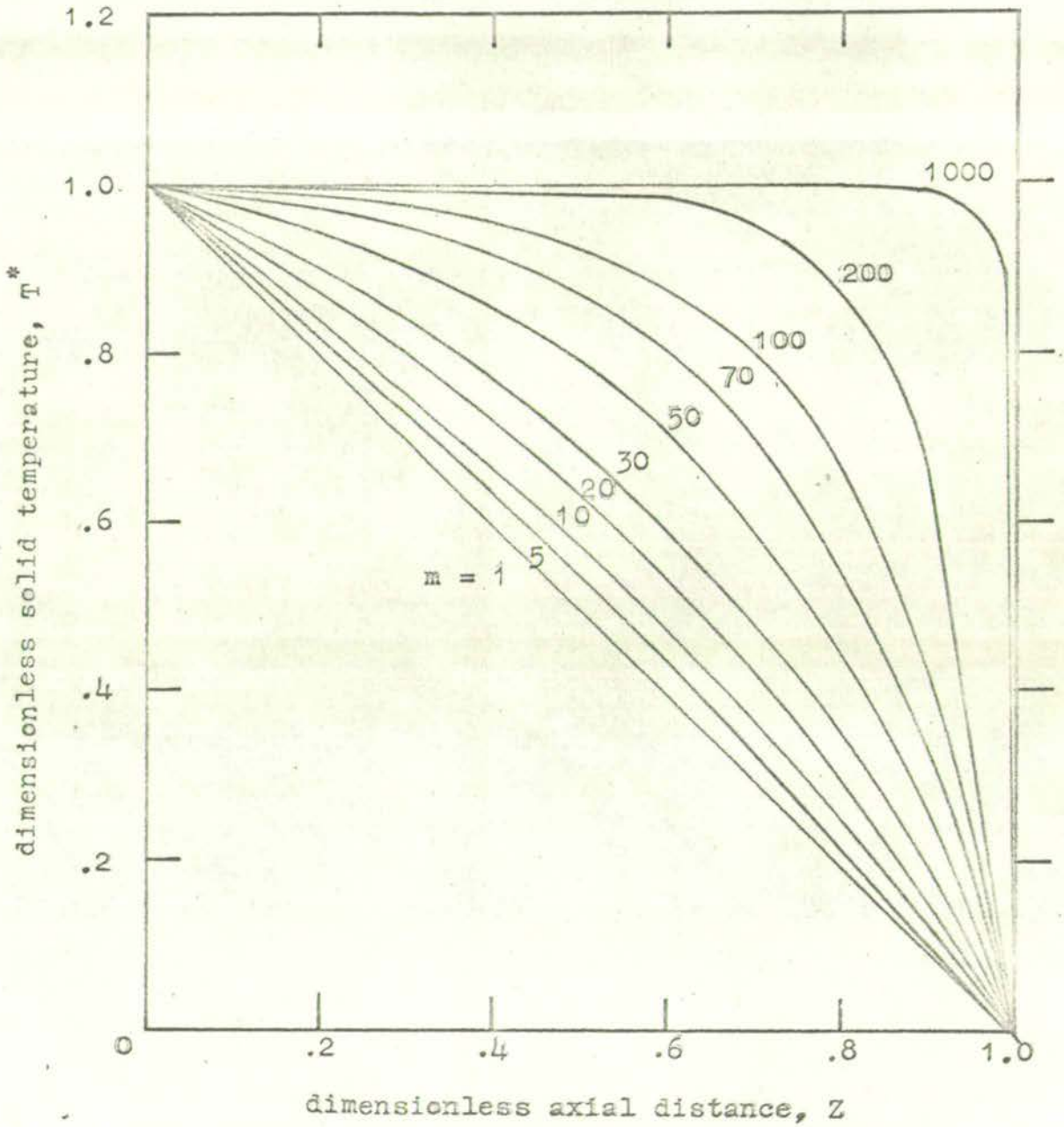

FIG. 4.14 EFFECT OF THE NUMBER OF MIXING CELLS, m, ON THE MIXING CELL MODEL SOLID TEMPERATURE PROFILE

model parameter values: $t_\theta^* = 1.0$, K = 17.5, H = 10, $N_p^* = 0$

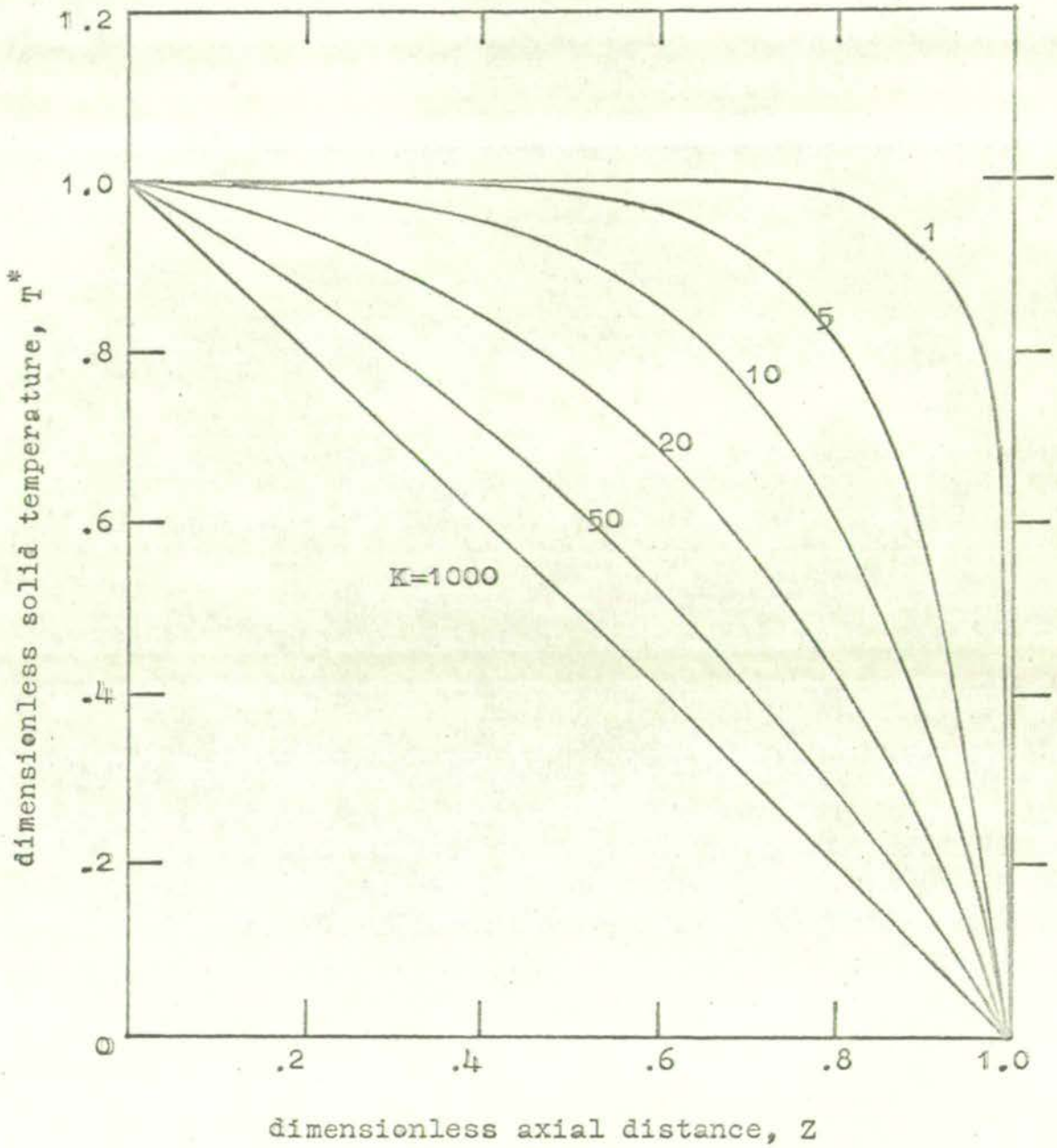

FIG. 4.15 EFFECT OF THE CONDUCTION PARAMETER, K, ON THE MIXING CELL MODEL SOLID TEMPERATURE PROFILE

model parameter values: $t_o^* = 1.0$, $H = 10$, $N_P^* = 0$, $m = 55$.

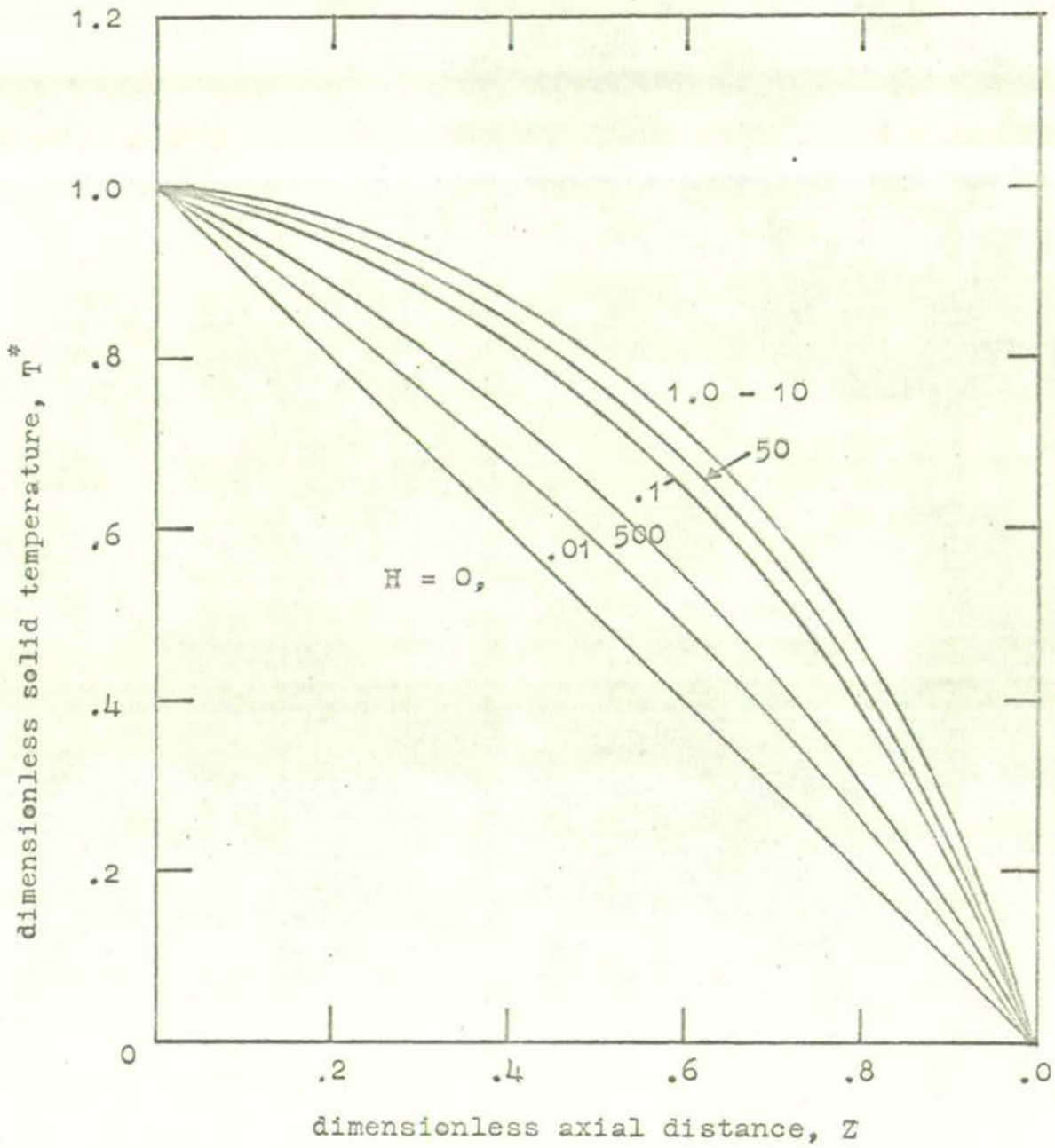

FIG. 4.16 EFFECT OF THE CONVECTION PARAMETER, H, ON THE MIXING CELL MODEL SOLID TEMPERATURE PROFILE

model parameter values: $t_o^* = 1.0$, $K = 17.5$, $N_P^* = 0$, $N = 55$.

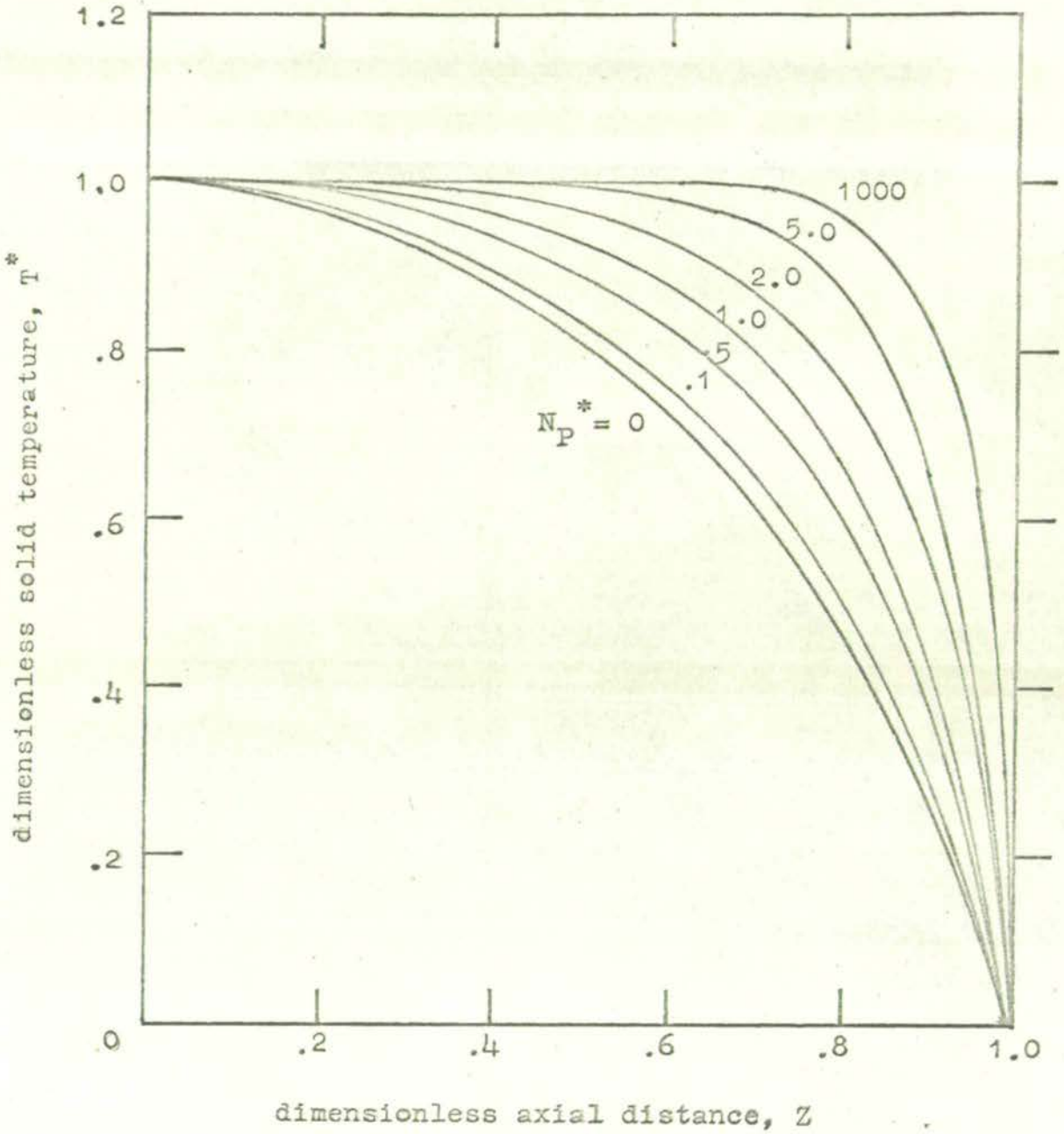

FIG. 4.17 EFFECT OF THE CONTACT POINT PARAMETER, N_P^*, ON THE MIXING CELL MODEL SOLID TEMPERATURE PROFILE

model parameter values: $t_o^* = 1.0$. K = 17.5, H = 10. m = 55.

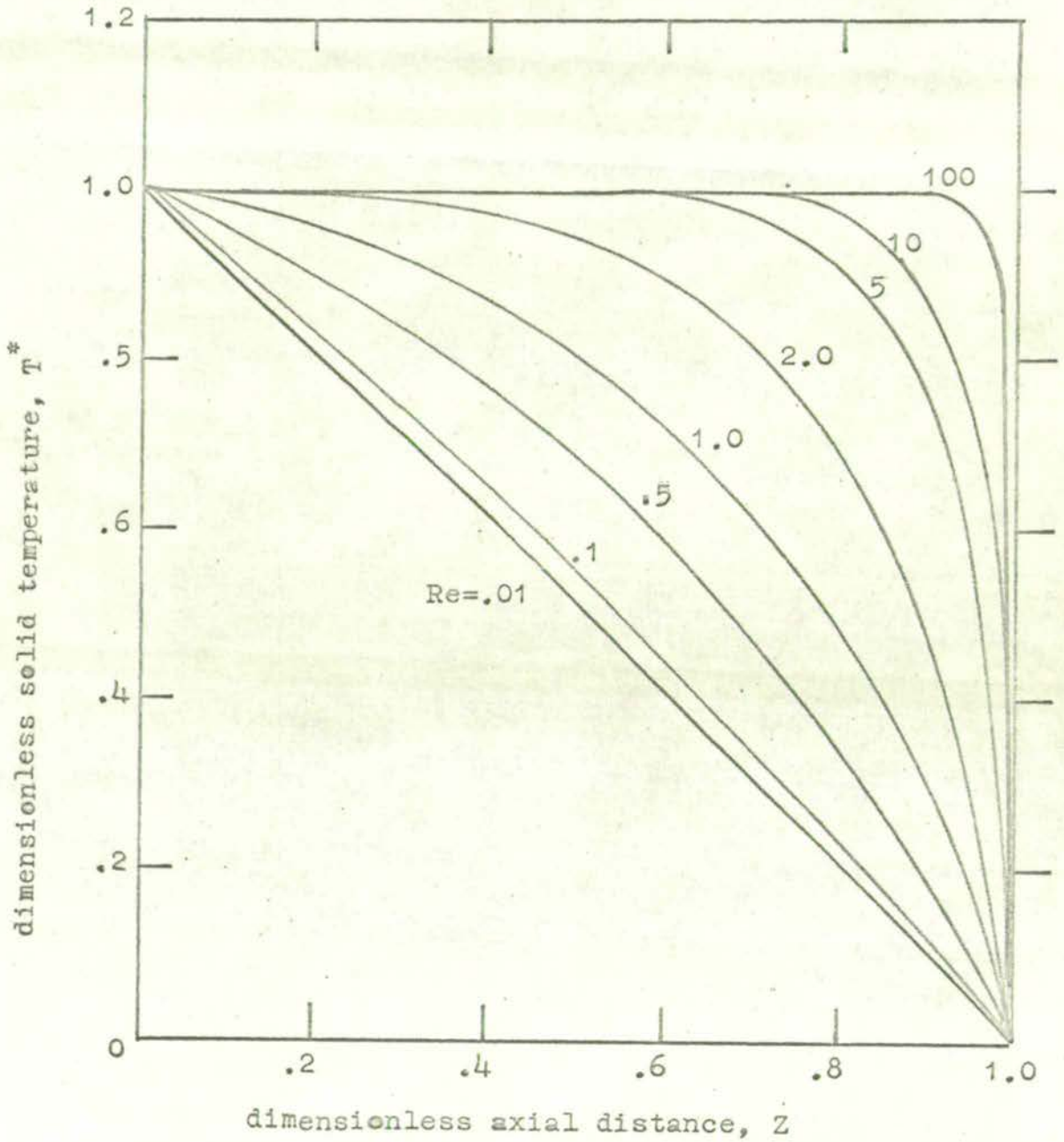

FIG. 4.18 EFFECT OF REYNOLDS NUMBER ON THE MIXING CELL MODEL SOLID TEMPERATURE PROFILE

model parameter values: $t_o^* = 1$, $N_P^* = 0$, $m = 55$.

dimensionless gas temperature, dimensionless gas-solid temperature difference and the heat flow parameter N_Q^*.

Table 4.4 and Fig. 4.13 show that the inlet gas temperature has very little effect on the solid temperature profile. Figures 4.14, 4.15, 4.17 and 4.18 respectively, show that increased values of the number of mixing cells m, (or bed length L), the conduction parameter K, the contact point parameter N_P^* and the Reynolds number give temperature profiles with greater curvatures. Fig. 4.16 shows that the effect of an increased value of the convection parameter, H, is initially to give a more curved profile but for $H > 10$, increased H gives a more linear profile.

Fig. 6.35 shows a typical model dimensionless gas temperature profile with the corresponding solid temperature profile.

4.3.19. Comparison of the mixing cell model with the diffusion model

The mixing cell model uses the parameters m, H, K and N_P^*. The diffusion model uses the parameters Pe_L, H_L and K_L. To compare solutions of the two models relationships between corresponding parameters are required.

From equation 4.85,

$$Pe_L = Pe\ (\frac{L}{D_P}) = 2m \qquad \ldots.(4.120)$$

From equations 4.51b and 4.111,

$$H_L = mH \qquad \ldots.(4.121)$$

TABLE 4.4 EFFECT OF INLET GAS TEMPERATURE (t_o^*) ON GAS AND SOLID TEMPERATURES (t^*, T^*) AT MID POINT OF BED ($Z = .5$)

$K = 17.5$ $H = 10.0$ $N_P = 0$ $m = 55$

t_o^*	t^* ($Z = .5$)	T^* ($Z = .5$)
2.00	.8436	.8357
1.50	.8309	.8231
1.20	.8220	.8143
1.15	.8220	.8143
1.10	.8208	.8131
1.05	.8195	.8118
1.00	.8182	.8106
0.9	.8157	.8080
0.5	.8055	.7980
0.1	.7954	.7880
- 0.5	.7802	.7729

Using equations 4.110, 4.113 and 4.51a and equating the combined conduction and contact point resistances for the two models gives

$$K_L \text{ (diffusion model)} = \frac{K}{m\,(1 + N_P^*)} \qquad \ldots.(4.122)$$

Fig. 4.19 compares the solid temperature profile given by the mixing cell model for m = 10 with the solid profile given by the diffusion model solution for exact boundary conditions (equations 4.78 - 4.81). The corresponding parameter values were taken from equations 4.120 - 4.122. Even for m = 10 the profiles are quite similar and agreement is even better for larger values of m corresponding to a longer bed.

Fig. 4.20 compares the solid temperature profiles within a typical unit cell for the two models. The diffusion model generally agrees closely with the mixing cell model at the cell boundaries and passes through the mid point of the temperature drop caused by the contact point resistance in the mixing cell model.

4.4. CONDUCTION-CONVECTION-RADIATION MODELS

Radiation may be allowed for in the diffusion and mixing cell models by including its effect in the value of the effective solid conductivity k_{es}.

Attempts were also made to include radiation as a specific mechanism in the mixing cell model (Fig. 4.21) but

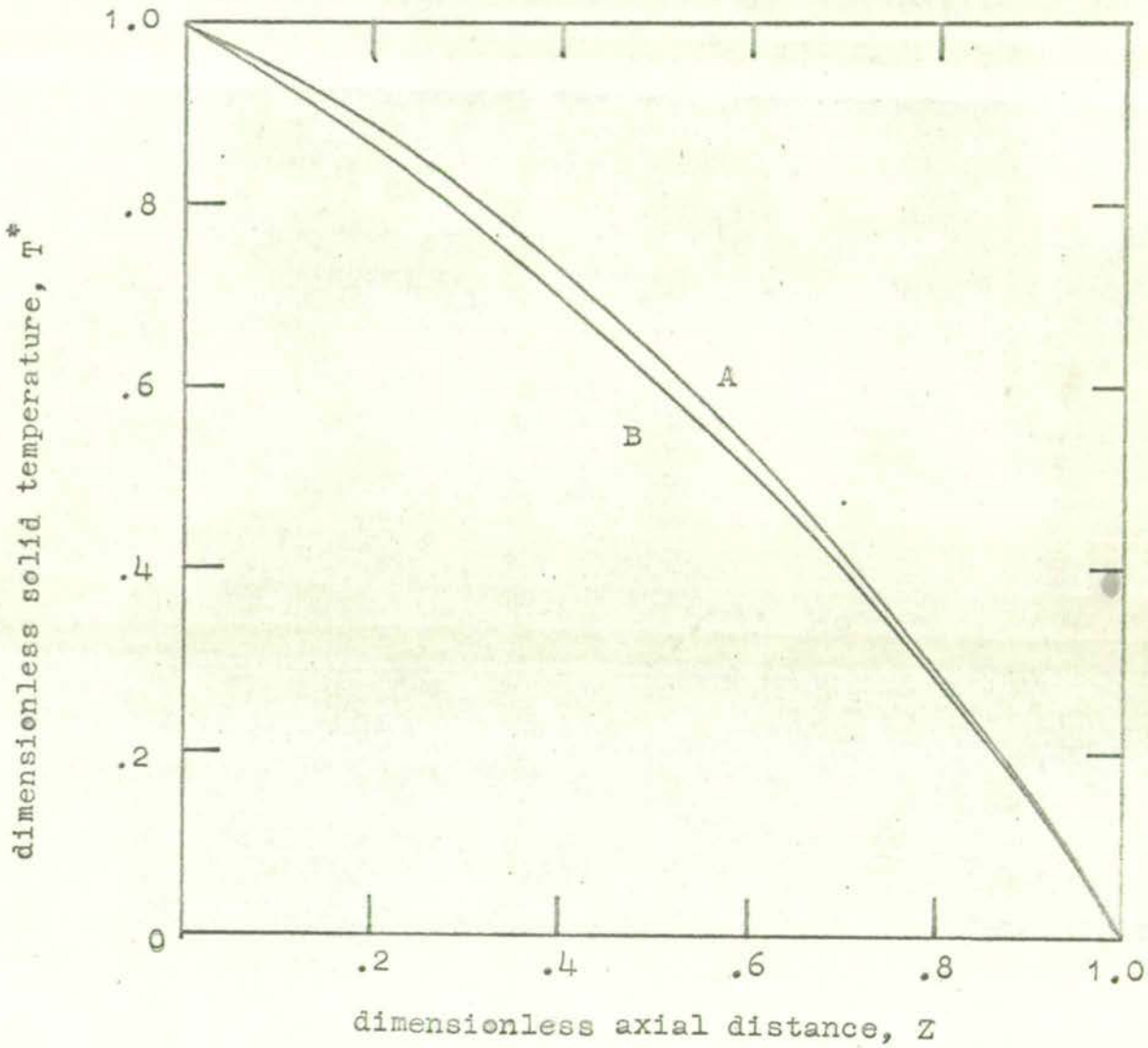

FIG. 4.19 COMPARISON OF DIFFUSION AND MIXING CELL MODELS - OVERALL PROFILES

A = mixing cell model: $t_o^* = 1.0$, K = 7.5, H = 10, $N_P^* = 0$, m = 10

B = diffusion model: $t_o^* = 1.0$, $K_L = .75$, $H_L = 100$, Pe = 2, $Pe_L = 20$

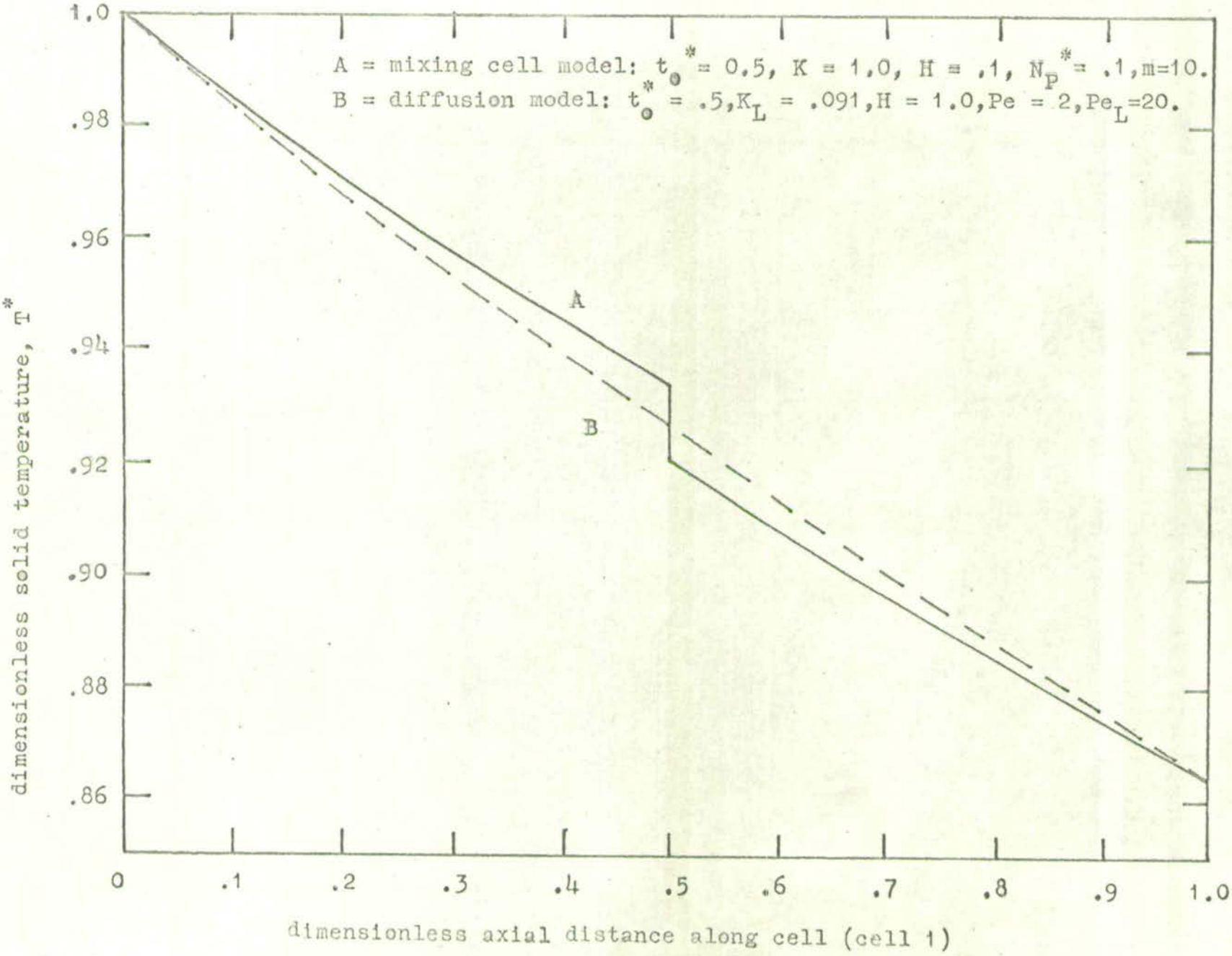

FIG. 4.20 COMPARISON OF DIFFUSION IN MIXING CELL MODELS - CELL PROFILES

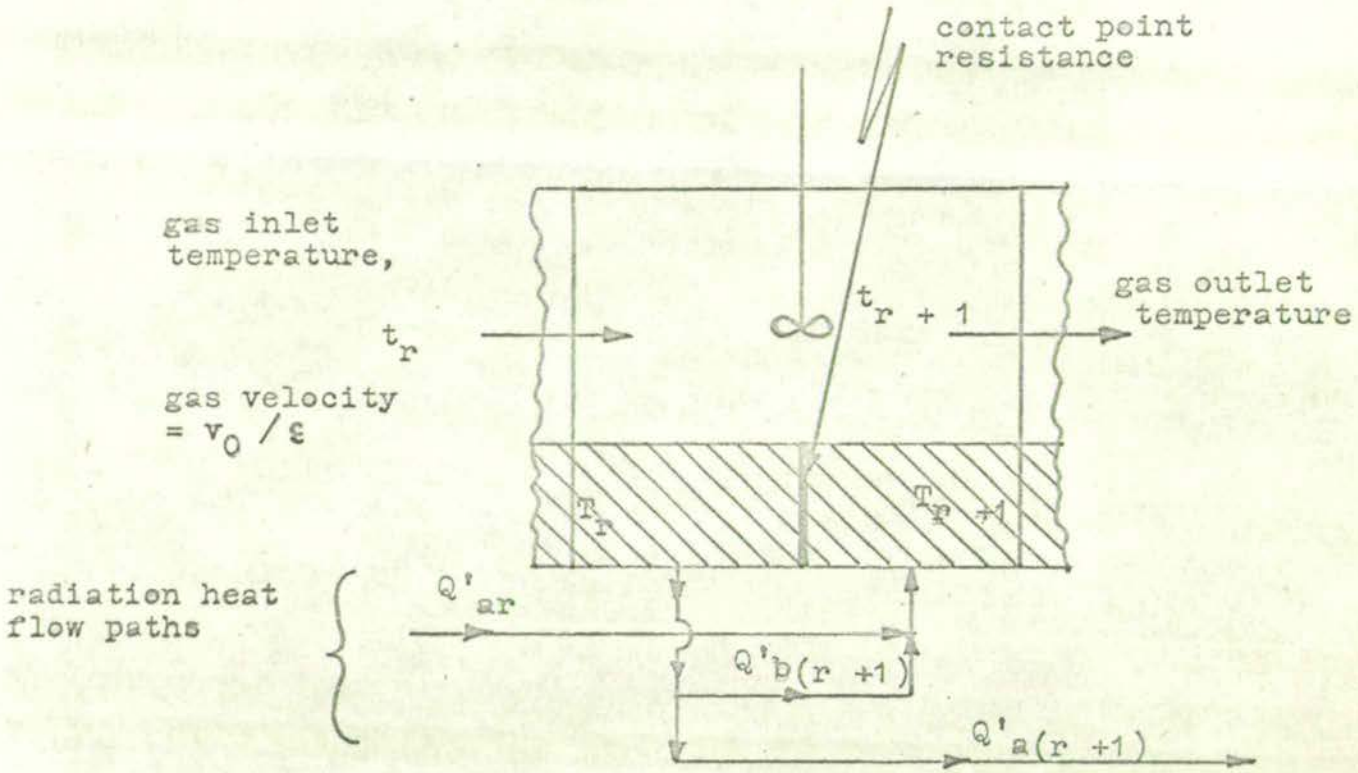

FIG. 4.21 CONDUCTION-CONVECTION-RADIATION MIXING CELL MODEL

Q'_a = intra-cell radiation heat flow (mechanism 6)

Q'_b = inter-cell radiation heat flow (mechanism 5)

complex unit cell equations were obtained. Even allowing only for intercell radiation, the solution of an equation involving seventh power terms was required for each successive cell along the bed length.

An alternative approach is to include radiation effects in the contact point parameter, N_P^*, by equating the conduction resistance for the mixing cell model and for the stagnant gas conduction-radiation model (4.2). Regarding the parallel gas paths in the two models as perfectly mixed in each unit cell and thus not contributing to the conduction resistance gives (from equations 4.118 and 4.40)

$$\frac{X(1-\varepsilon)}{1+N_P^*} = Y - \varepsilon = \varepsilon_{A1} H_r + \frac{1}{\frac{1}{X}\left(\frac{1-\alpha}{1-\varepsilon_{A1}}\right) + \frac{\alpha}{\varepsilon_{A2}(1+\alpha H_r) + X\,\varepsilon_{A3}}} \quad \ldots.(4.123)$$

If the gas in the series path is also perfectly mixed equation 4.123 becomes

$$\frac{X(1-\varepsilon)}{1+N_P^*} = \varepsilon_{A1} H_r + \frac{1}{\frac{1}{X}\left(\frac{1-\alpha}{1-\varepsilon_{A1}}\right) + \frac{\alpha}{\alpha H_r\,\varepsilon_{A2} + X\,\varepsilon_{A3}}} \quad \ldots(4.124)$$

Thus by solving equation 4.123 or 4.124 for N_P^*, radiation effects may be accounted for in each mixing cell of the mixing cell model.

5.1 EXPERIMENTAL SYSTEM

The reasons for the choice of the basic experimental system as axial, steady state heat transfer in an inert bed are discussed in 1.3.

5.1.1. Solid Packing

In order to simulate conditions in reacting gas-solid systems it was desirable that the inert solid should be randomly packed, coarse sized particles of a low conductivity material. A spherical shape was preferred to simplify geometric factors in the analysis of results. These conditions were fulfilled by the choice of ¼ in. dia. alumina silicate balls whose shape was approximately spherical. The relevant properties of the ball material are given in 6.1.2.

5.1.2. Gaseous Medium

Air is the usual gaseous medium in reacting gas-solid systems and thus was used in this investigation. The relevant properties of air are given in 6.1.1.

5.1.3. Bed Size and Shape

A cylindrical bed container was used for simplicity in construction and to give radial and angular uniformity of temperature and velocity. The 6 in. dia. bed ($D_T/D_P = 24$) was large enough to ensure that wall effects were negligible and to give a flat velocity profile across the bed. The bed length was 12 in. (48 D_P). This was sufficiently long to give

satisfactory temperature profile measurements, to avoid significant end effects and to apply a mixing cell model.

5.2. EXPERIMENTAL CONDITIONS

5.2.1. Directions of Gas and Heat Flow

To simulate the co-current and countercurrent gas and heat flow conditions present in reacting gas-solid systems (1.2), an electrically heated hot zone was placed across the centre of the inert packed bed.

It was most convenient for the air to enter at the bottom of the bed. This arrangement gave countercurrent gas and heat flow in the bottom half of the bed and co-current gas and heat flow in the top half.

To allow independent access to the lower half of the bed for repacking purposes, the hot zone and top half of the bed were supported on rollers which could be slid to one side when the two halves of the bed were disengaged. This was achieved by removing a one inch thick spacer ring from underneath the 6 - 9 in. enlarging section (Fig. 5.1) and lowering the bottom half of the bed away from the hot zone section on supporting cams.

Ideally, heat transfer measurements could have been made simultaneously on both halves of the bed. However, since this would have required duplication of equipment for radial heat loss compensation and for solid temperature measurements, attention was concentrated on the co-current gas and heat flows in the upper half of the bed. This half was chosen for study for the following reasons:

KEY TO FIG. 5.1

1. centrifugal blower
2. air inlet control
3. air bleed
4. orifice plate
5. pulsation dampener
6. micromanometer
7. 10 ft. vertical length of 6 in.dia. pipe containing brass gauzes.
8. 1 in. thick spacer ring
9. 6 in.-9 in. enlarging section
10. lower bed
11. rollers supporting hot zone and upper bed
12. refractory brick
13. silicon carbide elements
14. Sindanyo box enclosing hot zone
15. inlet gas thermocouple
16. gas mixing space
17. expanded stainless steel plate
18. Fiberfrax cylinders containing guard and test beds
19. test bed
20. guard bed
21. Fiberfrax cylinder supporting radial heaters
22. radial heaters (13 along bed length)
23. test bed particle thermocouple } 65 in total
24. guard bed particle thermocouple }
25. magnesium oxide insulation
26. aluminium sheet cylinder
27. Sindanyo sheet
28. outlet gas temperature meter (see Fig. 5.5)
29. copper coil
30. water bath
31. test bed gas rotameter
32. suction pump

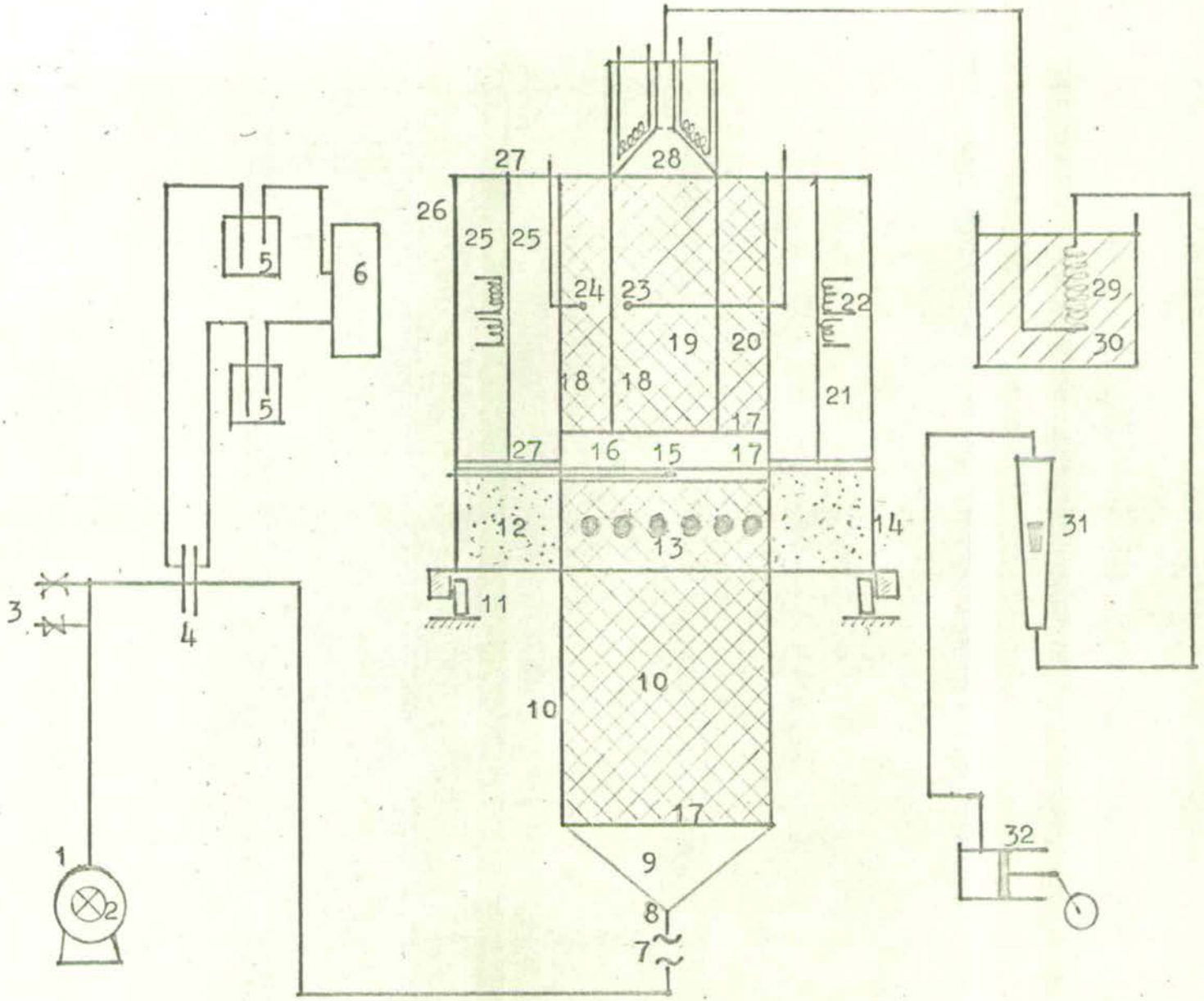

FIG.5.1 SCHEMATIC DIAGRAM OF EXPERIMENTAL EQUIPMENT - GAS FLOW RUNS

(For stagnant bed runs the outlet gas temperature meter was replaced by the brick heat flow meter (Fig. 5.4))

(a) In a reacting gas-solid system this is the section which is ahead of the moving reaction zone and thus has most effect on the zone velocity.

(b) The only previous experimental measurements of axial heat transfer for gas flow through packed beds have been for countercurrent gas and heat flow (3.4.4).

(c) Adiabatic conditions are easiest to achieve and temperature profile measurements are the most accurate for the flatter portion of the profile. For the upper half of the bed this portion occurs at the high temperature end of the bed where radiation effects are greatest and where accurate measurements are most desired.

(d) The axial heat flux is higher for the co-current case.

(e) The presence of the countercurrent section prior to the co-current section increases the uniformity of the gas velocity profile.

5.2.2. Range of Gas Flow Rates and Bed Temperatures

Various combinations of the basic experimental variables of gas flow rate and bed hot-face temperature[1] can cause the predominance of one or more heat transfer mechanisms. Thus it was necessary to provide experimental conditions for:

(a) stagnant gas - low temperatures (conduction mechanisms)

(b) stagnant gas - high temperatures (conduction - convection mechanisms)

(c) gas flow - low temperatures (conduction - convection mechanisms)

---

1. The temperature at the hot zone and gas inlet end of the bed.

(d) gas flow - high temperatures (conduction - convection - radiation mechanisms)

As the gas flow rate was increased from zero the high temperature end of the temperature profile became increasingly flatter and at higher flow rates the profile changed very little with increased flow rates. This limiting flow rate for which useful results could be obtained was greater the higher the hot-face temperature of the bed. The maximum flow rate used was 21.7 lb/ hr ft^2 which corresponded to a particle Reynolds number at the mid-point of the bed of 4.76.

The maximum bed hot-face temperature was limited by the maximum temperature that the radial heat loss heaters would withstand during continuous operation. For this reason, experiments were carried out at temperatures below 750°C.

5.3 EXPERIMENTAL EQUIPMENT

.3.1. Outline of Equipment

The experimental arrangement is indicated diagrammatically in Fig. 5.1.

Air was passed by a centrifugal blower through an orifice plate into the bottom section of the bed. The hot zone which generated the axial heat flow consisted of silicon carbide elements covered with packing and surrounded by refractory bricks. The hot zone was connected to the test bed and the surrounding guard bed by a gas mixing space. The guard bed was surrounded by a large cylinder of magnesium oxide powder containing the strip heaters which compensated

for the radial heat loss.

For stagnant bed runs a brick heat flow meter was placed on top of the bed. For gas flow runs an outlet gas temperature meter was connected to the top of the test bed. The test bed gas was drawn through this by a suction pump connected to a rotameter.

5.3.2. Air Flow Equipment

The air flow through the bed was provided by a Keith Blackman 20 in. dia., cast iron, two stage centrifugal blower. The blower was directly driven by a 6½ H.P. motor at 2900 rpm. and could deliver up to 750 cfm. at 30 ins. water gauge. The motor was cooled by the action of the blower. The air flow rate could be varied either by a bevelled disc closing over the blower intake, or by bleed-off valves on the outlet line from the blower.

The pressure drop through the outlet gas temperature meter was supplied by a Genevac suction pump driven by a 1 H.P. motor.

.3.3. Attainment of a Uniform Velocity Profile

The air was supplied to the bottom of the lower packed bed section through a vertical 10 ft. length of 6 in. dia. cast iron pipe. Pitot tube traverses at various axial positions on this calming length showed that the velocity was non-uniform. There was a minimum velocity towards the centre of the pipe. The position of this minimum varied with axial distance along the pipe indicating the presence of swirl in the air flow.

Three types of flow straightening devices were tested - radial vanes, a honeycomb insert and a brass gauze ($\frac{1}{16}$ in. dia. holes on a triangular pitch). Since the latter was found to be the most effective, three such gauzes were permanently installed at different axial positions along the calming length. With this arrangement, Pitot tube traverses (Fig.5.2) indicated a uniform velocity profile ($\pm$ 2%) at all points across the entrance pipe.

For velocity profile measurements downstream of the packing, a hot wire anenometer system was developed (Appendix 8) since the pitot tube manometer measurements were not sufficiently sensitive for this purpose. A typical profile is shown in Fig. 5.2 which indicated that the mean velocity profile across the bed was uniform. The peaks on the profile were due to the jet effect of the gas leaving the voids at the top of the bed.

5.3.4. Hot Zone Equipment

Electrical resistance heating is the best method for providing a continuous, variable and high temperature heat source. Silicon carbide heating rods (Morgan Crusilite Type T) were used in preference to wire wound heaters because of (a) higher maximum operating temperatures (up to 1575°C) (b) higher heat flux per unit volume (c) no effect from intermittent current switching (d) longer life (e) easy replacement.

To provide a narrow hot zone, as is the case in a reacting gas-solid system, a single row of rods was used at

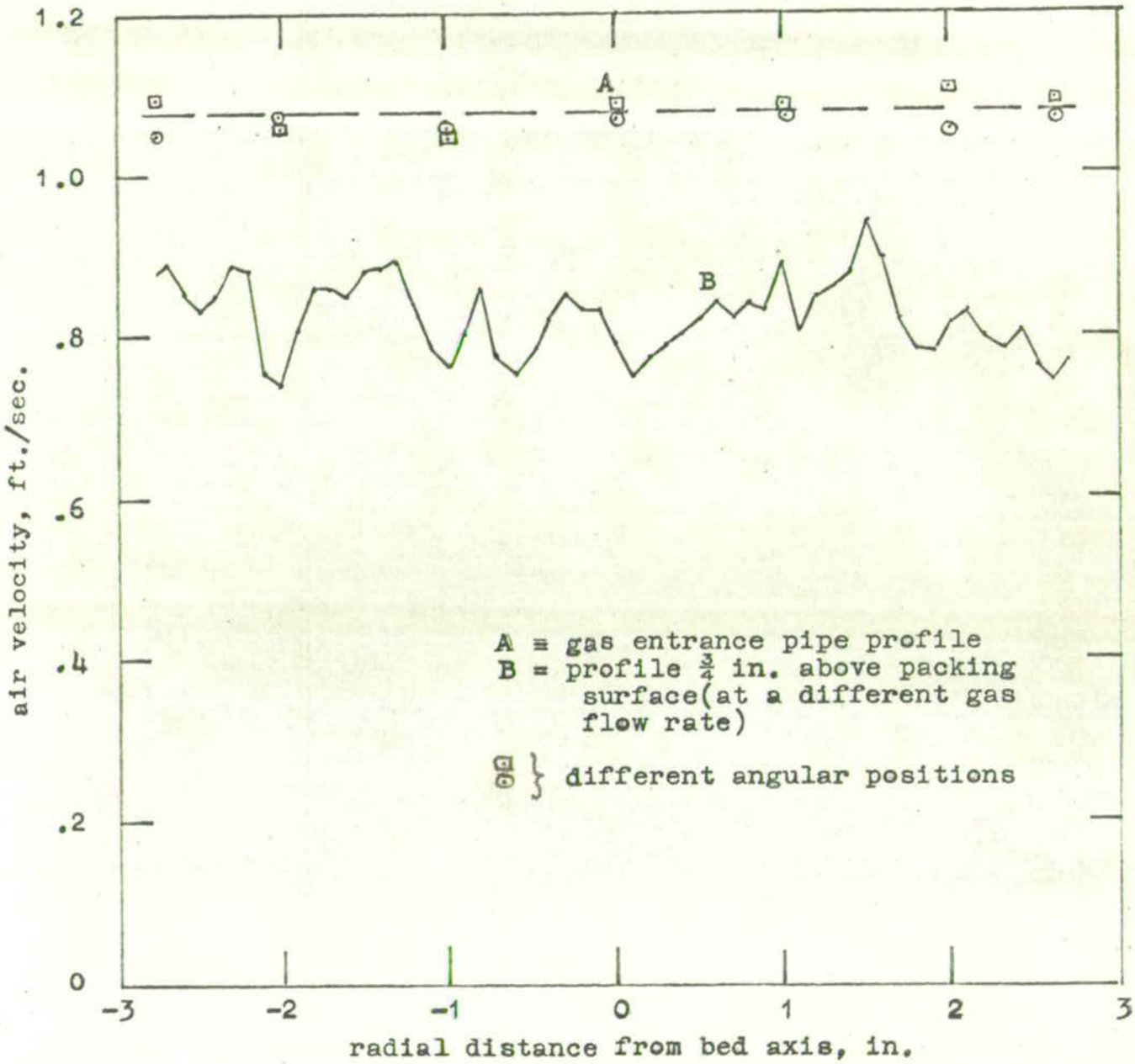

FIG. 5.2 VELOCITY PROFILES AT BED ENTRY AND EXIT

right angles to the bed axis. The minimum recommended centre-centre spacing for the rods was 2½ rod diameters. For a rod diameter of 1.4 cm. this enabled six rods of hot lengths 5.8 in. (x2), 7.85 in., and 9.05 in. (x2) to be installed. The resistance ratings at 800°C of these hot lengths were 2.0, 2.65 and 3.0 ohms respectively. Alternate rods were connected in series to form two independent circuits (Fig. 5.3). The power inputs to the circuits were controlled by independent variacs (0 - 270 volts, 0 - 30 amps). Thus the maximum power input obtainable from each rod circuit was 3.35 K.W. This allowed for more than the heat flow required in practice and made available adequate reserve voltage to compensate for any increase in rod resistance due to ageing with continuous use.

The heating rods were supported in ¾ in. dia. holes drilled in Morganite MI28 refractory bricks. The 9 in. x 4½ in. x 3 in. bricks were cut to fit into a 4½ in. high hexagonal Sindanyo box (Fig. 5.3) and to form a 9 in. dia. hole containing the rod hot lengths. In this way the bed hot zone was completely surrounded by at least a 6 in. thickness of refractory brick. The bricks interlocked with each other so that they remained in fixed positions inside the box. Four silica bricks were set into the refractory bricks to support the weight of the bed. The Sindanyo box was sealed with Araldite. The cement asbestos cylinder containing the 9 in. dia. lower bed fitted into the bottom of the Sindanyo box. This joint was sealed with sodium silicate. The heating rods were

KEY TO FIG. 5.3

1. $1\frac{1}{2}$ in. mild steel angle
2. $\frac{1}{4}$ in. thick mild steel plate
3. Sindanyo box enclosing hot zone
4. refractory bricks (M.I.28) surrounding 9 in.dia. gas flow section
5. 9 in. dia. gas flow section containing heating elements and packing
6. silicon carbide elements, 1.285 in. centre-centre spacing
7. silica bricks supporting expanded stainless steel plate

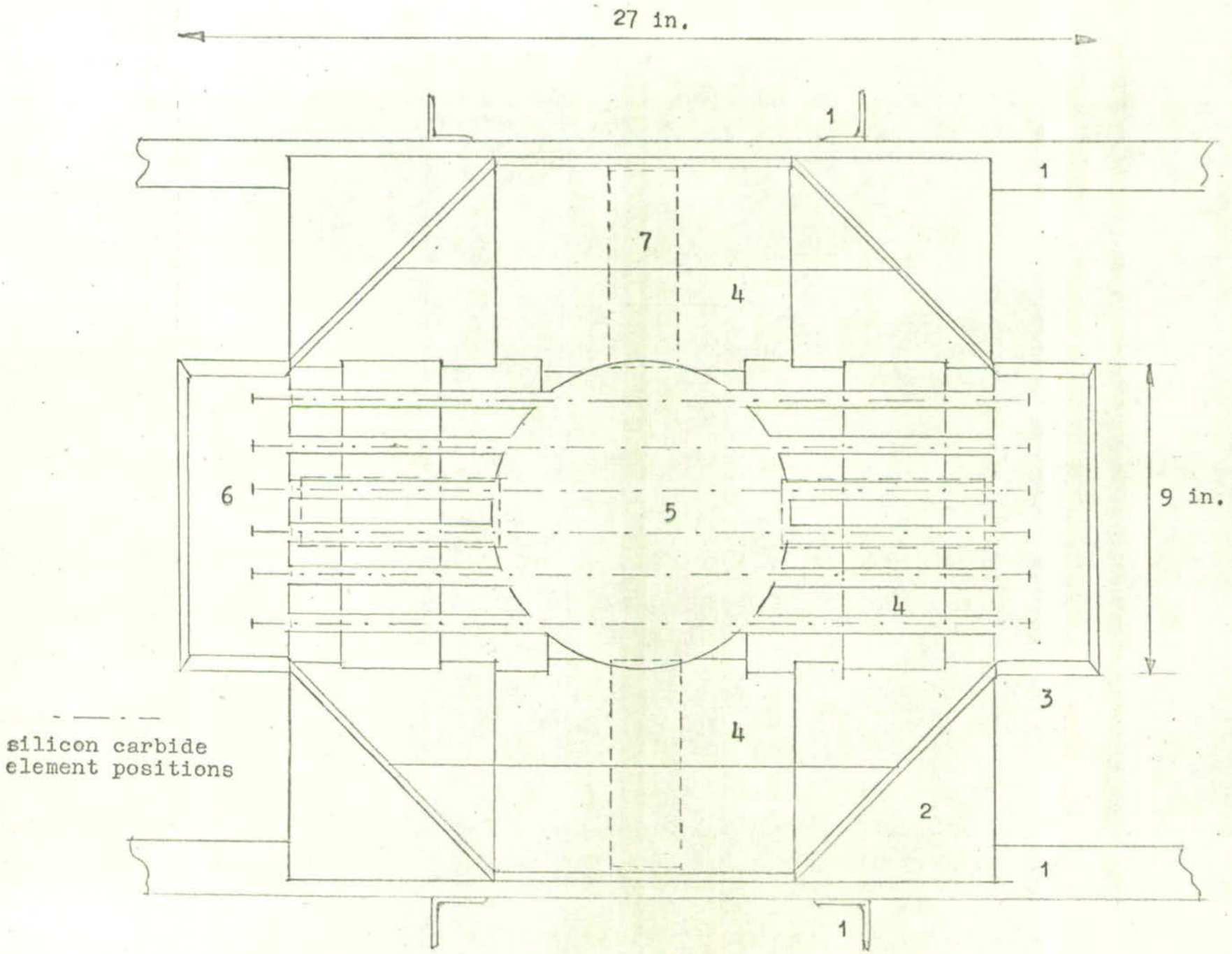

FIG. 5.3 HOT ZONE CONSTRUCTION

covered with packing since this was found to give a more uniform radial temperature distribution.

One of the heating rod circuits was actuated by a Smiths on-off controller which controlled the hot-face temperature of the bed to within $\pm$ 5°C of the set point. The sensing element for the controller was a particle thermocouple (5.4.3.) placed on the centre of the expanded metal disc supporting the bed (5.3.5).

5.3.5. Bed Container and Support

The test bed and guard bed were contained in specially constructed, rigid, ceramic fibre cylinders. The ceramic fibre material was .04 in. thick Carborundum Fiberfrax paper (grade 970F). This material was used since it could withstand high temperatures (up to 1260°C) without thermal shock, had a low thermal conductivity (k = .5-1.0 BTU/hr. $ft.^2$ (°F/in) at 0-815°C) and could be obtained in small thicknesses. The latter two properties enabled longitudinal heat conduction up the container walls to be kept to a minimum.

The cylinders were constructed by soaking the Fiberfrax paper in Fiberfrax rigidizer solution and laying the paper around a former of the required diameter (9 in. for the guard bed, 6 in. for the test bed). When the solution dried (at room temperature) a rigid cylinder was obtained.

The 18 in. dia. supporting cylinder for the radial heat loss heaters (5.3.6.) was similarly constructed from Fiberfrax paper. In this case, four layers of paper were used with successive layers being stuck together by Fiberfrax Coating

Cement (QF - 180 Blue).

The guard bed and test bed were supported on a $\frac{1}{16}$ in. thick, fine mesh, expanded stainless steel disc. This disc was connected to an identical disc by 3 in. x $\frac{3}{16}$ in. dia. steel rods. The space between the two discs acted as a mixing space (Fig. 5.1) for the gas leaving the heating rods to ensure a uniform gas temperature at the bed entrance. The two discs were sealed inside the bottom of the guard bed container with coating cement and the complete unit sealed into the top of the Sindanyo box so that the silica bricks supported the weight of the bed. The test bed container was placed on the top disc and kept in position by the packing on either side of the container wall.

5.3.6. Radial Heat Loss Compensation Equipment

The following possible methods for achieving local adiabatic conditions along the axial length of the bed were considered:

(a) A vacuum jacket surrounding the bed is a common method of preventing radial heat loss in axial thermal conductivity measurements in packed beds at low temperatures.[1] While this method minimises heat losses due to conduction and convection, losses due to radiation are still present and would be significant at the temperatures used in this work.

(b) A guard ring of the same material as the test material is also used in some methods of axial thermal conductivity measurement. Additional control over the radial heat loss

---

1. Yagi, Kunii, Wakao (1960); Kunii and Smith (1961); Masamune and Smith (1963).

could be obtained with the present system by providing independent variation of the gas flow rates through the guard bed and test beds.

(c) Sectional heating either by electrical resistance heating or by a heat transfer fluid would provide the most localized method of heat loss control.

Initially only method (c) was employed by using local resistance heating. But after preliminary trials a guard bed was also incorporated both to decrease the heater loads and to improve the detection of any radial heat loss.

The guard bed consisted of a $1\frac{1}{2}$ in. wide annulus of packing around the main bed and the presence of radial heat loss was detected from any difference in readings between thermocouples installed in the guard and test beds at the same axial positions (5.4.3.)

The local electrical resistance heating consisted of thirteen heaters wound on Micanite strips and supported on a Fiberfrax cylinder (5.3.5.) at one inch axial spacings. The heater strips were formed by cutting notches at $\frac{1}{8}$ in. spacings on $\frac{3}{4}$ in. wide Micanite to fix the resistance wire (Tophet 30, .0126 in. dia., 4.48 ohms/ft) in position. After winding on the wire, the shellac in the Micanite was burnt off so that the heater strip became flexible and could be wrapped around the supporting cylinder. Each heater unit was formed from two such wound strips joined in parallel to give a resistance of 110 ohms. The strips were insulated

from each other by a strip of Fiberfrax paper and supported on ceramic pegs pushed into the Fiberfrax cylinder. The $4\frac{1}{2}$ in. wide annulus between the heaters and the guard bed was filled with magnesium oxide powder. A similar annulus of powder around the outside of the heaters was contained in a 27 in. dia. cylinder of thin gauge aluminium which was screwed to a Sindanyo base.

On the outside of the cylinder a Sindanyo terminal board connected the heaters to the leads from the thirteen heater variacs (0 - 270 volts, 0 - 2.5 amps). Provision was made to connect an ammeter in series with one of the leads of each variac in turn to measure the currents drawn by each heater.

5.4 EXPERIMENTAL MEASUREMENTS

5.4.1. Gas Flow Rates

The gas flow rate through the test bed was measured by a rotameter (metric series 10 or 7). The calibrations were checked on a wet displacement gas meter. The gas in the outlet line from the test bed was cooled to room temperature on passing through 20 ft. of air-exposed, 1 in. dia. copper tubing and then a 25 ft. coil of $\frac{1}{2}$ in. dia. copper tubing (in a water bath) before entering the rotameter.

The total gas flow rate through both the guard and test beds was measured by a $\frac{11}{16}$ in. dia. B.S. orifice plate placed in the 3 in. dia. gas inlet line connecting the blower to the bed. The orifice plate was preceeded by a straight calming length of 10 ft. and the pressure drop across the plate was

measured on a Mercury Electronic micromanometer with a range of 0 - 30 m.m. water gauge.

.4.2. Heat Flow Rate for the Stagnant Bed

Measurement of the heat flow rate for the stagnant bed was based on the measurement of the temperature gradient in an adiabatic block of known thermal conductivity material placed in series with the bed.

The material chosen for this purpose was refractory brick (Morganite MI 28) since this satisfied the requirements of withstanding high temperatures and having a thermal conductivity similar to that of the bed. The variation of the thermal conductivity with temperature is given in Fig. 6.10.

The heat flow meter was constructed by cutting and cementing together several MI28 refractory bricks to form a $4\frac{1}{2}$ in. thick slab on top of the guard and test beds. Further bricks were cut and placed around the central section to form an insulating slab extending to a diameter of 27 ins.

Fine hypodermic tubing was used to drill holes through the brick in a horizontal plane to accommodate a Pyrotenax chromel-alumel thermocouple unit. Five holes were positioned in the guard brick and test brick sections as shown in Fig. 5.4 at every one inch along the brick axis.

.4.3. Solid Temperatures

The thermocouples for solid particle temperature measurements were formed by fusing together .0076 in. dia. chromel and alumel wires (British Driver-Harris T1/T2 thermocouple alloys). Each of the thermocouples was

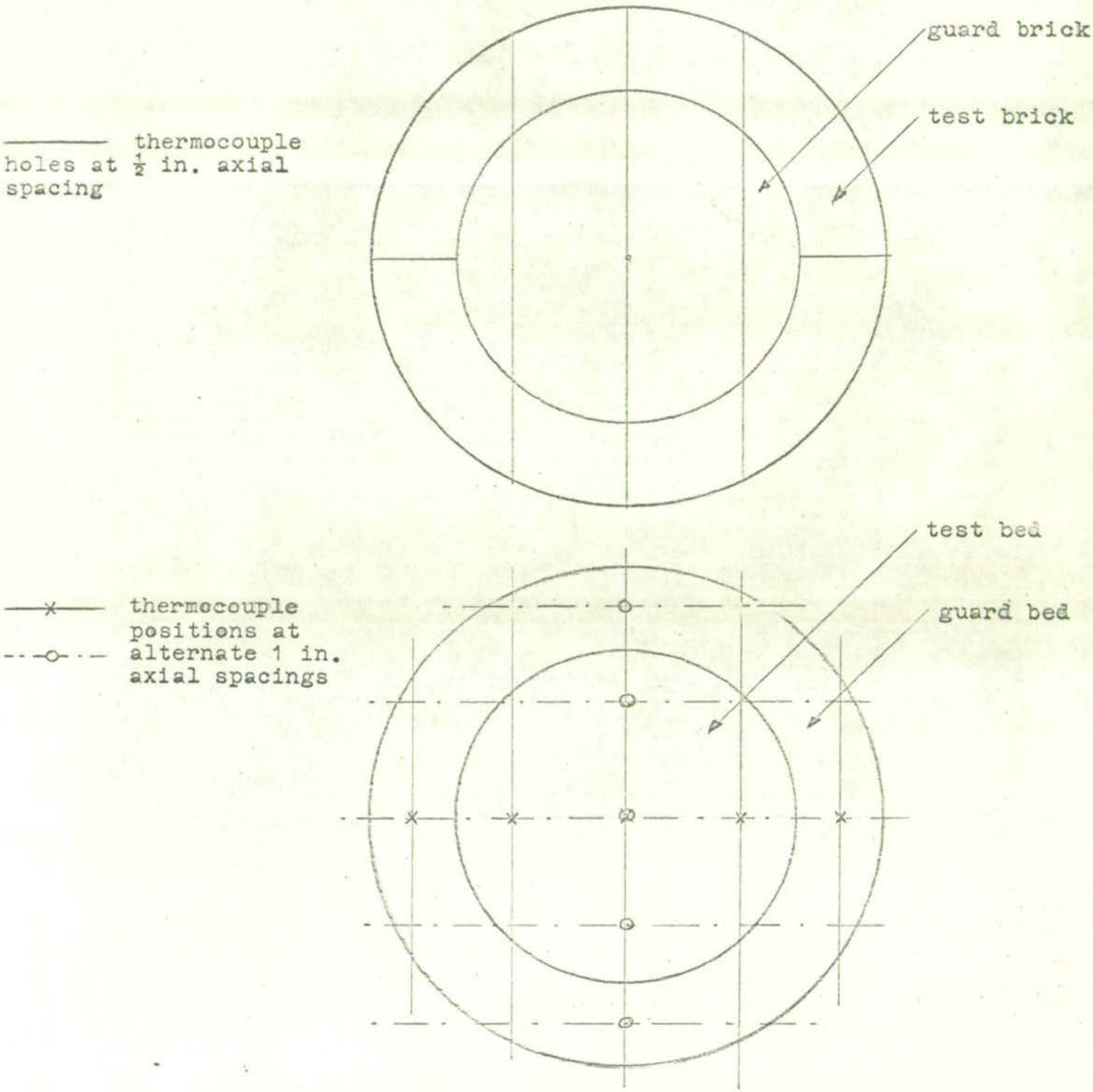

FIG. 5.4 THERMOCOUPLE POSITIONS IN PACKED BED AND BRICK HEAT FLOW METER

calibrated against a platinum resistance thermometer in a furance at 450°C. The emf. values obtained corresponded to the resistance thermometer temperatures to within the manufacturers specified tolerance (± .75%).

Balls of moist alumina silicate clay of ¼ in. dia. were prepared and the thermocouples embedded in the centre with the positive and negative wires passing diametrically through opposite sides of the balls. After drying at 150°C overnight, the balls were fired at 600°C. A higher firing temperature was not used since this tended to cause oxidation and disintegration of the thermocouple wires. A total of 65 thermocouples were prepared in this way.

At every one inch along the bed, starting from the supporting grid plate, five thermocouples were installed across a diameter in the positions shown in Fig. 5.4. The diameters along which the thermocouples were placed were at 90° to each other at the successive one inch intervals along the bed axis.

The particles containing thermocouples were placed in position by threading the thermoccuple wires through the Fiberfrax tubes containing the guard bed and test bed so that the wires were at right angles to each diameter along which the balls were placed (Fig. 5.4). The bed was then packed randomly by dropping in particles. As the bed level reached each thermocouple particle, it was placed in a stable position on the packing. The exact axial position of the particle was

then measured by placing a pointer attached to a steel rod on top of the particle. This rod could only be moved vertically inside a sleeve fixed above the bed. Measurement (with a ruler) of the distance between a fixed mark on the rod and the top of the sleeve enabled the axial position of the thermocouple to be estimated to within $\frac{1}{32}$ in. The rod and pointer were then removed and particles placed around and on top of the thermocouple particle without disturbing its position. This procedure was repeated until the complete bed was built up and every thermocouple was in a fixed and known position.

The thermocouple wires were then sealed into the Fiberbrax wall of the guard bed with Fiberfrax cement. The thermocouple wires from the lower half of the bed were passed downwards along the guard bed wall and out between the radial insulation support and the top of the hot zone. The thermocouple wires from the top half of the bed were passed upwards along the guard bed and out above the radial insulation jacket. Once the wires were away from the insulation jacket they were no longer fixed in position and were therefore insulated from each other with either ceramic or polythene sleeving.

All the thermocouple wires were taken to an ice junction where the chromel and alumel wires were brazed to insulated copper wiring. Each positive junction was fixed with sellotape in an individual $\frac{1}{8}$ in. dia. glass tube with a sealed lower end. The negative junctions at each axial

position were brazed together and placed in $\frac{1}{2}$ in. dia.test tubes. The glass tubes and test tubes were fixed with Araldite into the lid of an ice bath surrounded by polythene insulation. A mercury-in-glass thermometer graduated to $\frac{1}{10}$ ^{o}C could be placed in the ice bath in a number of positions to ensure that a temperature of 0^{o}C was maintained during any thermocouple temperature measurements.

The positive and negative copper leads were taken to a junction box where each lead was soldered to a small single pin socket. All the negative sockets were interconnected. The junction box also contained sockets connected to a potentiometer and a Sunvic 12 point recorder and a 3 point Ether indicorder. External connection between sockets enabled the emf. of any selected thermocouple in the bed to be read on the potentiometer to .01 m.v. or several selected thermocouple readings to be followed continuously on the recorder or indicorder to test for steady state conditions.

5.4.4. Gas Temperatures

The gas temperature at the inlet to the bed was measured with a Pyrotenax chromel-alumel thermocouple unit contained in a ceramic sheath. The sheath was sealed into the hot zone bricks just below the lower expanded metal disc (Fig. 5.1). The wiring and cold junctions for the thermocouple were installed in a similar manner to the solid particle thermocouple installation.

Fig. 5.5. shows the construction of the outlet gas temperature meter. This was intended to measure the mixed

KEY TO FIG.5.5

1. gas outlet end of test bed
2. gas outlet end of guard bed
3. Fiberfrax cylinder
4. jubilee clip
5. 3 in. high sheet brass cone
6. heating element wound in refractory cement
7. cone thermocouple pair
8. measuring thermocouple pair
9. brass cylinder screwed on to cone at lower end
10. orifice plate
11. brass gauzes
12. supporting collar
13. outlet gas to cooler, rotameter and suction pump

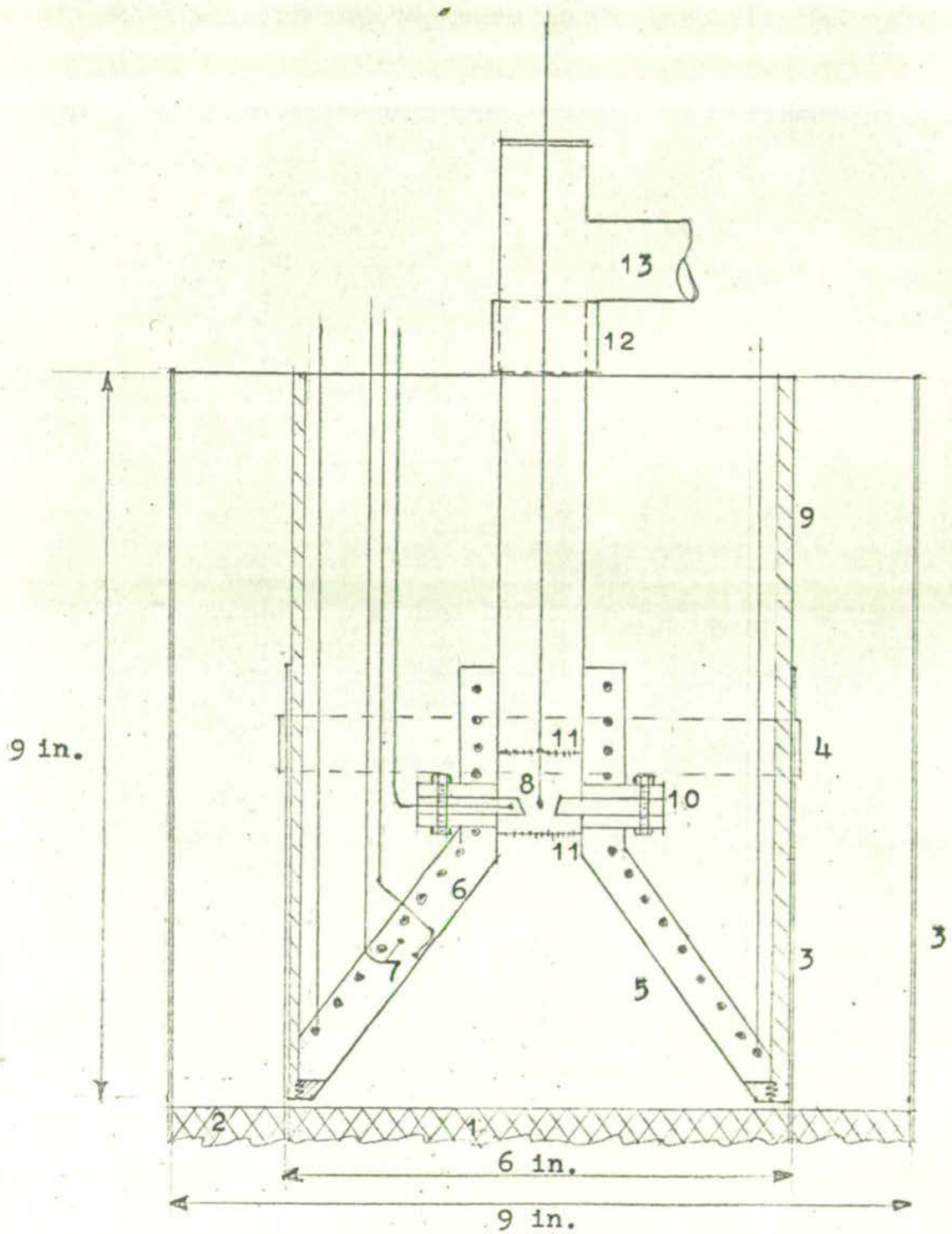

Scale: $\frac{1}{2}$ in. = 1 in.

FIG.5.5 OUTLET GAS TEMPERATURE METER CONSTRUCTION

mean outlet temperature of the gas from the test bed with a minimum of radiation effects on the measuring thermocouple. This meter consisted of a 3 in. high brass cone which collected the outlet gas from the bed into a 1 in. dia. copper tube containing coarse gauzes and an orifice plate to promote mixing of the gas as it flowed past the measuring thermocouple in the centre of the tube. The gauzes also shielded the measuring thermocouple from any radiation from the top of the bed or radiation to the cooler upper section of the outlet copper tube. To obtain adiabatic conditions a resistance heating wire was wrapped around the cone and tube on top of a $\frac{1}{2}$ in. thickness of refractory cement. The bottom of the cone screwed inside a 6 in. dia. brass cylinder which was filled with Vermiculite insulation. The cylinder was supported just above the top surface of the bed and the test bed Fiberfrax cylinder was sealed on to the brass cylinder with a jubilee clip. The air leaving the guard bed was passed upwards between the gas temperature meter and an extension of the Fiberfrax wall enclosing the guard bed.

Two Pyrotenax thermocouples were installed outside the cone wall. One of these was brazed to the outside of the wall and the other embedded $\frac{1}{4}$ in. out from the wall in the refractory cement (Fig. 5.5). A Pyrotenax thermocouple was also placed in a hole drilled into the orifice plate to form a thermocouple pair with the measuring thermocouple.

The power input to the heater was adjusted by a variac until the temperatures indicated by each of the individual

thermocouples forming a pair were equal. Fig. 5.6 shows the variation of the thermocouple temperature with the heater voltage for a typical run. The correct temperature of the orifice plate pair was slightly greater than the cone pair due to the mixing of the gas at this point. The outlet gas temperature was taken as the temperature of the measuring thermocouple when the above conditions were achieved.

5.5. EXPERIMENTAL PROCEDURE

5.5.1. Stagnant Bed Runs

The temperature controller set point was adjusted to a value slightly higher than the desired hot-face temperature of the bed. The axial heat flow variacs were adjusted to give a sufficient power input to maintain this temperature. When steady state conditions were attained as indicated by constant particle thermocouple readings, comparison of these readings in the guard bed and test bed was made along the axial length of the bed. Similar readings were made with a Pyrotenax chromel-alumel thermocouple in the guard brick and test brick portions of the heat flow meter. The radial heat loss heater variacs were individually adjusted in accordance with these temperature readings and the system was again allowed to attain steady state conditions.

This process was repeated until the guard bed and brick temperatures corresponded closely to the test bed and brick temperatures (Fig.6.5, 6.9) so that there was no radial heat loss from the test bed or test brick portion of the heat flow meter. Because of the large thermal capacity of

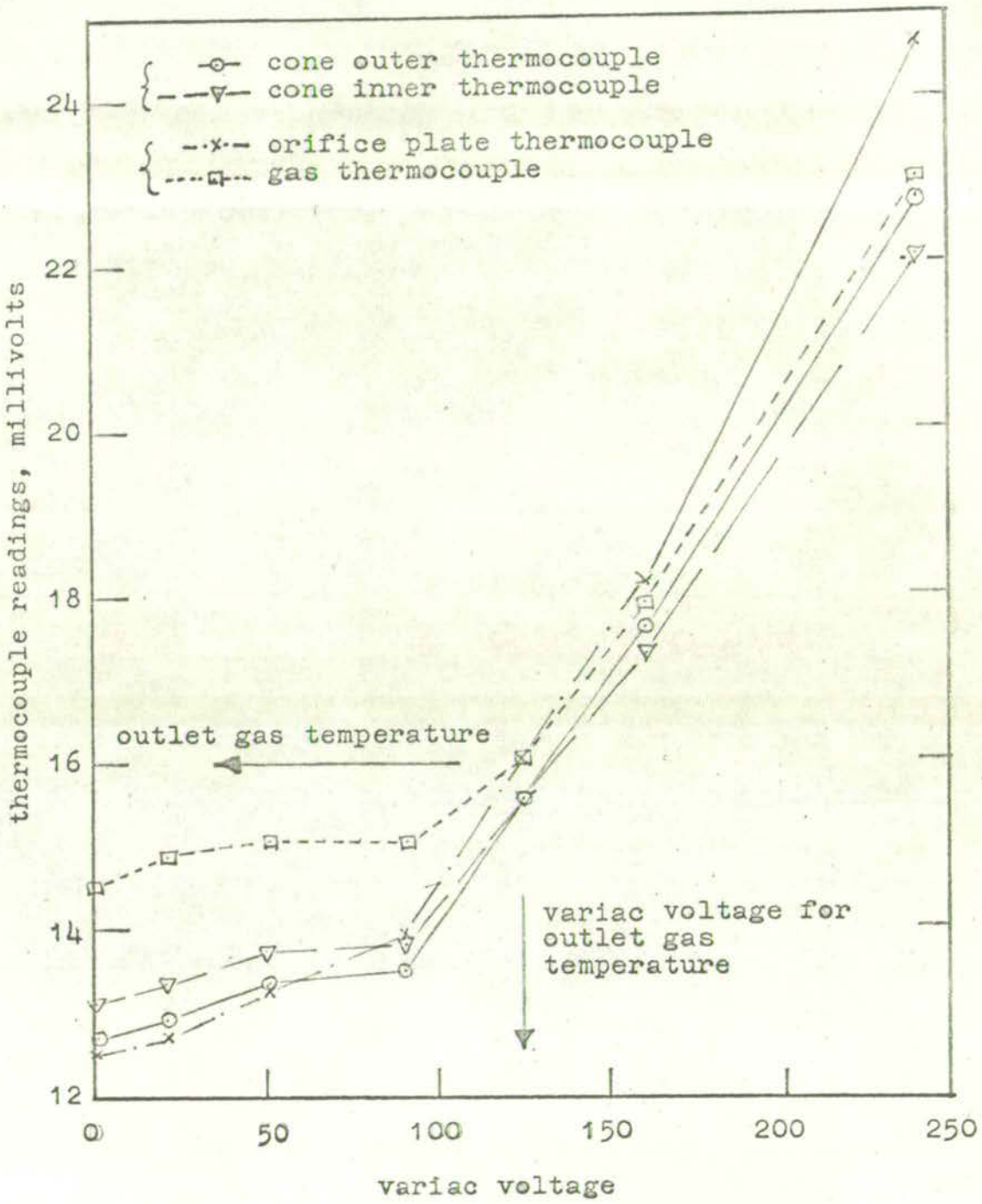

FIG. 5.6 DETERMINATION OF OUTLET GAS TEMPERATURE

the insulation jacket, the time required to achieve these conditions was 3 - 7 days. The solid particle temperature readings and the brick heat flow meter temperature readings were then recorded.

5.5.2. Gas Flow Runs

The outlet valve on the test bed gas line was adjusted to give the desired gas flow rate as indicated on the rotameter. The inlet valve on the blower was adjusted to give a total gas flow rate (as indicated by the orifice plate pressure drop) such that the gas flow rate per unit area would be the same in both the guard bed and the test bed. Steady state, radially adiabatic conditions for the desired hot-face temperature were then obtained by the same procedure as for the stagnant bed runs (Fig.6.5). The heat loss variac on the outlet gas temperature meter was similarly adjusted to give adiabatic conditions as indicated by the thermocouple pairs. The time required to achieve these conditions was again 3 - 7 days. The solid particle temperatures, inlet and outlet gas temperatures and the gas flow rate readings were then recorded.

CHAPTER 6 ANALYSIS AND DISCUSSION OF RESULTS

6.1. PROPERTIES OF THE SOLID AND GAS PHASES

The evaluation of the various heat transfer mechanisms from the experimentally determined thermal conductivity measurements requires information on a number of properties of the solid and gas phases.

6.1.1. Gas Phase Properties

(i) Bulk mean voidage

Since in situ measurement was not practicable, the bulk mean voidage was evaluated from experimental density measurements. The bulk density of the bed was 85 lb./ft.^{3} and the solid particle density 142 lb./ft.^{3} which corresponds to a voidage of 0.399. Thus a value 0.40 was used for the bulk mean voidage in all calculations.

(ii) Gas thermal conductivity

The variation of the thermal conductivity of air with temperature was taken from the data of Glassman and Bonilla (1953) and is given in Fig. 6.1.

(iii) Gas viscosity

The variation of the viscosity of air with temperature was taken from the nomogram given by Perry (1963) and is given in Fig. 6.1.

6.1.2. Solid Phase Properties

(i) Solid chemical composition

The alumina silicate balls were fired to complete vitrification and had a composition of SiO_2, 62%; Al_2O_3, 32%; Fe_2O_3, 1%; TiO_2, 2%; Alkalies 3% (Browning (1964)).

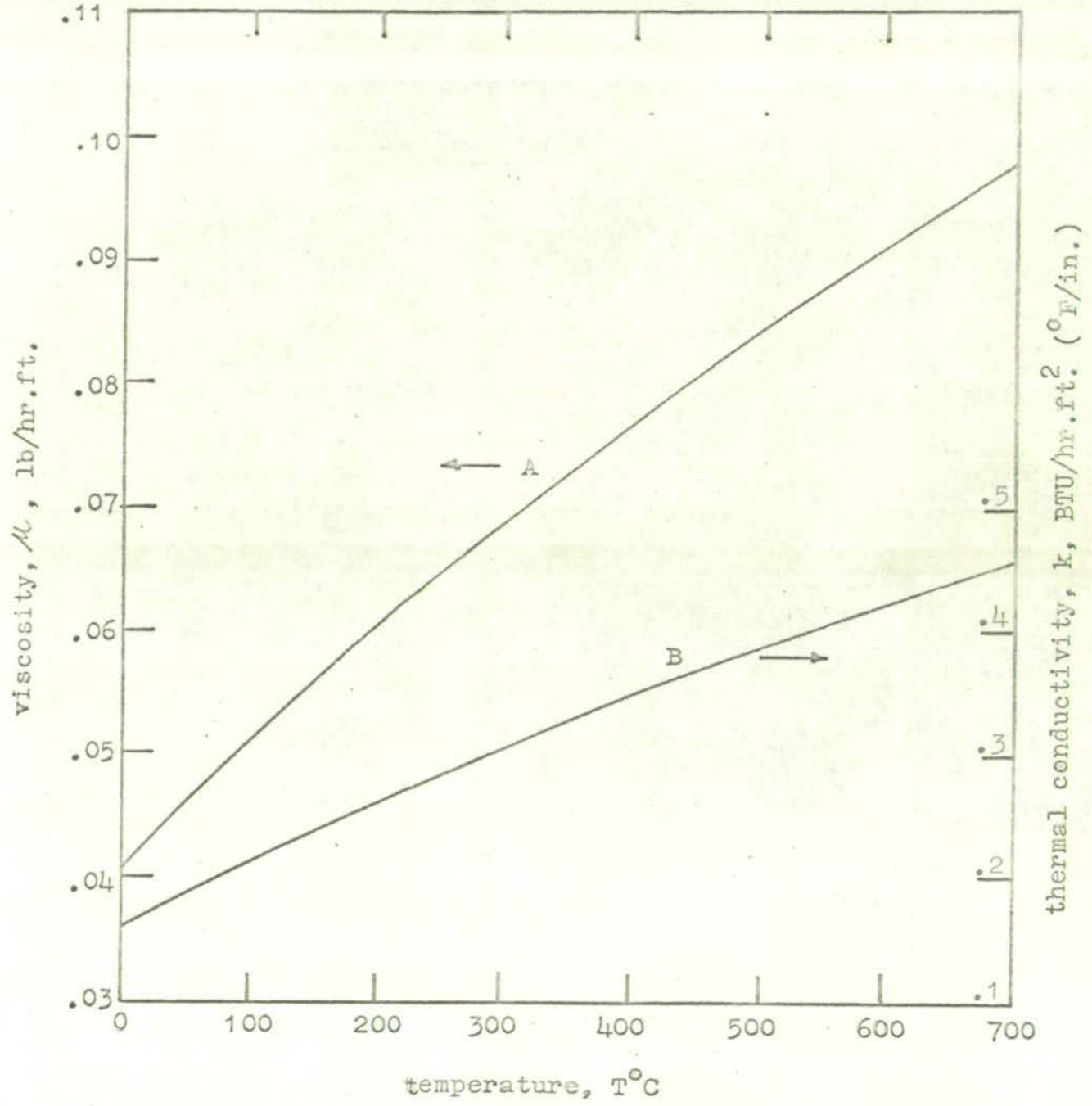

FIG. 6.1 VISCOSITY AND THERMAL CONDUCTIVITY OF AIR

A = viscosity, (Perry (1963))

B = thermal conductivity, (Glassman and Bonilla (1953))

(ii) Solid thermal conductivity

The solid thermal conductivity values used (Fig.6.2) were based on an experimental measurement at room temperature and the temperature variation of the thermal conductivity of a porcelain (Wologdine and Queneau (1909)) which had a very similar chemical composition to the particle material. The experimental measurement (Gordon (1966)) was based on the ball comparator method and is described in Appendix 9. The average value of the solid thermal conductivity obtained was 9.55 BTU/hr ft.^{2} ($^\circ$F/in.) at 20°C with a $\pm$ 10% scatter of results. The variation with temperature of the solid thermal conductivity is shown in Fig. 6.2 and relative to the gas thermal conductivity in Fig. 6.3.

(iii) Solid emissivity

The variation with temperature of the emissivity of the solid material may be taken from the data of Pirani (1939) for a fire clay of similar composition to the ball material (Fig. 6.4)

6.2. STAGNANT BED RESULTS

6.2.1. Temperature Profiles

The steady state temperature readings given by the particle thermocouples in the test bed and the guard bed are shown for a typical run in Fig. 6.5. The guard bed readings are close to the test bed readings at any axial position showing that radially adiabatic conditions were obtained in the test bed. Thus the nett heat flow was solely in the axial direction and the temperature profile was determined for each

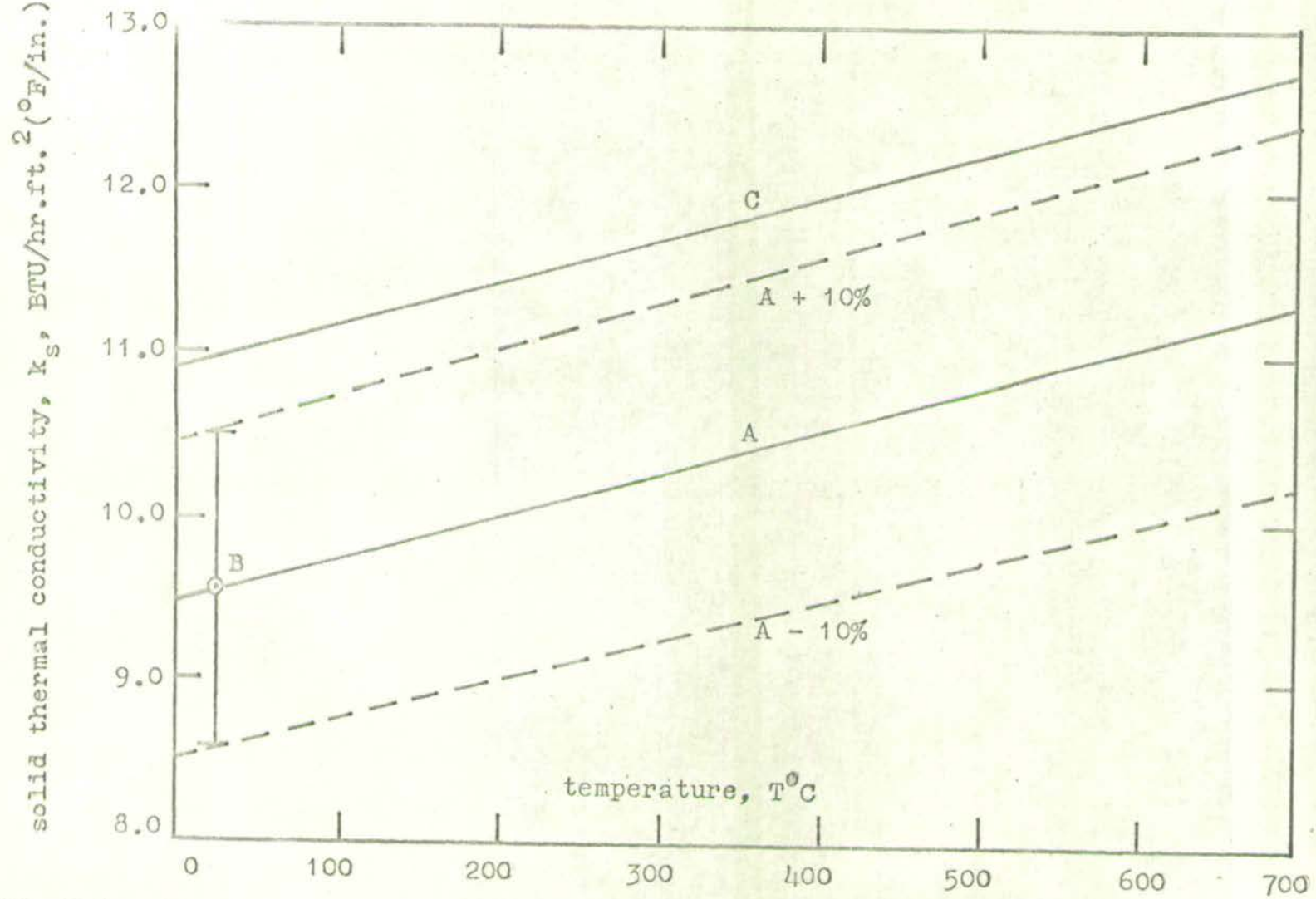

FIG. 6.2 THERMAL CONDUCTIVITY OF SOLID PARTICLE MATERIAL

A = estimated solid particle material thermal conductivity
B = experimental measurement (± 10%) for solid particle material thermal conductivity (Gordon (1966))
C = porcelain thermal conductivity (Wologdine and Queneau (1909))

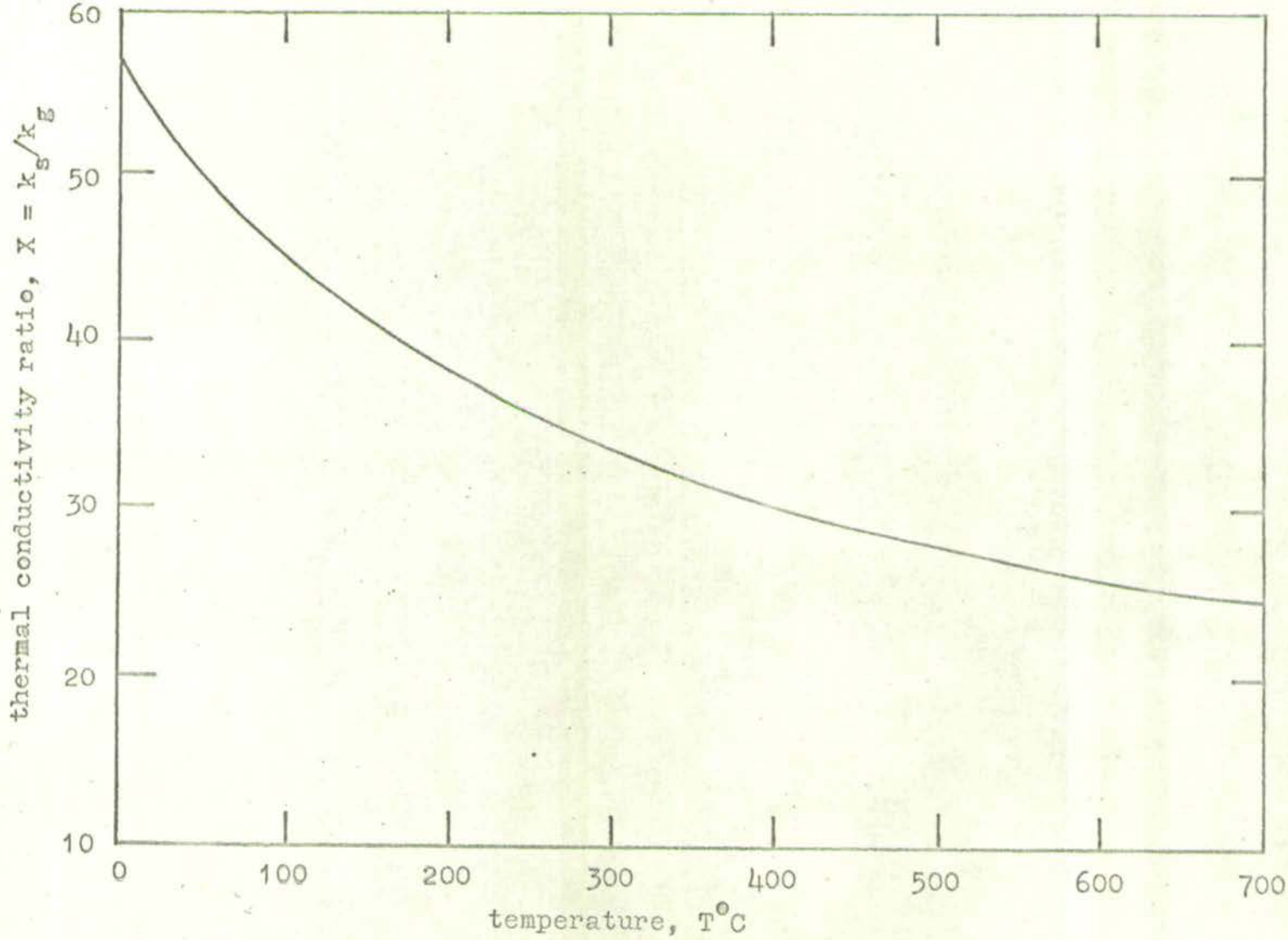

FIG. 6.3 THERMAL CONDUCTIVITY OF SOLID PARTICLE MATERIAL RELATIVE TO GAS

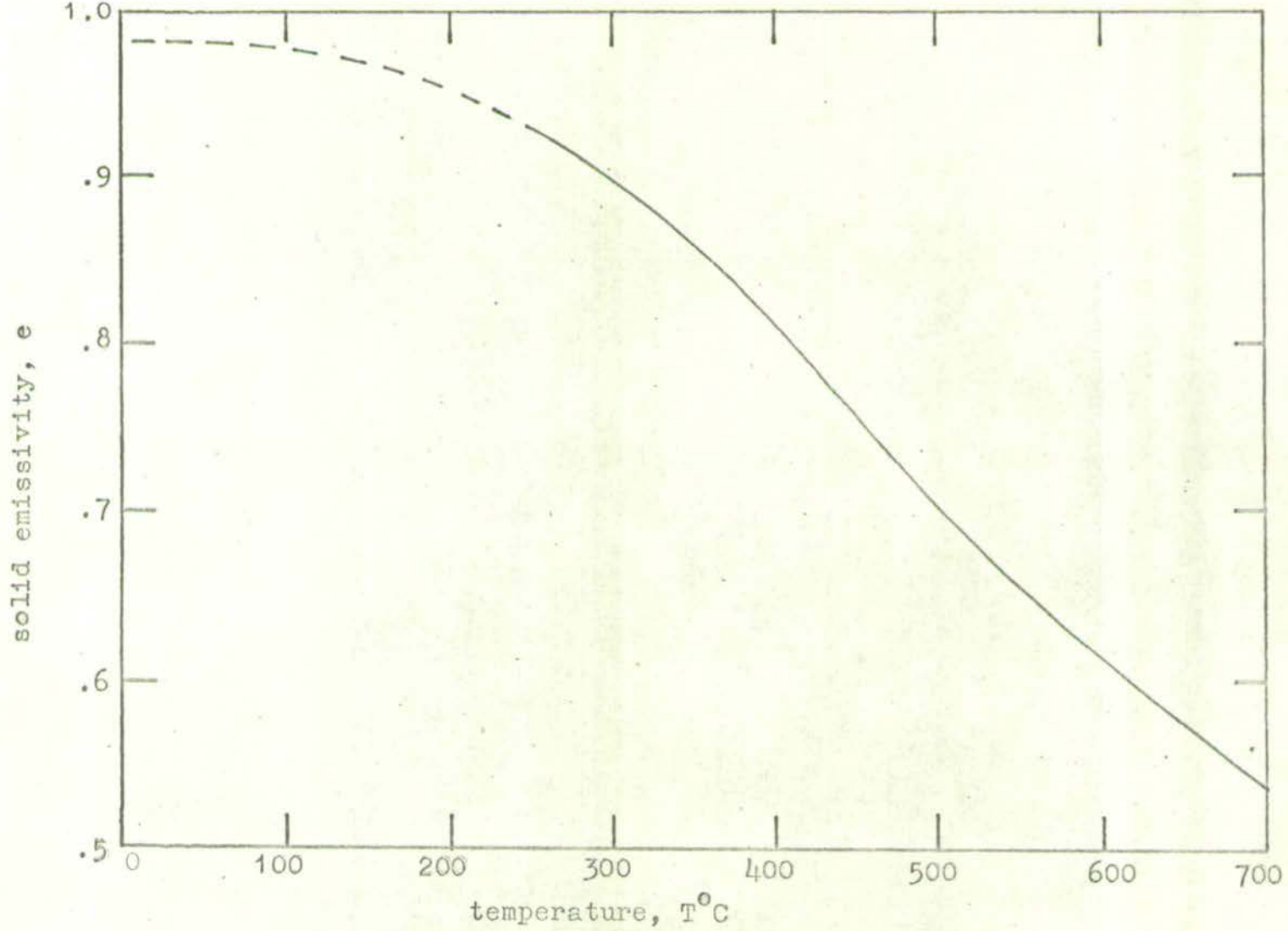

FIG. 6.4 EMISSIVITY OF SOLID PARTICLE MATERIAL (Pirani (1939))

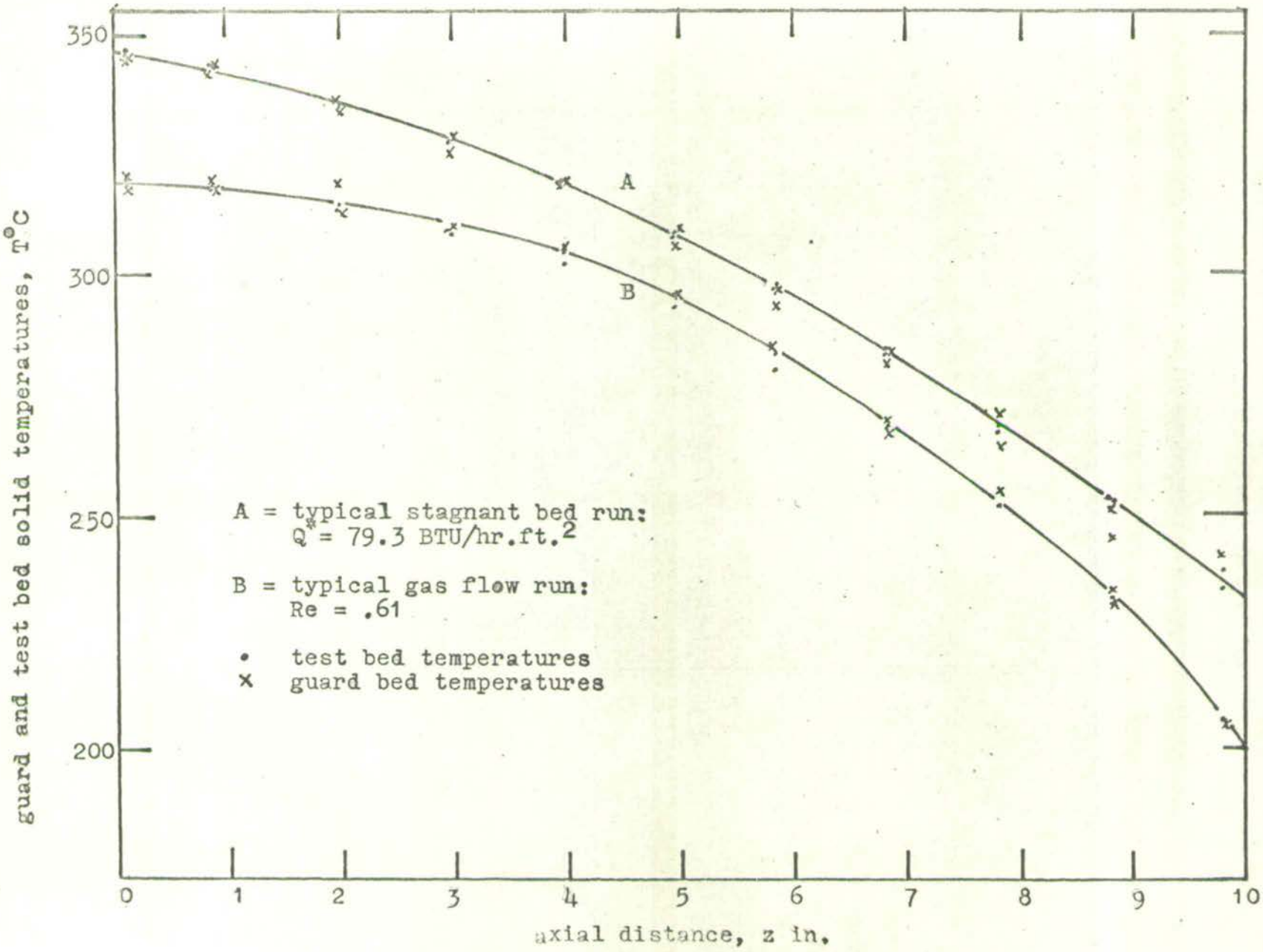

FIG. 5.5 STAGNANT BED TEMPERATURE PROFILES (TYPICAL) IN GUARD BED AND TEST BED

run by drawing a smooth curve through the test bed temperature readings. These profiles were reproducible to within 2% as shown in dimensionless form in Fig. 6.6. Experience of the effect of heater settings and guard-test bed temperature differences indicated that the correct adiabatic dimensionless profiles were obtained to within 5% error.

The experimental temperature profiles obtained using the refractory brick heat flow meter are given in Fig. 6.7. These covered a range of bed hot-face temperatures of 67 - 657°C. The steeper profiles obtained without the brick heat flow meter are given in Fig. 6.8. In these runs the cold end of the bed lost heat either to the atmosphere or to the gas temperature meter. The range of bed hot face temperatures was 74 - 778°C.

6.2.2. Heat Flow Rates

The refractory brick heat flow meter temperature profile is shown for a typical stagnant bed run in Fig. 6.9. Heat flow can be considered as solely axial since the profile is linear and the guard brick temperature readings are close to the test brick readings. Thus the axial heat flow rate per unit area, Q^*, is given by the Fourier equation as

$$Q^* = k_{br}\, dT_{br}/dz_{br} \qquad .....(6.1)$$

The value of the brick thermal conductivity, k_{br}, (Haigh (1965)) was taken from Fig. 6.10 at the mean brick temperature. The brick temperature gradient, dT_{br}/dz_{br} was taken as equal to the slope of the least squares straight line through the brick temperature readings plotted against the axial distance along the brick as in Fig. 6.9. It was

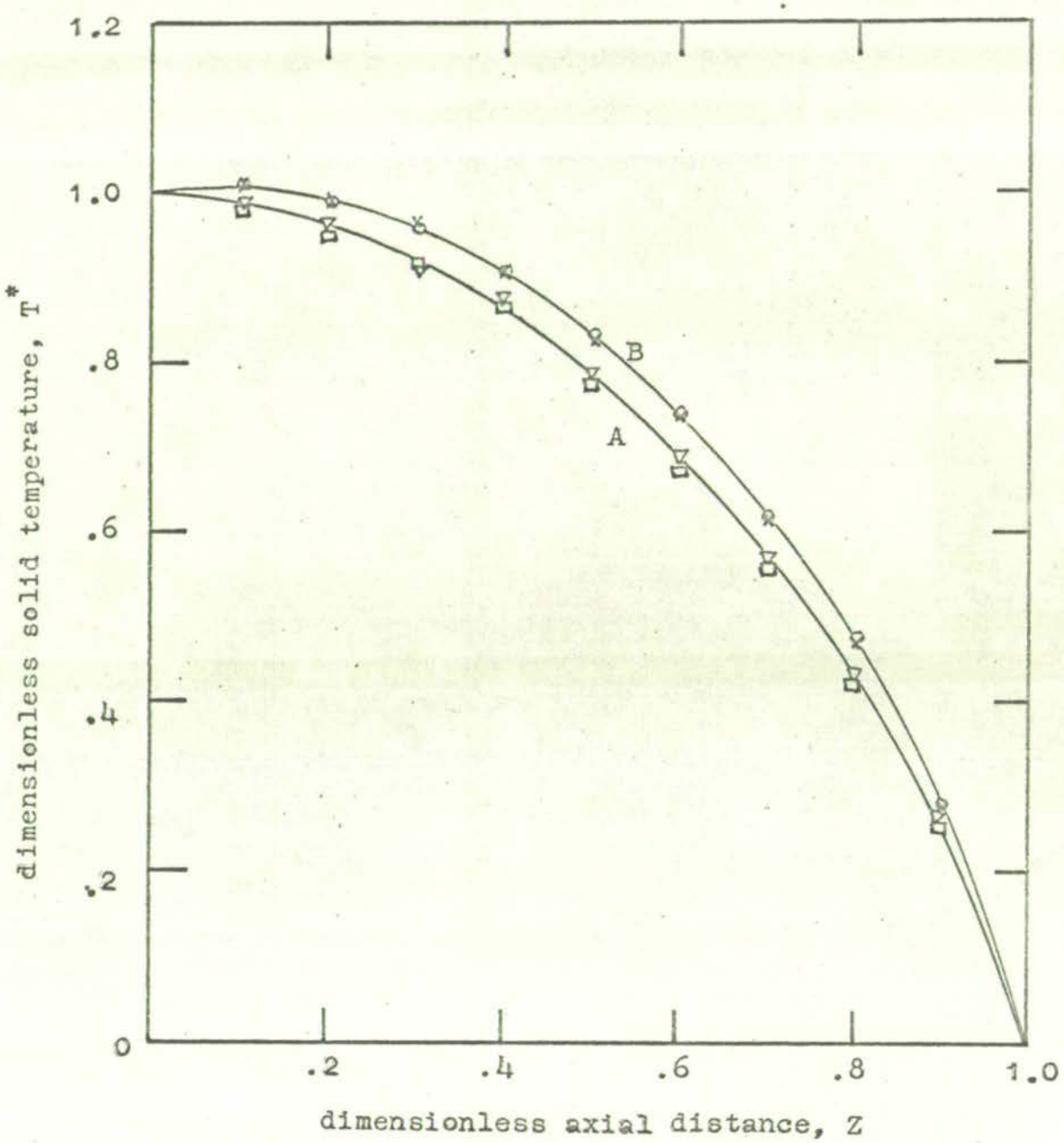

FIG. 6.6 REPRODUCIBILITY OF SOLID TEMPERATURE PROFILES

A = typical stagnant bed profile: ▽ , different runs for T_o=650.6°C, T_m=141.8°C.

B = typical gas flow profile: ⊙ Re = .584, T_o= 324°C, T_m= 122°C,

× Re = .612, T_o= 316.9°C, T_m= 120°C.

FIG. 6.7 STAGNANT BED TEMPERATURE PROFILES (WITH HEAT FLOW METER)

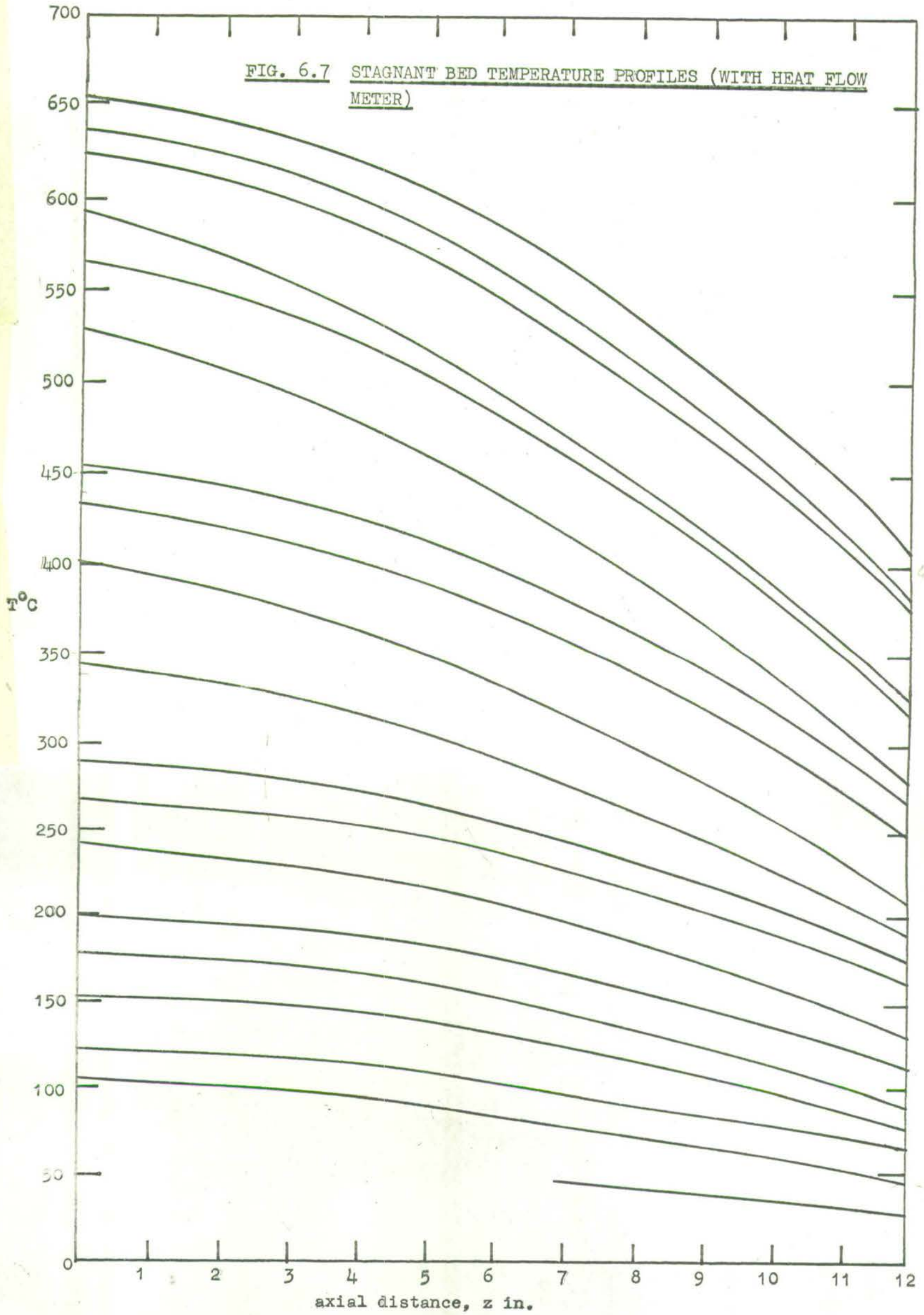

FIG. 6.8 STAGNANT BED TEMPERATURE PROFILES (WITHOUT HEAT FLOW METER

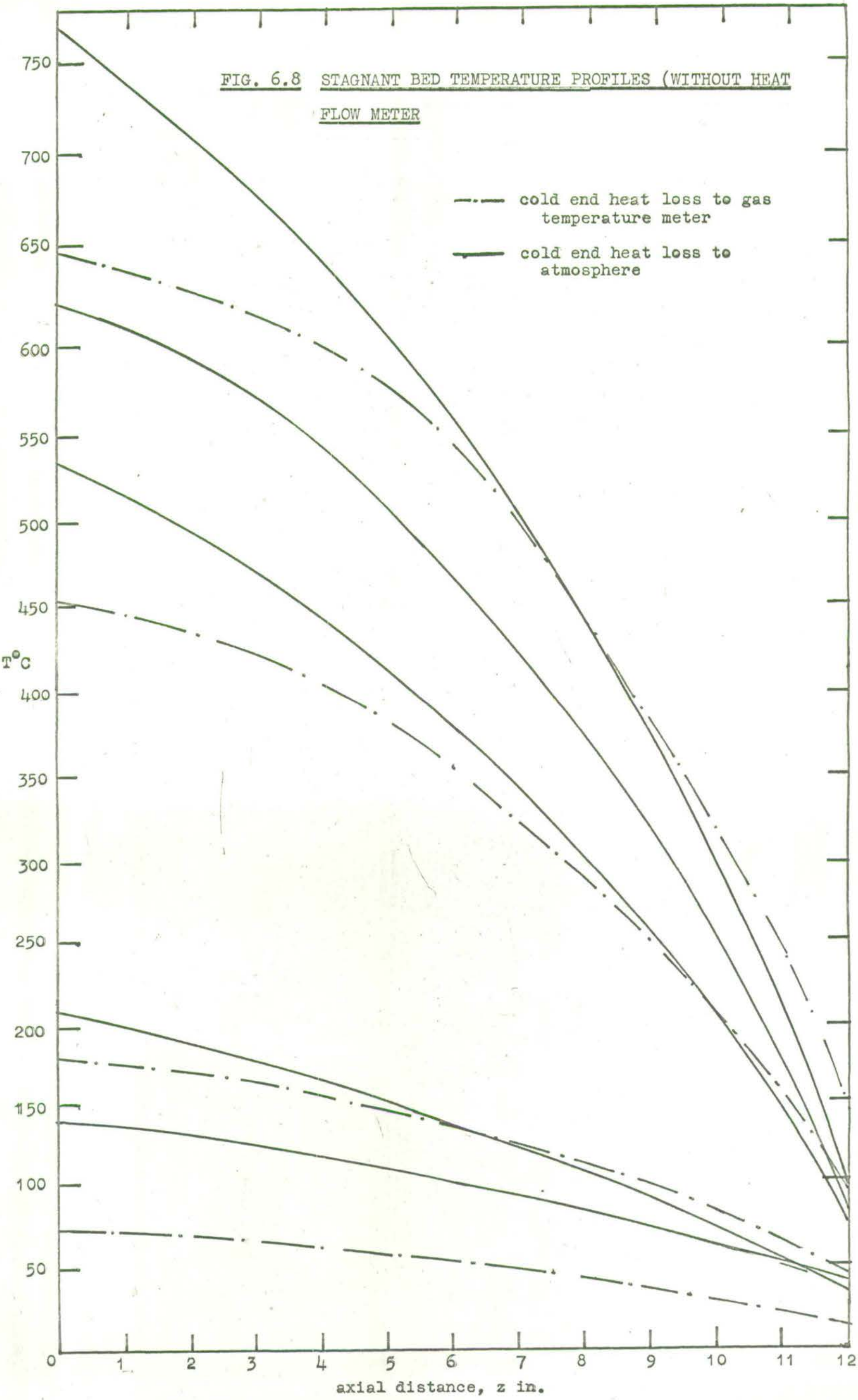

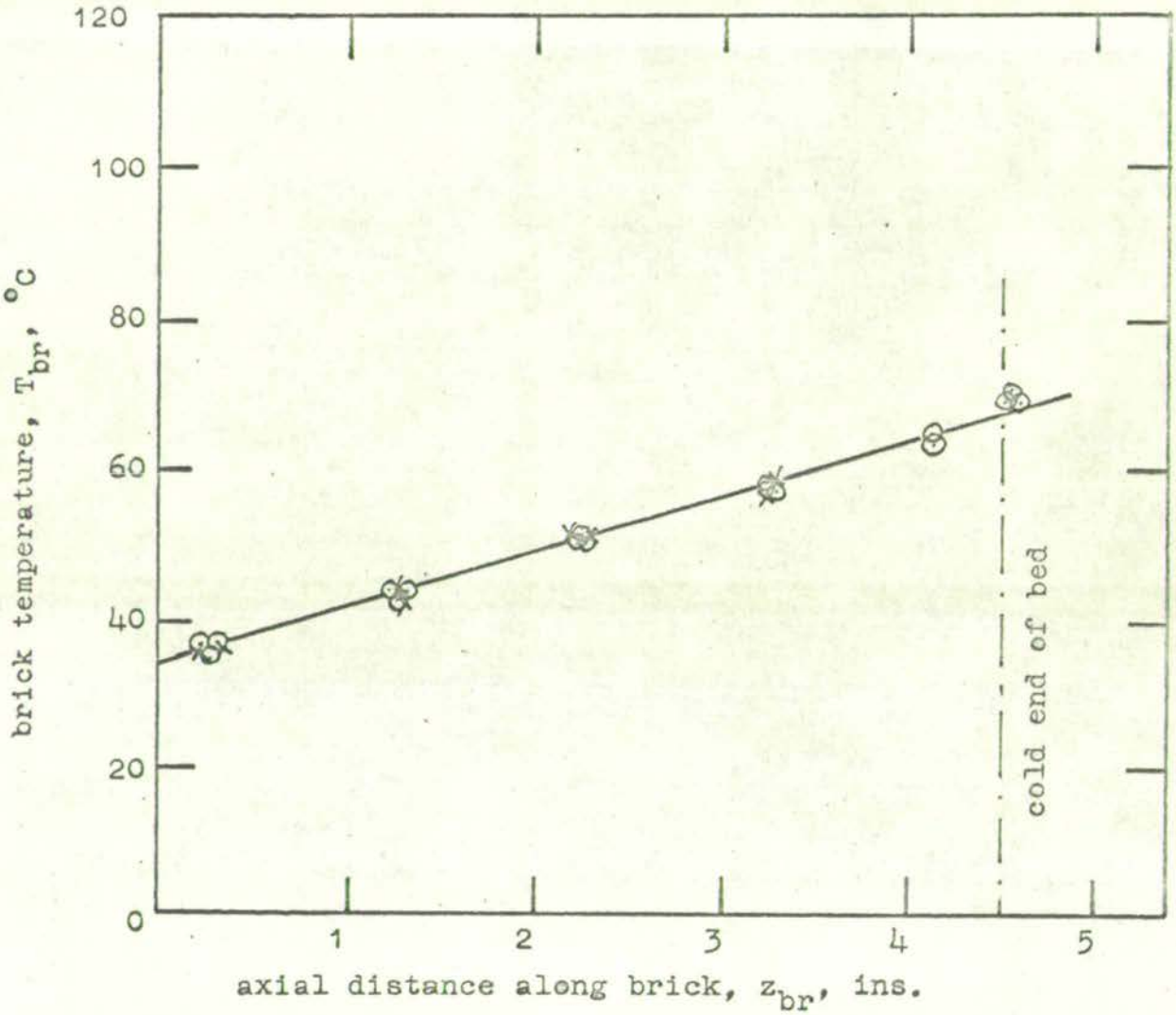

FIG. 6.9 TYPICAL REFRACTORY BRICK HEAT FLOW METER TEMPERATURE PROFILE

$Q^* = 20.0$ BTU/hr.ft.^{2}

⊙ test brick temperatures

× guard brick temperatures

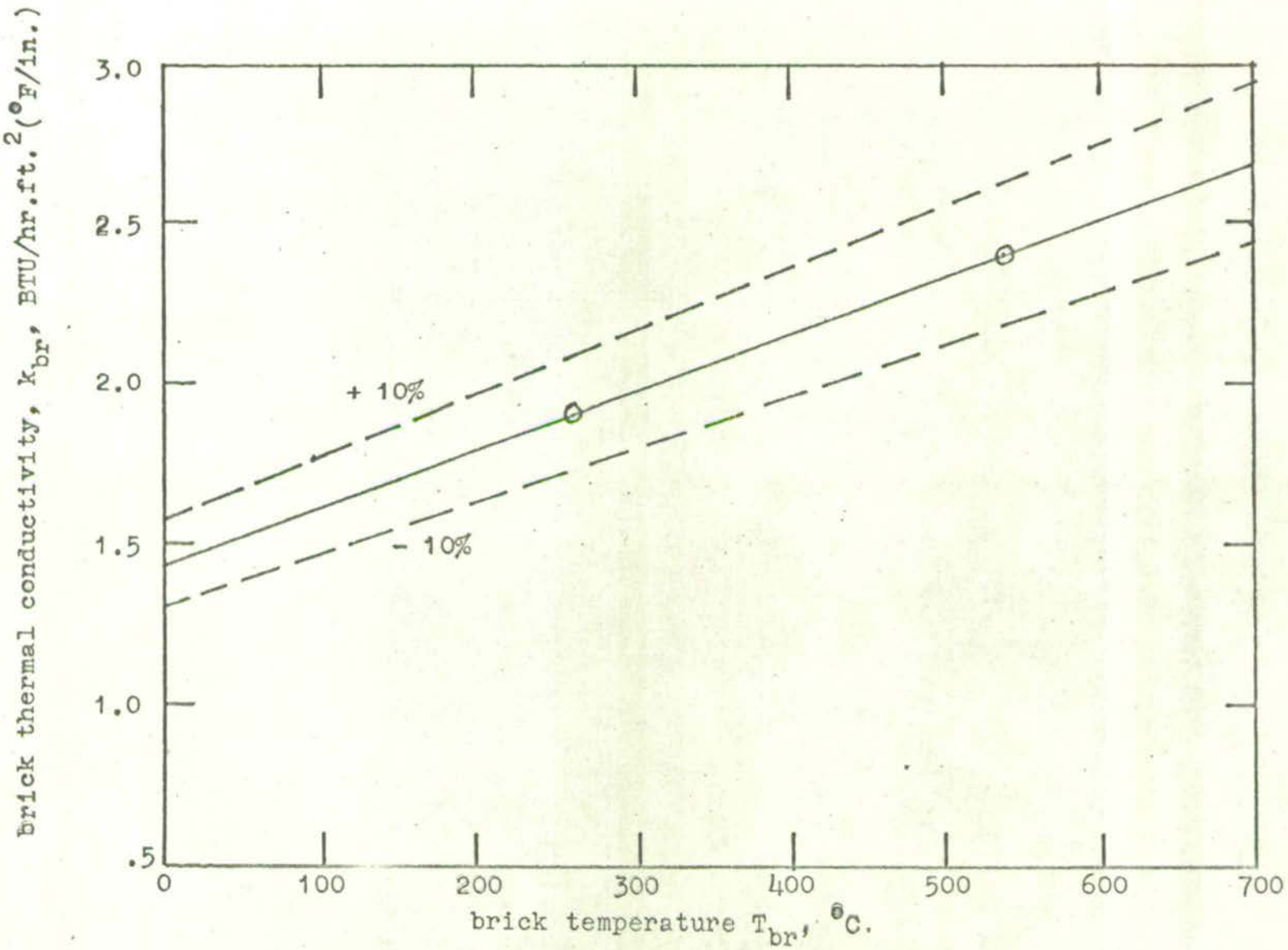

FIG. 6.10 THERMAL CONDUCTIVITY OF REFRACTORY BRICK (MORGANITE M.I. 28)

Data of Haigh (1965) give $k_{br} = 1.43 + .0018T_{br}(\pm 10\%)$.
Higher temperature data points lie on the line shown on the graph.

assumed that the uncertainty in z_{br} was insignificant compared with the uncertainty in T_{br}. Thus it follows that

$$\frac{dT_{br}}{dz_{br}} = \frac{\sum^{N} T_{br}\, z_{br} - (\sum^{N} T_{br})(\sum^{N} z_{br})/N}{\sum^{N} z_{br}^2 - (\sum^{N} z_{br})^2 /N} \qquad \ldots(6.2)$$

where N is the number of brick temperature readings for a given run.

Fig. 6.11 shows the values of Q^* obtained from equations 6.1 and 6.2 plotted against the hot face temperature, T_o. The effect of radiation is apparent at the higher temperatures where the curve becomes non linear.

6.2.3. Overall Effective Thermal Conductivity

The overall effective thermal conductivity of the bed, k_{OV}, may be defined as the thermal conductivity value which gives the overall temperature drop, $T_o - T_m$, for a heat flow rate per unit area, Q^*. Thus from the Fourier equation it follows that

$$k_{OV} = \frac{Q^* L}{(T_o - T_m)} \qquad \ldots.(6.3)$$

The value of k_{OV} includes any end effects in the bed (for example radiation from the supporting hot face plate) and averages out the variation in local thermal conductivity with the temperature at each axial point along the bed.

Fig. 6.12 shows the values of k_{OV} obtained from equation

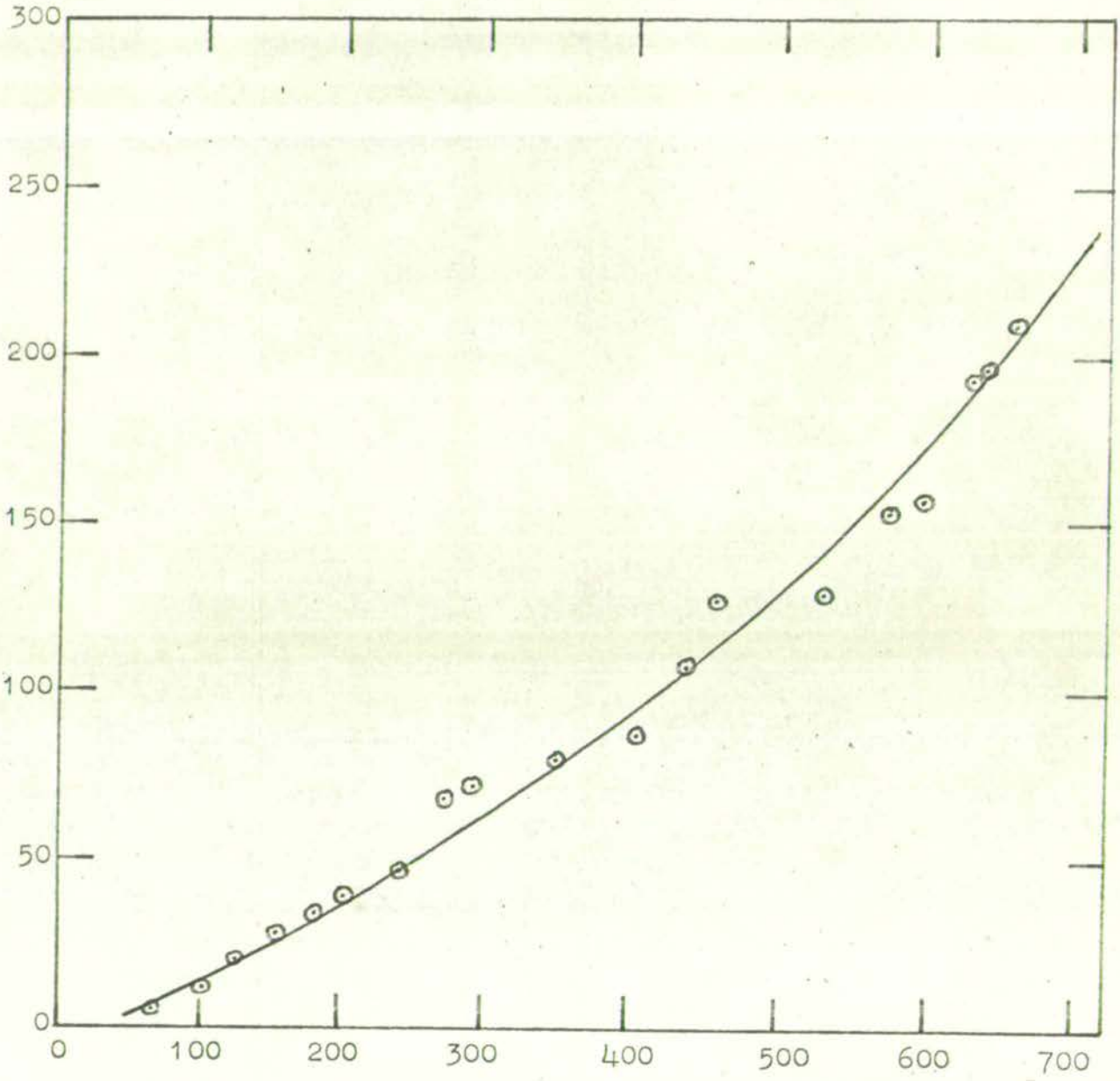

FIG. 6.11. STAGNANT BED AXIAL HEAT FLOW RATES

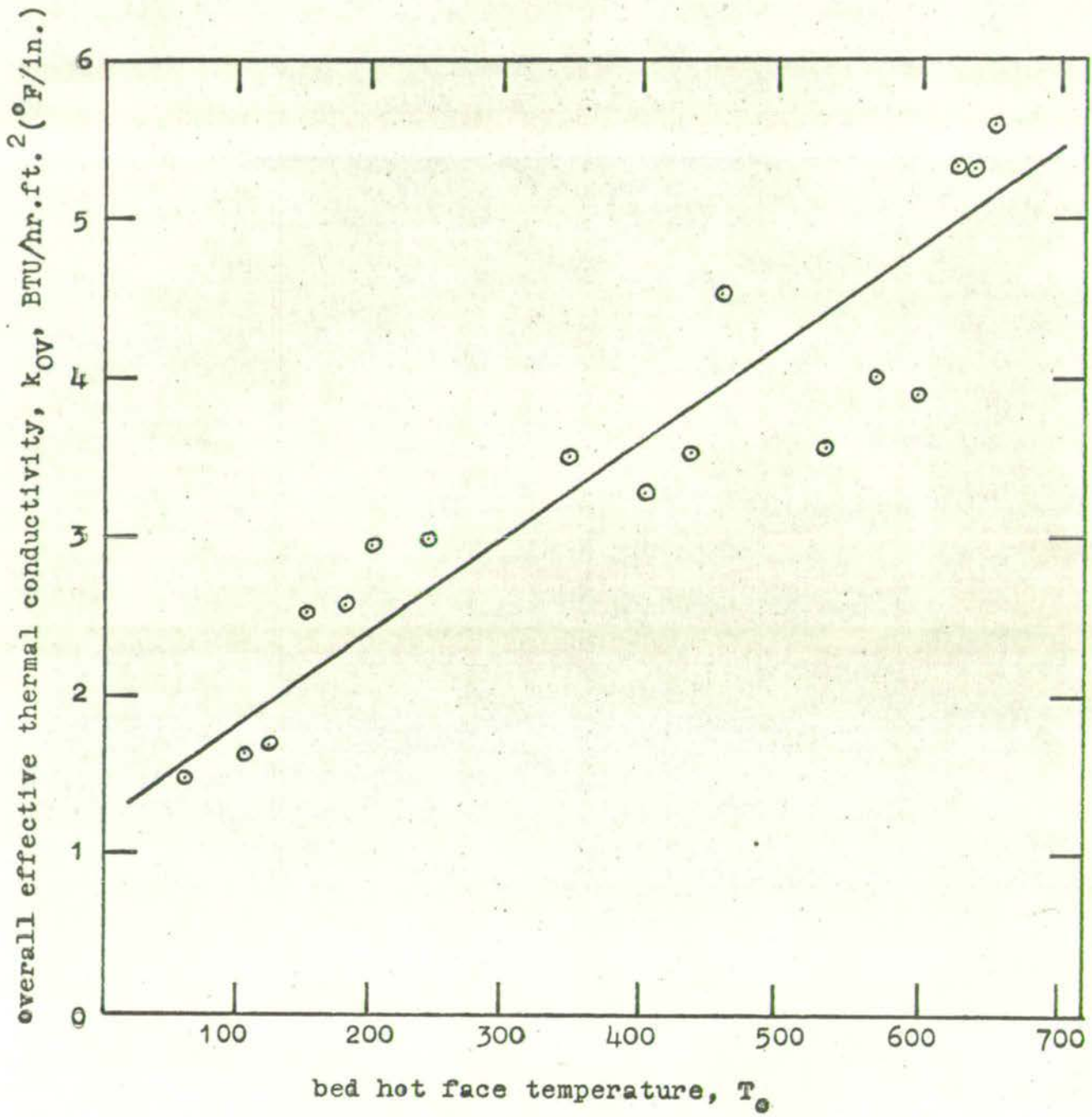

FIG. 6.12 OVERALL EFFECTIVE THERMAL CONDUCTIVITY OF STAGNANT BED

6.3 using the values of Q^* given by the points on Fig. 6.11 and the values of $T_o - T_m$ shown on Fig. 6.7. The value of the overall conductivity increases with temperature as would be expected.

6.2.4. Local Effective Thermal Conductivity

The local effective thermal conductivity of the stagnant bed, k_{eo}, is defined as the thermal conductivity value which gives the measured local solid temperature gradient, dT/dz for a heat flow rate, Q^*.

Therefore $k_{eo} = Q^*/(dT/dz)$ ....(6.4)

The local temperature gradients were measured graphically after plotting the profiles given in Fig. 6.7. and 6.8 on large scale graph paper. To determine k_{eo} at a given local bed temperature the temperature gradients, dT/dz, obtained at that temperature in the various runs were plotted against Q^* as shown in Fig. 6.13. For a typical temperature level, the linearity of this plot shows that there is apparently no effect of heat flow rate on the local effective thermal conductivity over the temperature range studied. Thus k_{eo} was evaluated from equation 6.4 as the inverse of the slope of the least squares line through the origin for the above plot. It was assumed that the uncertainty in Q^* was negligible compared with the uncertainty in $\frac{dT}{dz}$. Thus it follows that

$$k_{eo} = \frac{\sum^{N} Q^{*2}}{\sum^{N} Q^{*}\left(\frac{dT}{dz}\right)} \qquad \ldots.(6.5)$$

where N is the number of temperature gradient measurements

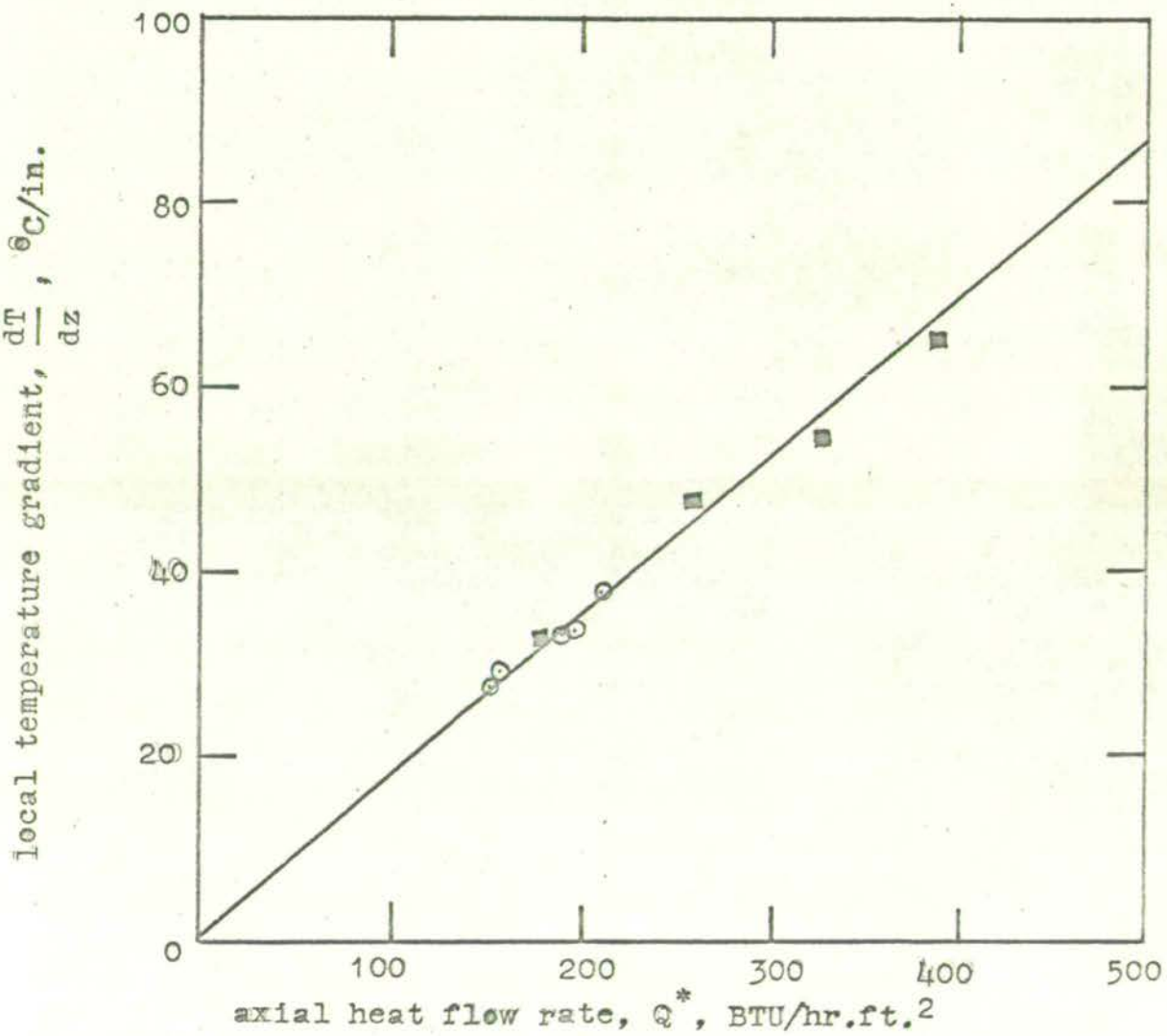

FIG. 6.13 TYPICAL LOCAL TEMPERATURE GRADIENTS FOR STAGNANT BED

T = 414.3°C, k_{e0} = 3.18 BTU/hr.ft.²(°F/in.)

⊙ Q* measured directly

■ Q* measured indirectly

at a given local bed temperature.

To include the temperature gradient data obtained from Fig. 6.8 it was necessary to determine the heat flow rates Q_2^* for these runs indirectly. This was done by comparison of the corresponding temperature gradients, $(\frac{dT}{dz})_2$ of these runs with the gradients, $(\frac{dT}{dz})_1$, of the runs with directly measured heat flows, Q_1^*, at the same temperature. Thus from the Fourier equation

$$k_{eo} = \frac{Q_1^*}{(\frac{dT}{dz})_1} = \frac{Q_2^*}{(\frac{dT}{dz})_2} \qquad \ldots\ldots(6.6)$$

The value of Q_2^* at a given temperature was obtained from the average of such comparisons with N_1 directly measured heat flow runs and these Q_2^* values were then averaged over N_2 different temperature levels so that

$$Q_2^* = \frac{\sum^{N_1 N_2} \left[\frac{Q_1^*}{(\frac{dT}{dz})_1} \quad (\frac{dT}{dz})_2 \right]}{N_1 N_2} \qquad \ldots\ldots(6.7)$$

The values of the local effective thermal conductivity k_{eo}, based on equation 6.5 using all the temperature gradient measurements described above are given in Curve A of Fig. 6.14. The effect of the radiation mechanisms is apparent from the significant non-linearity of the curve above about 200°C.

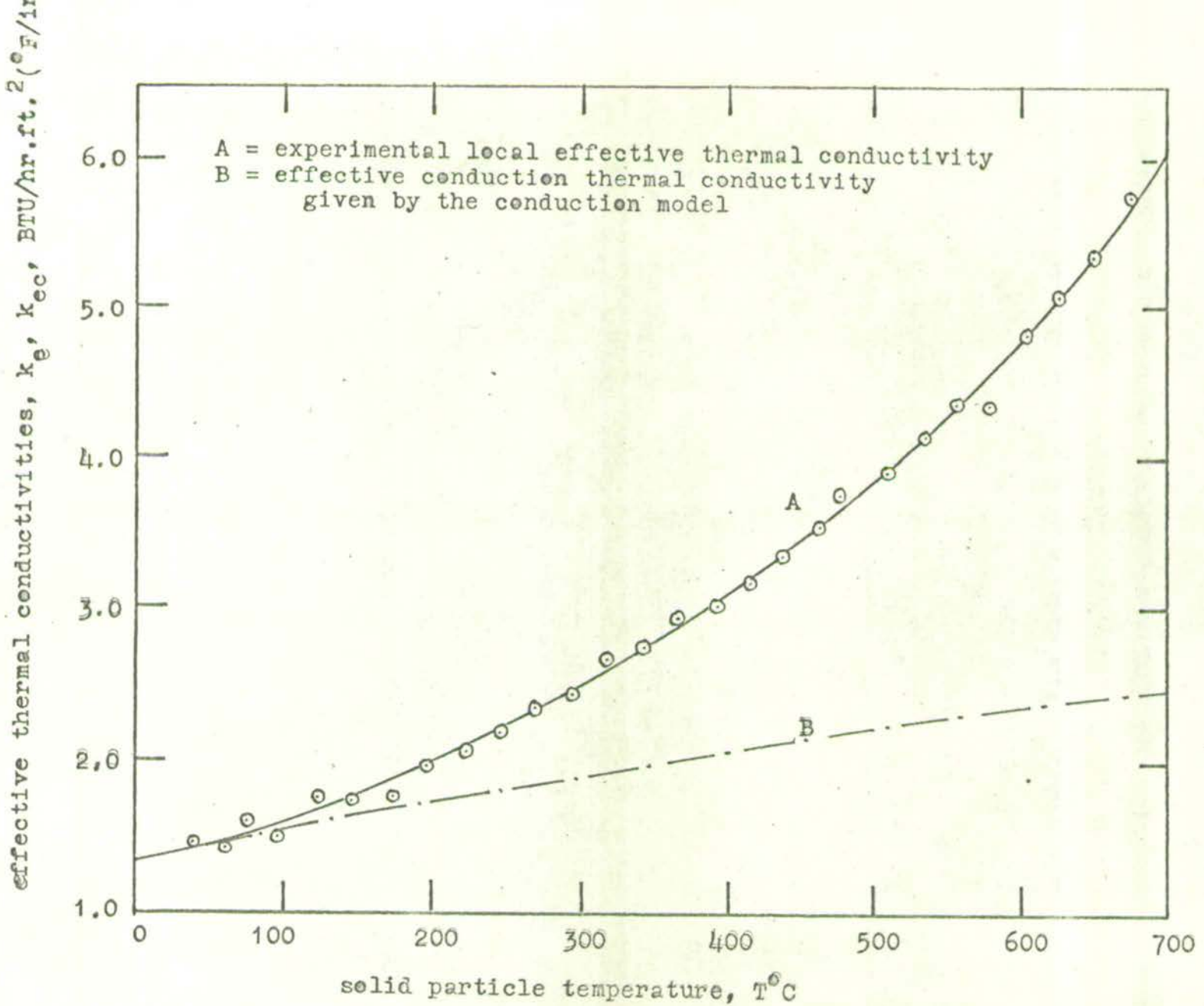

FIG. 6.14 EXPERIMENTAL AND CONDUCTION MODEL EFFECTIVE THERMAL CONDUCTIVITIES FOR THE STAGNANT BED

6.3. ANALYSIS OF HEAT TRANSFER MECHANISMS FROM STAGNANT BED RESULTS

6.3.1. Conduction Mechanisms for the Present Experimental Results

The conduction model (4.1) was used to evaluate the contributions of the conduction mechanisms from the experimental stagnant bed results and to predict the conduction effective thermal conductivity at any temperature.

It was assumed that at 0°C no radiation effects contributed to the effective thermal conductivity of the bed so that this would be completely predicted by the conduction model. Fig. 6.14, gives the value of the effective thermal conductivity at 0°C as 1.34 BTU/hr ft.^{2} (°F/in.) which corresponds to an effective conduction thermal conductivity ratio relative to the gas, Y_C, of 8.02. This value was used to calculate the contact point area, ε_{A3}, from equation 4.32 using the model parameter values given in Table 6.1. From equation 4.14 these parameters give the dependence of the effective conduction thermal conductivity ratio, Y_C, on the solid-gas thermal conductivity ratio, X, as

$$Y_C = .3076 + \frac{1}{\frac{1.248}{X} + \frac{.1355}{.6823 + .01011X}} \quad \ldots\ldots(6.8)$$

Substituting values of X from Fig. 6.3 into equation 6.8 gives the variation of Y_C with temperature shown in Fig. 6.15 or in terms of k_{ec} in Fig. 6.14 (curve B).

Table 6.2 gives the relative contributions of the four conduction mechanisms to conduction heat transfer in the experimental system. The contributions have been evaluated

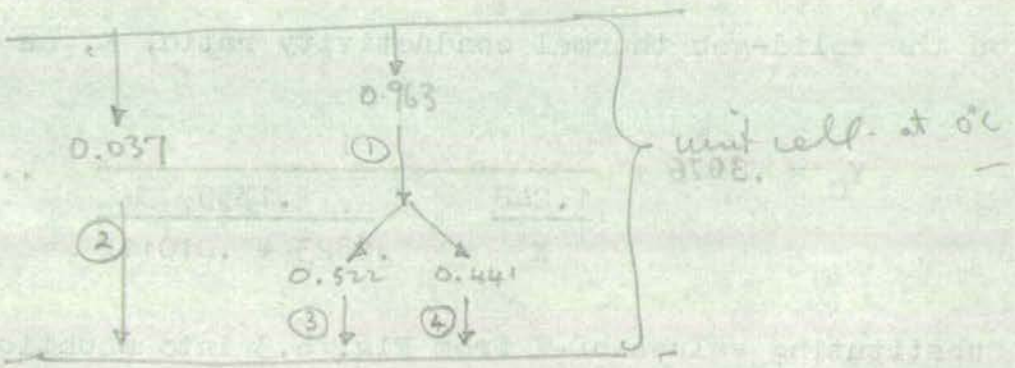
0.963
0.037
①
unit cell at 0°C.
②
0.522
0.441
③
④

TABLE 6.1 CONDUCTION MODEL PARAMETERS FOR THE EXPERIMENTAL SYSTEM

Parameter	Value	Determining Equation
n	6.714	4.17
θ_{PR}	$42^{\circ}\ 36'$	4.16
α^*	0.09245	4.23
α	.1355	4.22
ε_{A1}	.3076	4.27
ε_{A2}	.6823	4.28
ε_{A3}	.01011	4.32
θ_P	$3^{\circ}\ 19'$	4.34

TABLE 6.2 RELATIVE CONTRIBUTIONS OF THE CONDUCTION MECHANISMS TO CONDUCTIVE HEAT TRANSFER IN THE EXPERIMENTAL SYSTEM

Mechanism	Fraction of total conductive heat flow through the mechanism path			
		T=0°C	T=300°C	T=700°C
1. Solid series path	$1 - \frac{\varepsilon}{Y_C}$	.963	.951	.943
2. Gas parallel path	$\frac{\varepsilon}{Y_C}$	.037	.049	.057
3. Gas series path	$(1 - \frac{\varepsilon}{Y_C})(\frac{\varepsilon_{A2}}{X\varepsilon_{A3} + \varepsilon_{A2}})$	.522	.682	.692
4. Solid contact point path	$(1 - \frac{\varepsilon}{Y_C})(\frac{X\varepsilon_{A3}}{X\varepsilon_{A3} + \varepsilon_{A2}})$	.441	.268	.251

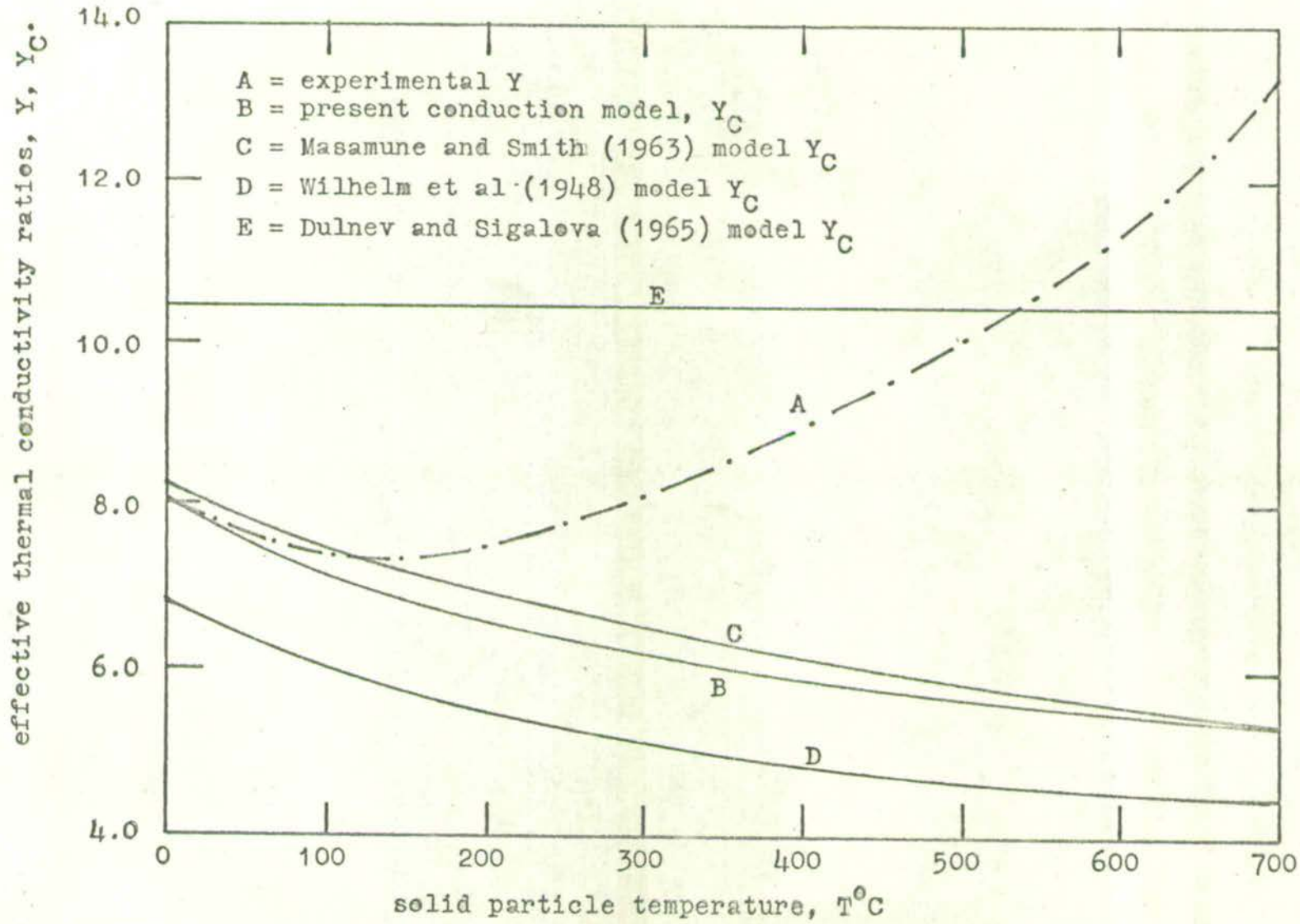

FIG. 6.15 EXPERIMENTAL EFFECTIVE THERMAL CONDUCTIVITY RATIO, Y, AND EFFECTIVE CONDUCTION THERMAL CONDUCTIVITY RATIOS, Y_C GIVEN BY MODELS WHICH INCLUDE CONTACT POINT CONDUCTION

from the fraction of the total heat flow which passes through the various mechanism paths. From Table 6.2 the order of importance of the conduction mechanisms is

(i) mechanism 1 - solid series path

(iii) mechanism 4 - solid contact point path

(ii) mechanism 3 - gas series path

(iv) mechanism 2 - gas parallel path

The latter mechanism accounts for less than 6% of the heat flow. Since X decreases with increasing temperature (Fig. 6.3) the contributions of the solid mechanisms (1 and 4) decrease with increased temperature whereas the contributions of the gas mechanisms (2 and 3) increase. The relative contribution of the solid contact point mechanism is quite significantly dependent on temperature at low temperatures.

Fig. 6.15 compares the Y_C values of the present model with those given by previous models which explicitly include conduction at the contact points. Most previous models do not account for this and their predictions for Y_C cover a wide range of values as shown in Fig. 6.16. For comparison line C shows the prediction of the present model if $\varepsilon_{A3} = 0$

Equation 4.15 gives the predicted vacuum conductivity ratio as

$$Y_C^* = X/14.658 \qquad \ldots.(6.9)$$

At 0^oC this gives $Y_C^* = 3.885$ or $k_{eo}^* = .643$ BTU/hr.ft.^{2}(^oF/in.).

KEY TO FIG. 6.16

A = Yagi and Kunii (1957)

B = Baddour and Yoon (tetrahedral)(1960)

C = present model for $\varepsilon_{A3} = 0$

D = Kunii and Smith (1960)

E = Deissler and Eian (1952)

F = Baddour and Yoon (rectangular)(1960)

G = Schumann and Voss (1934)

H = Gorring and Churchill (1961)

I = Maxwell's equation (1892)

J = series limiting case (minimum) (p41)

K = Godbee and Ziegler (1966)

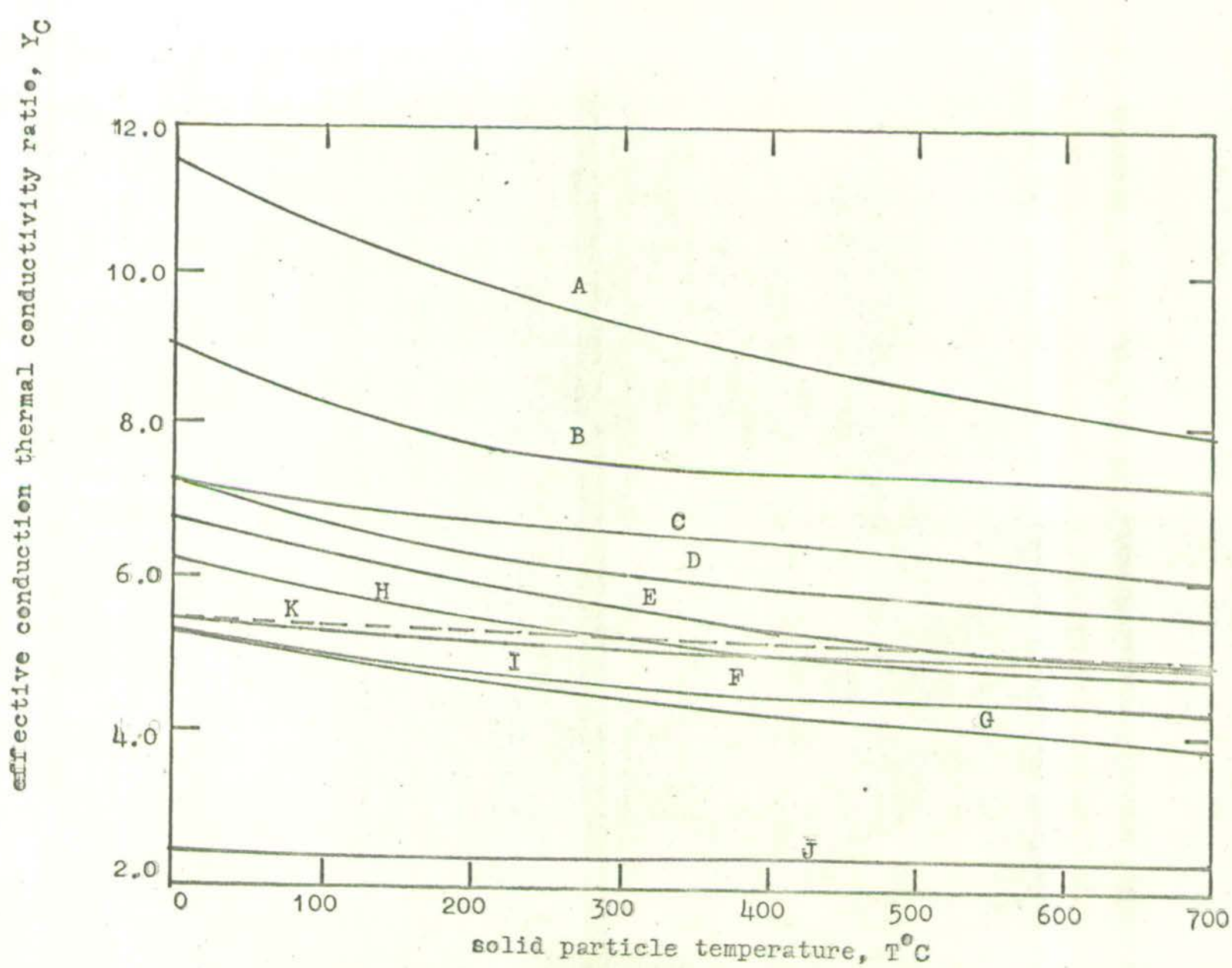

FIG. 6.16 EFFECTIVE CONDUCTION THERMAL CONDUCTIVITY RATIOS, Y_C FOR MODELS WHICH DO NOT INCLUDE CONTACT POINT CONDUCTION

6.3.2. Conduction Mechanisms for the Literature Experimental Results

(i) vacuum thermal conductivity measurements

Vacuum thermal conductivity measurements made in conjunction with atmospheric pressure thermal conductivity measurements enable an independent test of the validity of the model predictions. Table 6.3 shows the literature results available for steady state conductivity measurements under both conditions for packed beds of spheres. The value of the contact area, ε_{A3}, was predicted from the vacuum thermal conductivity measurements by means of equation 4.31 and along with the other conduction model parameters (equations 4.16, 4.17, 4.23) used to predict the model value for the effective thermal conductivity at atmospheric pressure (equation 4.14). Table 6.3 shows that there is good agreement between the model and the experimentally measured values both for low and high solid thermal conductivities. Data measured by unsteady state methods (Schumann and Voss (1934), Woodside and Messmer (1961)) did not show good agreement with either steady state experimental results on the same materials or with the conduction model. This is most probably because the contact between the spheres and the heat transfer surface has a very significant effect on the results for unsteady state methods, particularly under vacuum conditions.

(ii) atmospheric pressure thermal conductivity measurements

The available literature data for the effective thermal conductivity at atmospheric pressure of random packed

TABLE 6.3 COMPARISON OF EXPERIMENTAL MEASUREMENTS AND CONDUCTION MODEL PREDICTIONS FOR EFFECTIVE THERMAL CONDUCTIVITIES OF RANDOM PACKED BEDS OF SPHERES

Reference	System	X	Experimental method	Y_C^* (exptal)	Y (exptal)	Y (model)
Masamune and Smith (1963)	glass spheres $2.9 - 47.0 \times 10^{-3}$ cm.dia. $\epsilon = .38$	38.53	axial steady state	1.913	6.62	6.40
Masamune and Smith (1963)	stainless steel shot 7.1×10^{-3} cm.dia. $\epsilon = .265$	600.0	axial steady state	0.639	9.26	9.36
Kannuluik and Martin (1933)	glass powder $\epsilon = .35$	44.9	radial steady state	1.31	6.62	6.65

beds of spheres was extrapolated to 0°C to eliminate radiation effects and analysed by the conduction model using the method employed for the present experimental results (6.3.1).

Fig. 6.18 shows the contact area angles, θ_p which determine the contact point heat transfer, as obtained by such an analysis. The scatter of the data points which cover a voidage range, ε = .38 -.50, and a solid thermal conductivity ratio, X = 4.5 - 8410 indicate the significant effect the surface characteristics and loading of the particles have on this mechanism particularly for lower solid thermal conductivity systems.

6.3.3. Radiation Mechanisms for the Present Experimental Results

(1) radiation parameter, H_r

The conduction-radiation model (4.2) was used to evaluate the radiation mechanisms (5 and 6) from the effective thermal conductivity measurements in the stagnant bed over a temperature range 40 - 700°C. Radiation absorption by the gas (mechanism 7) was ignored since this is negligible for air (3.4.3).

Values of the effective thermal conductivity ratio, Y, from Fig. 6.15 and the conduction parameters X, ε_{A1}, ε_{A2}, α, ε_{A3} (from Table 6.1) were substituted into equation 4.41 to obtain the values for the radiation parameter, H_r, shown in Fig. 6.19. The value of H_r increases markedly at the higher temperatures showing the importance of radiation. The radiation parameter H_r may be written in terms of an emissivity factor $\Psi(e)$, a view factor F^*, the cell length βD_p, and the

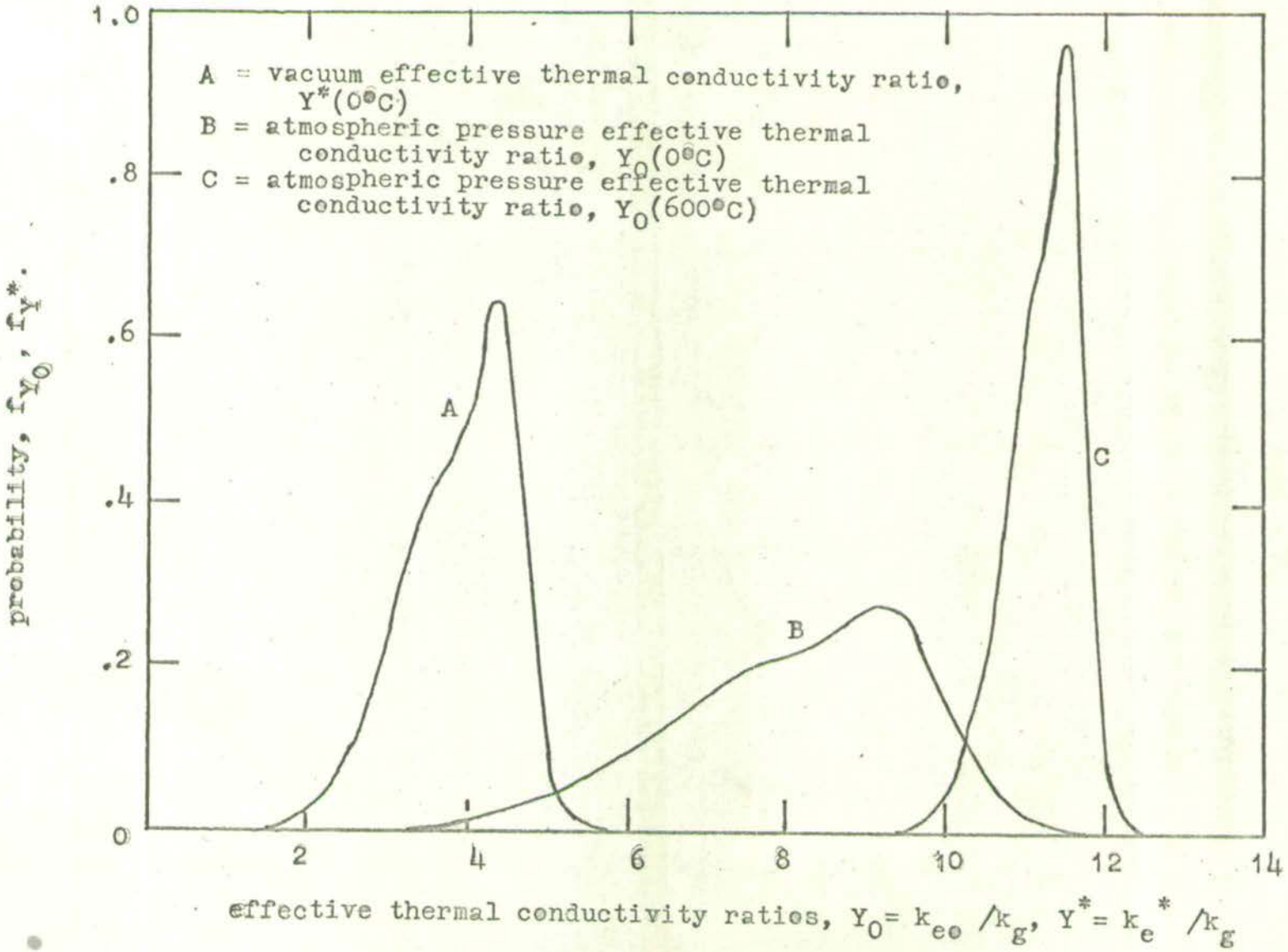

FIG. 6.17 PROBABILITY DISTRIBUTIONS OF EFFECTIVE THERMAL CONDUCTIVITY RATIOS FOR THE EXPERIMENTAL SYSTEM

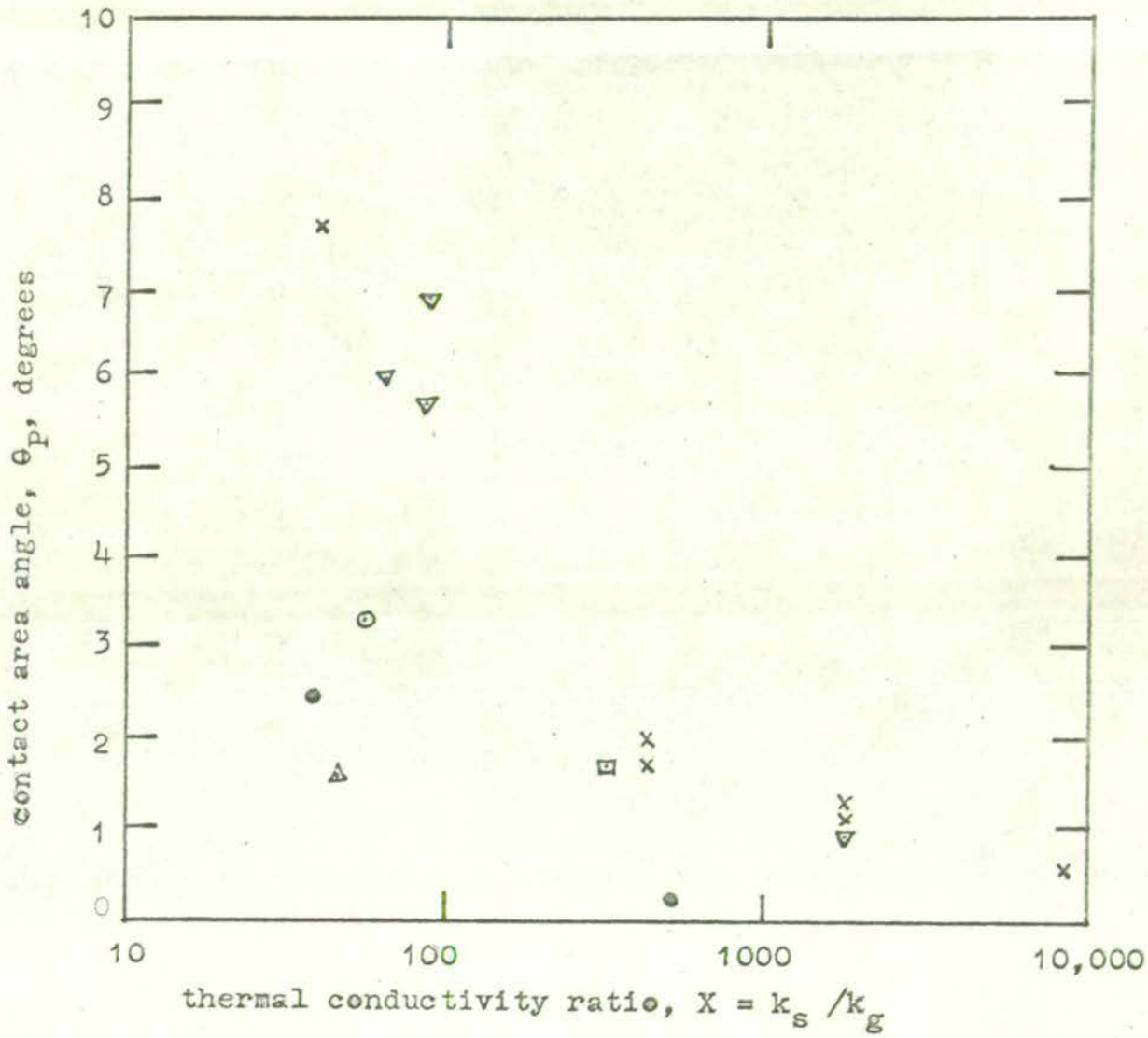

FIG. 6.18 CONTACT AREA ANGLES, θ_p, FOR RANDOM PACKED BEDS OF SPHERES

(ε = .38 - .50)

⊙ present results
⊡ Hill and Wilhelm, (1959)
× Baddour and Yoon (1960)
▽ Yagi and Kunii (1957)
● Masamune and Smith (1963)
△ Kannuluick and Martin (1933)

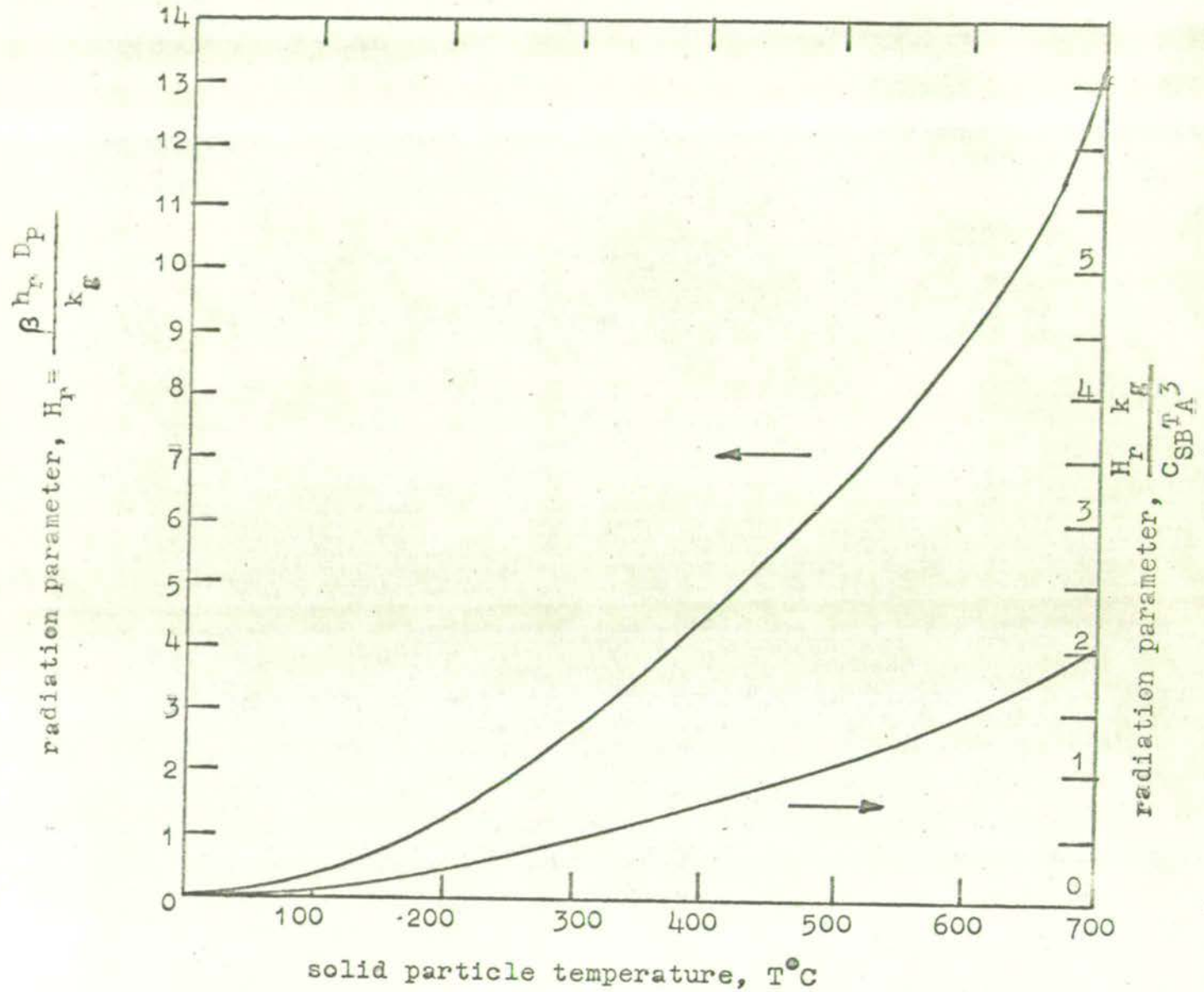

FIG. 6.19 RADIATION PARAMETERS FOR THE STAGNANT BED

absolute temperature T_A as (4.2.2, 3.4.1)

$$H_r = \frac{\beta h_r D_P}{k_g} = \frac{\beta D_P \Psi(e) F^* C_{SB} T_A^3}{k_g} \quad \ldots.(6.10)$$

therefore $$\beta \Psi(e) F^* = \frac{H_r k_g}{C_{SB} T_A^3} \quad \ldots.(6.11)$$

The latter parameter increases with temperature as shown in Fig. 6.19 even although the solid emissivity decreases with temperature Fig. 6.4. This behaviour indicates that radiation scattering (3.4.1) increases the value of the view factor, F^* at increased temperatures.

From equation 4.40 and Table 6.1, the variation of the effective thermal conductivity ratio, Y_0, with temperature is given by

$$Y_0 = .3076(1 + H_r) + \frac{1}{\frac{1.248}{X} + \frac{.1355}{.6823(1 + .1355\, H_r) + .01011X}} \quad \ldots(6.12)$$

where X and H_r are given in Fig. 6.3 and Fig. 6.19 respectively.

The probability distribution of local effective thermal conductivities may be obtained at any temperature from equation 4.40 with the model parameters given in Table 6.1 for ε_{A1}, ε_{A2}, ε_{A3} and α and from the probability distribution of local mean voidage (Fig. A.9)[1] Fig. 6.17 shows the

---

1. Table A.3 gives the relationship between Y_0, Y_0^* and the local mean voidage, $\overline{\varepsilon}$.

estimated thermal conductivity distribution of the experimental system at temperatures of 0°C and 600°C. It is seen that the effect of radiation is to smooth out the variations in local effective thermal conductivity. At 0°C the standard deviation is 19% of the mean effective thermal conductivity ratio compared with 4% at 600°C. Fig. 6.17 also shows the estimated vacuum effective thermal conductivity ratio distribution (based on equation 4.15[1]) at 0°C.

(ii) relative contributions of conduction and radiation mechanisms

Table 6.4 gives the relative contributions of the conduction and radiation mechanisms to heat transfer in the experimental system. As in 6.3.1 the contributions have been evaluated from the fraction of the total heat flow which passes through the various mechanism paths. From Table 6.4 it is seen that the order of importance of the mechanisms is dependent on the temperature. At 700°C where radiation has a significant effect, the order is

(i) mechanism 1 - solid series path conduction

(ii) mechanism 6 - intra-cell radiation

(iii) mechanism 5 - inter-cell radiation

(iv) mechanism 3 - gas series path conduction

(v) mechanism 4 - solid contact point path conduction

(vi) mechanism 2 - gas parallel path

---

1. Table A.3 gives the relationship between Y_0, Y_0^* and the local mean voidage, $\bar{\varepsilon}$.

TABLE 6.4 RELATIVE CONTRIBUTIONS OF THE CONDUCTION AND RADIATION MECHANISMS TO HEAT TRANSFER IN THE EXPERIMENTAL SYSTEM

Mechanism	Fraction of total heat flow through the mechanism path			
		T = 0°C	T = 300°C	T=700°C
1. Solid series path	$\left[1 - \frac{\varepsilon(1 + H_r)}{Y_0}\right]$	.963	.818	.542
2. Gas parallel path	$\frac{\varepsilon}{Y_0}$	.037	.048	.032
3. Gas series path	$\left[1- \frac{\varepsilon(1+ H_r)}{Y_0}\right]\left[\frac{\varepsilon_{A2}}{\varepsilon_{A2}(1+\alpha H_r) + X \varepsilon_{A3}}\right]$	.522	.435	.171
4. Solid contact point path	$\left[1- \frac{\varepsilon(1+H_r)}{Y_0}\right]\left[\frac{X \varepsilon_{A3}}{\varepsilon_{A2}(1+\alpha H_r) + X \varepsilon_{A3}}\right]$	.441	.218	.062
5. Inter-cell radiation	$\left[1- \frac{\varepsilon(1+ H_r)}{Y_0}\right]\left[\frac{\varepsilon_{A2} \alpha H_r}{\varepsilon_{A2}(1+ \alpha H_r) + X \varepsilon_{A3}}\right]$	0	.165	.309
6. Intra-cell radiation	$\frac{\varepsilon H_r}{Y_0}$	0	.134	.426
7. Gas radiation		0	0	0

The latter mechanism accounts for less than 5% of the heat flow at all temperatures.

The relative contribution of mechanism 4 decreases markedly with increased temperature. As expected the contributions of the radiation mechanisms increase relative to the contributions of the conduction mechanisms as the temperature increases. Intra-cell radiation heat transfer increases slightly relative to inter-cell radiation heat transfer as the temperature increases. At 300°C 29.9% of the heat flows through the radiation paths. At 700°C this has increased to 73.5%.

(iii) effective radiation thermal conductivity

Previous workers (e.g. Hill and Wilhelm (1959), Baddour and Yoon (1960)) have evaluated the radiation contribution to packed bed heat transfer in terms of an effective radiation thermal conductivity (3.4.2). This procedure is of doubtful validity due to the interaction between the radiation and conduction mechanisms and is followed here only for the purpose of comparing the present model and experimental results with the models and results of previous workers.

The effective radiation thermal conductivity, k_r (Fig. 6.20) was obtained by subtracting the effective conduction thermal conductivity, k_{ec}, (line B, Fig. 6.14) from the experimental effective thermal conductivity measurements, k_{eo}, (line A, Fig. 6.14). The results are also given relative to the gas thermal conductivity in Fig. 6.21 and relative to the effective conduction conductivity in Fig. 6.22.

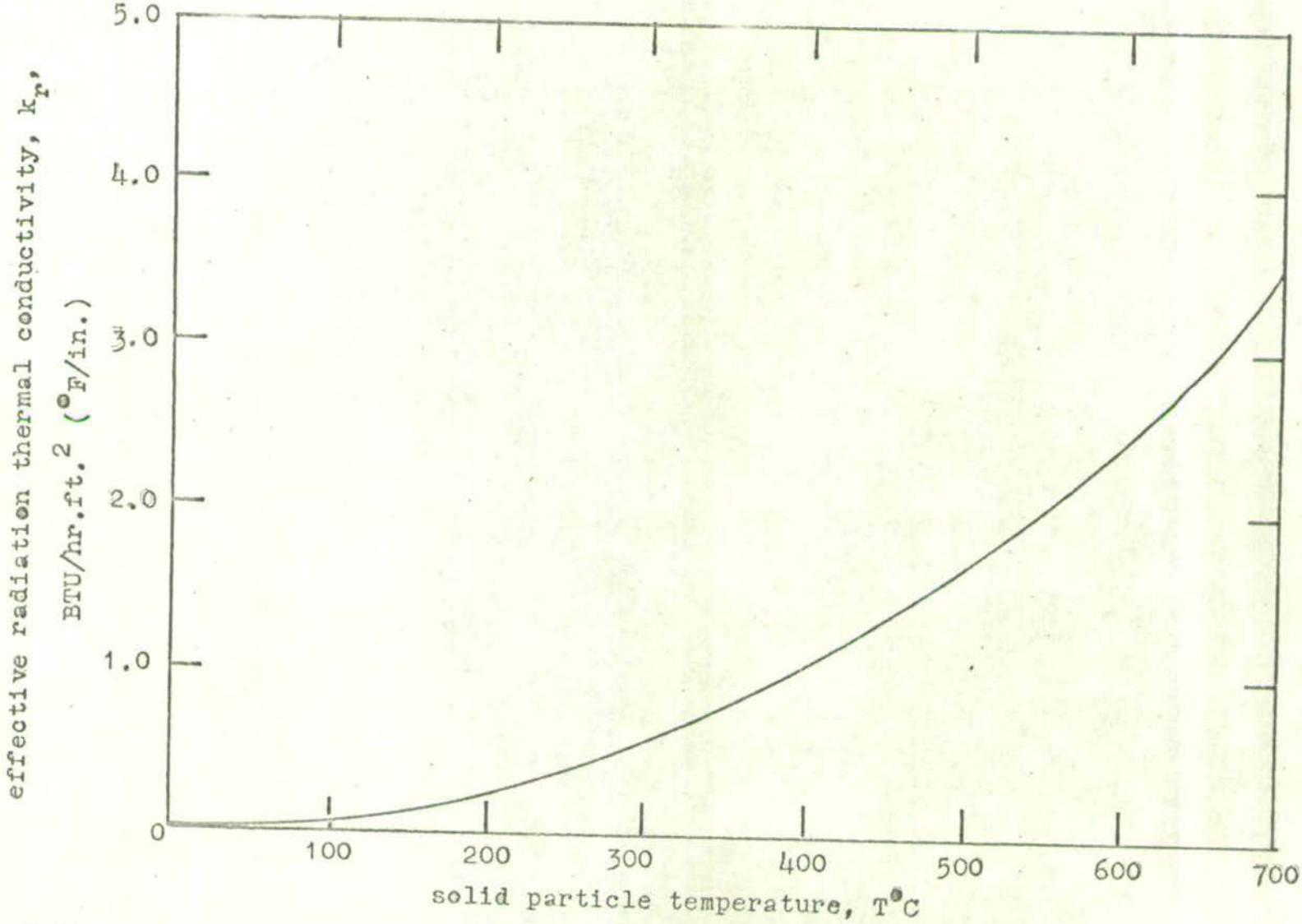

FIG.6.20 EFFECTIVE RADIATION THERMAL CONDUCTIVITY FOR THE STAGNANT BED

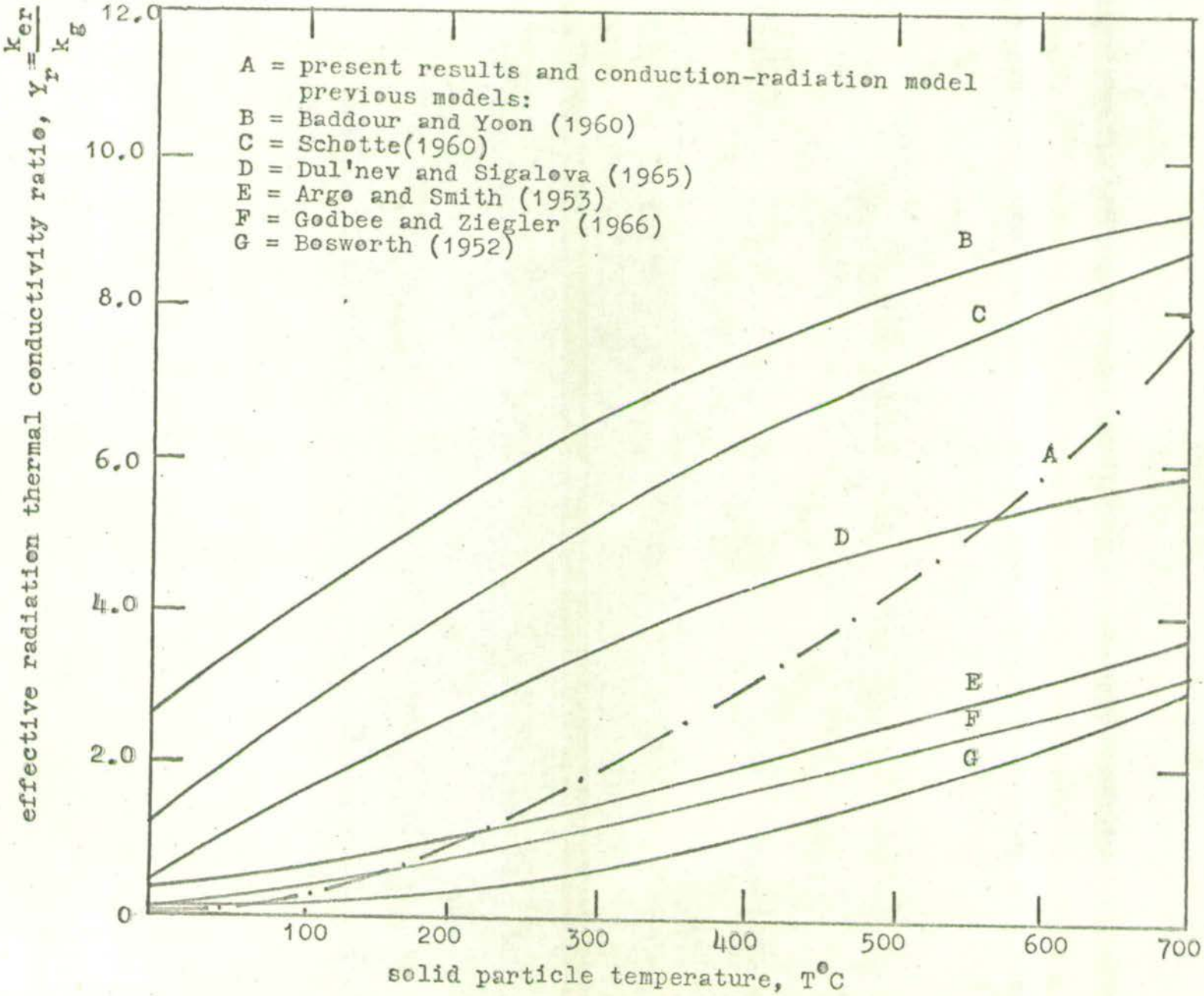

FIG. 6.21 EFFECTIVE RADIATION THERMAL CONDUCTIVITY RATIO FOR THE STAGNANT BED

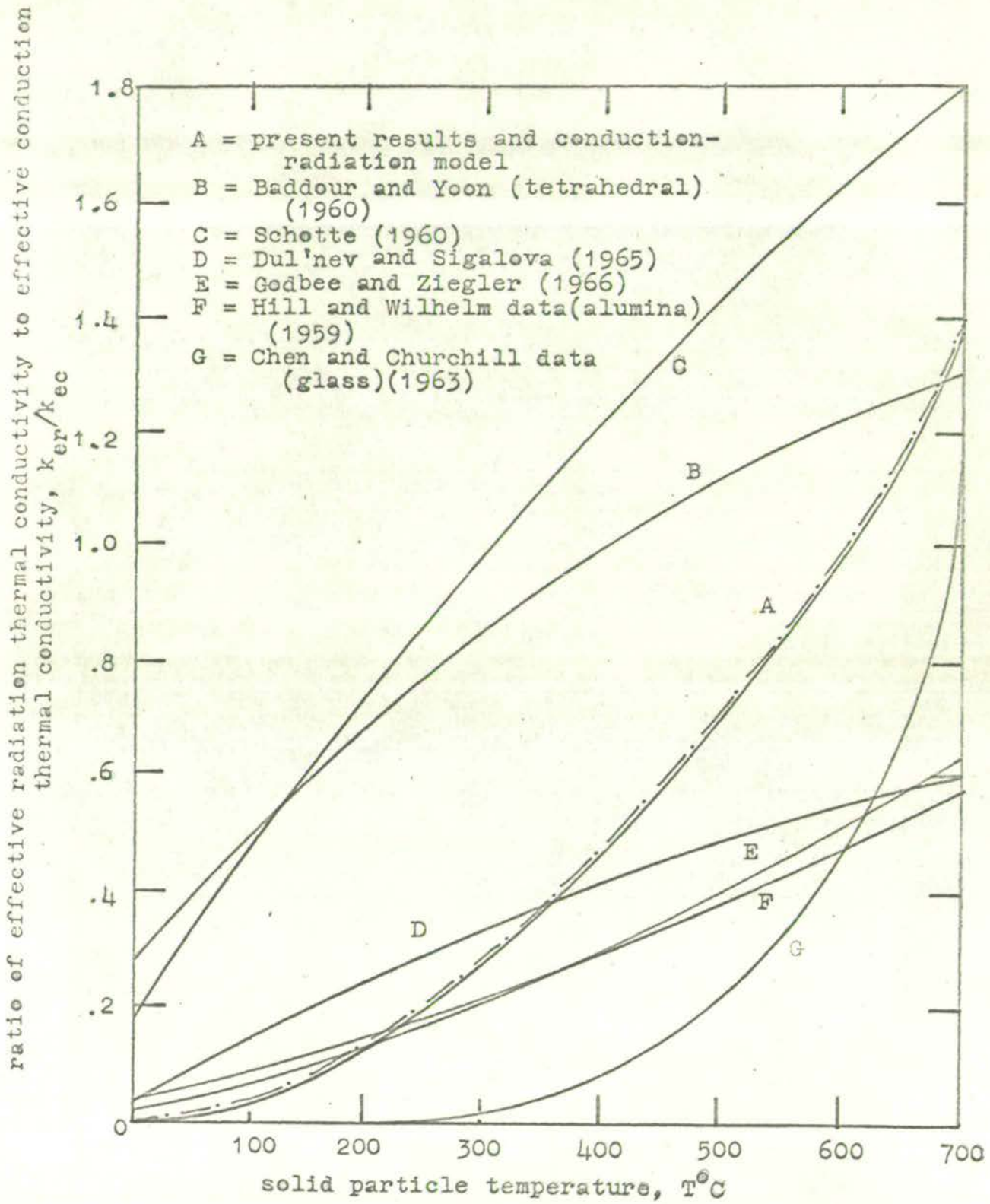

FIG. 6.22 RADIATION HEAT TRANSFER RELATIVE TO CONDUCTION HEAT TRANSFER FOR THE STAGNANT BED

The predictions of previous radiation models (3.4.2.) cover a wide range of values (Fig. 6.21, 6.22) and the present model and experimental results lie near the middle of this range and show the expected increase in radiation as the temperature increases. The radiation models of Chen and Churchill (1963), Glaser (1961), Van der Held (1952) and Hill and Wilhelm (1959) require knowledge of radiation absorption, scattering and transmission parameters which is not available for the material used in the present experiments.

Fig. 6.23 compares the total effective thermal conductivity ratio, Y_o, for the present model and experimental results with the predictions of previous models which add conduction and radiation effective thermal conductivities.

6.3.4. Radiation Mechanisms for the Literature Experimental Results

Fig. 6.24A and 6.24B show the values of the radiation parameter $\frac{H_r k_g}{C_{SB} T_A^3}$ derived by applying the conduction-radiation model to the experimental results available in the literature for the effective thermal conductivities of random packed beds of spheres. The values were obtained by the procedure used for the present experimental results (6.3.3.) and show a similar increasing trend with temperature. Some effect of particle diameter is also apparent in some cases. Extrapolation of the curves indicates that the assumption of negligible radiation at $0^{\circ}C$ is a good one.

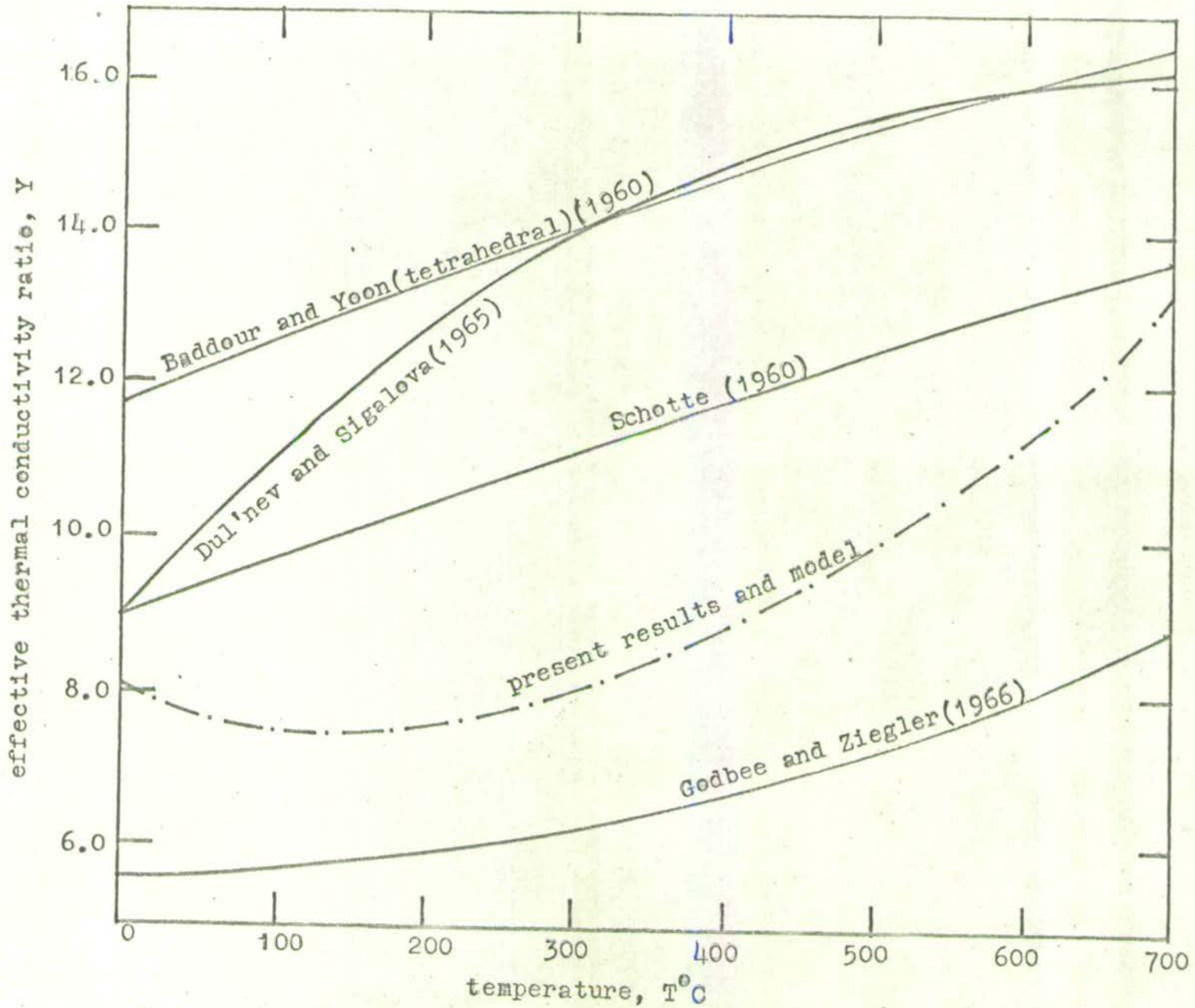

FIG. 6.23 EFFECTIVE THERMAL CONDUCTIVITY FOR THE STAGNANT BED COMPARED WITH MODEL PREDICTIONS

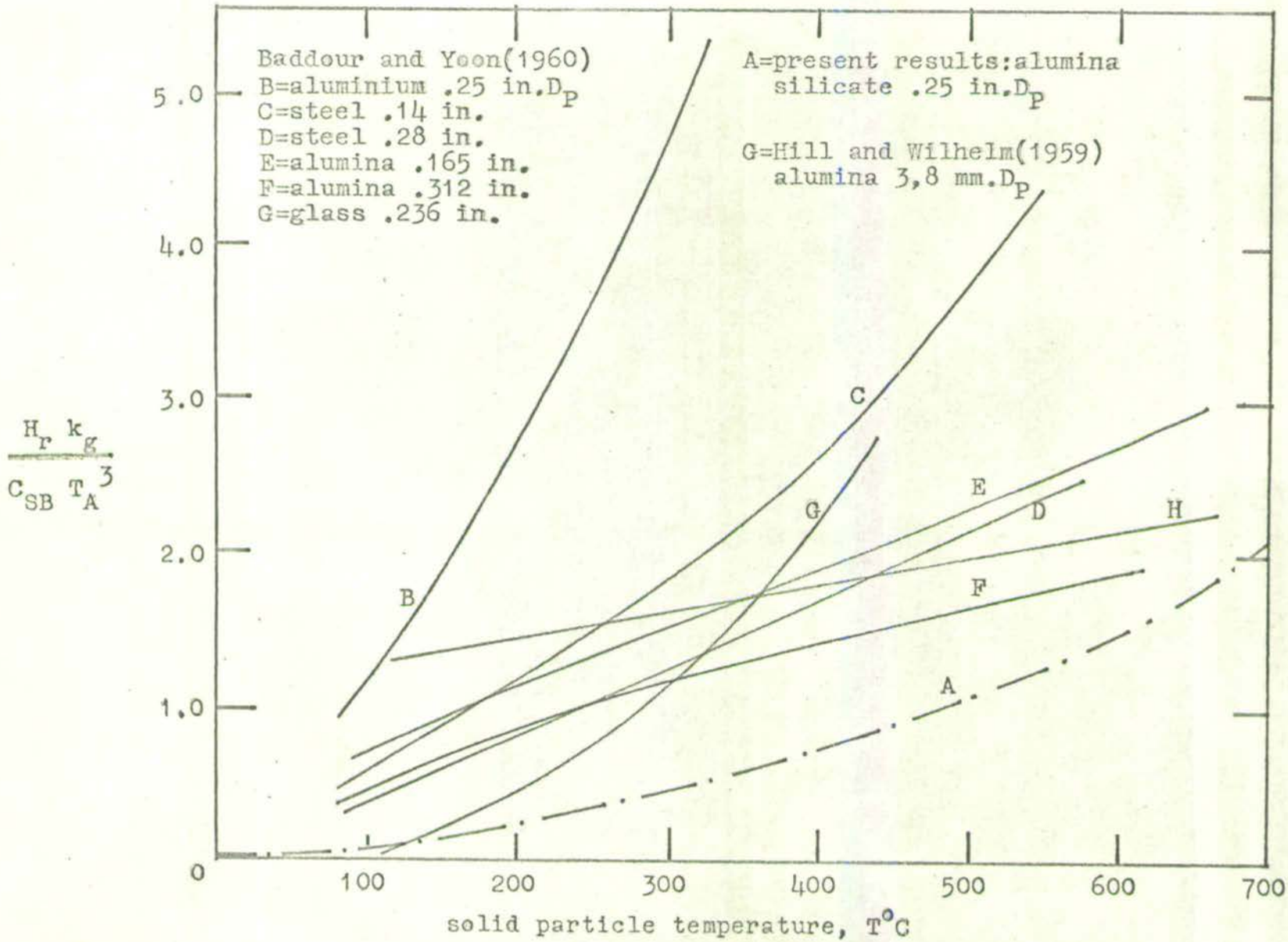

FIG. 6.24A RADIATION PARAMETERS FOR STAGNANT BEDS OF RANDOM PACKED SPHERES

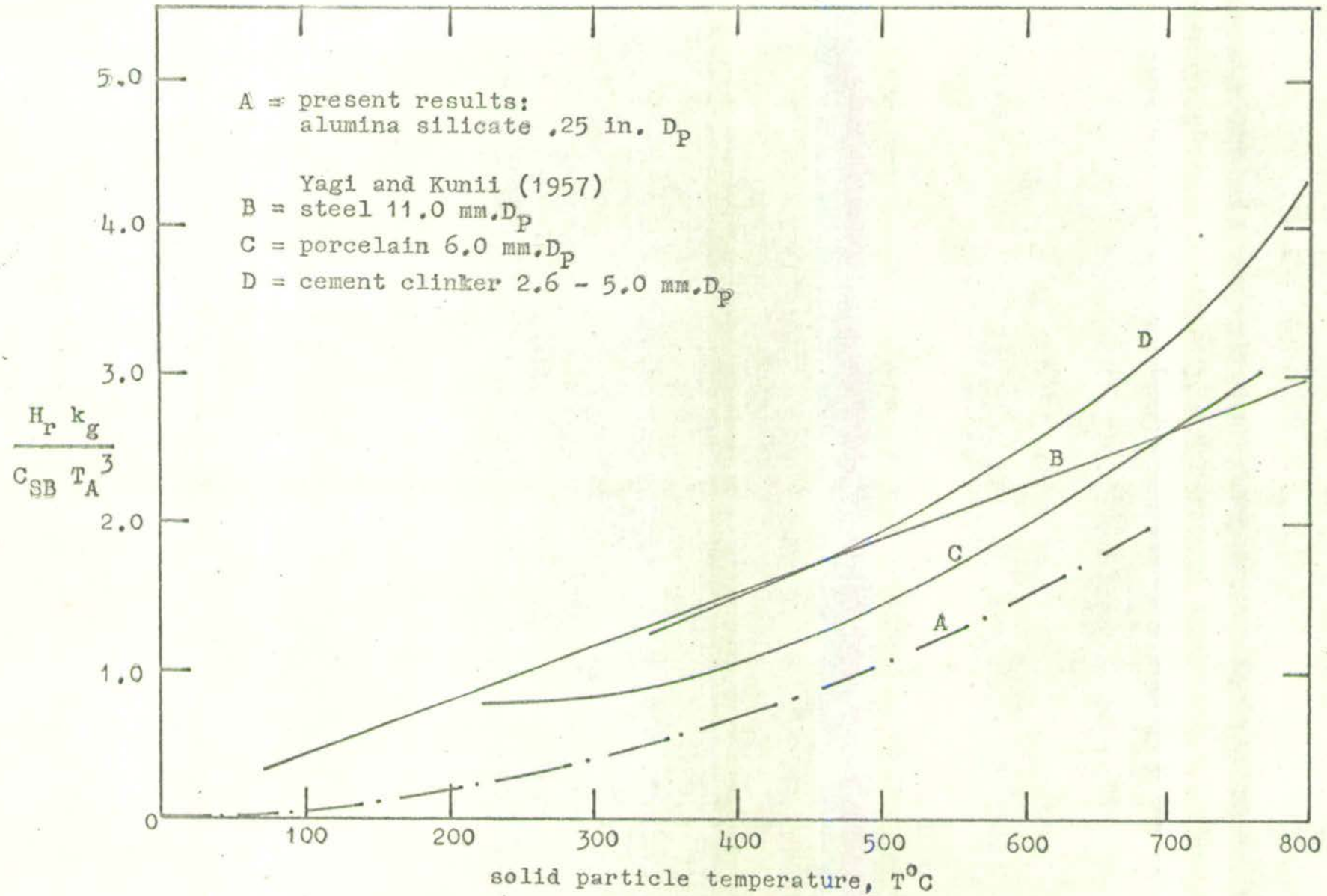

FIG. 6.24B RADIATION PARAMETERS FOR STAGNANT BEDS OF RANDOM PACKED SPHERES

6.4. GAS FLOW RESULTS

6.4.1. Temperature Profiles

The steady state readings given by the particle thermocouples in the test bed and the guard bed are shown for a typical gas flow run in Fig. 6.5. The guard bed readings are close to the test bed readings at any axial position showing that radially adiabatic conditions were obtained in the test bed. Thus the nett heat flow was solely in the axial direction and the temperature profile was determined for each run by drawing a smooth curve through the test bed temperature readings. These profiles were reproducible to within 2% as shown in the dimensionless form in Fig. 6.6. Experience of the effect of heater settings and guard-test bed temperature differences indicated that the correct adiabatic dimensionless profiles were obtained to within 5% error.

Fig. 6.25 shows the complete set of gas flow temperature profiles. Fig. 6.26 - 6.28 show the profiles in dimensionless form for bed mid point temperature levels of 147 - 180°C, 371 - 455°C, 555 - 647°C respectively.

6.4.2. Effect of Gas Flow on Temperature Profiles

From Fig. 6.25 it can be seen that increasing the gas flow rate has a marked effect on the solid temperature profile and gives a flatter profile over the high temperature end of the bed. The effect of gas flow rate on the temperature profile is greater for higher hot-face temperatures. The dimensionless profiles (Fig. 6.26 - 6.28) show a slightly greater effect of gas flow rate for lower hot face temperatures.

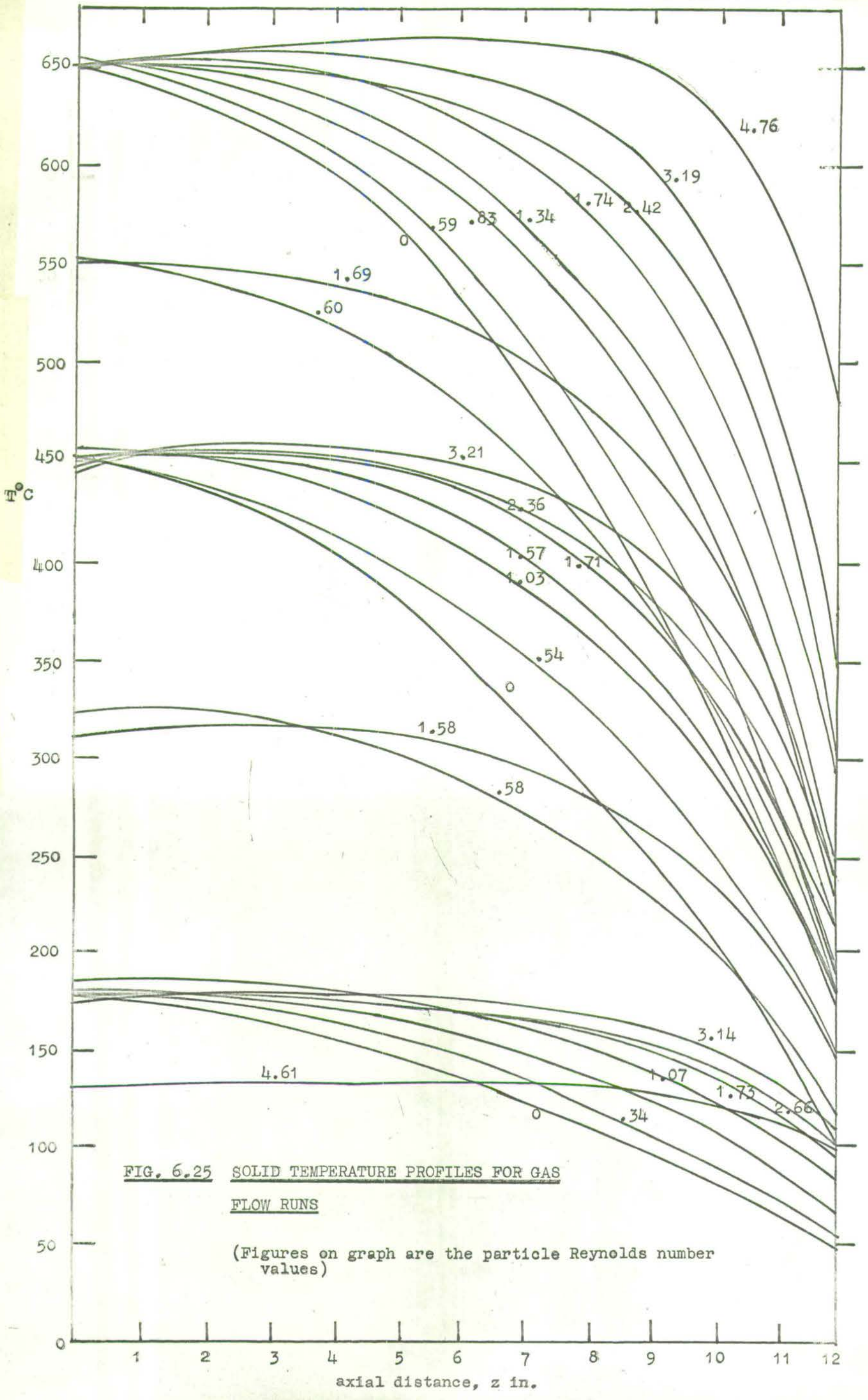

FIG. 6.25 SOLID TEMPERATURE PROFILES FOR GAS FLOW RUNS

(Figures on graph are the particle Reynolds number values)

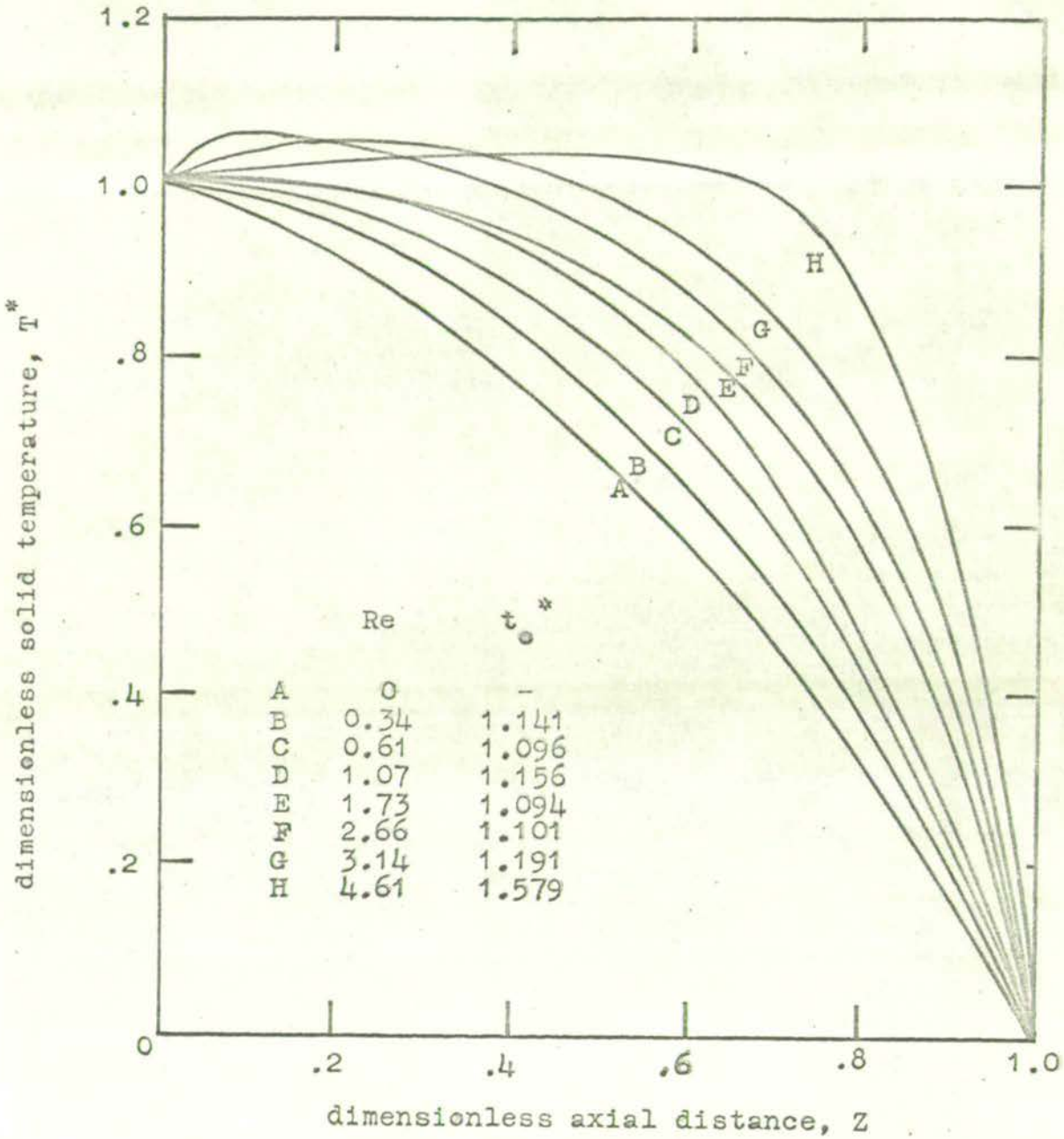

FIG. 6.26 GAS FLOW RUNS - EFFECT OF GAS FLOW RATE

($T_{Z = .5}$ = 147 - 175°C)

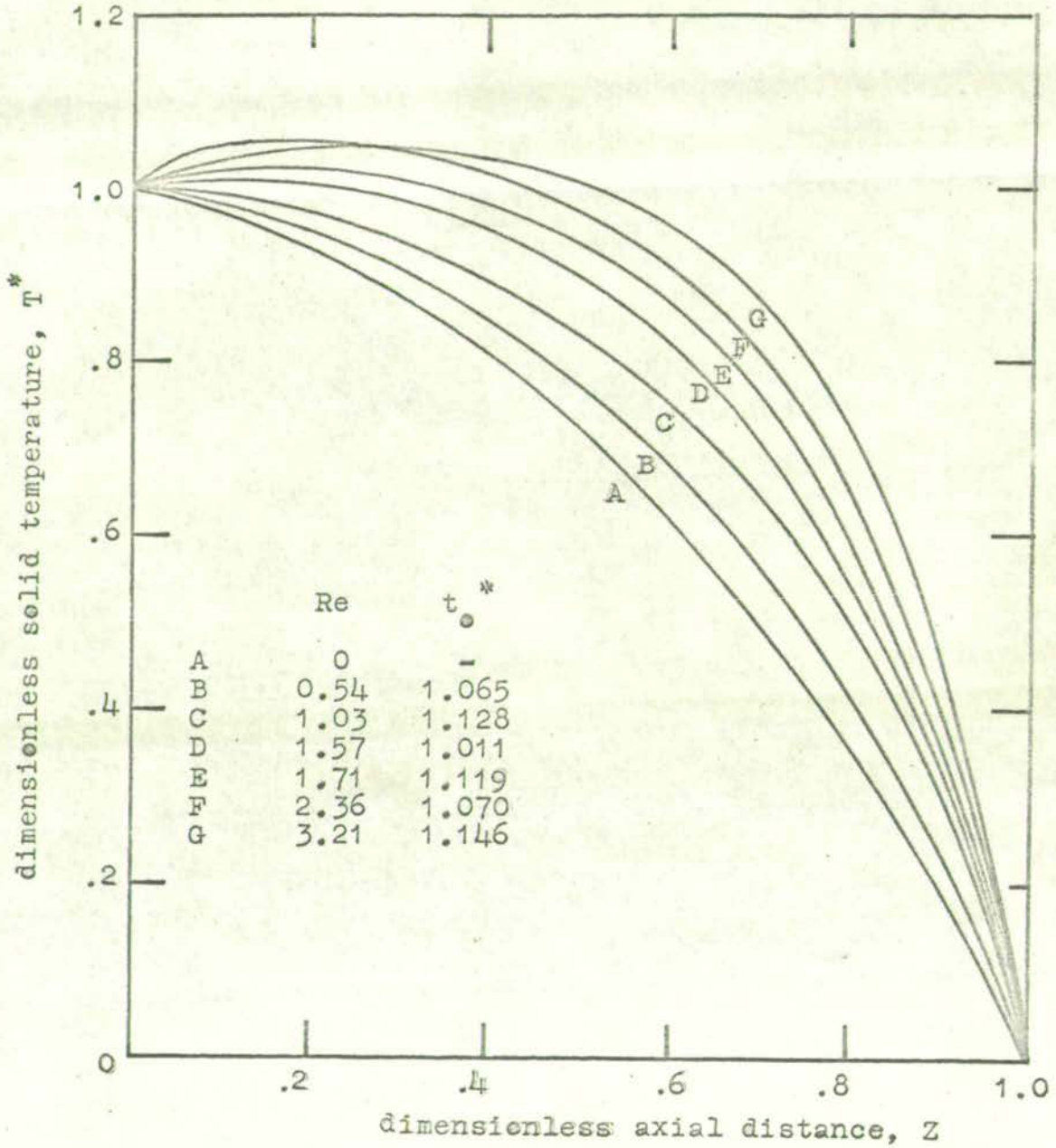

FIG. 6.27 GAS FLOW RUNS - EFFECT OF GAS FLOW RATE
($T_{Z = .5}$ = 371 - 455°C)

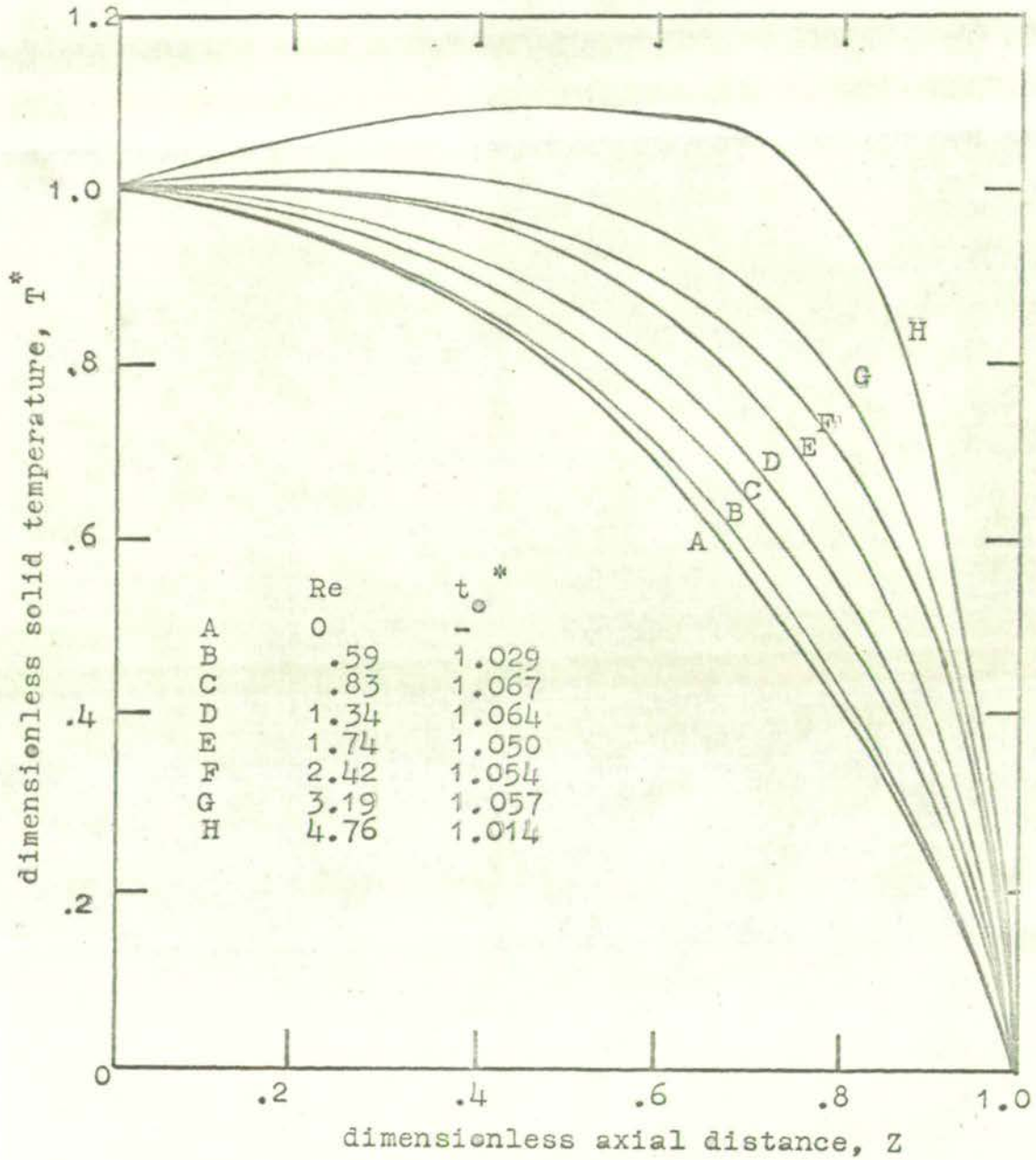

FIG. 6.28 GAS FLOW RUNS - EFFECT OF GAS FLOW RATE ($T_{Z = .5}$ = 555 - 647°C)

6.4.3. Effect of Temperature Level on Temperature Profiles

For the same gas flow rate a greater temperature level gives a steeper profile (Fig. 6.25). The dimensionless profiles show very little effect of temperature level(Fig.6.29).

For each set of gas flow runs at a given temperature level (Figs. 6.26 - 28) a stagnant gas run was made to define the zero gas flow rate dimensionless temperature profile. Fig. 6.30 shows that the curvature of these stagnant profiles increased with increased temperature due to the greater radiation transfer described in 6.33. Fig. 6.30 also shows that even at the lowest temperature level (180°C) there was appreciable curvature of the stagnant gas solid temperature profile.

The equality of the guard bed and test bed temperatures showed that the bed was radially adiabatic and even when the guard bed temperatures were kept slightly below the test bed readings a curved profile was still obtained. For heat transfer solely by conduction mechanisms a straight dimensionless profile would be obtained. Thus the curvature could only have been caused by the following two factors

a) the effect of a temperature dependent conduction effective thermal conductivity (due to radiation effects and temperature dependent phase conductivities.

b) natural convection effects either in the voids or through the bed

Fig. 6.14 shows that the radiation effects at temperatures of 180°C and below are very small and that the temperature dependence of the effective thermal conductivity at these

FIG. 6.29 EFFECT OF TEMPERATURE LEVEL (AT CONSTANT GAS FLOW RATE) ON THE SOLID TEMPERATURE PROFILE FOR GAS FLOW RUNS

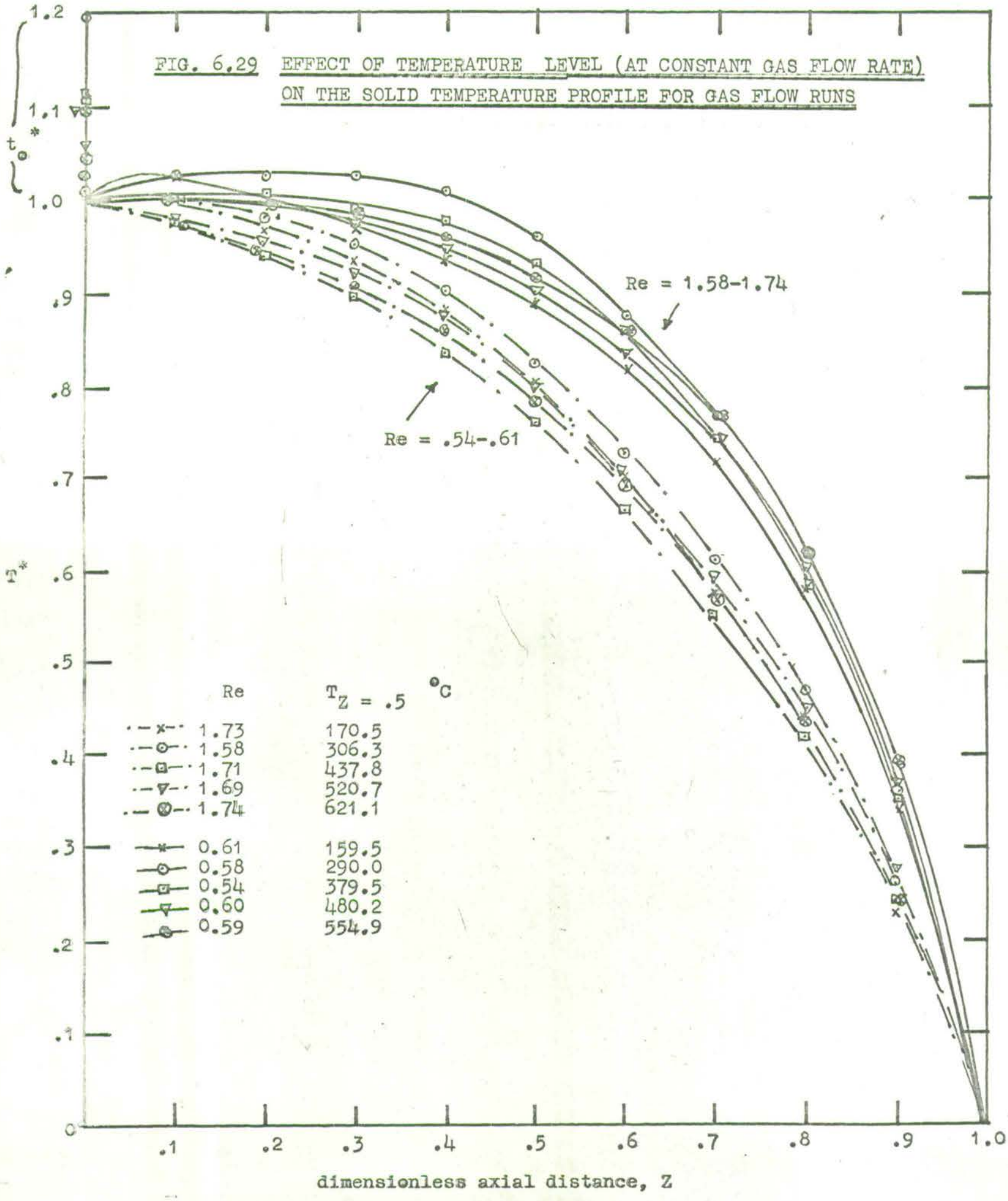

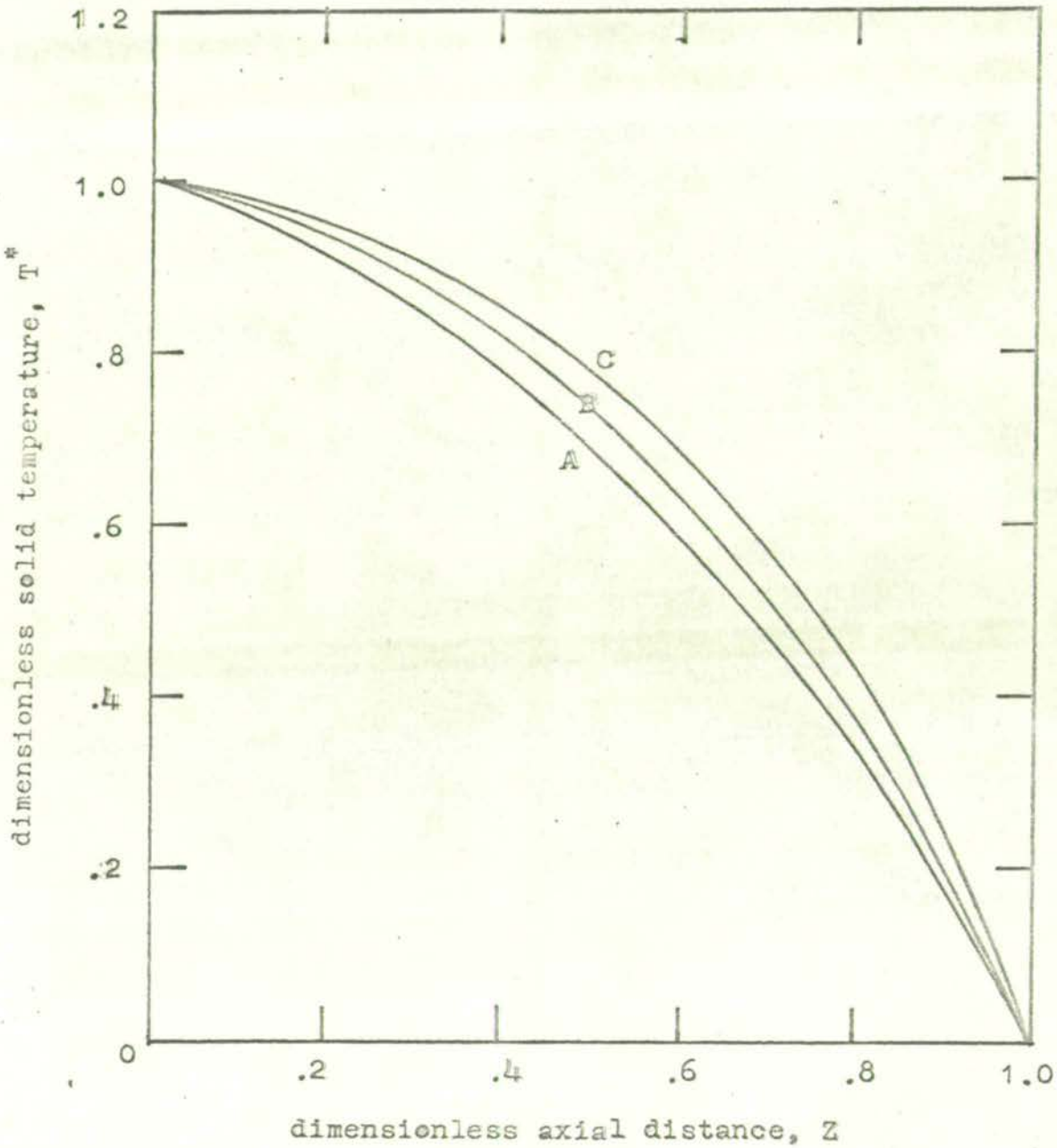

FIG. 6.30 EFFECT OF BED TEMPERATURE - STAGNANT BED RUNS

$T_Z = .5$:
A = 137.0°C
B = 355.8°C
C = 533.8°C

temperatures is virtually linear. The effect of such a temperature dependence on the temperature profile obtained from Appendix 5 is given in Fig. 6.31 which shows that the effect is small. It is thus apparent that the curvature is due to natural convection effects. Substituting experimental parameter values into equation 3.39 showed that the critical Rayleigh number for natural convection originating within the voids was not exceeded. However using the bed length instead of the void length in equation 3.39 showed that the critical Rayleigh number for natural convection through the bed was easily exceeded. Thus it is apparent that for the stagnant gas runs in the gas flow equipment, natural convection was initiated in the gas mixing space below the bed hot-face and enabled to persist by movement of air out of the top of the bed into the outlet gas temperature meter.

For the stagnant gas runs with the brick heat flow meter partially sealing the top of the bed (Fig. 6.7) the natural convection curvature effect was much less pronounced and was not detected in the analysis of the local effective thermal conductivity results (6.2.4) since no significant effect of axial heat flow rate was found.

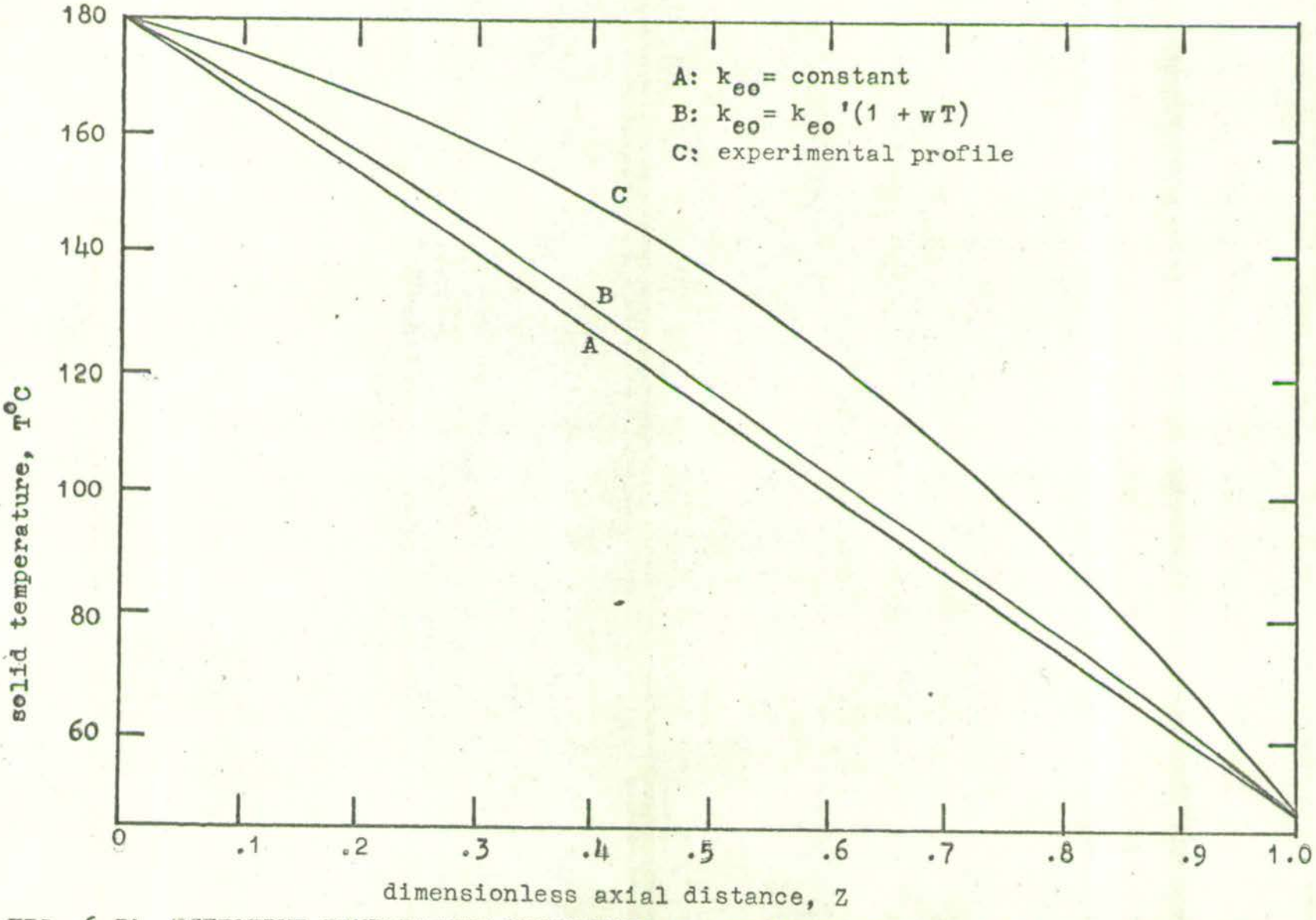

FIG. 6.31 EFFECTIVE TEMPERATURE DEPENDENCE OF EFFECTIVE THERMAL CONDUCTIVITY OF THE STAGNANT BED

6.5. ANALYSIS OF HEAT TRANSFER MECHANISMS FROM GAS FLOW RESULTS

6.5.1. Conduction-Convection-Radiation Mechanisms for the Present Experimental Results

(i) effective solid phase thermal conductivity from the diffusion model

The diffusion model solution based on assumed equal solid and gas temperatures (Table 4.1) was used to derive effective thermal conductivity values from the dimensionless temperature profiles. An effective thermal conductivity value derived in this way thus lumped together the effect of all the conduction and radiation mechanisms along with the solid-gas convection contributions. The bulk flow convection contribution was included explicitly in the model.

The effective thermal conductivity at a given gas flow rate was determined from the value of the parameter K_L which gave a diffusion model profile (Fig. 4.8) corresponding most closely to the slope of the experimental dimensionless profile at the Z = 1 end of the bed. From the definition of K_L it follows that

$$Y' = k_{es}'/k_g = K_L \, Re \, Pr(L/D_p) = 33.1 \, K_L \, Re \qquad ....(6.13)$$

The profiles could only be fitted at the Z = 1 end of the bed since at the Z = 0 end an inlet gas temperature of $t_o^* > 1$ can give $T^* > 1$ which is not accounted for in the equal gas and solid temperature diffusion model

Figs. 6.32, 6.33 and 6.34 respectively show the values of K_L, $Y'(= k_{es}'/k_g)$ and k_{es}' derived in this way from

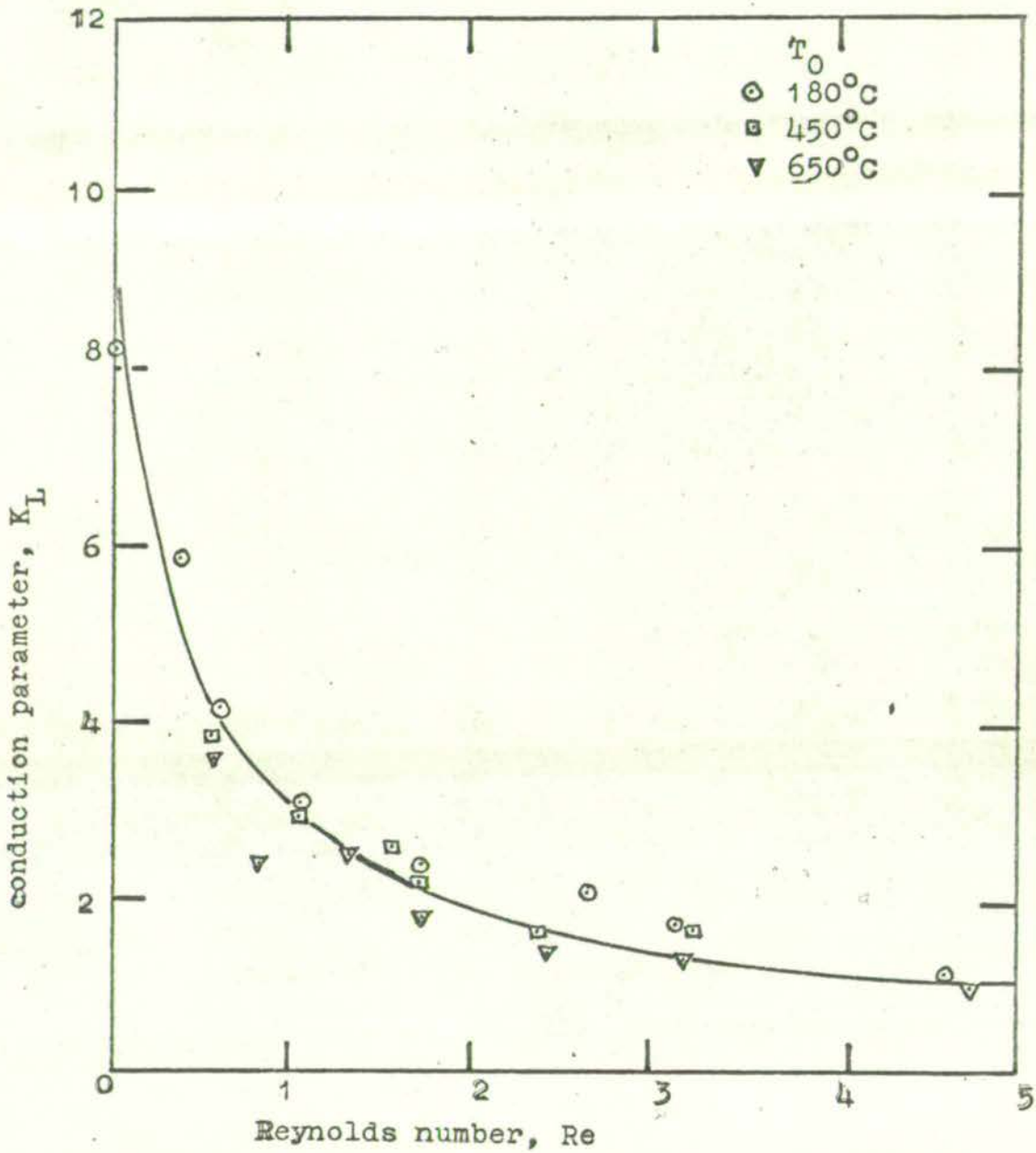

FIG.6.32 DIFFUSION MODEL CONDUCTION PARAMETER, K_L, FOR GAS FLOW RUNS

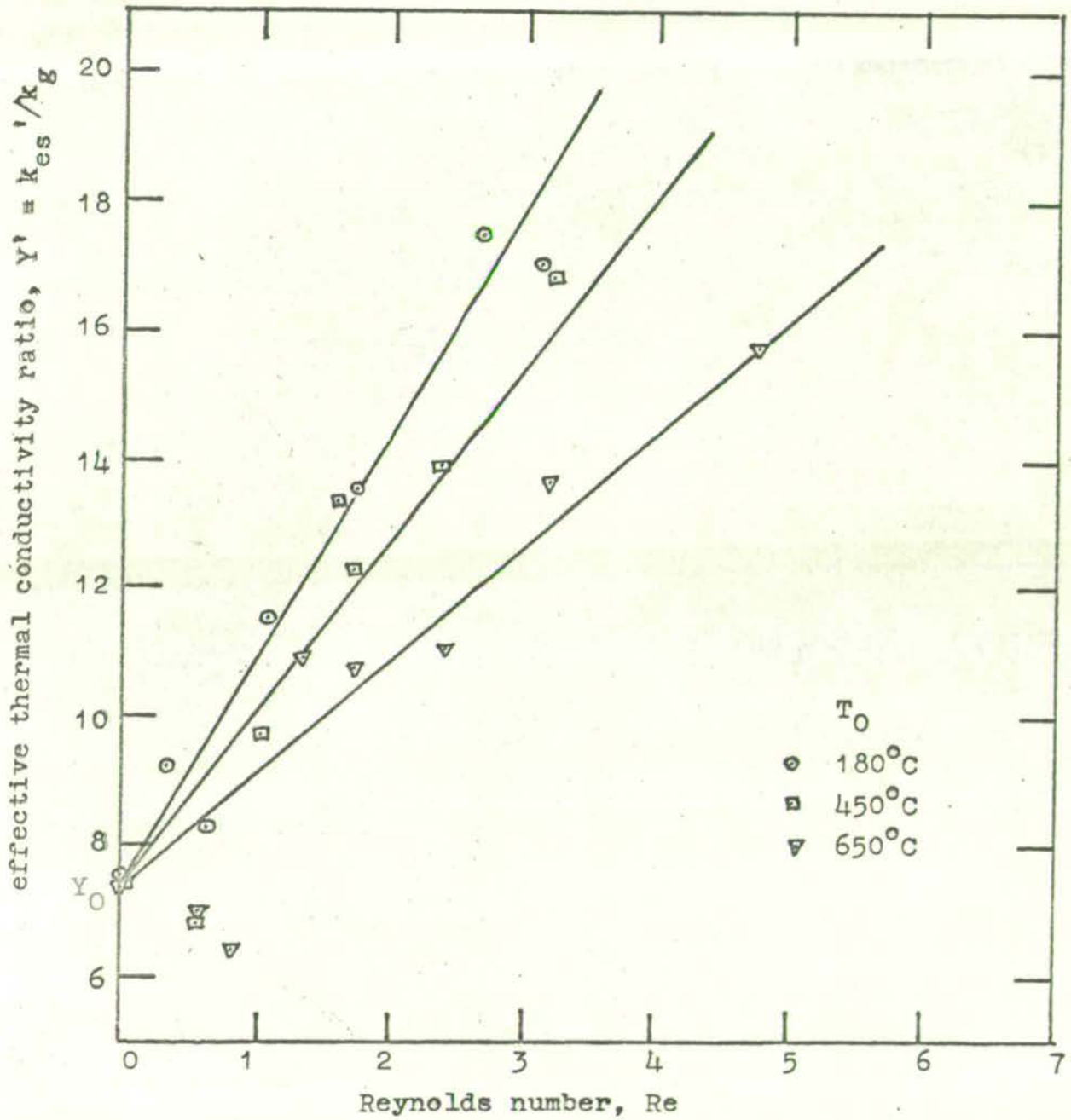

FIG. 6.33 DIFFUSION MODEL EFFECTIVE THERMAL CONDUCTIVITY RATIO FOR GAS FLOW RUNS

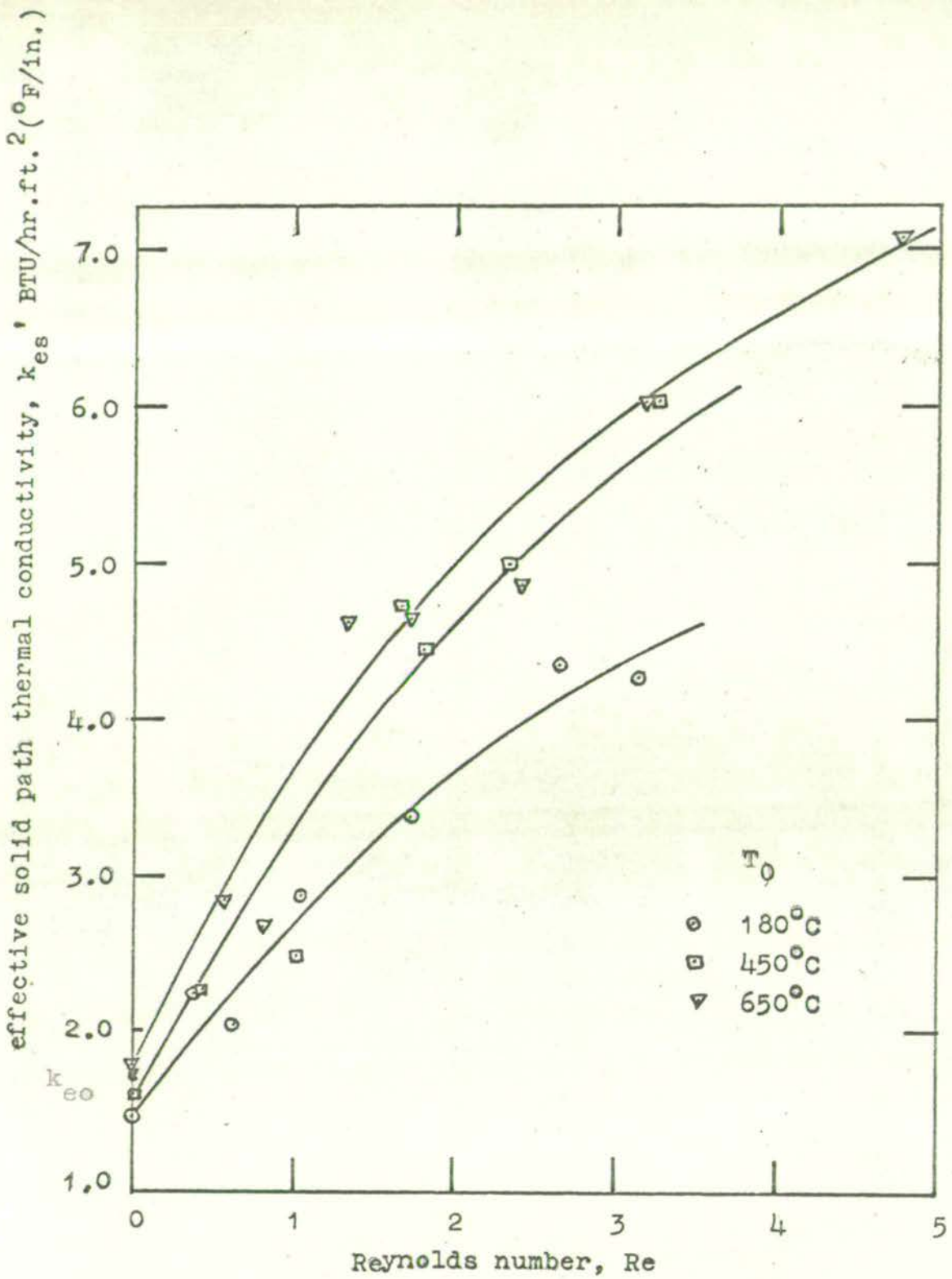

FIG. 6.34 DIFFUSION MODEL EFFECTIVE THERMAL CONDUCTIVITY FOR GAS FLOW RUNS

Fig. 6.26, 6.27, 6.28. The values for k_g were taken from Fig. 6.1 at the temperature of the Z = 1 end of the bed. The values of K_L show a decreasing exponential dependence on Reynolds number whereas Y' increases linearly and k_e increases approximately linearly due to the increased contribution of the gas-solid convection mechanism. The effect of radiation is apparent in the lower values of K_L and Y' and higher values of k_{es}' for the higher hot-face temperature runs. The divergence of the results at different temperatures is more pronounced at greater Reynolds numbers indicating greater interaction between the radiation mechanisms and the solid-gas convection mechanism under these conditions.

(ii) effective solid phase thermal conductivity from the mixing cell model

The mixing cell model developed in 4.3.14 for axial heat transfer in a packed bed with non-equal solid and gas temperatures is dependent on an effective conduction parameter, K, a convection parameter, H, and a contact point resistance parameter N_P^*. If we put $N_P^* = 0$ the model is dependent on only two parameters and the effective conduction parameter now includes the contact point conduction resistance as well as solid phase conduction and any radiation effects present. Thus this model can yield more information concerning heat transfer mechanisms than the diffusion model used in 6.5.1.(i) since the solid-gas convection mechanism is separated from the conduction and radiation mechanisms.

The mixing cell model requires one dimensionless gas temperature for solution. Since it was found that the solid

temperature profile was markedly dependent on the value of t_m^* but only slightly dependent on the value of t_o^* (4.3.18) the experimental values of t_o^* were used in the analysis of results.

No account was taken of the variation of the model parameters with the temperature along the length of the bed so that the values of K obtained were average values for the range of bed temperatures. Fig. 6.31 shows that at low temperatures the temperature variation of K would have negligible effect on the profile. The Reynolds number and gas thermal conductivity were evaluated at the temperature of the mid-point of the bed which is a good approximation to the integrated mean bed temperature.

Attempts were initially made to fit the model parameters K and H simultaneously to the experimental dimensionless solid temperature profiles using a least squares regression technique for non-linear equations (Scarborough (1955)). The experimental and model dimensionless profiles necessarily coincided at Z = 0 but for arbitrary initial values of the model parameters the least squares difference between the two profiles increased rapidly as Z increased. Because of this ill-conditioning, unless the arbitrary initial values for the model parameters were very close to the best fit values, the least square alterations in the parameters produced values which, initially at least, diverged rapidly from the best fit values and either generated numbers out of the range of a

Ferranti Sirrius computer or failed to converge after a reasonable number of iterations.

Thus it was decided to fix the convection parameter from a known correlation and to obtain the conduction parameter by a technique based on regression of the areas under the experimental and model profiles. The most suitable correlation for the solid-gas convection coefficient, h, under the present experimental conditions is the J_h correlation of Williamson, Bazaire and Geankoplis (1963) (3.5.2). Since the surface area per unit volume of packing is given by equation 2.4 and since L = 12 in., $D_p = \frac{1}{4}$ in. and $\epsilon = 0.40$ for the present system, equation 4.111 gives

$$H = \frac{554\ Re^{-.66}}{m} \qquad \ldots.(6.14)$$

From equation 4.85, $m = 24\ Pe$ $\ldots.(6.15)$

where the Peclet number is given as a function of Reynolds number in Fig. 2.11. The areas under the experimental and model profile curves were closely approximated by dividing the bed length into tenths and using the trapezoidal rule to give

$$A = 0.1\left[\frac{1}{2}\left(T_o^* + T_m^*\right) + \sum_{Z=0.1}^{0.9} T_Z^*\right] \qquad \ldots.(6.16)$$

$$= 0.1\left[0.5 + \sum_{Z=0.1}^{0.9} T_Z^*\right] \qquad \ldots.(6.17)$$

Using equations 6.14, 4.102 - 107, 4.108a, b, and an arbitrary initial value for K, the area under the model profile was

evaluated from equation 6.17. This equation was also used to evaluate the area under the experimental profile.

Since Fig. 4.15 shows that a larger area under the profile is given by a smaller value of K, an improved value of K was calculated from the relationship

$$K_2 = K_1 \, A_1 \, / A_{exp} \qquad \ldots.(6.18)$$

where K_1 and K_2 are respectively the initial and improved values of K and A_{exp} and A_1 are respectively the experimental profile area and the model profile area (based on K_1). An Autocode programme was written to carry out this regression procedure on a Ferranti Sirrius computer and five figure regression of the experimental and model profile areas was obtained after 5 - 10 iterations for K based on equation 6.18 and about 5 minutes of computer time.

Fig. 6.35 shows the good agreement of a typical experimental solid profile and the model solid profile for equal areas under the two profiles. The gas profile given by the model is also shown in Fig. 6.35.

From the definition of K (equation 4.110) it follows that

$$Y = \frac{k_{es}}{k_g} = \frac{K \, Re \, Pr \, L}{(1 - \varepsilon) \, m \, D_p} = 55.1 \, \frac{K \, Re}{m} \qquad \ldots(6.19)$$

Figs. 6.36, 6.37, 6.38 show the values of K, Y and k_{es} as functions of the particle Reynolds number for the three hot-face temperature levels used in these experiments. From Fig. 6.36 it is seen that for $Re < 1$, the values of K

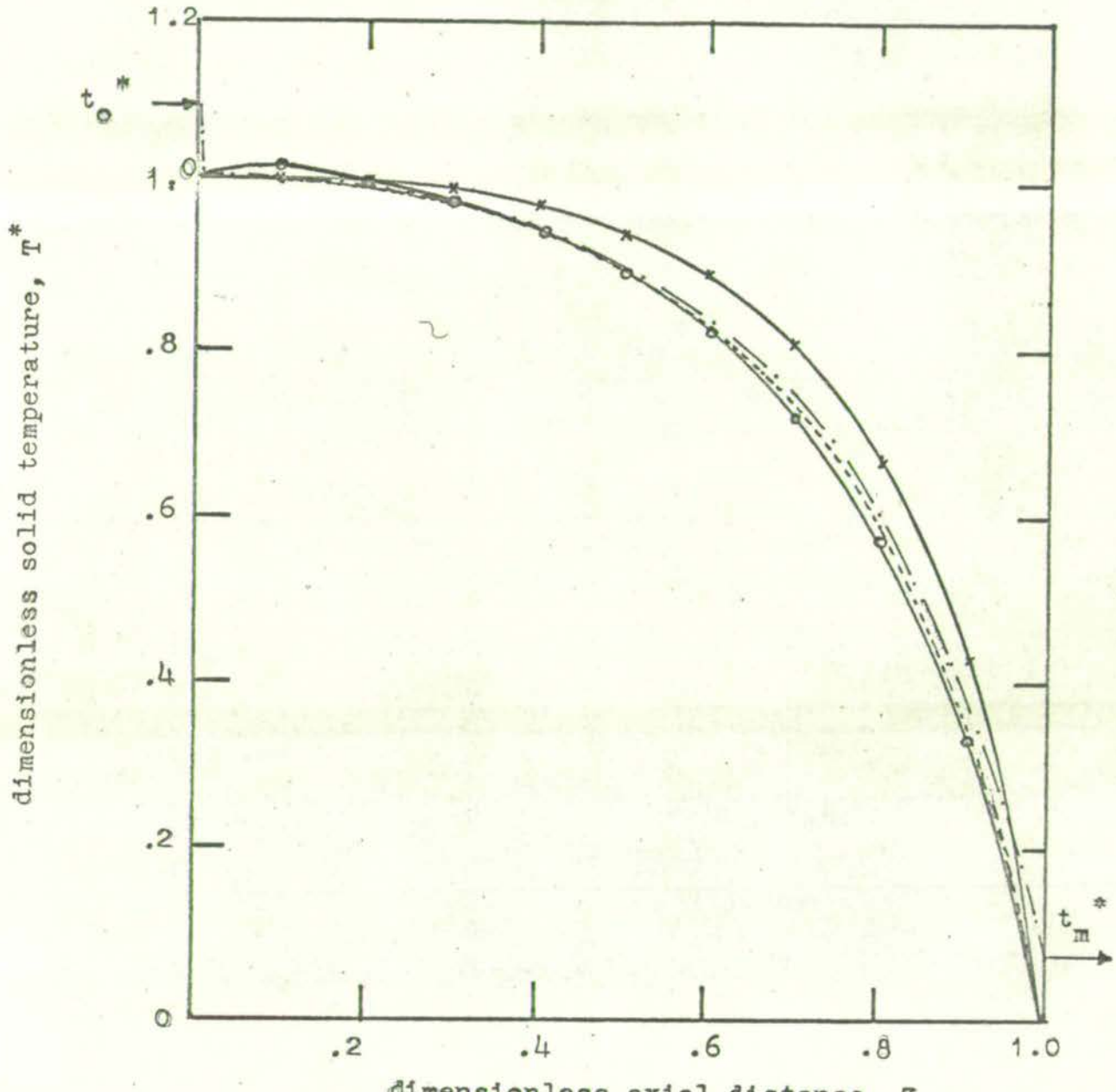

FIG. 6.35 COMPARISON OF A TYPICAL EXPERIMENTAL PROFILE (LOW TEMPERATURE) WITH MIXING CELL MODEL PROFILES

experimental solid profile: $t_o^* = 1.094$, Re = 1.73, $T_{Z=.5} = 170^\circ C$, $T_o - T_m = 85.5^\circ C$

mixing cell model solid profile (from area regression): K = 7.72, H = 9.9, $N_p^* = 0$, m = 39

mixing cell model gas profile corresponding to area regression

mixing cell model solid profile using an N_p^* value based on the stagnant bed thermal conductivity: K = 16.39, H = 9.9, $N_p^* = 2.45$, m = 39

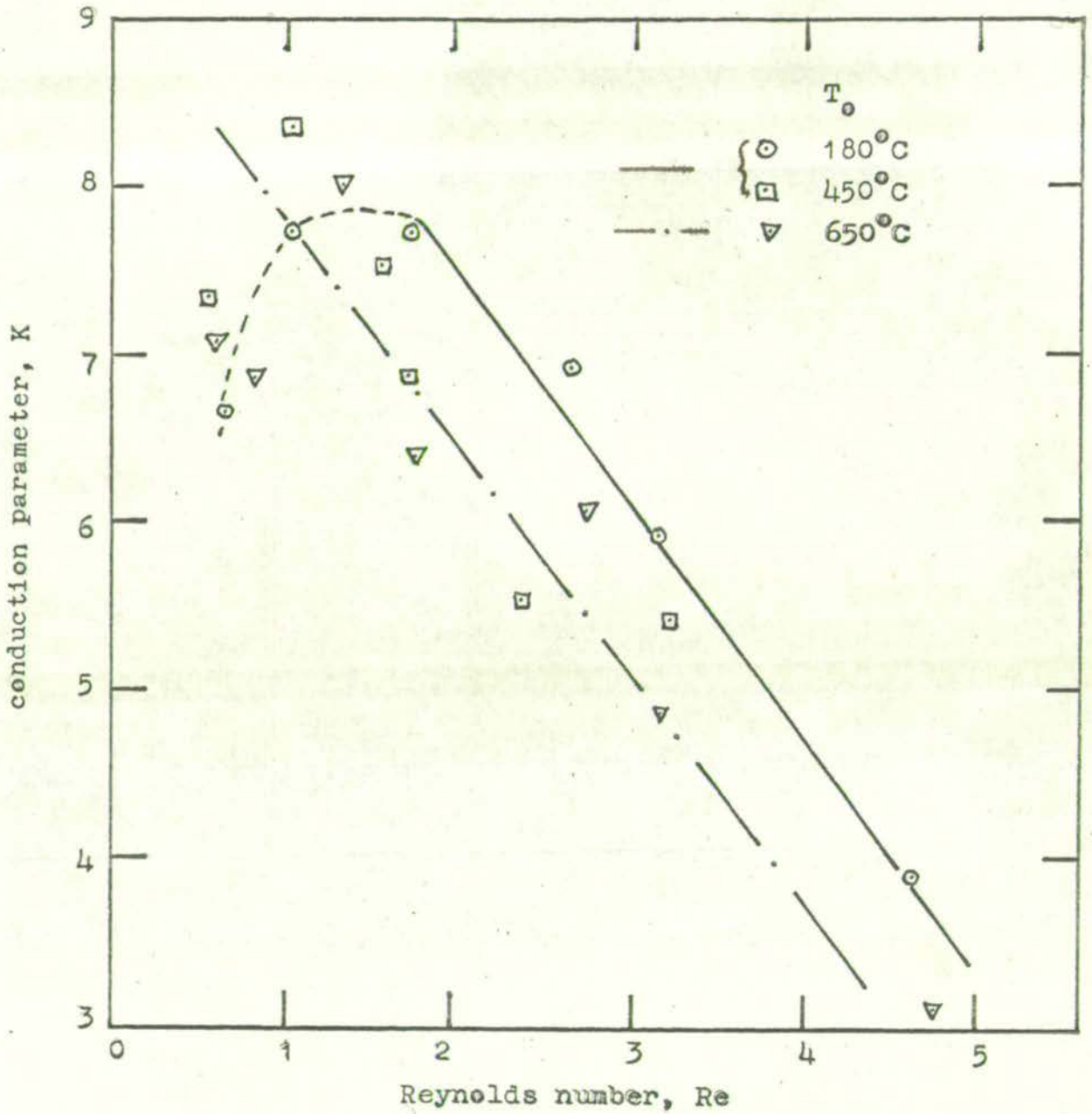

FIG. 6.36 MIXING CELL MODEL CONDUCTION PARAMETER K, FOR GAS FLOW RUNS

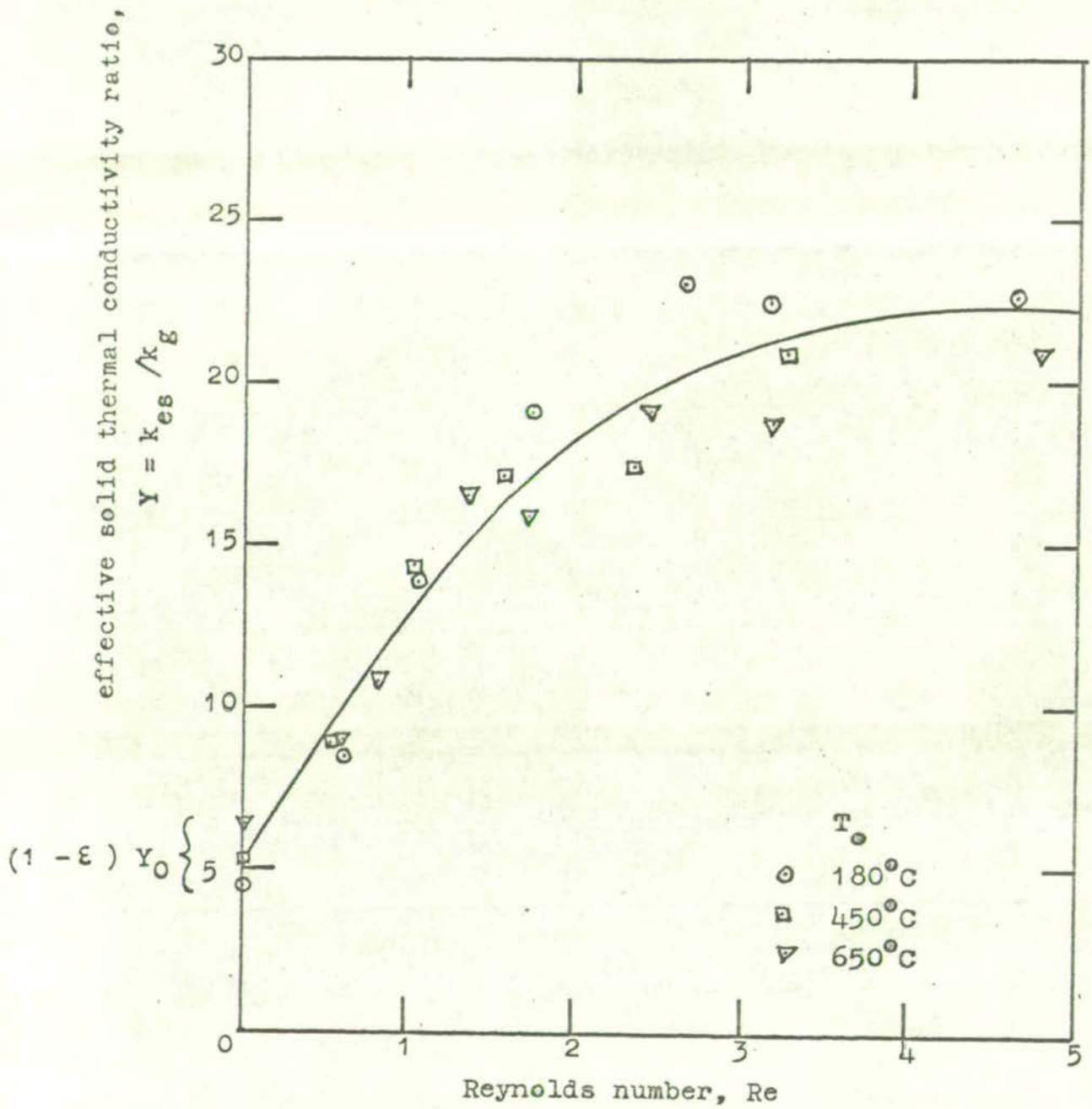

FIG. 6.37 GAS FLOW EFFECTIVE SOLID THERMAL CONDUCTIVITY RATIO

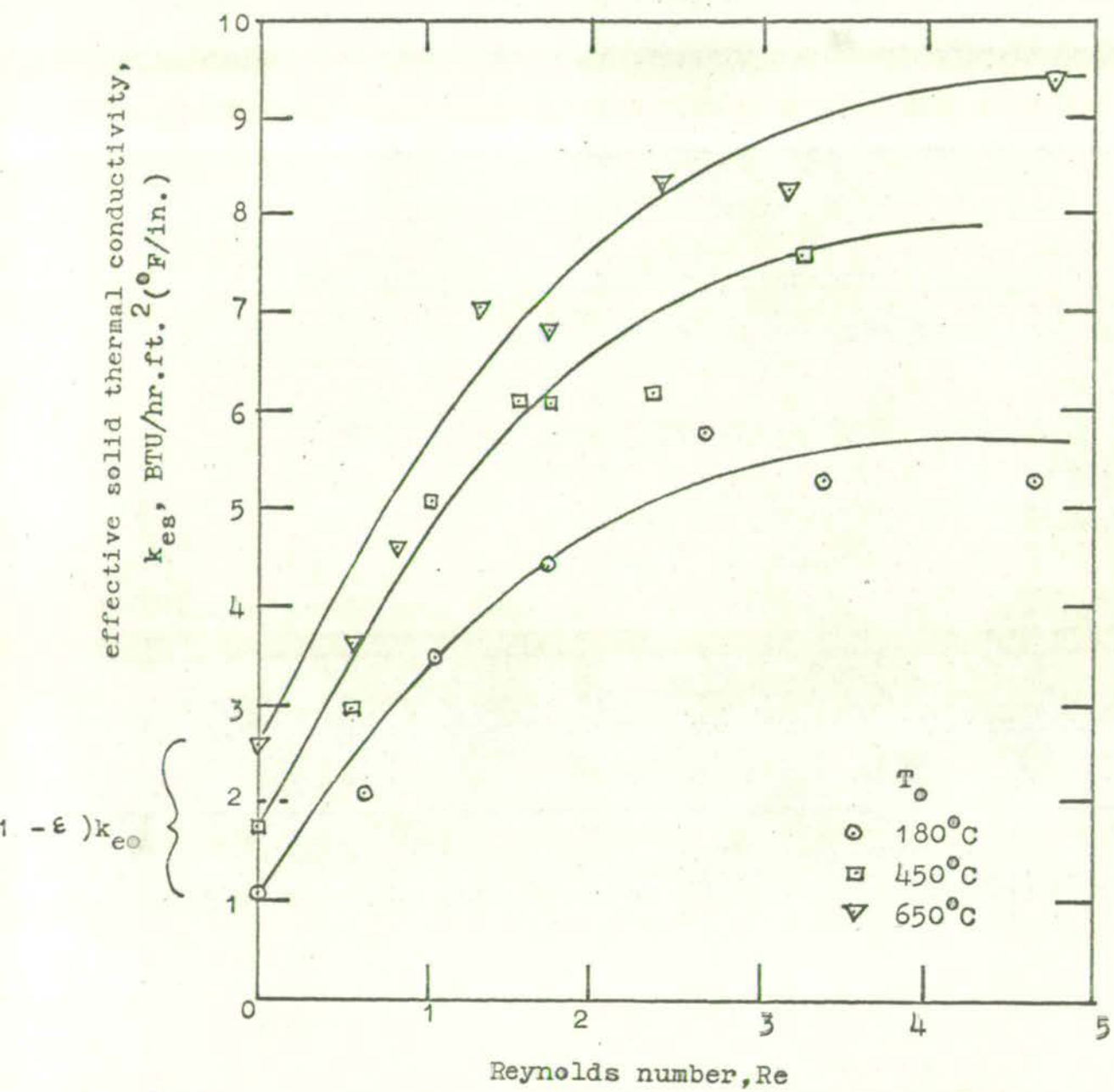

FIG. 6.38 GAS FLOW EFFECTIVE SOLID THERMAL CONDUCTIVITY

are slightly low due to the effect of natural convection through the bed accentuating the curvature of the stagnant bed profile (6.4.3). The values of K have been determined from the profile over the complete bed length and from Fig. 4.15 it is seen that the greater the profile curvature, the lower the value of K.

Figs. 6.37 and 6.38 show that Y and k_{es} initially increase linearly with Reynolds number from the stagnant gas values[1] at Re = 0 but tend to constant values at about Re = 3. This is due to the increasing values of Peclet number in the range Re = 0 - 3 (Fig. 2.11) giving increased void mixing of the stagnant gas. For Re > 3 the Peclet number is approximately constant so that the stagnant film or pendular gas ring around each contact point is not decreased further and the solid path effective thermal conductivity remains constant. The limiting value of increased conduction in the bed due to gas flow may be characterised by the ratio Y/Y_0 which has the values 3.1 (180°C level), 2.4 (450°C level) and 2.0 (650°C level). Thus gas flow has more effect on the effective conduction in the bed at lower temperatures as would be expected.

The effect of radiation at the higher bed temperature levels is apparent from the higher values of k_{es} (Fig. 6.38)

---

1. The stagnant gas values are plotted as $(1 - \varepsilon)\, Y_0$ and $(1 - \varepsilon)k'_{eo}$ since k'_{eo} and Y_0 are based on the complete bed area while Y and k_{es} are based on the solid path area $(1 - \varepsilon)$.

at all Reynolds numbers. Relative to the gas thermal conductivity the effective solid thermal conductivity is approximately the same at all temperature levels (Fig. 6.37).

(iii) gas-solid temperature difference from the mixing cell model

Fig. 6.39 shows that the divergence of the outlet gas temperatures (equation 4.103 with r = m) from the experimental outlet solid temperatures increases with increased Reynolds number for Re > 1. The value of

$$t_m^* = \frac{t_m - T_m}{T_o - T_m} = 0.1$$

at Re = 3.4 indicates that it is generally not adequate to assume equal solid and gas temperatures. Fig. 6.35 shows a typical gas temperature profile predicted by the mixing cell model.

(iv) axial heat flow rate from the mixing cell model

Fig. 6.40 gives the effect of Reynolds number on the mixing cell model heat flow parameter, N_Q^*, (equation 4.115) for the experimental results. Using these values for N_Q^* the axial heat flow rates, Q^*, were calculated from equation 4.114. The values of Q^* increase linearly with Reynolds number at a greater rate for a higher temperature level and tend to the stagnant profile heat flow rates (from equation 6.7) as Re → 0.(Fig, 6.41).

(v) temperature profiles using the mixing cell model parameter, N_P^*

The values of the parameter N_P^* corresponding to the experimental gas flow run conditions were estimated

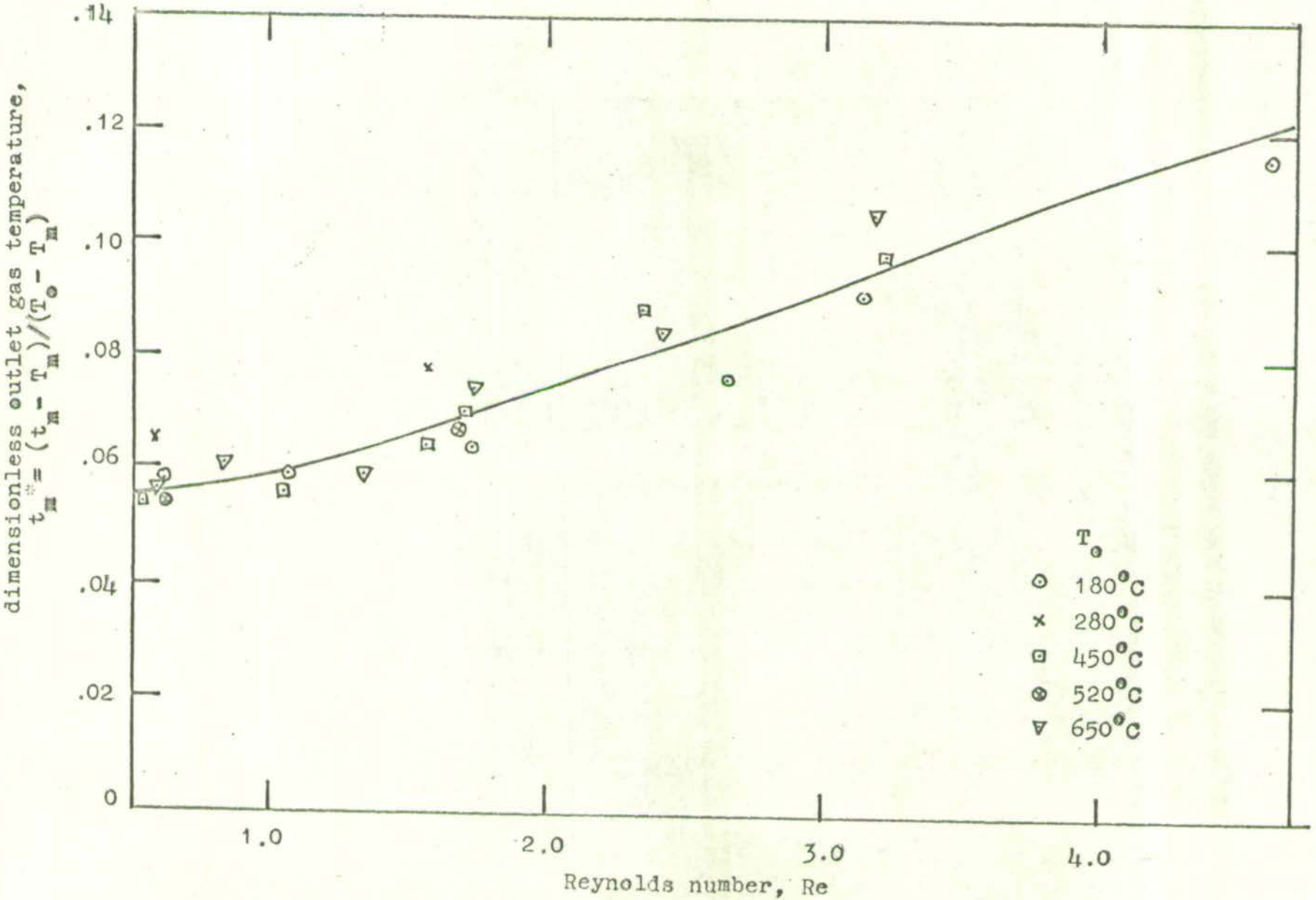

FIG. 6.39 OUTLET GAS TEMPERATURES FOR GAS FLOW RUNS(FROM MIXING CELL MODEL)

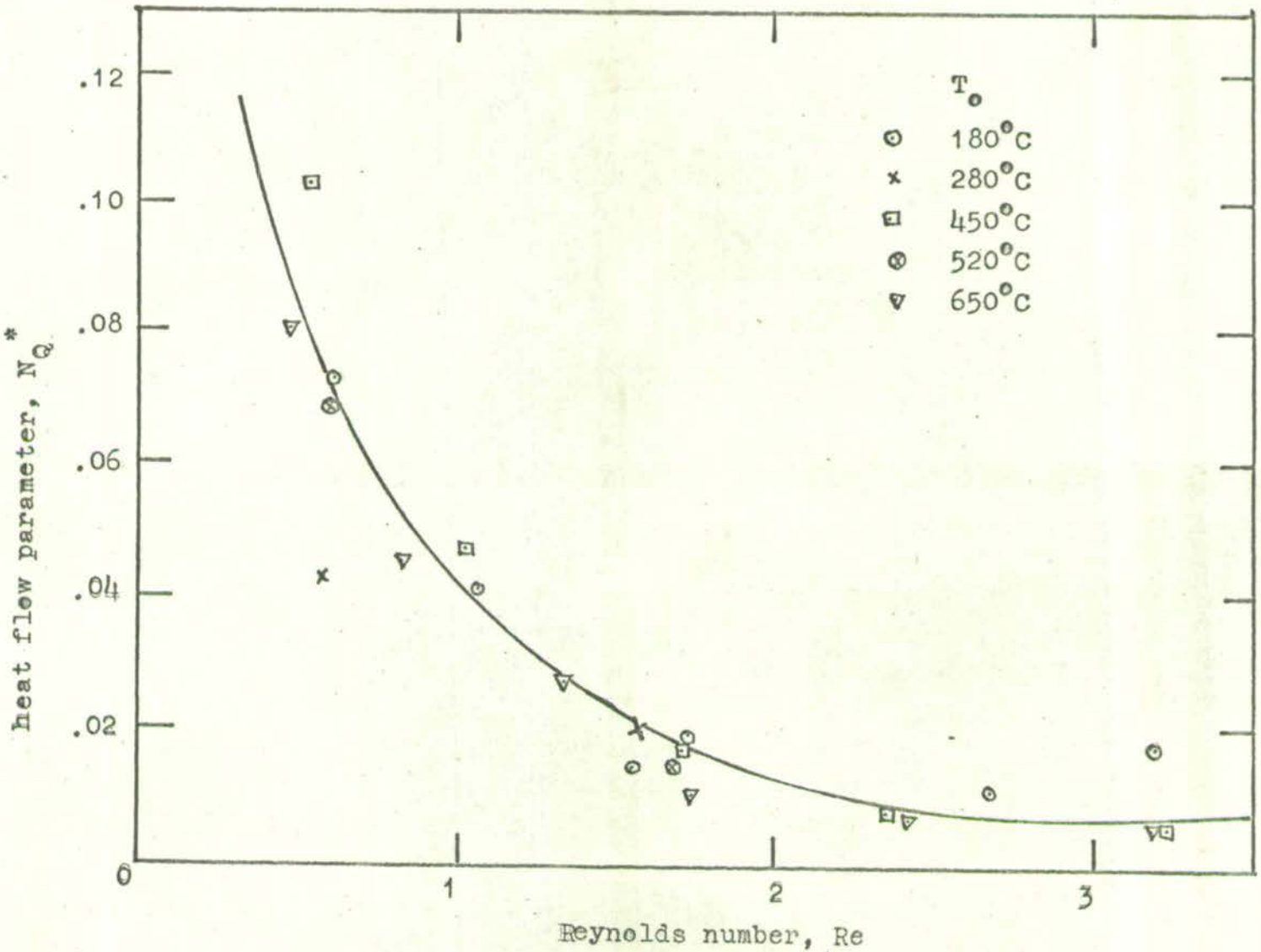

FIG. 6.40 MIXING CELL MODEL HEAT FLOW PARAMETER, N_Q^*, FOR GAS FLOW RUNS

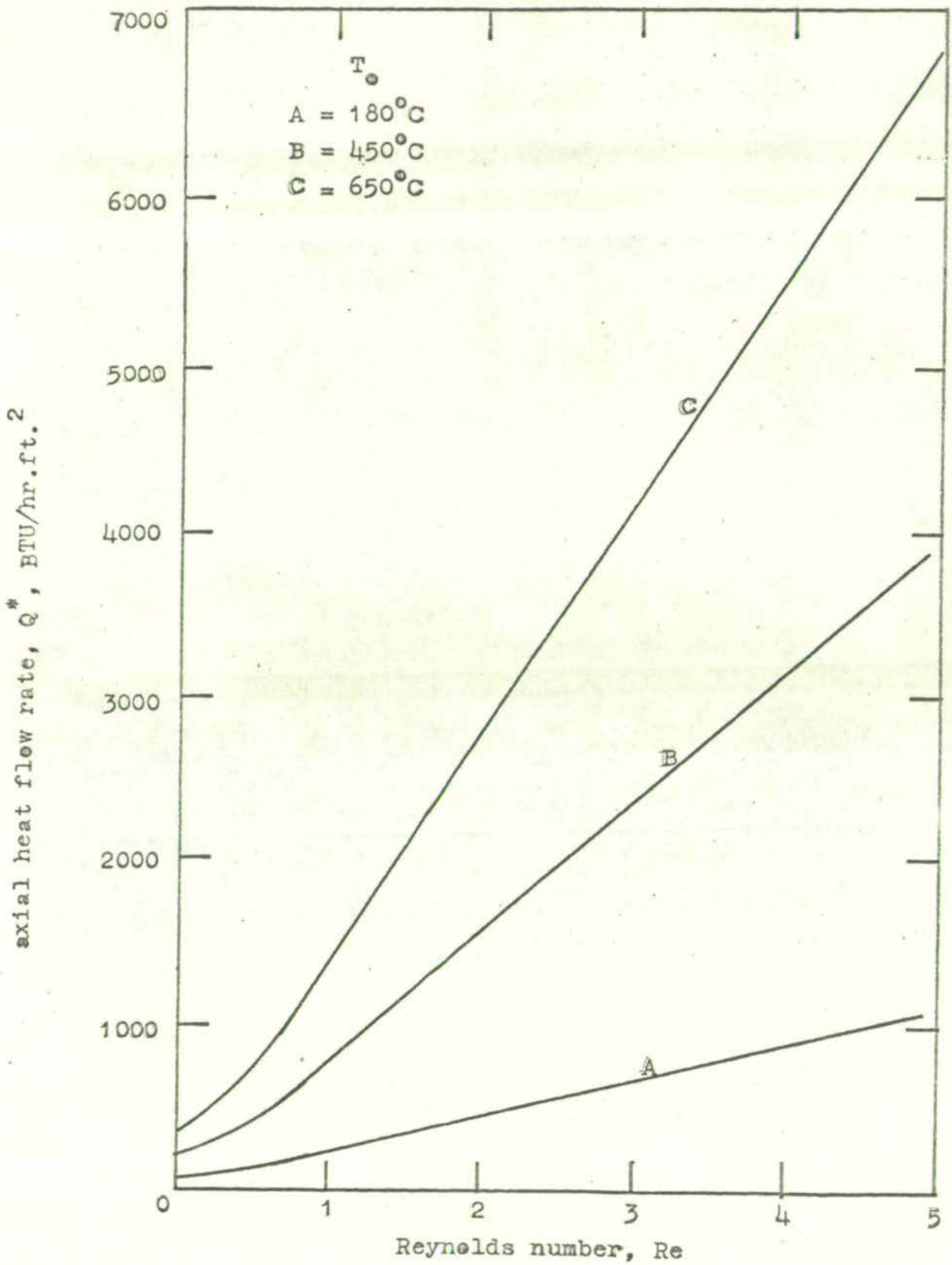

FIG. 6.41 AXIAL HEAT FLOW RATES FOR GAS FLOW RUNS

from the stagnant gas effective thermal conductivities by the conduction-radiation model equations for two cases; firstly, complete mixing of the unit cell gas in the parallel path (equation 4.123) and secondly, complete gas mixing (equation 4.124). Thus the N_P^* values shown in Fig. 6.42 as a function of temperature include the contact point resistance and the effect of the radiation mechanisms.

The conduction parameter, K, was evaluated by using the solid thermal conductivity, k_s in equation 4.110 so that

$$K = Xm/55.1\ Re \qquad \ldots.(6.20)$$

The convection parameter, H, and the number of mixing cells, m, were evaluated from equations 6.14 and 6.15 respectively. The temperature profiles were then given directly by the mixing cell model from equations 4.102 - 109.

The areas under the model solid temperature profiles are compared with the areas under the experimental profiles in Table 6.5. Due to the natural convection effects (6.4.3), the experimental profiles for $Re < 1$ lie above the model profiles. However for $Re > 1$ there is good correspondence between the profiles. The N_P^* values based on complete mixing of the unit cell gas in the parallel path show the best agreement. For this case the average deviation ($Re > 1$) is 6% for the low temperature runs and 1% for the high temperature runs. Fig. 6.35 and 6.43 show the agreement between typical model and experimental profiles.

TABLE 6.5 COMPARISON OF EXPERIMENTAL PROFILE AREAS WITH MIXING CELL MODEL PROFILE AREAS USING N_P^* VALUES BASED ON STAGNANT BED THERMAL CONDUCTIVITIES

Re	$T_{Z=.5}$	Profile Area			% deviation	
		exptal	model(a)**	model(b)**	model(a)**	model(b)**
.34	147.3	.6641	.5272	.5432	- 20.6	- 18.2
.61	159.5	.7054	.6407	.6814	- 9.2	- 3.4
1.07	170.8	.7455	.7431	.7989	- 3.2	+ 6.7
1.73	170.0	.7813	.8238	.8743	+ 5.4	+ 11.9
2.66	170.5	.8225	.8834	.9196	+ 7.3	+ 11.8
3.14	175.0	.8569	.9092	.9441	+ 6.1	+ 10.2
4.61	132.8	.9718	1.0026	1.0508	+ 8.5	+ 14.5
					6.1*	11.0*
.54	379.5	.6823	.6161	.6441	- 9.7	- 5.6
1.03	409.3	.7330	.7143	.7594	- 2.6	- 3.6
1.57	425.8	.7758	.7828	.8245	+ 0.9	+ 0.5
1.71	437.8	.7991	.8017	.8417	+ 0.3	+ 5.3
2.36	438.5	.8412	.8476	.8795	+ 0.8	+ 4.6
3.21	449.8	.8655	.8921	.9181	+ 3.1	+ 6.1
					1.5*	4.0*
.59	554.9	.6944	.6213	.6349	- 10.5	- 8.6
.83	583.0	.7300	.6681	.6810	- 8.5	- 6.7
1.34	597.8	.7565	.7521	.7635	- 0.6	+ 0.9
1.74	621.1	.8046	.7951	.8008	+ 1.2	+ 0.5
2.42	630.8	.8326	.8479	.8497	+ 1.8	+ 2.1
3.19	647.0	.8696	.8808	.8778	+ 1.3	+ 0.9
4.76	662.7	.9603	.9100	.9064	+ 0.5	- 0.6
					1.1*	1.0*

* average % deviation (neglecting sign) for Re > 1

** model (a) - parallel gas path completely mixed

*** model (b) - all gas in void completely mixed

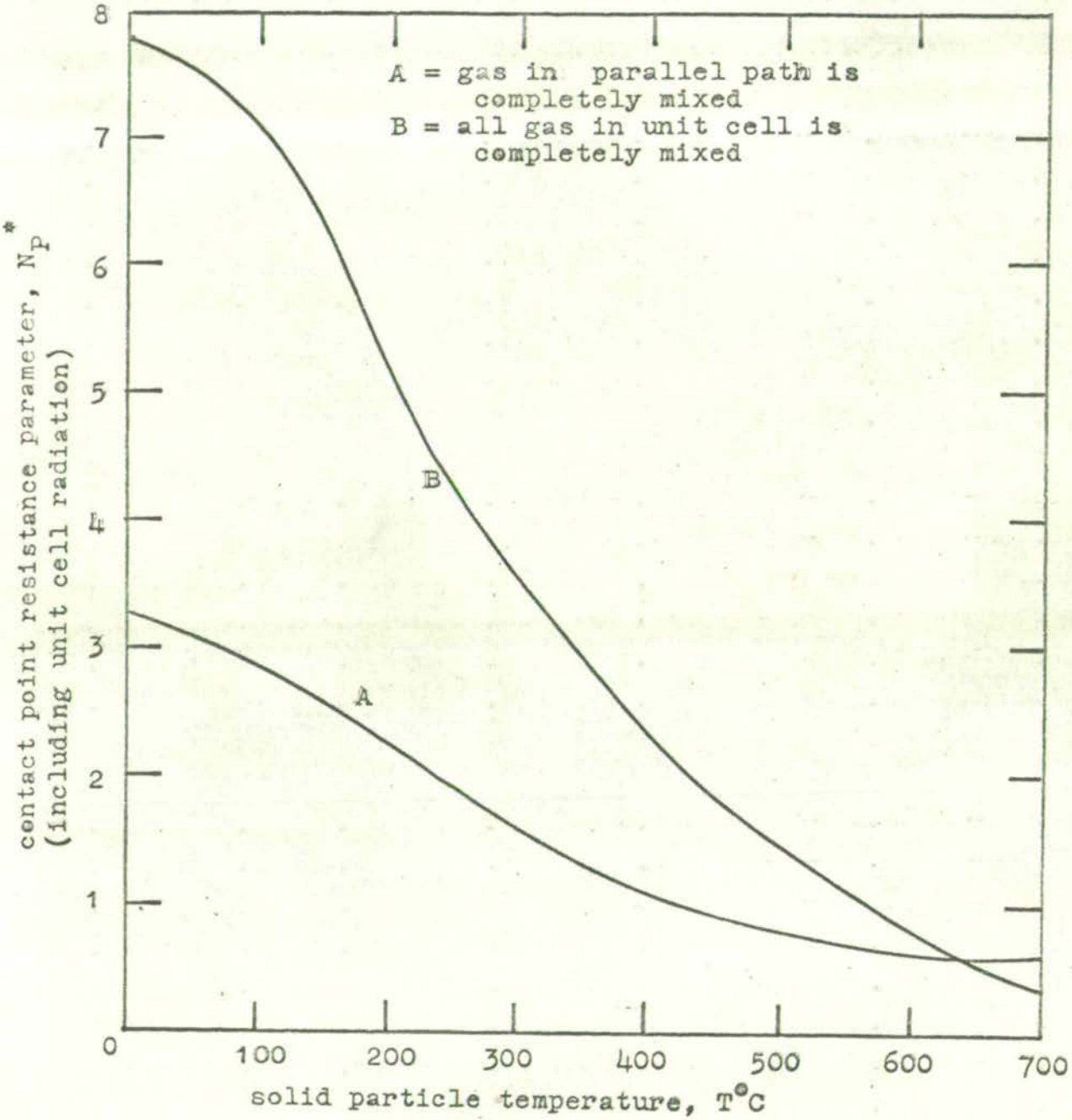

FIG. 6.42 MIXING CELL MODEL CONTACT POINT RESISTANCE PARAMETER, N_P^*, DERIVED FROM THE STAGNANT BED EFFECTIVE THERMAL CONDUCTIVITY

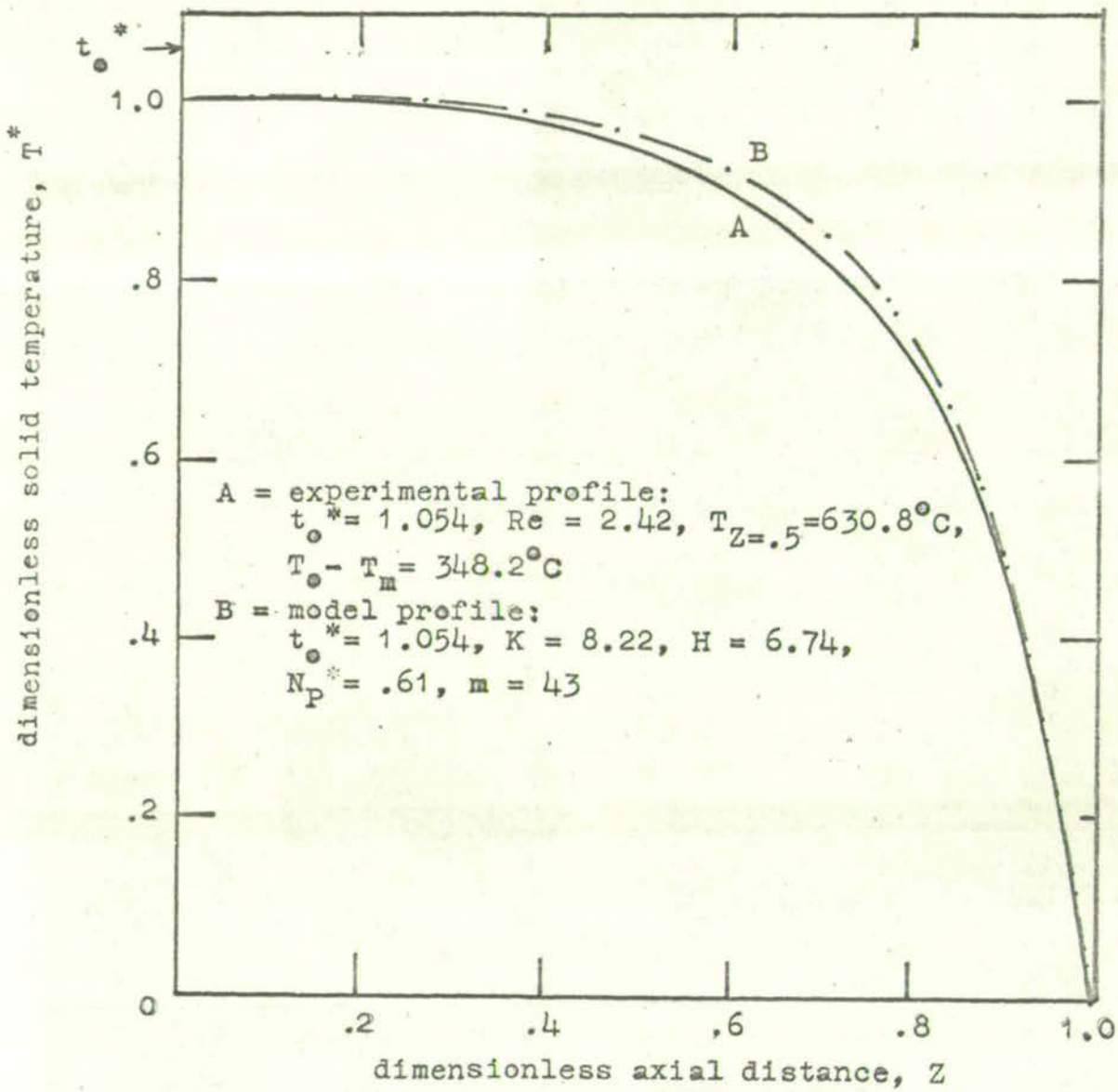

FIG. 6.43 COMPARISON OF A TYPICAL HIGH TEMPERATURE EXPERIMENTAL SOLID PROFILE FOR GAS FLOW THROUGH THE BED WITH THE MIXING CELL MODEL USING A N_P^* VALUE BASED ON THE STAGNANT BED THERMAL CONDUCTIVITY

(vi) relative contributions of the gas flow convection mechanisms

Table 6.6 shows some typical values of the relative heat flow parameters Φ_A and Φ_B. The value of Φ_A (equation 4.116) expresses the ratio of the heat flow in the solid to the heat flow in the gas and is thus a measure of the bulk gas flow convection contribution. The value of Φ_A varies along the length of the bed and the values shown in Table 6.6 are integrated mean values over the bed length.[1] It is seen that an increased Reynolds number markedly increases the bulk gas flow contribution but increased temperature has little effect. Thus at high temperatures the increased radiation contribution to the solid path heat transfer is counterbalanced by the increased enthalpy of the gas.

The value of Φ_B (equation 4.116b) expresses the enthalpy rise of the gas through the bed relative to the total axial heat flow and is thus a measure of the gas-solid convection contribution. The values of Φ_B in Table 6.6 indicate that this is a significant mechanism and its contribution is relatively unaffected by increased Reynolds number or bed temperature.

The relative contributions of the conduction and radiation mechanisms under gas flow conditions may be estimated from

---

1. The Φ_A values at the bed inlet and outlet were ignored in the integration since at the bed inlet solid heat flow can occur in the countercurrent direction and at the bed outlet Φ_A rises very rapidly to a large value.

TABLE 6.7 MIXING CELL MODEL ANALYSIS OF THE DATA OF YAGI, KUNII AND WAKAO (1960)

Packing	D_p, mm	ε	X	Re	Slope − ln K v. ln Re (least squares)	$Y_{average}$	$Y_\bullet$	$\frac{Y}{Y_\bullet}$
Glass beads	0.91 - 6.0	.40	24	.89 - 12.6	.990 ± .038	13.74	7.5	1.8
Limestone broken pieces	1.3 - 3.4	.43	57.6	2.0 - 12.9	.902 ± .027	17.6	10.0	1.8
Porcelain Raschig rings	4.0 - 9.0	.50 - .69	67.4	10.9 - 27.3	1.19 ± .035	8.2	7.0	1.2
Steel balls	3.0 - 4.8	.40	1922	14.6 - 38.7	1.03 ± .039	19.3	13.0	1.5

TABLE 6.6 RELATIVE HEAT FLOW PARAMETERS Φ_A, Φ_B.

Re	$T_{Z=.5}$, °C	$(\Phi_A)_{average}$	Φ_B
.61	159.5	.65	.39
3.14	175.0	.17	.27
.59	554.9	.70	.39
3.19	647.0	.13	.30

Table 6.4 and the value of Φ_A. The fraction of the total heat flow by the gas is $\frac{1}{1+\Phi_A}$ and the fraction of the total heat flow through the solid is $\frac{\Phi_A}{1+\Phi_A}$.

Thus the contributions shown in Table 6.4 are diminished by $\Phi_A/(1+\Phi_A)$ for gas flow through the bed. Under these conditions there is also no contribution from the gas parallel path but this has little effect. Thus using an average value $(\Phi_A)_{average}$, of 0.41 reduces the percentage contributions shown in Table 6.4 by multiplying them by the fraction 0.29.

6.5.2. Conduction-Convection Mechanisms for the Literature Experimental Results

(i) effective solid phase thermal conductivity from the diffusion model

There are no gas flow results in the literature at temperatures such that radiation is significant.

For countercurrent gas and heat flow Yagi, Kunii and Wakao (1960) and Ikeda, Nishimura and Kubota (1964) obtained linear increases in Y' with increased Reynolds number as is the case for the present cocurrent results. However the slope of the lines in the cocurrent case is greater than the slope for the countercurrent case. For the cocurrent case the gas temperature is above the solid temperature (since $t_o^* > 1$ in these experiments) while for the countercurrent case the solid temperature is above the gas temperature. Thus in the cocurrent case the gas-solid heat transfer increases the

solid phase heat flow and thus the effective solid thermal conductivity is greater in comparison with the countercurrent case where the solid-gas heat transfer gives a lower solid phase heat flow and hence a lower effective solid conductivity.

(ii) effective solid phase thermal conductivity from the mixing cell model

The countercurrent data of Yagi, Kunii and Wakao (1960) enabled the mixing cell model to be applied to a greater range of Reynolds numbers (1.03 - 52.3) than was possible in the present experimental work. Yagi, Kunii and Wakao also used packings with both high and low thermal conductivities. To apply the mixing cell model to these results the following assumptions were made.

a) The experimental temperature profiles were assumed to be gas temperature profiles since the thermocouples were placed in the voids and would thus have indicated a temperature closer to the gas temperature than the solid temperature. Radiation effects could be regarded as negligible since the maximum temperature was 140°C. In any case the alternative assumption that the experimental temperatures were the solid temperatures only gave a .3% difference in the values of Y given by the model.

b) The experimental results were given in the form of a temperature gradient (on a semi-logarithmic plot) determined from the temperature readings in the upper section of the bed. In applying the mixing cell model it was assumed that this section was one third of the bed length.

c) The temperature difference between the solid temperatures at the ends of the bed, $(T_o - T_m)$, was assumed equal to the difference between the gas inlet temperature and the hot-face thermocouple reading.

d) The values of the convection parameter, H, were determined from equation 6.14. Since Fig. 2.9 shows that the Peclet number has attained the limiting constant value for this range of Reynolds numbers equations 4.82 and 2.5 were used to evaluated the number of mixing cells, m.

The values of the conduction parameter, K, were then obtained by applying a regression technique similar to that described in 6.5.1(ii) to one third of the bed length at the hot-face end. The model temperature gradient (on a semi-logarithmic plot) was calculated from the slope of the least squares line through the cell gas temperature values. Since K was approximately proportional to this gradient, comparison with the experimental gradient enabled an improved estimate of K to be made. This process was repeated until good agreement of the model and experimental gradients was obtained.

From Table 6.7 it is seen that K is inversely proportional to Reynolds number indicating that the limiting values of k_{es} and Y have been reached for the Reynolds number range of the results (Fig. 6.44). It is seen that the increased conduction with gas flow in the bed as characterised by the ratio Y/Y_0 is approximately constant (1.5 - 1.8) for all granular packings with a slightly lower value for Raschig

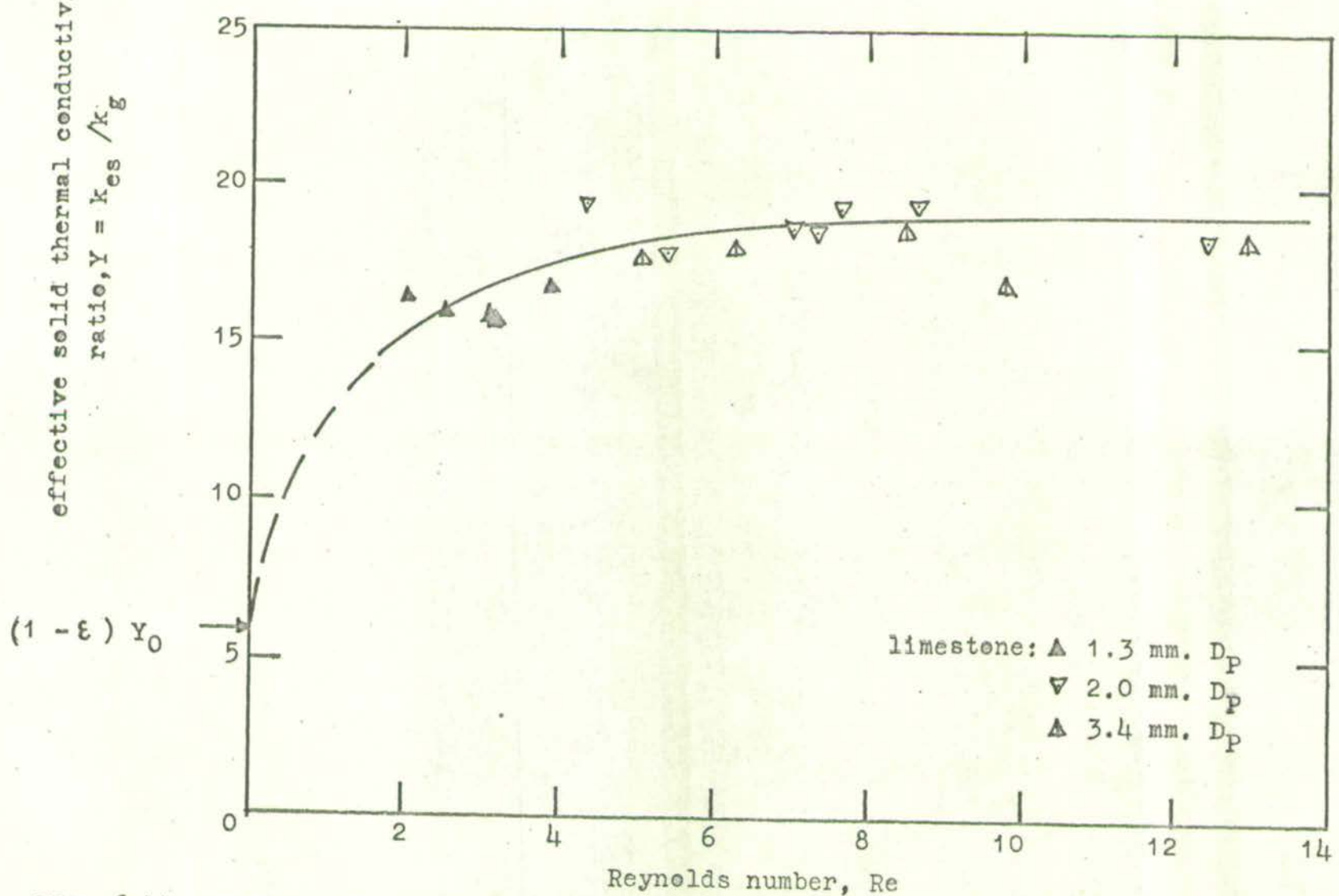

FIG: 6.44 MIXING CELL MODEL EFFECTIVE SOLID THERMAL CONDUCTIVITY RATIOS FOR THE DATA OF YAGI, KUNII AND WAKAO (1960)

rings (≈1.2). These countercurrent gas and heat flow ratios are lower than the cocurrent values for the present experiments (≈3.1 at a comparable temperature level). This indicates that there is solid conduction path interaction with the increased solid heat flow due to gas-solid heat transfer in the cocurrent case and with the decreased solid heat flow due to solid-gas heat transfer in the countercurrent case. It is also observed that Y'/Y_0 (= $(1 - \varepsilon)Y/Y_0$) ≈ 1 for the countercurrent results so that based on the complete bed area the conduction heat transfer in the bed with gas flow is the same as in the stagnant bed. This agrees with a reported analysis of Hiby and Schummer.

Fig. 6.45 shows values(for one packing)of the ratio H/K which is a measure of the relative importance of solid-gas convection compared with conduction. The increase in H/K with Reynolds numbers is most pronounced at low values of Reynolds number as would be expected.

(iii) <u>solid-gas temperature difference from the mixing cell model</u>

Fig. 6.46 shows that the solid gas temperature difference at the hot-face end of the bed (Z = 1 for the countercurrent case) increases markedly with Reynolds number but is not very dependent on the solid particle thermal conductivity. For Re < 5 the values are similar to the present cocurrent results. For Re > 5 the values of t_m^* indicate that the assumption of equal solid and gas temperatures used by Yagi, Kunii and Wakao (1960) in applying the diffusion model was unjustified.

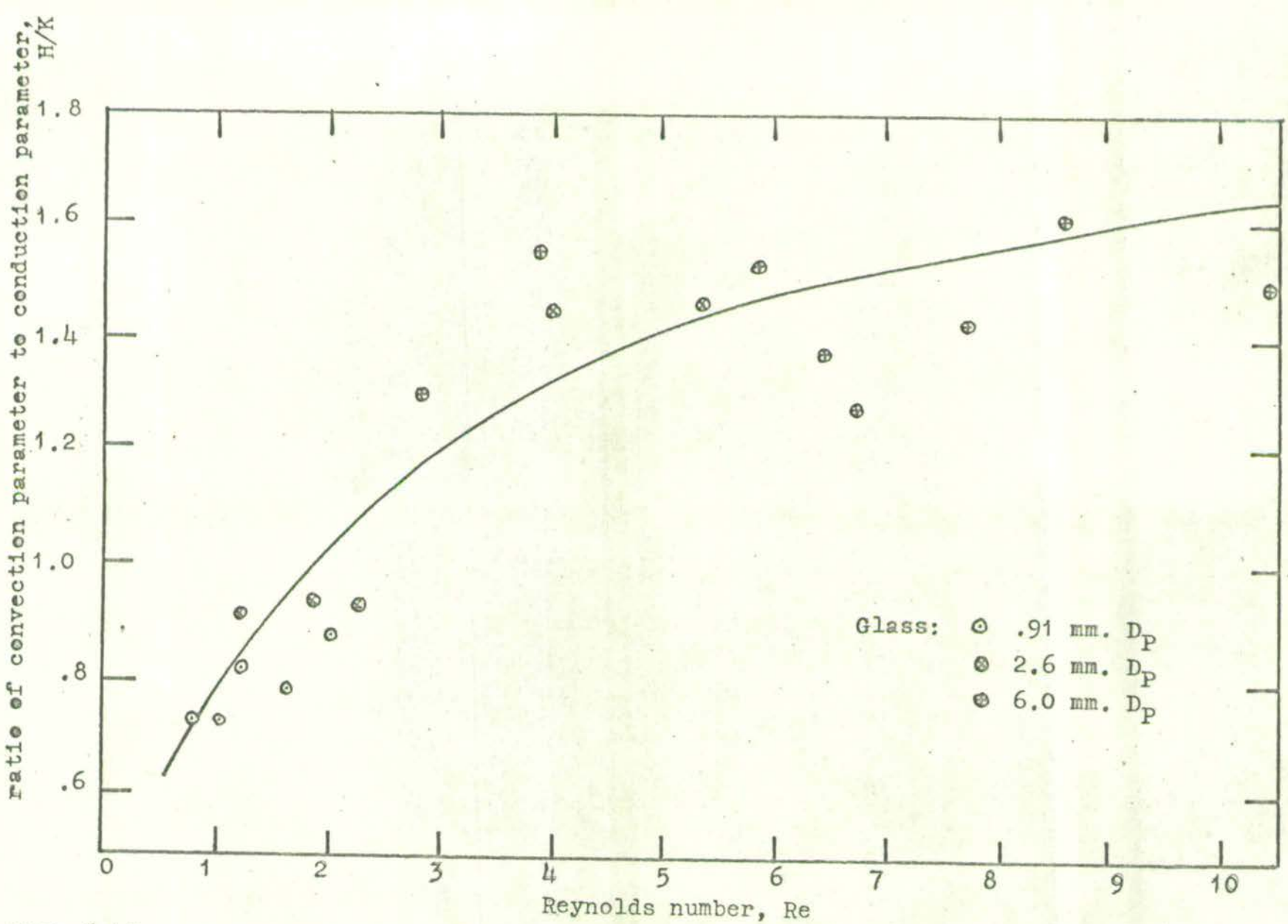

FIG. 6.45 MIXING CELL MODEL RATIO, H/K, FOR THE DATA OF YAGI, KUNII AND WAKAO (1960)

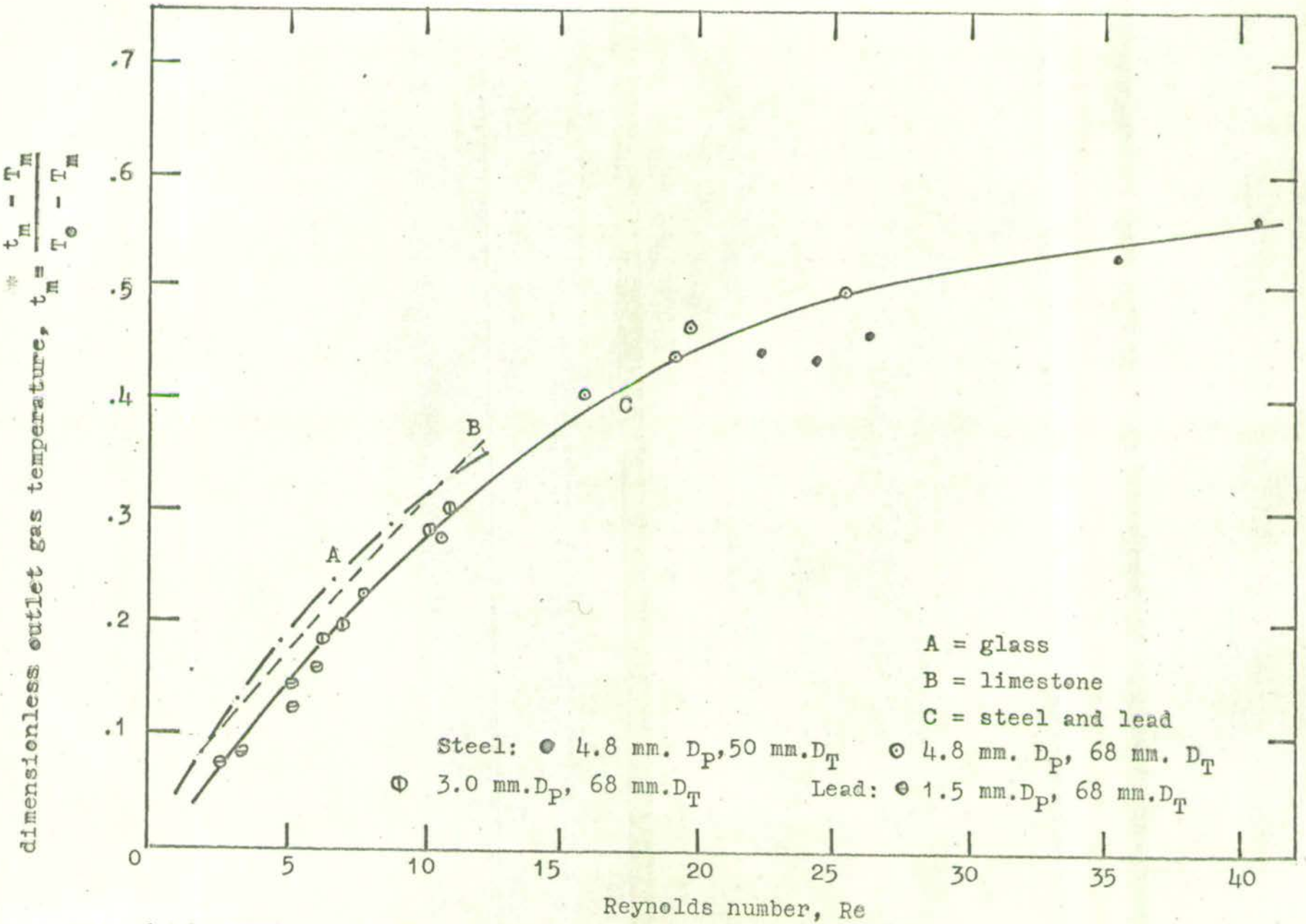

FIG. 6.46 MIXING CELL MODEL DIMENSIONLESS OUTLET GAS TEMPERATURES FOR THE DATA OF YAGI, KUNII AND WAKAO (1960)

(iv) heat flow rates from the mixing cell model

Values of the heat flow parameter N_Q^* obtained from equation 4.115 were correlated for different particle sizes by plotting ln (N_Q^*/m) against the Reynolds number (Fig.6.47). The decreased value of N_Q^* with smaller particle size (increased number of mixing cells, m, for the same bed length) or higher solid thermal conductivity is a measure of the increased axial heat flow rates under these conditions .

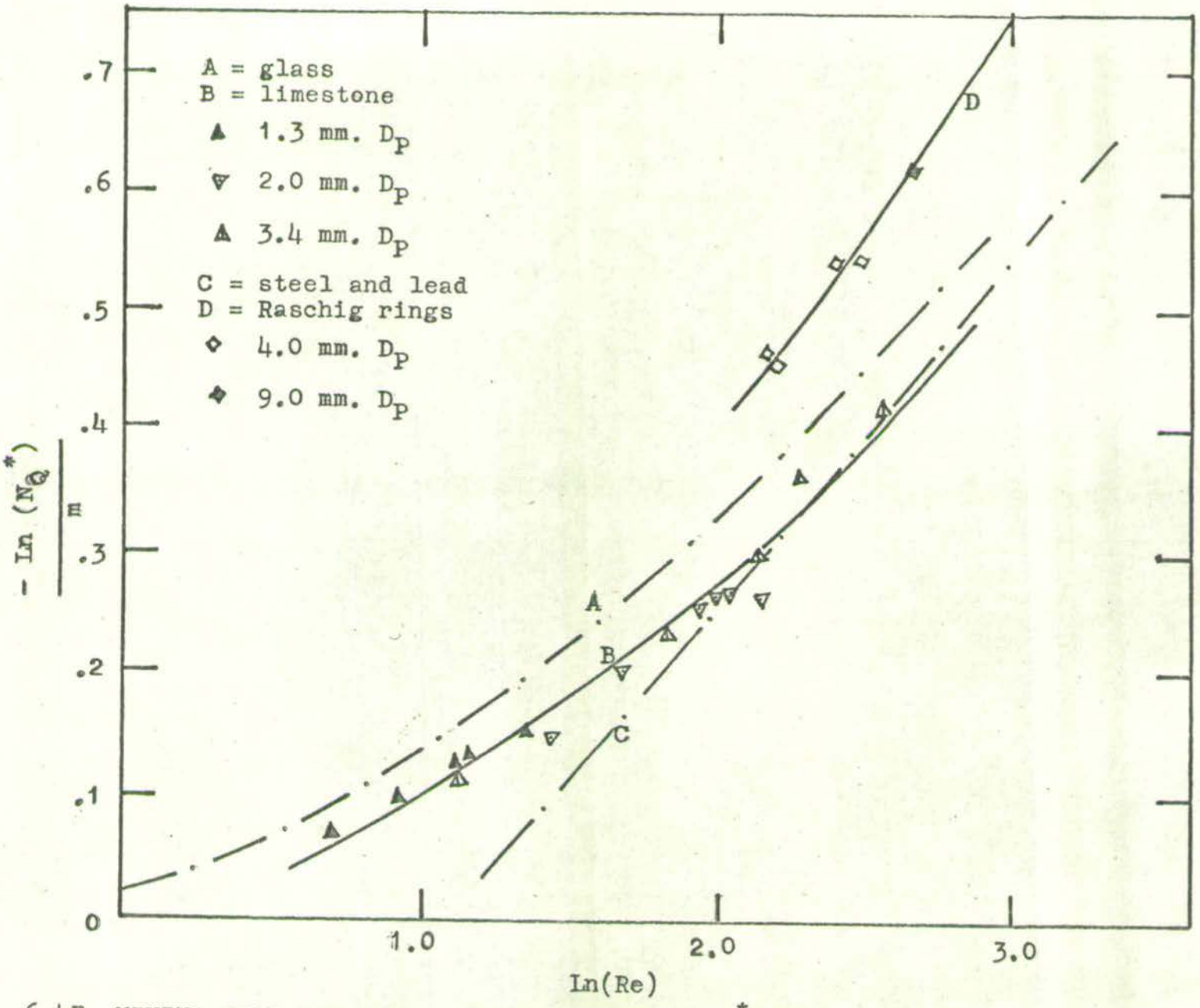

FIG. 6.47 MIXING CELL MODEL HEAT FLOW PARAMETER, N_Q^* FOR DATA OF YAGI, KUNII AND WAKAO(1960)

CHAPTER 7 CONCLUSIONS

7.1. LOCAL PACKING STRUCTURE AND ITS EFFECT ON LOCAL HEAT TRANSFER

In order to predict the effect of the local packing structure on the geometric and heat transport properties which determine axial heat flow, the local mean voidage with reference to a base sphere in a randomly packed bed of equal - sized spheres has been estimated in three ways, each based on a different experimental measurement. The co-ordination number approach gives the probability distribution at each distance from the base sphere while the sphere centre and integrated local voidage approaches only give the mean value at each distance.

The probability distributions show good qualitative agreement with available two-dimensional distributions and are similarly skewed due to the existence of a definite lower voidage limit dictated by the closest possible local packing, while the upper limit varies for each co-ordination number. Over a region of two sphere diameters (R = 1.0) around any sphere centre the standard deviation in the local mean voidage is eight to fourteen per cent about the mean value while the standard deviation of the bulk mean voidage on the other hand is only 0.41%. The choice of R equal to unity to define the unit cell is confirmed by the correspondence of the local mean voidage values with bulk mean voidage values, both for each value of the co-ordination number and for the complete distribution. For this unit cell the triangular closepacked and equispaced models give the basis

for suitable local regular packing models to define the limits of close and loose random packing.

The local voidage fluctuates with distance from the base sphere in a similar manner to that for spheres packing randomly against a cylindrical wall but the fluctuations decay more rapidly. The mean value of the local mean voidage also fluctuates with distance and the variation given by the co-ordination number method agrees well with that using the sphere centre data, and is similar to that for spheres packing randomly against a cylindrical wall.

It has been shown that the local variation in structural and transport properties of a packed bed can be calculated from the local mean voidage distribution. The standard deviations of these local properties generally vary from 3 - 25% of the mean values and the property distributions are skewed in a similar manner to the local mean voidage distributions. One exception is the pressure drop variation which is 54 - 72% of the mean value. The theoretical distribution of void hydraulic diameters agrees well with an experimental distribution. The variation in heat transfer parameters is small for gas flow through the bed but significant for stagnant beds at low temperatures. At higher temperatures radiation tends to smooth out the local heat transfer variations.

7.2. EXPERIMENTAL TECHNIQUE

It has been demonstrated that a technique of thermocouple temperature measurement in solid particles within a packed bed surrounded by a guard bed and sectional heaters is suitable for obtaining temperature profiles under solely axial heat flow

conditions at temperatures up to 750°C. The major disadvantage of the method is the long time required to achieve steady state conditions after a heater adjustment due to the necessarily large heat capacity of the surrounding insulation jacket. The method is also necessarily restricted to low Reynolds numbers.

7.3. THEORETICAL MODELS

Conceptually simple models have been developed to evaluate axial heat transfer in packed beds under conditions such that conduction, conduction-radiation, conduction-convection and conduction-convection-radiation mechanism combinations are controlling. The suitability of these models has been verified by comparison with the present experimental results and with the low temperature, countercurrent results of Yagi, Kunii and Wakao (1960) who used a greater range of phase, structural and operating variables. The models account for the following variables: solid and gas thermal conductivities, bed radiation characteristics, voidage, particle size and shape, bed length, gas inlet or outlet temperature, solid particle temperature and axial temperature gradient, particle Reynolds number or gas pressure, directions of gas and heat flows.

7.4. HEAT TRANSFER MECHANISMS

Application of the theoretical models to the experimental results gave the following conclusions as to the contributions of the various heat transfer mechanisms (based on the percentage of the total heat flow passing through the mechanism path):

a) stagnant bed

(i) The gas parallel path accounts for less than 5% of the heat flow in all cases.

(ii) The majority of the heat flow passes through the solid series path but the proportion decreases as temperature increases.

(iii) The gas series path and the solid contact point path account for a significant proportion of the heat flow at lower temperatures.

(iv) At high temperatures both the inter-void and intra-void radiation mechanisms become very significant.

(v) For heating an unsealed packed bed from below natural convection through the bed can cause increased curvature of the temperature profile

b) gas flow through the bed

For gas flow through the bed significant gas-solid temperature differences can occur and these increase with Reynolds number. It is not generally justified to assume equal solid and gas temperatures and the gas-solid convection mechanism has a significant effect under all gas flow and temperature conditions.

For the average of the range of conditions of the present experiments about 30% of the heat flow occurs through the solid path by the conduction and radiation mechanisms present in the stagnant bed and about 70% by bulk gas flow convection. The gas flow percentage increases with Reynolds number but is little affected by temperature.

It is thus apparent that in high temperature reacting gas-solid systems convection, radiation and conduction mechanisms will all contribute to the axial heat transfer and for the usual industrial system conditions will be in this order of importance.

7.5. EVALUATION OF AXIAL HEAT TRANSFER IN PACKED BEDS

Axial heat transfer in packed beds may be evaluated in terms of a number of model parameters which may each account for only one heat transfer mechanism or which may lump together the effects of two or more mechanisms. From the comparison of the theoretical models and the experimental results it has been possible to build up a comprehensive picture of axial heat transfer for a stagnant bed and for both cocurrent and countercurrent gas and heat flow conditions.

For a stagnant bed a geometric model with no adiabatic boundaries within the solid phase was shown to effectively allow for flux line bending within the solid phase. This is particularly important under vacuum conditions which can be used to evaluate the contact area parameter. This model was extended to include inter-void and intra-void radiation at higher temperatures. Theoretical determination of the radiation parameter is not possible due to the complex and unknown dependence on view factors, emissivity factors and scattering factors.

For gas flow through the bed the heat transfer may be evaluated in three ways:

(i) Application of the diffusion model with equal gas and solid temperatures gives an effective solid thermal

conductivity ratio Y' (based on the bed area) which includes the conduction-radiation mechanisms and the gas-solid convection mechanism. The heat transfer due to the bulk gas flow is directly accounted for in the diffusion model solution. The value of Y' increases linearly with Reynolds number from the stagnant bed value Y_0 with a greater slope for cocurrent than for countercurrent conditions and for low temperatures than for high temperatures. Gas-solid heat transfer increases the solid path heat flow rate and hence the value of Y' for the cocurrent case compared with the reverse effect for the countercurrent case.

(ii) Application of the mixing cell model with $N_P^* = 0$ gives an effective solid thermal conductivity ratio Y (based on the solid area) which accounts for the conduction-radiation mechanisms. The solid-gas convection and the bulk gas convection are directly accounted for in the mixing cell model equations. For both cocurrent and countercurrent conditions Y increases from the stagnant bed value $(1 - \varepsilon) Y_0$ but tends to a constant value for $Re > 3$. This constant value is higher for cocurrent conditions ($Y/Y_0 = 3.1$ at low temperatures) compared with countercurrent conditions ($Y/Y_0 = 1.5 - 1.8$) due to solid conduction path interaction with the gas-solid heat transfer effects.

(iii) By equating effective conduction thermal conductivities under defined void gas mixing conditions, values of the mixing cell parameter N_P^* may be evaluated from the stagnant bed measurements. The value of N_P^* accounts for the contact

point conduction and the radiation mechanisms. The solid path conduction, gas-solid convection and bulk gas flow convection are directly accounted for by the mixing cell model equations. The best agreement of the cocurrent experimental profiles and the model profiles was obtained for the assumption of complete mixing of the parallel path gas.

7.6. SUGGESTIONS FOR FUTURE WORK

(i) Extension of the present work to obtain measurements of temperatures greater than 750°C would be desirable since the temperatures of interest in gas-solid reactions are as high as 1500°C. The main difficulty in using the present equipment for higher temperatures would be in materials of construction and in radial heater burn-out. More suitable refractory materials would have to be used in place of the Sindanyo box and a high temperature alloy in place of the expanded stainless steel discs. It is recommended that a vacuum jacket be installed around the bed in any future work to decrease the load on the radial heaters. It would also be necessary to have the thermocouples in loose holes in the particles to allow for expansion.

(ii) The aim in the present work has been to base the evaluation of model parameters as far as possible on known bed and phase properties such as voidage and thermal conductivities. It has not been possible to do this for contact point heat transfer and radiation heat transfer parameters. It would thus be desirable for specific studies to be made of these individual mechanisms to enable all parameters to be qualitatively predicted from known properties.

Much work, both theoretical and experimental, has recently been done on contact heat transfer for flat metallic surfaces. Similar studies need to be made to determine the effect of surface characteristics and loading properties on contact heat transfer in particulate systems.

For the radiation parameter information is required on view factors, emissivity factors and scattering factors. A study of light transmission on a local scale in various large scale model packings would be helpful in this respect. When such information is available attempts should be made to extend the mixing cell model along the lines indicated in Fig. 4.21 to specifically account for the radiation mechanisms. Efficient computing procedures should also be developed to enable the model to be applied to experimental results when the temperature dependence of the parameters along the length of the bed is allowed for.

(iii) The mixing cell model could profitably be applied to unsteady state heat transfer by using Laplace transform techniques to obtain solutions to the model equations for step changes or sinusoidal changes in the inlet conditions. Extension to two dimensional heat transfer should also be possible.

(iv) The local mean voidage distributions obtained from the local sphere shell models might profitably be used to develop a statistical theory for residence time distributions and for Peclet number values. This would allow for the statistical variation of local mixing cell volumes and hence variation in average velocities and residence times.

APPENDIX 1. DEFINITION OF THE GEOMETRIC PROPERTIES OF PACKED BEDS

(with particular reference to beds of equal-sized spheres)

(i) Bulk Properties

These properties apply to the bed as a whole.

Overall voidage, ε_0: the fractional free volume of a packed bed in a container.

Bulk mean voidage, ε: the fractional free volume in an effectively infinite bed which is not affected by the presence of external surfaces.

Number of spheres in the bed, N_S: Since the volume of one sphere is $\pi D_P^3/6$ and the solid voume per unit bed volume is $1 - \varepsilon$ it follows that $N_S = 6(1 - \varepsilon)/\pi D_P^3$ ....(A.1)

Solid surface area, S: Since the surface area of one sphere is πD_P^2 it follows that

$$S = N_S \cdot \pi D_P^2 = 6(1 - \varepsilon)/D_P \quad \text{....(A.2)}$$

Layer Spacing, βD_P: The average distance between particle centres in two successive layers of particles (effective or pseudo-layers in the case of random packing) which defines the length of a unit cell.

(ii) Local Properties

These properties apply to a local portion of the bed.

Inter-particle distance, RD_P: The position coordinates of neighbouring particles relative to a given particle completely define the local structure of a packed bed and determine the radial distribution of the distance RD_P between the centre of a base sphere and the centres of surrounding spheres in the neighbourhood.

Coordination number, n: the number of points of contact between a particle and adjacent particles.

Contact angle, θ_n: The angle subtended at the centre of a particle by two adjacent points of contact.

Local voidage, ε', ε'_R and local area fraction, ε'_A, ε'_{AR}:

In general the local voidage, ε', is the fractional free volume in an element of bed volume, as in a thin strip or shell. For spherical coordinates the local voidage, ε'_R, is the fractional free volume in a spherical shell of radii $(R \pm \delta) D_p$ measured from the centre of a base sphere as shown in Fig. 2.1. As the volume of the element is decreased to its zero limit the local voidage tends to the point voidage. Alternatively as the width of the element is decreased to zero the local voidage tends to the local free area fraction ε'_A or ε'_{AR} for spherical coordinates.

Local mean voidage, $\bar{\varepsilon}$, $\bar{\varepsilon}_R$ and local mean wall voidage, $\bar{\varepsilon}_W$:

In general the local mean voidage, $\bar{\varepsilon}$, is the fractional free volume in a local region of the bed volume, V', consisting of the local elements between a reference point and the outer limit of the region of interest. For spherical coordinates the local mean voidage, $\bar{\varepsilon}_R$, is the fractional free volume within a spherical envelope of radius RD_p from the centre of the base sphere (Fig. 2.1). The value of R is chosen so as to define the volume within which the local packing configuration influences the local mean transfer coefficients at the surface of the base sphere. For the investigation of local effects adjacent to the base sphere, reasonable limits for R are $\frac{1}{2} < R < \frac{3}{2}$ with $R = 1$ being a representative value. For the local mean wall voidage, $\bar{\varepsilon}_W$ the container wall forms the outer limit of the local bed volume element. For regular packings the inner limit of the local wall region may be defined as the outer limit of the first complete unit cell. The relationships between the local, local mean and bulk mean voidages are

$$\bar{\varepsilon} = \int_0^{V'} \frac{\varepsilon' dV'}{V'} \qquad \ldots.(A.4)$$

and

$$\varepsilon \approx \sum \bar{\varepsilon} V' / \sum V' \qquad \ldots.(A.5)$$

APPENDIX 1 (Continued)

Local hole size, D_H, and volume, V_H: The diameter of a spherical hole associated with a particular sphere may be defined from the relationship

$$V_H = \frac{\pi D_H^3}{6} = \left(\frac{\bar{\varepsilon}}{1 - \bar{\varepsilon}}\right) \frac{\pi D_P^3}{6} \qquad \ldots.(A.6)$$

therefore

$$D_H = D_P \left(\frac{\bar{\varepsilon}}{1 - \bar{\varepsilon}}\right)^{\frac{1}{3}} \qquad \ldots.(A.7)$$

Other definitions are given by Scheidegger (1960) and Prager (1963).

The zeroth moment of the hole void volume distribution is the bulk mean voidage, ε.

$$M_0 = \int_0^\infty f_{V_H} \, d V_H = \varepsilon \qquad \ldots.(A.8)$$

Thus since $\bar{\varepsilon}^* \approx \varepsilon$, $f_{V_H} \, dV_H = f_{\bar{\varepsilon}} \cdot d\bar{\varepsilon}$ $\ldots.(A.9)$

The first moment determines local concentration and temperature fluctuations (Lamb and Wilhelm (1963)) and is thus given by

$$M_1 = \int_0^\infty V_H \, f_{V_H} \, dV_H = \int_0^\infty \frac{\pi D_P^3}{6} \left(\frac{\bar{\varepsilon}}{1 - \bar{\varepsilon}}\right) f_{\bar{\varepsilon}} d\bar{\varepsilon} \ldots.(A.10)$$

APPENDIX 2. STRUCTURE OF REGULAR PACKINGS OF EQUAL-SIZED SPHERES

The fundamental building block is a row of contacting spheres with their centres arranged in a straight line. Contacting rows of spheres arranged parallel to each other in the same plane form a layer. There are two limiting layer forms (Fig. A.1, A.2); firstly, the square layer where the angle of intersection of the rows is 90°; secondly, the triangular or simple rhombic layer where the angle of intersection of rows is 60°. Any number of special rhombic layer forms with intersection angles between these two values are possible but the most commonly used regular packings are built up from either of the limiting layer forms.

Fig. A.1 and A.2 illustrate the three stable ways in which two square or triangular layers may be stacked relative to each other.

(i) Each second sphere is placed vertically above a first layer sphere (square stacking 1 and triangular stacking 1).

(ii) Each second layer sphere is placed in a saddle formed between two contacting first layer spheres. For square layers only every second saddle is filled, thus forming either square stacking 2 or 3. For triangular layers only every third saddle is filled thus forming either triangular stacking 2, 3 or 4.

(iii) Each second layer sphere is placed in the hole formed between contacting spheres of the first layer. For square layers every hole formed from four first layer spheres is filled (square stacking 4). For triangular layers only every second hole formed from three first layer spheres is filled thus forming either triangular stacking 5 or 6.

A regular packing is built up by a vertical stacking of layers in a repeating pattern of some of the relative stackings listed above. The order of the packing is the number of layers in a repeating pattern. The most common

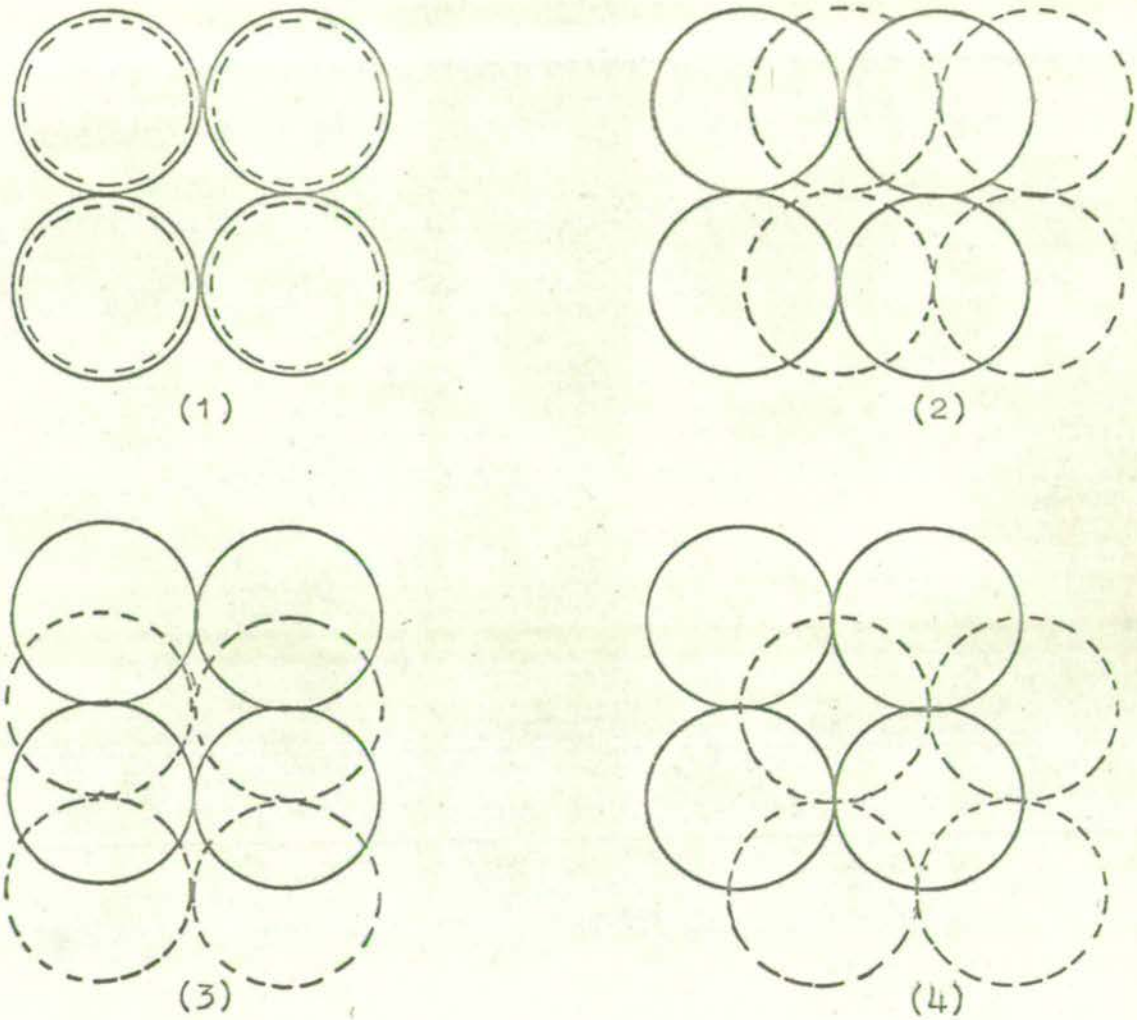

FIG. A.1 RELATIVE SQUARE LAYER STACKINGS IN REGULAR PACKINGS OF SPHERES

——— consecutive layers
- - - - -

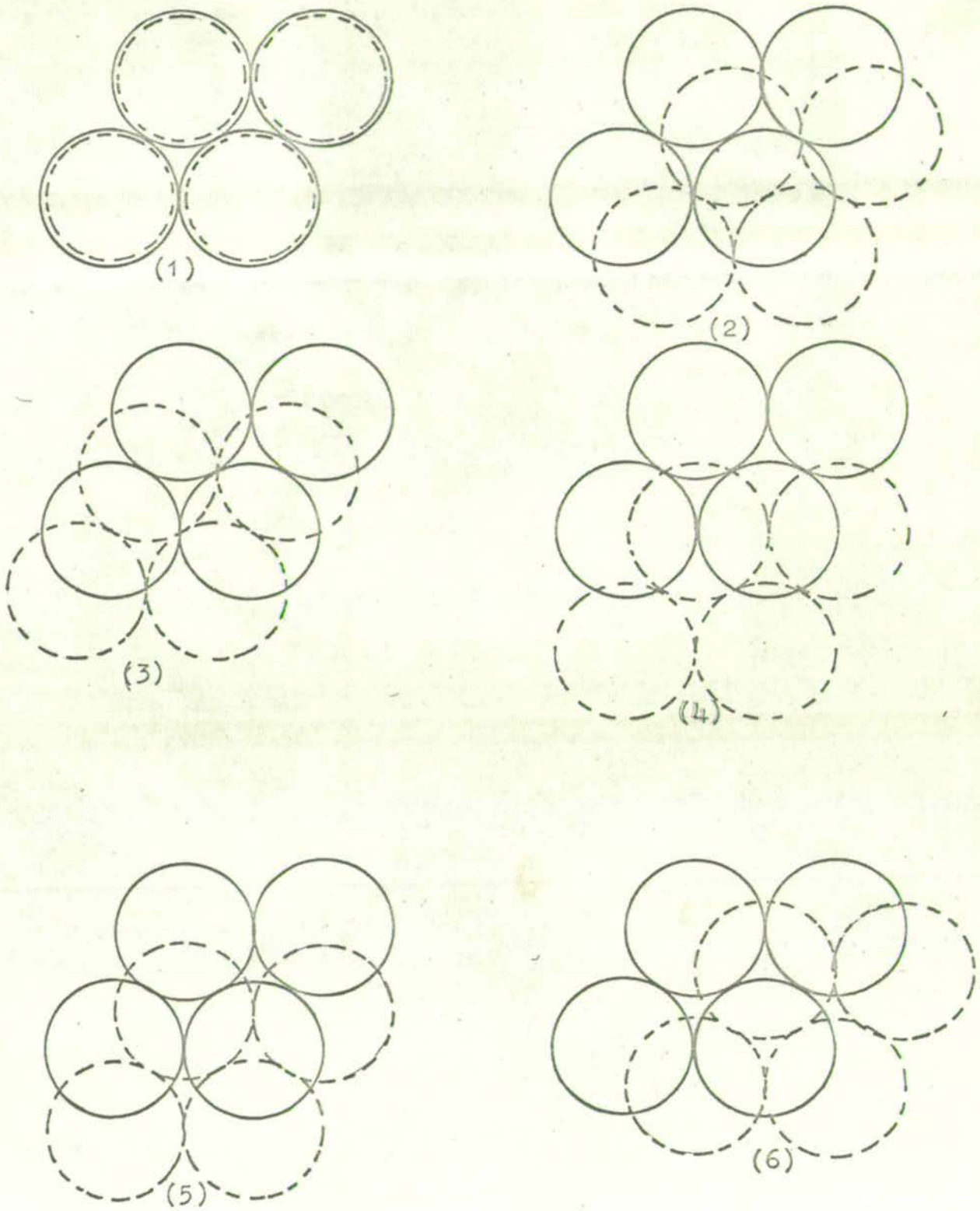

FIG. A.2 RELATIVE TRIANGULAR LAYER STACKINGS IN REGULAR PACKINGS OF SPHERES

——— consecutive layers

- - - - -

APPENDIX 2 (Continued)

regular packings are first, second and third order packings (Table 2.1). These may be grouped into cubic, orthorhombic, tetragonal-sphenoidal and rhombohedral packings which have distinct internal configurations and hence distinct bulk mean voidage values. There are only these four distinct packings since several of the possible patterns of relative sphere stackings produce packings with identical internal structures which differ only in their orientation with respect to the base plane on which the packing is built up. The difference in orientation is in some cases reflected in either a clear passage or a blocked passage for fluid flowing through the voids from a direction perpendicular to the base plane.

There are also various types of open structured regular packings which are relatively loose arrangements in which at least some of the spheres would be free to move with respect to each other if they were not constrained from doing so by a bonding force operating at the point of contact between spheres, as, for example, in crushing (Meissner, Michaels and Kaiser (1964)) and in flocculation (Hutchinson and Sutherland (1965)).

The unit cells of the regular packings described in Table 2.1 are bounded by six planes which pass through the centres of adjacent spheres and form a parallelopiped of edge length D_p. The unit cells contain parts of eight spheres which total one complete sphere. The unit voids consist of a large void bounded by several connecting channels which may be "square" (bounded by four spheres) or "triangular" (bounded by three spheres). The cross sectional areas of the channels between voids are much smaller than the mean cross-sectional area of the void. Graton and Fraser (1935) give an extensive description of the various unit cells and unit voids.

The problem of obtaining the densest regular packing of spheres in a finite container of definite shape has been studied for the cases of a cubical box (e.g. Brown and Hawksley (1946)), a cylinder (Supnik (1949)) and a sphere (Hadwiger (1952)).

APPENDIX 3. LOCAL VOIDAGE VARIATION IN A RANDOMLY PACKED BED OF EQUAL-SIZED SPHERES

A3.1. LOCAL MEAN VOIDAGE DISTRIBUTION - CO-ORDINATION NUMBER BASIS

Although the co-ordination number, n, is not a direct indication of local voidage (MacCrae and Gray (1961)), since it is possible to distort the packing and change the voidage without altering n, it is possible to derive maximum and minimum limits for the local mean voidage for a given n by consideration of geometric packing models. Spheres which lie close to the base sphere but do not touch it are not included in n. To include their contribution to local voidage it is assumed that the voidage for a given n is normally distributed about the mean of these limits. The probability distribution of the local mean voidage may then be derived from the available data (2.1.4) on the frequency distribution of n for a random bed.

A3.1.1. Local packing models for assemblies of equal-sized spheres

A random bed would not be expected to have any recognisable pattern on the large scale, but when viewed locally relative to a particular single sphere, unit cells will be found which are repeated throughout the random structure. The present approach describes the unit cell in terms of shells of spheres arranged around the reference or base sphere. The first shell refers to those spheres placed on the surface of the base sphere while the second shell refers to those spheres which fit into the holes in the first shell layer but which do not touch the base sphere.

In regular packings the spheres are placed uniformly in plane layers. Thus application of the present spherical model to these packings implies that second shell penetration will commence at varying values of R_2 depending upon the angular view. A cubic packing will have six first shell spheres, and two sets of effective second shell spheres (twelve at $R_2 = 0.914$ and eight at $R_2 = 0.1233$). Similarly for a blocked passage tetrahedral packing with twelve first shell spheres, there will be four sets of second shell spheres,

APPENDIX 3 (Continued)

six at $R_2 = 0.914$ in the square holes formed by sets of four first shell spheres, twelve at $R_2 = 1.133$ in the triangular holes formed by sets of three first shell spheres, twelve at $R_2 = 1.234$ and twelve at $R_2 = 1.50$.

On the other hand for random packings it would be advantageous to use a simpler unit cell model which referred to first and second shell spheres centred at certain fixed distances from the base sphere. The unit cell can then be used for any physically possible value of n (regular unit cells are only valid for even values of n) and the single parameter R can define the geometric properties of the system at a given distance from the reference point. Two such models are now proposed - the triangular close packed and the triangular equispaced models. In both models the n first shell spheres are placed on the base sphere to form p triangular holes into which the second shell spheres are placed. It is not necessary to consider further shells since the models are intended for local effects near the base sphere, for example, $R < 1.5$, and would not be used for extrapolation purposes.

The local mean voidage within a spherical envelope of radius R sphere diameters from the base sphere centre is given for either model by

$$\overline{\varepsilon}_R = \frac{(\text{volume of spherical envelope - volume of solid within envelope})}{(\text{volume of spherical envelope})}$$

Thus in the first shell $(R_1 < R < R_2)$

$$\overline{\varepsilon}_R = 1 - \frac{1 + nV_1}{8R^3} \qquad \ldots.(A.11)$$

and in the second shell $(R_2 < R < R_3)$

$$\overline{\varepsilon}_R = 1 - \frac{1 + nV_1 + pV_2}{8R^3} \qquad \ldots.(A.12)$$

where V_1 and V_2 are defined in A3.4.1.

APPENDIX 3 (Continued)

a) Triangular close packed model

In this model the first three of the n spheres are placed together on the base sphere surface in a close packed triangular cluster. The additional first shell spheres are then added successively to this cluster to form further such triangular holes so that each additional sphere touches at least two others in the first shell. The p second shell spheres are then placed in each of the triangular holes so formed.

The local mean voidage as given by equations (A.11) and (A.12) is plotted in Fig. A.3 as a function of n and R, the shell limits being $R_2 = 1.1327$, $R_3 = 1.4915$ (A3.4.2).

b) Triangular equispaced model

The n first shell spheres do not touch each other but are spaced equi-distant from each other over the whole of the surface of the base sphere. The p second shell spheres are placed in each of the triangular holes so formed. Thus the effect of increasing n by one is a complete rearrangement of the packing spheres compared with the close packed model where an additional triangular first shell hole accommodating a further second shell sphere is simply added to the cluster.

For $n \gg 6$ the second shell spheres do not touch the base sphere but for $n = 3, 4, 5$ the triangular holes are large enough for them to do so. Thus since $p = 2n - 4$ (A3.4.2) the packing for $n = 5$ reverts to that for $n = 5 + p = 11$. Similarly the case for $n = 4$ is given by $n = 4 + p = 8$ and $n = 3$ is given by $n = 3 + p = 5$ which is equivalent to $n = 11$.

The local mean voidage given by equations (A.11) and (A.12) is plotted in Fig. A.4 as a function of n and R, the shell limits R_2, R_3 (A3.4.2) being given in Table A.1 for each n.

A3.1.2. Application of models to packing limits for a given n

Fig.2.1 shows the local voidage envelope around a sphere for a coordination number n of 3. Other spheres

Table A.1. Shell limits for triangular models.

Model	n	R_2	R_3
Equispaced	6	0.6547	1.2629
	7	0.7824	1.3559
	8	0.8761	1.4089
	9	0.9479	1.4410
	10	1.0048	1.4613
	11	1.0510	1.4747
	12	1.0893	1.4836
Close packed	all	1.1327	1.4915

Table A.2. Mean value and standard deviation of local mean voidage (R = 1.0) for random packings.

Packing	ε	$\overline{\varepsilon}^*$	$\sigma_{\overline{\varepsilon}}$	$\sigma_{\overline{\varepsilon}}/\overline{\varepsilon}^*$
Close random	.36	.3584	.04530	.1264
Poured random	.375	.3638	.05077	.1396
Loose random	.40	.3820	.05271	.1380

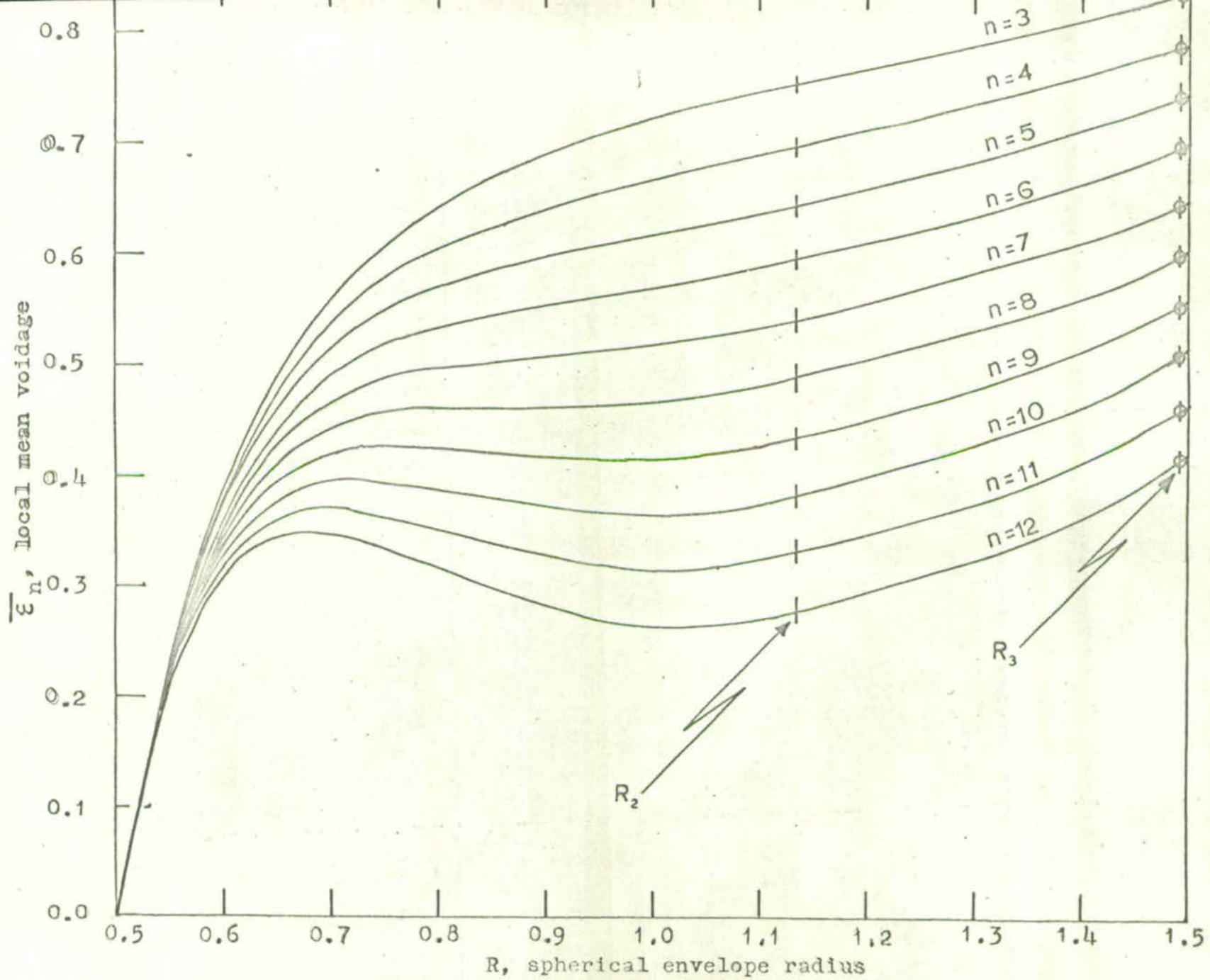

FIG. A.3 LOCAL MEAN VOIDAGE, $\overline{\varepsilon}_n$ FOR COORDINATION NUMBER n - TRIANGULAR CLOSE-PACKED MODEL

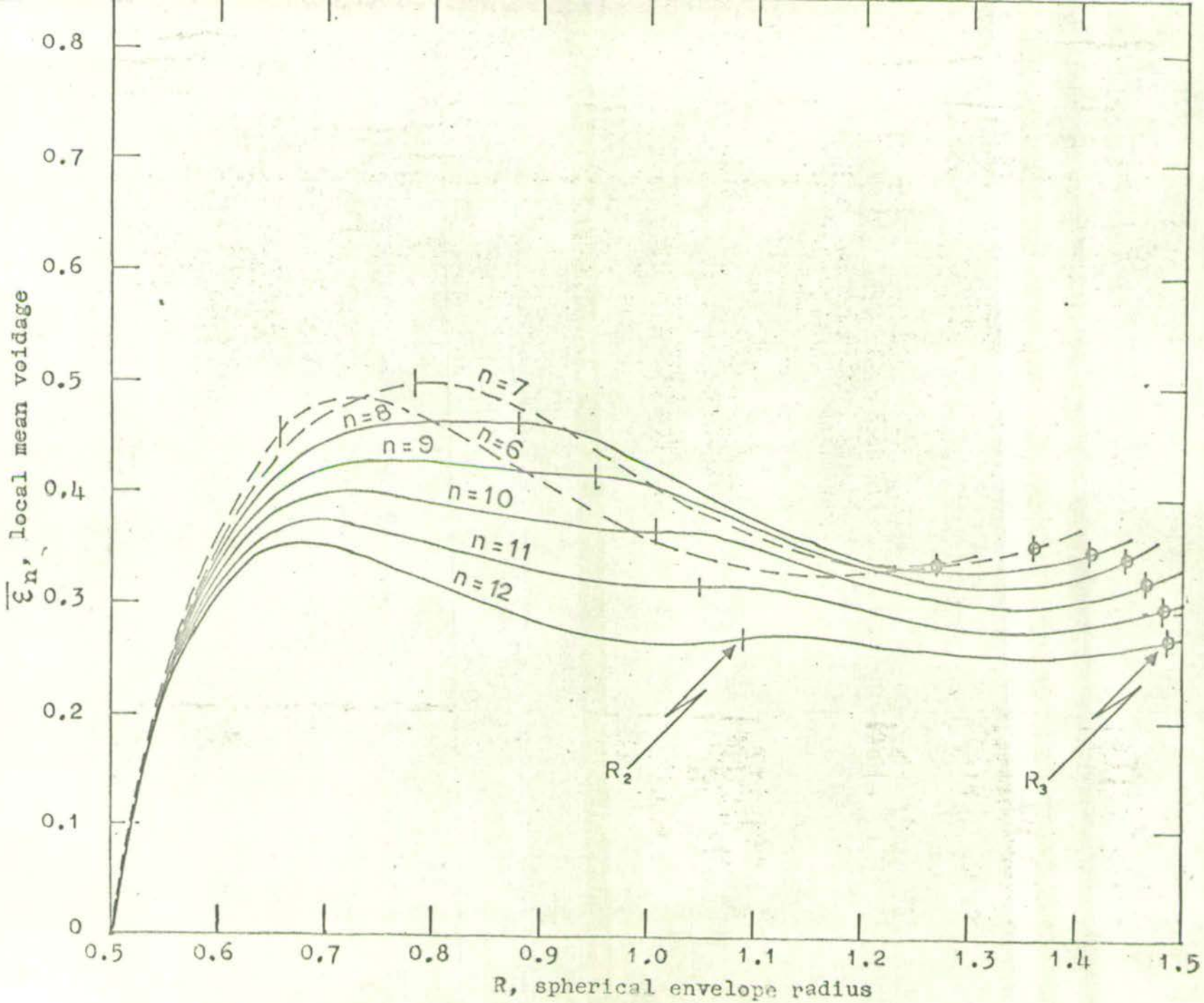

FIG.A.4 LOCAL MEAN VOIDAGE, $\overline{\varepsilon}_n$, FOR COORDINATION NUMBER n - TRIANGULAR EQUI-SPACED MODEL

besides the three contacting spheres may penetrate the local envelope as shown. However the maximum local mean voidage, $\overline{\varepsilon}_{na}$, is obtained when only the n contacting spheres penetrate the local voidage envelope with all other surrounding spheres bridging the holes outside of the envelope. In contrast the minimum local mean voidage, $\overline{\varepsilon}_{nb}$, is obtained when as many spheres as possible touch or almost touch the base sphere. Since the maximum value of n is 12 this situation is obtained when n spheres touch the base sphere and 12-n spheres just fail to touch.

Thus the value of $\overline{\varepsilon}_{nb}$ for any n is given by equation (A.11) with n = 12 in the first shell, $\frac{1}{2} < R < R_2$. Since for n = 12 the triangular equispaced model gives the densest possible local packing, the outer limit of the first shell will be $R_2 = 1.0893$ and in the second shell, $1.0893 < R < 1.4836$, $\overline{\varepsilon}_{nb}$ is given by equation (A.12) with n = 12, p = 20. The line for n = 12 in Fig. A.4 thus represents $\overline{\varepsilon}_{nb}$ for both shells, $0.5 < R < 1.4836$.

In the first shell (as defined above) $\overline{\varepsilon}_{na}$ is given by equation (A.11) using the appropriate value of n. In the second shell continued use of the close packed model would imply an unrealistic amount of bridging. Thus for the second shell the equispaced model is used for $\overline{\varepsilon}_{na}$ as given by euqation (A.12) with the appropriate values of n and p. Thus $\overline{\varepsilon}_{na}$ is given by the appropriate n curve in Fig. A.3 for $0.5 < R < 1.0893$ and in Fig. 4 for $1.0893 < R < 1.4836$.

A3.1.3. Estimation of local mean voidage distribution

Since it is assumed that, for each n, $\overline{\varepsilon}$ is normally distributed between $\overline{\varepsilon}_{na}$ and $\overline{\varepsilon}_{nb}$, we get the mean value $\overline{\varepsilon}_n^*$ as

$$\overline{\varepsilon}_n^* = (\overline{\varepsilon}_{na} + \overline{\varepsilon}_{nb}) / 2 \qquad \ldots.(A.13)$$

The graph (Fig. 2.4) of the values for R = 1.0 is very close to the line of best fit through the experimental measurements of mean co-ordination number and bulk mean voidage.

To define a probability distribution it is necessary to define the standard deviation $\sigma_{\overline{\varepsilon}_n}$. In experiments on

APPENDIX 3 (Continued)

multiple re-packing of a random bed Denton (1957) obtained a standard deviation of 0.41% of the mean value of the bulk mean voidage for a range of 2.3%. Hence the range was $5.62\,\sigma_{\varepsilon}$. It is assumed here that the range, $\overline{\varepsilon}_{na} - \overline{\varepsilon}_{nb}$, is $6\,\sigma_{\overline{\varepsilon}_n}$ implying that 99.73% of the area under the probability curve lies between the $\overline{\varepsilon}_{na}$, $\overline{\varepsilon}_{nb}$ limits. The probability of a local mean voidage for a co-ordination number of n is then

$$f_{\overline{\varepsilon}_n} = \frac{\exp\left[(\overline{\varepsilon}_n - \overline{\varepsilon}_n^{*})^2 / 2\,\sigma_{\overline{\varepsilon}_n}^{2}\right]}{\sigma_{\overline{\varepsilon}_n}\sqrt{2\pi}} \qquad \ldots\ldots(A.14)$$

where $\sigma_{\overline{\varepsilon}_n} = (\overline{\varepsilon}_{na} - \overline{\varepsilon}_{nb})/6$, values of $f_{\overline{\varepsilon}_n}$ being plotted in Fig. A.5 for R = 1.0.

Since the bed contains a known distribution, F_n, of values of n (Fig. 2.3) the complete local mean voidage distribution may then be found to be

$$f_{\overline{\varepsilon}} = \sum_{n=3}^{12} F_n \, f_{\overline{\varepsilon}_n} \qquad \ldots\ldots(A.15)$$

The distributions of $f_{\overline{\varepsilon}}$ for close, poured and loose random packings are given in Fig. 2.6 for R = 1.0. The effect of R ($0.5 < R < 1.4836$) on the distribution of $f_{\overline{\varepsilon}}$ for close random packing is given in Fig. A.6.

The mean value of the local mean voidage can be calculated from

$$\overline{\varepsilon}^{*} = \sum_{n=3}^{12} F_n \, \overline{\varepsilon}_n^{*} \qquad \ldots\ldots(A.16)$$

The values compare quite well with experimental data on bulk mean voidage (Table A.2). The standard deviation of the distribution can be written as

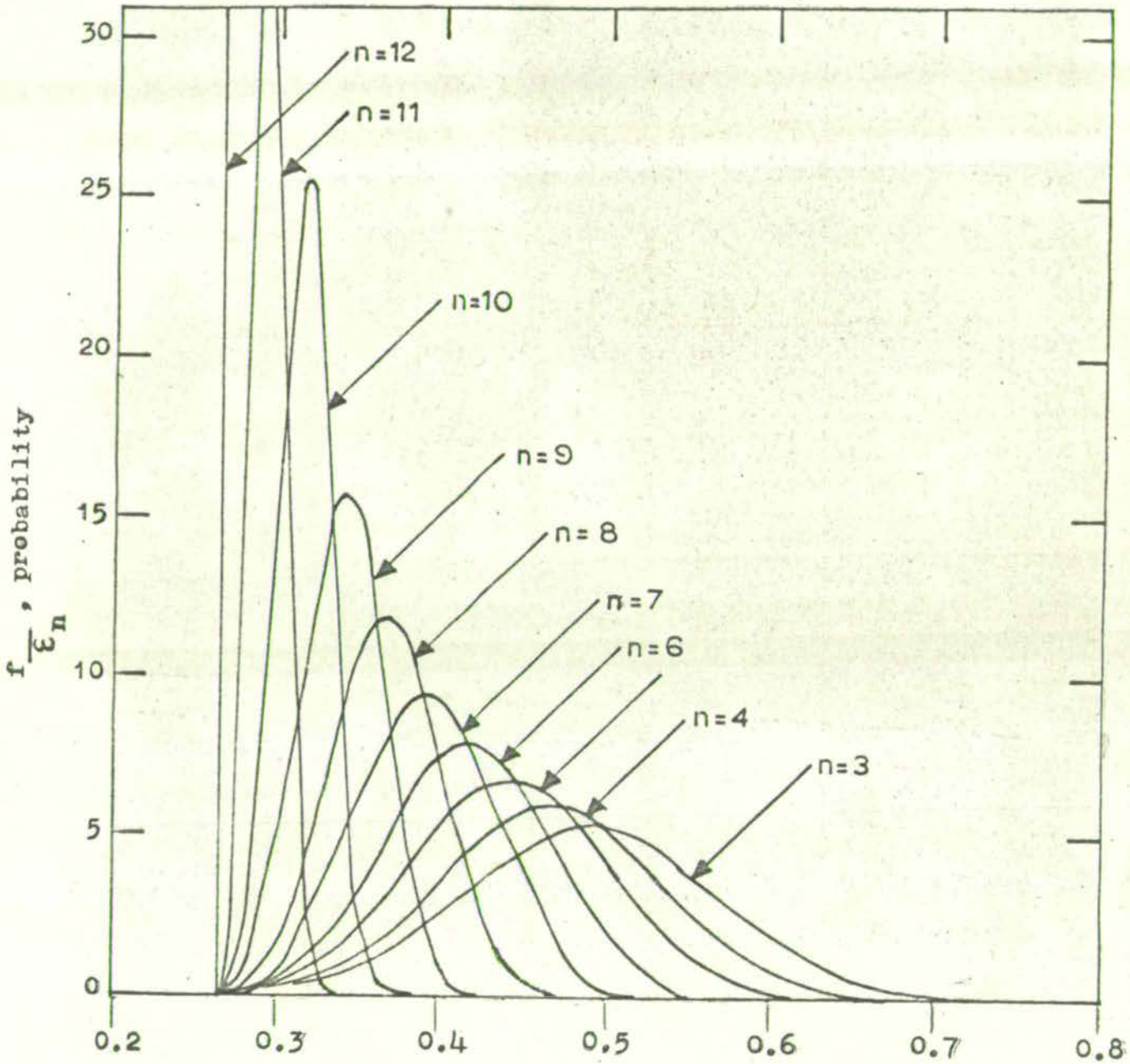

FIG. A.5 EFFECT OF COORDINATION NUMBER, n, ON LOCAL MEAN VOIDAGE PROBABILITY DISTRIBUTION, $f_{\overline{\varepsilon}_n}$

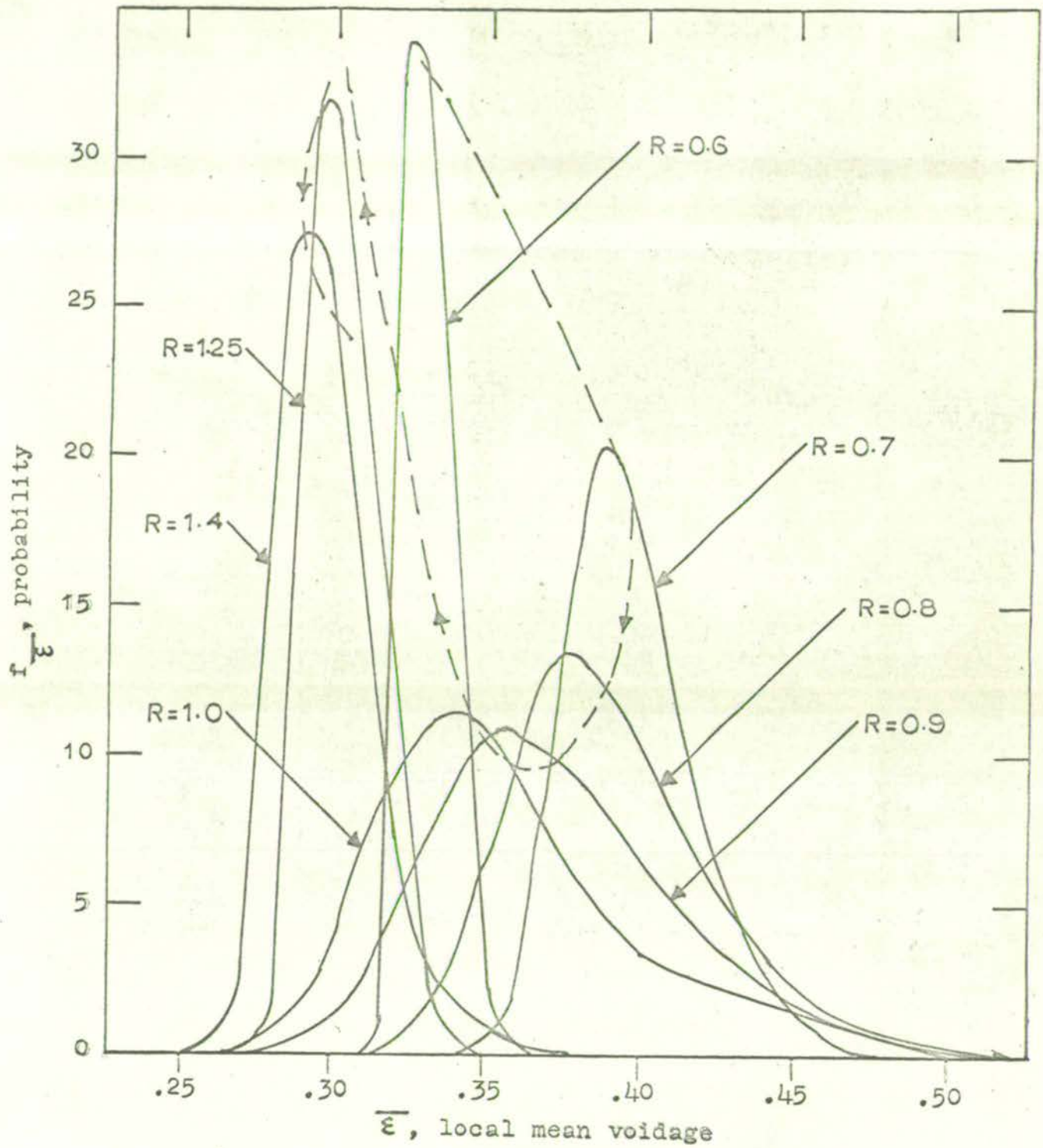

FIG. A.6 EFFECT OF ENVELOPE RADIUS R ON LOCAL MEAN VOIDAGE PROBABILITY DISTRIBUTION, $f_{\bar{\varepsilon}}$

$$\sigma_{\bar{\varepsilon}}^{2} = \sum_{n=3}^{12} F_n \left[\sigma_{\varepsilon_n}^{2} + (\bar{\varepsilon}_n^{*} - \bar{\varepsilon}^{*})^2 \right] \quad \ldots.(A.17)$$

values of $\sigma_{\bar{\varepsilon}}$ and $\frac{\sigma_{\bar{\varepsilon}}}{\bar{\varepsilon}^{*}}$ being given in Table A.2. Fig.2.7 gives the effect of R on $\bar{\varepsilon}_n^{*}$ and $\sigma_{\bar{\varepsilon}}$ for close random packing.

A3.1.4. Comparison with experimental two-dimensional distributions

The only experimental distributions which may be compared with the derived distributions for local mean voidage are two dimensional (i.e. based on the intersection of a plane with a packed bed). However, qualitative comparison is possible.

Thoenes (1957) obtained a distribution of equivalent channel diameters for the voids in a randomly packed bed of spheres. This has a similar shape to the derived three dimensional distributions i.e. skewed to the left but as would be expected the spread or variance of the two dimensional distribution is greater. The range of channel diameters for Thoenes' distribution is 0.2 - 2.0 (as a fraction of the mean value) and the range of area fractions will be approximately the square of these values. This may be compared with 0.71 - 1.56 for the range of the derived local mean volume voidage distribution (close random packing). The histograms for local two dimensional area voidage given by Brown and Hawksley (1945) show similar effects.

Experimentally a three dimensional voidage distribution could only be obtained directly by sub-dividing a packed bed which had been fixed in position (e.g. by wax) into local volume elements, such as cubes, and measuring the free volume of each of the elements. This would be difficult, tedious and would not give the local voidage distribution based on the envelope surrounding a sphere as has been used here.

The only way in which a distribution corresponding to the local voidage definition used here could be obtained

experimentally is to obtain the co-ordinates of all the spheres in a packed bed and then calculate the local voidage from the amount of penetration into the local voidage envelope of the spheres surrounding each sphere. The sphere co-ordinates could be generated by Monte Carlo methods or better be obtained from actual experimental measurement as Scott and Bernal et al have done for close random packing.

A3.2. LOCAL MEAN VOIDAGE - SPHERE CENTRE BASIS

The sphere centre data of Scott (1960) (Curve A, Fig.2.2) may be used to calculate the local mean voidage variation with position.

All spheres lying completely within the spherical envelope of radius R will have their centres lying within an envelope of radius $R - \frac{1}{2}$. The total volume of these spheres is then

$$\frac{\pi}{6}\left\{1 + \sum_{r^*=1}^{R-\frac{1}{2}} 4\pi r^{*2}\left[N_{AV}/4\pi r^{*2}\right]\right\} \quad \ldots(A.18)$$

All spheres whose centres lie in the spherical shell of radii $R - \frac{1}{2}$ and $R + \frac{1}{2}$ will be cut by the envelope of radius R, part of the sphere lying within the envelope and part without.

These spheres will thus lie in the region defined by $R + \beta^*$ where $\beta^* = \pm 0.4, \pm 0.2, 0$. Their total volume is thus given by

$$\sum_{\beta^*}\left\{4\pi(R+\beta^*)^2 \frac{\pi}{6} V_{R+\beta^*}\left[N_{AV}/4\pi(R+\beta^*)^2\right]\right\} \quad \ldots(A.19)$$

$V_{R+\beta^*}$ being defined in Appendix A3.1.1. Hence the local mean voidage $\overline{\varepsilon}_R$ is given by

$$\overline{\varepsilon}_R = 1 - \frac{1}{8R^3}\left[\left\{1 + \sum_{r^*=1}^{R-\frac{1}{2}} 4\pi r^2\left[\frac{N_{AV}}{4\pi r^{*2}}\right]\right.\right.$$

$$\left.\left. + \sum_{\beta^*}\left\{4\pi(R+\beta^*)^2 V_{R+\beta^*}\left[\frac{N_{AV}}{4\pi(R+\beta^*)^2}\right]\right\}\right\}\right] \quad \ldots(A.20)$$

being plotted as curve B of Fig. 2.7 as a function of R.

APPENDIX 3 (Continued)

Due to the importance of the region $1 < R < 1.1$, Scott's value of 9.24 average sphere centres at R = 1.0 was modified according to Bernal and Mason's results, being replaced by 6.4 centres at R = 1.0, 2.1 at R = 1.0 - 1.05, and 0.74 at R = 1.05 - 1.1.

A3.3. LOCAL MEAN VOIDAGE - INTEGRATED LOCAL VOIDAGE BASIS

It is also possible to calculate the local mean voidage from information on local voidages which has been reviewed for both local area fractions, ε'_A, and local volume fractions, ε', in 2.1.4.

Volume integration of the local voidage data on a spherical basis may be carried out using the expression

$$\overline{\varepsilon}_R = \sum_{r^* = s + \frac{1}{2}}^{R-s} \frac{\varepsilon' \left[(r^* + s)^3 - (r^* - s)^3 \right]}{R^3} \quad \ldots\ldots(A.21)$$

For spherical geometry experimental local data are not available but for the purpose of comparison, the integrated local mean voidage data of Benenati and Brosilow (1962) for random packing of spheres against a cylindrical container wall has been applied to the shell between the base sphere surface and radius R to give the local mean voidage with reference to the centre of the base sphere (as shown by line C of Fig. 2.7).

In the absence of direct experimental data for spherical geometry, the average value of the local volume fraction, ε'_R, over the spherical shell of radii R + s and R - s may be derived by the reverse process from the local mean voidage values obtained by the sphere centre method. Thus

$$\varepsilon'_R = \frac{\overline{\varepsilon}_{R+s} (R + s)^3 - \overline{\varepsilon}_{R-s} (R - s)^3}{(R + s)^3 - (R - s)^3} \quad \ldots\ldots(A.22)$$

and the variation with R is given by line A of Fig. 2.8.

APPENDIX 3 (Continued)

A3.4. GEOMETRIC DETAILS OF SPHERE SHELLS MODELS

A3.4.1. Fractional volume of a sphere cut by a spherical envelope

Consider the system as shown in Fig. A.7 in which a sphere of unit diameter is cut by a spherical envelope of radius R. The partial volume of the sphere enclosed is the sum of the spherical segments ABED and ABEF

$$\text{therefore} \quad V = 3x^2(y + z) + y^3 + z^3 \qquad \ldots.(A.23)$$

$$\text{Since} \quad x^2 = AO^2 - OB^2 = R^2 - (R - z)^2 = z(2R - z)$$

$$\text{and} \quad x^2 = AC^2 - BC^2 = (\tfrac{1}{2})^2 - (\beta^* + z)^2$$

$$\text{therefore} \quad z = \tfrac{1}{2}\left(\frac{\frac{1}{4} - \beta^{*2}}{R + \beta^*}\right) \qquad \ldots.(A.24)$$

$$\text{Thus} \quad V = \alpha'\left[\alpha'^2 - 3\alpha' z + 6zR\right] \qquad \ldots.(A.25)$$

For first shell spheres (since they touch the base sphere)

$$R + \beta^* = 1 \qquad \ldots.(A.26)$$

where the limiting values of β^* are $\pm \tfrac{1}{2}$.
Hence since $\alpha' = y + z = \tfrac{1}{2} - \beta^*$, it follows from (A.26),(A.24) that V_1 will be calculated with values of

$$\alpha' = (R - \tfrac{1}{2}) \qquad \ldots.(A.27)$$

$$z = \tfrac{1}{2}(R - \tfrac{1}{2})(\tfrac{3}{2} - R) \qquad \ldots.(A.28)$$

For second shell spheres we have

$$R + \beta^* = R_2 + \tfrac{1}{2} \qquad \ldots.(A.29)$$

Thus it similarly follows that V_2 will be found using values of

$$\alpha' = (R - R_2) \qquad \ldots.(A.30)$$

$$z = (R - R_2)(1 - R + R_2)/2(R_2 + \tfrac{1}{2}) \qquad \ldots.(A.31)$$

The volume V_i enclosed by radius i can be found from (A.25) using R = i.

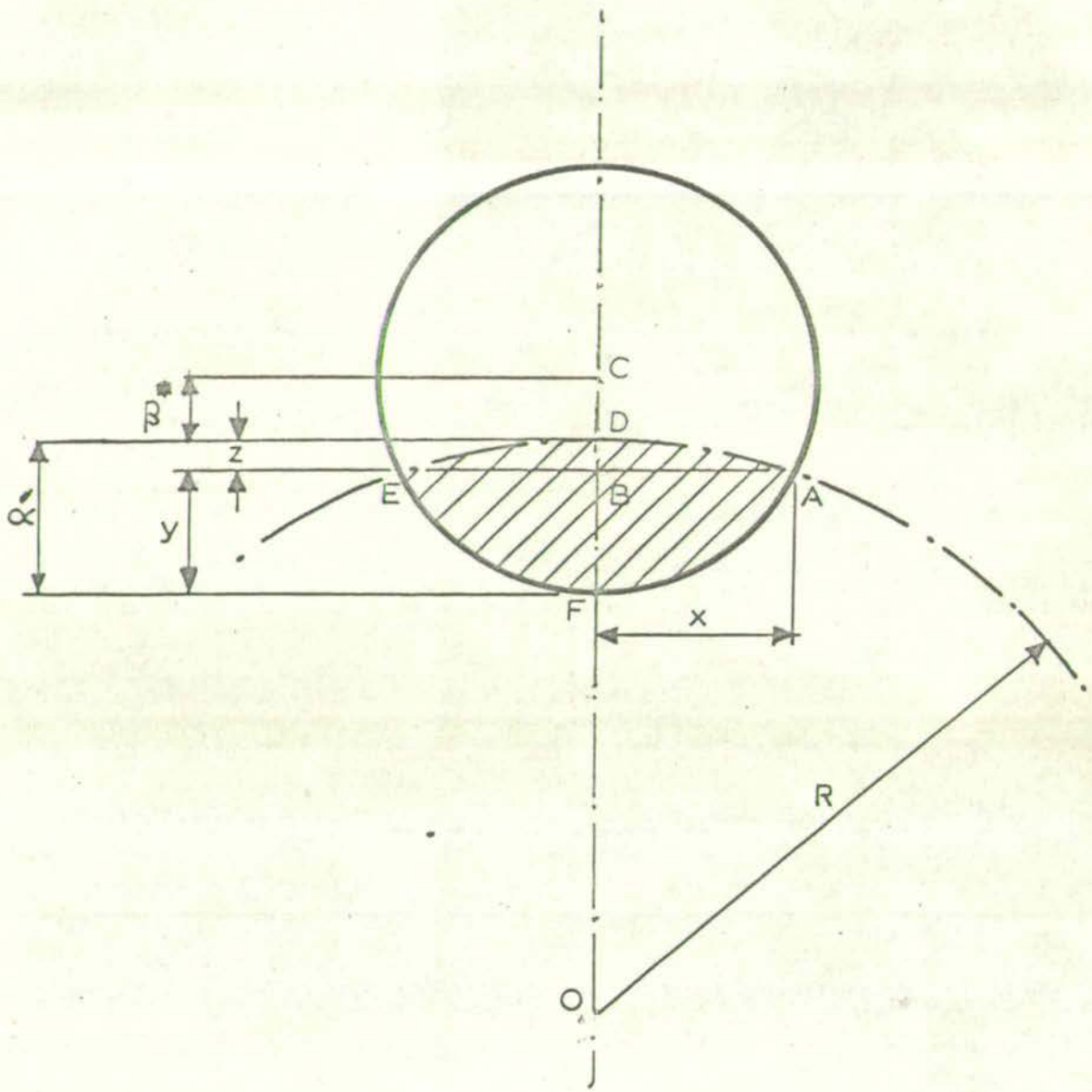

FIG. A.7 GEOMETRIC REPRESENTATION OF A SPHERE CUT BY A SPHERICAL ENVELOPE OF RADIUS R

APPENDIX 3 (Continued)

A3.4.2. Geometry of the Triangular Models

(i) Value of R_2

Consider three first shell spheres (centres A, B, C) arranged equidistant from each other on the surface of the base sphere (centre O) as in Fig. A.8. The second shell sphere (centre D) is placed in the triangular void so formed.

Let AB = BC = CA = q, AOB = ϕ^*

therefore $q = 2 \sin \phi^*/2$ ....(A.32)

Let M be the median of ΔABC, R be the mid point of AB and OM = h^*.

Therefore $MR = \frac{1}{3} CR = q/2\sqrt{3}$ ....(A.33)

$$OM^2 = RO^2 - MR^2$$

Therefore $h^{*2} = \cos^2 \phi^*/2 - q^2/12$ ....(A.34)

From (A.32), (A.33) $h^* = (1 - q^2/3)^{\frac{1}{2}}$ ....(A.35)

$$R_2 = 2h^* = \tfrac{1}{2}$$ ....(A.36)

(ii) Value of R_3

The closest possible position for a third shell sphere (centre G) is in the void formed by two second shell spheres (centre E, F) and one first shell sphere (centre C). From the geometry of the system it may be proved that:

$$R_3 = \sqrt{2}\left[1 - \cos\left(\cos^{-1}\left\{\sqrt{2}\left[\frac{5}{8}\left(\frac{1 + 3h^{*2}}{1 - h^{*2} + 4h^{*2}}\right) - 8h^{*2}\left(\frac{1 - h^{*2}}{1 + 3h^{*2}}\right) - 1\right]\right.\right.\right.$$

$$\left.\left.\left. + 2\left[\frac{1 - h^{*2} + h^{*4}}{1 + 3h^{*2}}\right]^{\frac{1}{2}}\right\} - 1 + \cos^{-1}\left\{\frac{1 + h^{*2} - 6h^{*4}}{(1 - h^{*2} + 4h^{*4})(1 + 3h^{*2})}\right\}\right)\right]^{\frac{1}{2}} - \frac{1}{2}$$

....(A.37)

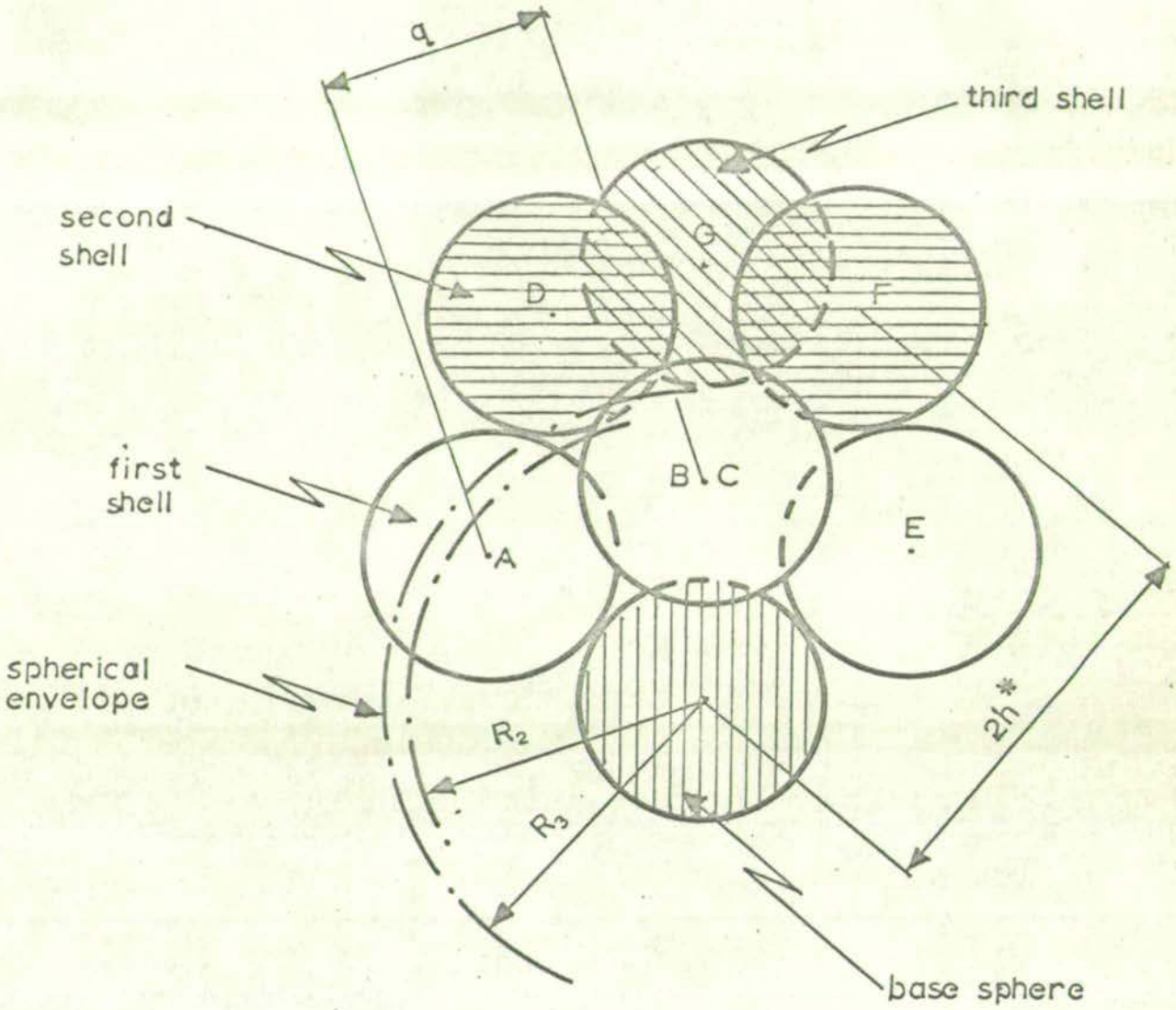

FIG. A.8 CLOSEST APPROACH OF SECOND AND THIRD SHELL SPHERES FOR TRIANGULAR MODELS

APPENDIX 3 (Continued)

(iii) Triangular close packed model

The first shell spheres are arranged close packed on the surface of the base sphere i.e. q = 1

From (A.32), $\sin \phi^*/2 = \frac{1}{2}$ ....(A.38)

For n = 3 one second shell sphere may be placed. The addition of each further first shell sphere enables one more second shell sphere to be placed.

Therefore $p = n - 2$ ....(A.39)

From (A.35), (A.36), (A.37)

$h^* = (2/3)^{\frac{1}{2}}$ ....(A.40)

$R_2 = 1.1327$ ....(A.41)

$R_3 = 1.4915$ ....(A.42)

(iv) Triangular equispaced model

If four first shell spheres (centres, A, B, C, E) are arranged equi-distant from each other over the whole surface of the base sphere, the four sphere centres form four equilateral spherical triangles on a spherical surface of radius equal to a sphere diameter. In the void created by each spherical triangle a second shell sphere may be placed. For each additional contact point, after rearrangement to satisfy the equidistant condition two more triangles are formed

Therefore $2(n - 4) = p - 4$

Therefore $p = 2n - 4$ ....(A.43)

Therefore $A_{\Delta ABC} = \frac{4\pi}{p} = \frac{4\pi}{2n - 4}$ ....(A.44)

But $A_{\Delta ABC} = (\hat{A} + \hat{B} + \hat{C} - \pi) = 3\theta - \pi$ ....(A.45)

Therefore $\theta = \pi n/3(n - 2)$ ....(A.46)

Now $\cos \phi^* = \frac{\cos C + \cos B \cos A}{\sin B \sin A} = \frac{\cos \theta}{1 - \cos \theta}$ ....(A.47)

From (A.35), (A.32), (A.47), (A.46)

$$h^* = \left[\frac{1}{3}\left\{1 + \frac{2\cos\left[\pi n/3\,(n-2)\right]}{1-\cos\left[\pi n/3\,(n-2)\right]}\right\}\right]^{\frac{1}{2}} \quad \ldots.(A.48)$$

Substitution of (A.48) into (A.36) and (A.37) gives R_2, R_3 for the triangular equispaced model, shown in Table A.1.

A3.5. CALCULATION OF THE LOCAL MEAN VOIDAGE DISTRIBUTION TO GIVE EXACT CORRESPONDENCE OF THE MEAN VALUE OF THE LOCAL MEAN VOIDAGE AND THE EXPERIMENTAL BULK MEAN VOIDAGE

By definition $$\overline{\varepsilon}_a = \sum_{n=3}^{12} F_n \cdot \overline{\varepsilon}_{na} \quad \ldots.(A.49)$$

and $$\overline{\varepsilon}_b = \sum_{n=3}^{12} F_n \cdot \overline{\varepsilon}_{nb} \quad \ldots.(A.50)$$

The mean value of the local mean voidage is defined to correspond exactly to the experimental bulk mean voidage.

Thus $$\varepsilon = \overline{\varepsilon}^* = \overline{\varepsilon}_a + C_{\overline{\varepsilon}^*}(\overline{\varepsilon}_a - \overline{\varepsilon}_b) \quad \ldots.(A.51)$$

where $C_{\overline{\varepsilon}^*}$ defines the position of the mean value of $\overline{\varepsilon}$ relative to the limits $\overline{\varepsilon}_a$ and $\overline{\varepsilon}_b$. But this equation may also be applied to any coordination number n. Thus

$$\overline{\varepsilon}_n^* = \overline{\varepsilon}_{na} + C_{\overline{\varepsilon}^*}(\overline{\varepsilon}_{na} - \overline{\varepsilon}_{nb}) \quad \ldots.(A.52)$$

Substituting for $C_{\overline{\varepsilon}^*}$ from equation A.51 gives

$$\overline{\varepsilon}_n^* = \overline{\varepsilon}_{na} + \left(\frac{\varepsilon - \overline{\varepsilon}_b}{\overline{\varepsilon}_a - \overline{\varepsilon}_b}\right)(\overline{\varepsilon}_{na} - \overline{\varepsilon}_{nb}) \quad \ldots.(A.53)$$

Thus from equations (A.49), (A.50), and (A.53)

$$\overline{\varepsilon}_n^* = \overline{\varepsilon}_{na} + \left[\frac{\varepsilon - \sum_{n=3}^{12} F_n \overline{\varepsilon}_{nb}}{\sum_{n=3}^{12} F_n \overline{\varepsilon}_{na} - \sum_{n=3}^{12} F_n \overline{\varepsilon}_{nb}} \right] (\overline{\varepsilon}_{na} - \overline{\varepsilon}_{nb}) \quad \ldots(A.54)$$

The local mean voidage probability distribution may be obtained by substituting equation (A.54) into equation (A.14).

This has been done in Fig. A.9 for a bulk mean voidage of 0.40 corresponding to the experimental system. The values of F_n were taken from the coordination number measurements of Bernal and Mason (1960) for loose random packings ($\varepsilon = .40$).

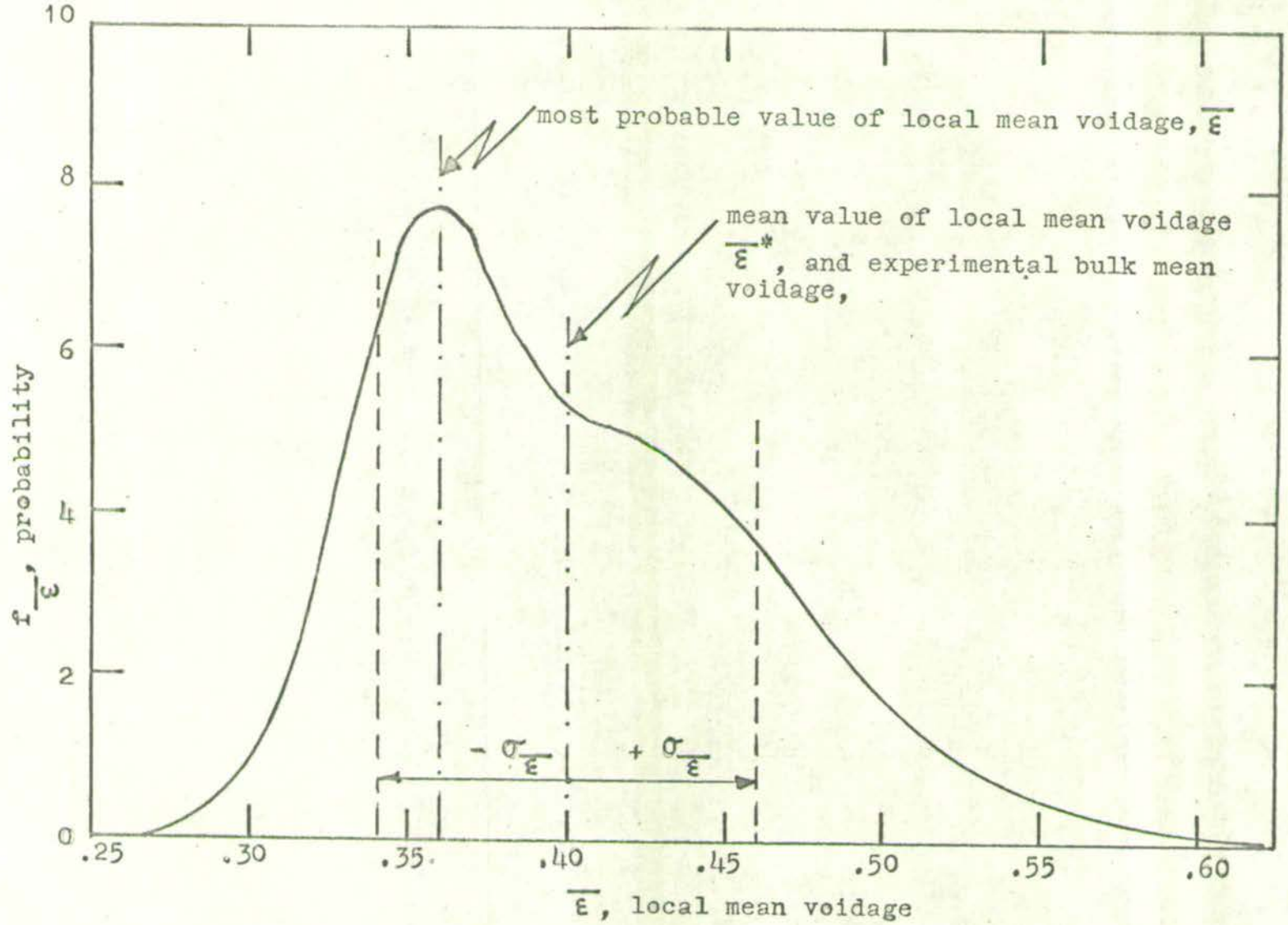

FIG. A.9 LOCAL MEAN VOIDAGE PROBABILITY DISTRIBUTION, $f_{\overline{\varepsilon}}$, FOR RANDOM PACKING WITH A MEAN LOCAL MEAN VOIDAGE, $\overline{\varepsilon}^*$, CORRESPONDING TO THE EXPERIMENTAL BULK VOIDAGE, $\varepsilon = .40$

APPENDIX 4 LOCAL PROPERTY VARIATIONS IN A RANDOMLY PACKED BED OF EQUAL-SIZED SPHERES

The local voidage variations in a packed bed give rise to local variations in structural and transport properties. For example, since there will be a distribution of cell lengths (as defined by the mixing cell model of a packed bed), interstitial velocities and specific particle surface areas, complete prediction of local fluid velocity and local heat and mass transfer can only be obtained from a knowledge of the local bed structure and not from the use of bulk properties.

While bulk mean transfer coefficients are taken to refer to the bed as a whole, local coefficients are usually taken to refer to point coefficients on the surface of a particle. Since the point coefficients must be related to the local angular velocity around a particle in a random bed (which is normally unknown) their usefulness in the design of a packed bed system is limited. A local mean coefficient, h_l, based upon the total surface area, A_s, of one particular sphere in the bed may be related to the two extremes of bulk mean and point coefficients, h_m and h_p respectively, as follows

$$h_l = \frac{\int_0^{A_s} h_p \, dA_s}{\int_0^{A_s} dA_s} \qquad \ldots\ldots(A.54a)$$

and

$$h_m = \frac{\sum_{N} h_l}{N} \qquad \ldots\ldots(A.54b)$$

The local mean coefficient will be determined by the local mean velocity (with respect to the compete sphere) which is dependent on the local mean voidage, $\overline{\varepsilon}$, in the immediate vicinity of the sphere.

Such local effects are particularly important where high rates of heat or mass transfer are involved, for example in high temperature gas-solid reactions or in packed bed heat

exchangers with gas flow opposing heat flow.

The probability distributions of local structural and transport properties which are dependent on voidage may be estimated from the local mean voidage distributions obtained in Appendix 3. The areas under the probability distributions of the local mean voidage, $\overline{\varepsilon}$, and any local property, x^*, are both unity.

Hence $$\int_0^1 f_{\overline{\varepsilon}}\, d\overline{\varepsilon} = \int_0^\infty f_{x^*}\, dx^* = 1 \qquad \ldots.(A.55)$$

therefore $$\sum_{\overline{\varepsilon}=0}^{1} f_{\overline{\varepsilon}}\, \Delta\overline{\varepsilon} = \sum_{x^*=0}^{\infty} f_{x^*}\, x^* = 1 \qquad ..(A.56)$$

But since $$x^* = \Psi(\overline{\varepsilon}) \qquad \ldots.(A.57)$$

it follows that $$x_1^* = \Psi_1(\overline{\varepsilon}_1),\ x_2^* = \Psi_2(\overline{\varepsilon}_2) \qquad ..(A.58)$$

where $$\Delta x^* = x_1^* - x_2^* \text{ and } \Delta\overline{\varepsilon} = \overline{\varepsilon}_1 - \overline{\varepsilon}_2 \qquad \ldots.(A.59)$$

Thus if the two distributions are divided into strips where Δx^* is determined from $\Delta\overline{\varepsilon}$ by equations A.58 and A.59, it follows from equation A.56 that

$$f_{x^*}\, \Delta x^* = f_{\overline{\varepsilon}}\, \Delta\overline{\varepsilon} \qquad \ldots.(A.60)$$

therefore $$f_{x^*} = f_{\overline{\varepsilon}}\, (\Delta\overline{\varepsilon} / \Delta x^*) \qquad \ldots.(A.61)$$

Thus by use of equations A.61, A.58 and A.59 the probability distribution of x^* may be obtained from the probability distribution of $\overline{\varepsilon}$.

The first, second and third moments of the probability distribution of x^* give the mean, variance and skewness of the distribution. It may be shown that

$$x^*_m = M_1(x^*) = \frac{\int_0^\infty x^* f_{x^*}\, dx^*}{\int_0^\infty f_{x^*}\, dx^*} \quad \frac{\sum x^* f_{x^*}}{\sum f_{x^*}} \qquad \ldots.(A.62)$$

$$\sigma^2_{x^*} = M_2(x^*) = \frac{\int_0^\infty (x - x^*_m)^2 f_{x^*}\, dx^*}{\int_0^\infty f_{x^*}\, dx^*} = \frac{\Sigma_{x^*}{}^2 f_{x^*}}{\Sigma f_{x^*}} - x^{*2}_m \qquad \ldots.(A.63)$$

$$\pi^3_{x^*} = M_3(x^*) = \frac{\int_0^\infty (x - x^*_m)^3 f_{x^*}\, dx^*}{\int_0^\infty f_{x^*}\, dx^*}$$

$$= \frac{\Sigma_{x^*}{}^3 f_{x^*}}{\Sigma f_{x^*}} - \frac{3x^*_m \Sigma_{x^*}{}^2 f_{x^*}}{\Sigma f_{x^*}} - 2x^{*3}_m \qquad \ldots.(A.64)$$

Table A.3 gives the distribution parameters of various structural and transport properties relevant to the present experimental system for the cases of close, loose and poured random packings of equal-sized spheres.

These distributions were obtained by dividing the local mean voidage distributions into 19 strips of thickness .02 (local mean voidage units) and using the above relationships between the voidage and property distributions.

The shapes of the local property distributions are very similar to the shape of the local mean voidage distribution (Fig. A.9). The values of the parameter $\pi^3_{x^*}/\sigma^2_{x^*}$ given in Table A.3 are measures of the skewness of the distribution. It is interesting to note that the most probable value of the local mean voidage of the loose packed experimental system is 0.36 which is the bulk mean voidage of the most stable random packing - the close random packing state. Hoelscher (1958) and Gottschlich (1963) chose skewed beta or gamma distributions to describe the local variations in stagnant mixing and diffusion film thicknesses around particles in packed beds. The choice of these distribution forms is confirmed by the

TABLE A.3 LOCAL PROPERTY DISTRIBUTION PARAMETERS FOR RANDOM PACKED B

Property	x^*	Equation number	$\Psi(\bar{\varepsilon})$	loose packed				lo
				x^*_m	x^*	σ_{x^*}/x^*_m	$\frac{\pi^3_{x^*}}{\sigma^3_{x^*}}$	x^*_m
local mean voidage	$\bar{\varepsilon}$	A.15	$\bar{\varepsilon}$	.3812	.0540	.1417	.6273	.40
local fractional layer spacing and mixing cell length	β	2.5	$.74(1-\bar{\varepsilon})^{-1/3}$	.8670	.0252	.0291	1.0256	.8756
local particle surface area	$6\,S_V D_P$	2.4	$(1-\bar{\varepsilon})$	3.7127	.3242	.0873	- .6276	3.5982
local void equivalent spherical hole diameter	D_H/D_P	A.7	$(\frac{\bar{\varepsilon}}{1-\bar{\varepsilon}})^{1/3}$	.8499	.0650	.0765	.7166	.8724
local void equivalent spherical hole volume	$\frac{V_H}{(\pi D_P^3/6)}$	A.6	$(\frac{\bar{\varepsilon}}{1-\bar{\varepsilon}})$	.6043	.1402	.2319	1.2286	.6516
local void hydraulic diameter	$\frac{3\,D_h}{2\,D_P}$	2.12	$(\frac{\bar{\varepsilon}}{1-\bar{\varepsilon}})$	.6043	.1402	.2319	1.2286	.6516
local heat or mass transfer coefficient	$\frac{h_l}{h}$	3.49	$\frac{}{\varepsilon} - .33$	1.3690	.0638	.0466	- .1039	1.3465
local heat or mass transfer coefficient	$\frac{h_l}{h}$	3.43	$\frac{1-(1-\bar{\varepsilon})^{5/3}}{C\,\bar{\varepsilon}}^{1/3}$	.7621	.0179	.0235	.6580	.7685
local mixing cell model convection parameter	$\frac{H_l}{H}$	4.111	$.74\,\bar{\varepsilon}\,.66(1-\bar{\varepsilon})^{2/3}$	.2901	.0076	.0263	- 1.967	.2920
local mixing cell model conduction parameter	$\frac{K_l}{K}$	4.110	$1.35\bar{\varepsilon}(1-\bar{\varepsilon})^{4/3}$	.2717	.0046	.0169	- 2.5904	.2721
local interstitial Reynolds number	$\frac{Re^*_l}{Re^*}$		$\frac{1}{\varepsilon}$	2.5733	.3652	.1419	.1611	2.4454
local pressure drop	$\frac{\Delta P_l}{\Delta P}$	2.9	$\left[\frac{1-\bar{\varepsilon}}{\varepsilon^3}\right]$	5.6242	3.6901	.6561	1.3515	4.4171
local effective thermal conductivity ratio (0°C)	Y_0	4.14[2]	$11.92-25.69(\bar{\varepsilon}-.25)$	8.5557	1.3853	.1619	- .6272	8.0665
local vacuum effective thermal conductivity ratio (0°C)	Y_0^*	4.15	$5.61-11.6(\bar{\varepsilon}-.25)$	4.0879	.6267	.1533	- .6272	3.8666
local effective thermal conductivity ratio (600°C)	Y_0	4.40[2]	$12.42-7.69(\bar{\varepsilon}-.25)$	11.4110	.4155	.0364	- .6219	11.264

1. Appendix 3.5 2. Extrapolated for $\bar{\varepsilon} > .47$

S OF EQUAL-SIZED SPHERES

e packed (with $\overline{\varepsilon^*} = \varepsilon$)[1]			poured packed				close packed			
σ_{x^*}	σ_{x^*}/x^*_m	$\frac{\pi^3 x^*}{\sigma^3 x^*}$	x^*_m	σ_{x^*}	σ_{x^*}/x^*_m	$\frac{\pi^3 x^*}{\sigma^3 x^*}$	x^*_m	σ_{x^*}	σ_{x^*}/x^*_m	$\frac{\pi^3 x^*}{\sigma^3 x^*}$
.0597	.1490	.6211	.3641	.0504	.1384	.9043	.3587	.0438	.1222	.9496
.0290	.0331	1.0562	.8594	.0227	.0264	1.2626	.8572	.0195	.0227	1.4164
.3580	.0995	- .6211	3.8155	.3023	.0792	- .9042	3.8480	.2630	.0683	-.9484
.0724	.0830	.7492	.8296	.0602	.0726	.9799	.8234	.0523	.0635	1.0071
.1644	.2523	1.3092	.5631	.1239	.2201	1.5078	.5524	.1062	.1922	1.4864
.1644	.2523	1.3092	.5631	.1239	.2201	1.5078	.5524	.1062	.1922	1.4864
.0660	.0490	- .0662	1.3903	.0633	.0455	- .3667	1.3984	.0563	.0402	-.4602
.0200	.0260	.7003	.7564	.0166	.0219	1.0762	.7547	.0144	.0191	1.0095
.0058	.0198	- 2.4789	.2873	.0095	.0331	-1.0661	.2853	.0098	.0342	-.6472
.0039	.0145	- 3.0926	.2704	.0058	.0215	-1.8938	.2699	.0059	.0218	-1.6186
.3649	.1492	.1996	2.6970	.3738	.1386	- .1097	2.7492	.3365	.1224	- .2097
3.1653	.7166	1.5085	6.8827	4.3009	.6249	.9739	7.6699	4.1366	.5393	.7665
1.5297	.1896	- .6210	8.9949	1.2919	.1436	- .9043	9.1338	1.1239	.1230	- .9493
0.6921	.1790	- .6210	4.2866	.5845	.1363	- .9045	4.3495	.5085	.1169	-.9500
0.4588	.0407	- .6274	11.5427	.3874	.0336	- .9044	11.5844	.3372	.0291	-.9991

shape of the present local mean voidage distribution which will directly determine such local film thicknesses.

The standard deviations, σ_{x^*} of the local property distributions range from 2 - 25% of the mean property values, x^*_m, except for local pressure drop which has standard deviation values of 54 - 72% of the mean value. Apart from the pressure drop values, the differences between the distributions for close, poured and loose random packings are small. A closer packing gives a slightly smaller property variation. In rank order of σ_{x^*}/x^*_m values, which are a measure of the local variation of the property x^*, the local properties are: pressure drop, void equivalent hole volume, effective thermal conductivity ratio ($0^\circ C$) interstitial Reynolds number, vacuum effective thermal conductivity ($0^\circ C$) local mean voidage, particle surface area, void equivalent hole diameter, heat or mass transfer coefficient, effective thermal conductivity ratio ($600^\circ C$), layer spacing or mixing cell length, mixing cell model convection parameter and mixing cell model conduction parameter.

Fig. A.10 shows the good agreement of the theoretical distribution of hydraulic diameters relative to the root mean square value (based on equation 2.12), with the experimental distribution of Thoenes (1957).

Lamb and Wilhelm (1963) developed a perturbation theory which predicted the temperature or concentration fluctuations during fluid flow through a packed bed. The present mixing cell model could be used for a similar purpose where solid conduction also affects the heat transfer. It could be assumed that local temperatures are equalised at the start of each mixing cell along the bed length but within each cell local temperature variations can occur as given by the mixing cell model for the model local parameter distributions. But from Table A.3 the local variation in the conduction and convection parameters is very small. Thus significant local temperature variations for gas flow through the bed would not be expected. Larger variations would be expected in a stagnant bed at low temperatures (Fig.6.17).

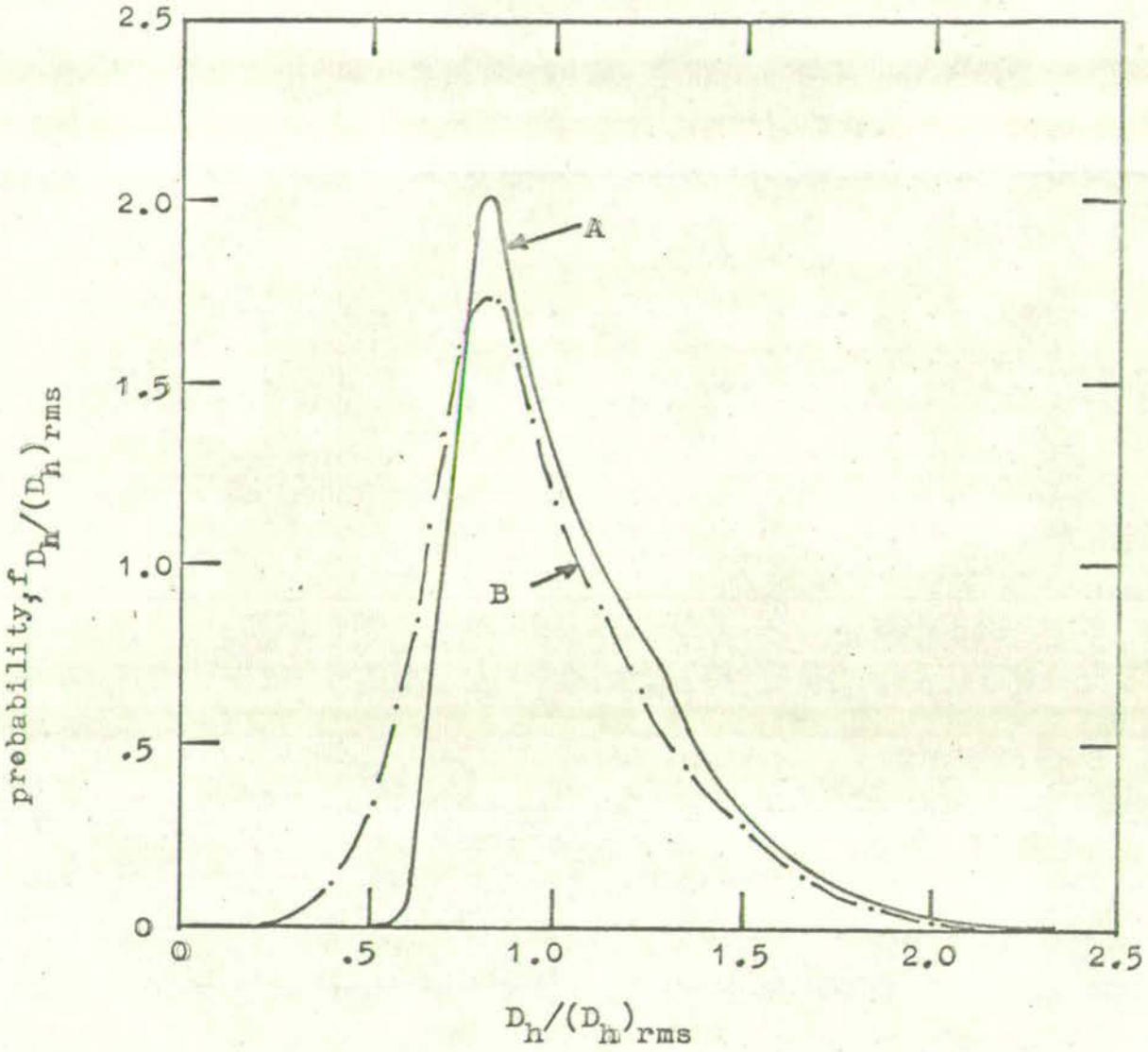

FIG. A.10 DISTRIBUTION OF RELATIVE HYDRAULIC DIAMETERS

A = derived from present local mean voidage theory

B = experimental, Thoenes (1957)

APPENDIX 4 (Continued)

It should be noted that these calculations of property variations have assumed that the property values in each local void cell are affected solely by the voidage of that cell and not by interaction with other surrounding cells. In practice some interaction will generally occur and this would most usually have the effect of smoothing out the variations between cells. Thus the variations calculated here are best regarded as maximum estimates.

APPENDIX 5 EFFECT OF A TEMPERATURE DEPENDENT THERMAL CONDUCTIVITY ON THE TEMPERATURE PROFILE FOR CONDUCTION

For a constant thermal conductivity, k, Laplace's equation is

$$\nabla^2 T = 0 \qquad \ldots.(A.65)$$

therefore

$$T = C_1 z + B \qquad \ldots.(A.66)$$

Boundary conditions $T = T_1$ at $z = 0$ and $T = T_2$ at $z = L$

give

$$T = T_1 - \frac{z}{L}(T_1 - T_2) \qquad \ldots.(A.67)$$

therefore

$$\frac{T_1 - T}{T_1 - T_2} = z \qquad \ldots.(A.68)$$

For a non-constant thermal conductivity, k, this Laplace equation solution may be used by replacing T by the variable Θ (Carslaw and Jaegar (1948)) where

$$\Theta = \frac{1}{k_\sigma} \int_{T_\sigma}^{T} k \, d T \qquad \ldots(A.69)$$

and k_σ is the thermal conductivity at temperature T_σ.

If the thermal conductivity is linearly dependent on temperature

$$k = k_\sigma \left[1 + w (T - T_\sigma) \right] \qquad \ldots.(A.70)$$

where w is the thermal conductivity temperature coefficient. Let $T_\sigma = 0$ for simplicity so that

$$k = k_\sigma \left[1 + wT \right] \qquad \ldots.(A.71)$$

Thus from equations A.68, A.69, and A.70

$$\Theta = T \left(1 + \frac{w}{2} T\right) \qquad \ldots.(A.72)$$

and

$$\frac{\Theta_1 - \Theta}{\Theta_1 \; \Theta_2} = z \qquad \ldots.(A.73)$$

and

$$T = \frac{-1 \pm \sqrt{1 + 2 w \Theta}}{w} \qquad \ldots.(A.74)$$

APPENDIX 6 FURTHER DIFFUSION MODEL SOLUTIONS

The diffusion model equations and boundary conditions for these solutions are given in Table 4.1.

(i) unequal solid and gas temperatures, plug flow, finite bed

$$T^* = \frac{\Lambda_1^2 e^{(\Lambda_1 + \Lambda_2 Z)} - \Lambda_2^2 e^{(\Lambda_2 + \Lambda_1 Z)} + e^{(\Lambda_1 + \Lambda_2)}(\Lambda_2^2 - \Lambda_1^2)}{\Lambda_1^2 e^{\Lambda_1} - \Lambda_2^2 e^{\Lambda_2} + e^{(\Lambda_1 + \Lambda_2)}(\Lambda_2^2 - \Lambda_1^2)} \quad \ldots(A.75)$$

$$t^* = \frac{K\Lambda_1\Lambda_2(\Lambda_1 e^{(\Lambda_1 + \Lambda_2 Z)} - \Lambda_2 e^{(\Lambda_2 + \Lambda_1 Z)}) + e^{(\Lambda_1 + \Lambda_2)}(\Lambda_2^2 - \Lambda_1^2)}{\Lambda_1^2 e^{\Lambda_1} - \Lambda_2^2 e^{\Lambda_2} + e^{(\Lambda_1 + \Lambda_2)}(\Lambda_2^2 - \Lambda_1^2)}$$

$$\ldots.(A.76)$$

(ii) unequal solid and gas temperatures, finite Peclet number, infinite bed

Yagi, Kunii Wakao (1960) and Ikeda, Nishimura, Kubota (1964) gave solutions for this case which the latter showed reduced to

$$T^* = e^{\Lambda Z} \quad \ldots.(A.78)$$

$$t^* = \left(1 - \frac{\Lambda^2}{C}\right) e^{\Lambda Z} \quad \ldots.(A.79)$$

where Λ is the negative root of

$$\Lambda^3 + Pe\,\Lambda^2 - CX\left[\frac{Pe}{RePr} + \frac{1}{X}\right]\Lambda - C\,Pe = 0 \quad \ldots.(A.80)$$

and $C = \dfrac{Nu\ S\ D_P}{X}$

APPENDIX 7 MIXING CELL MODEL UNIT CELL EQUATIONS

The following equations completely define the temperatures within a unit cell (Fig. 4.12) from the inlet values where $C = \sqrt{H/K}$

section z = a

Inlet values T_a, $(\frac{\partial T}{\partial z})_a$, t_r

$$K\,1\,(\frac{\partial T}{\partial z})_a = (t_r - \frac{Q}{Gcg}) \quad \ldots.(A.81)$$

$$t_{r+1}-t_r = H\left[1(\frac{\partial T}{\partial z})_a \frac{1}{C^2}\ (\cosh C + \frac{N_P^* C}{2} \sinh C - 1) + (T_a - t_{r+1})\frac{1}{C}(\sinh C + \frac{N_P^* C}{2}(\cosh C - 1))\right] \quad \ldots.(A.82)$$

section a - b

$$T - t_{r+1} = \frac{1}{C}(\frac{\partial T}{\partial z})_a \sinh \frac{C(z-a)}{1} + (T_a - t_{r+1}) \cosh \frac{C(z-a)}{1} \quad \ldots(A.83)$$

$$(\frac{\partial T}{\partial z}) = (\frac{\partial T}{\partial z})_a \cosh \frac{C(z-a)}{1} + \frac{C}{1}(T_a - t_{r+1}) \sinh \frac{C(z-a)}{1} \quad \ldots(A.84)$$

section z = b

$$\text{At } z=b_-,\ T_{b_-} - t_{r+1} = \frac{1}{C}(\frac{\partial T}{\partial z})_a \sinh \frac{C}{2} + (T_a - t_{r+1}) \cosh \frac{C}{2} \quad \ldots(A.85)$$

$$(\frac{\partial T}{\partial z})_{b_-} = (\frac{\partial T}{\partial z})_a \cosh \frac{C}{2} + \frac{C}{1}(T_a - t_{r+1}) \sinh \frac{C}{2} \quad \ldots(A.86)$$

$$\text{At } z=b_+,\ T_{b+} - t_{r+1} = \frac{1}{C}(\frac{\partial T}{\partial z})_a (\sinh \frac{C}{2} + \frac{N_P^* C}{2} \cosh \frac{C}{2}) + (T_a - t_{r+1})(\cosh \frac{C}{2} + \frac{N_P^* C}{2} \sinh \frac{C}{2}) \quad \ldots.(A.87)$$

$$\left(\frac{\partial T}{\partial z}\right)_{b+} = \left(\frac{\partial T}{\partial z}\right)_a \cosh\frac{C}{2} + \frac{C}{l}(T_a - t_{r+1}) \sinh\frac{C}{2} \quad \ldots.(A.88)$$

section b - c

$$T - t_{r+1} = \frac{l}{C}\left(\frac{\partial T}{\partial z}\right)_a \left[\sinh\frac{C(z-b)}{l} \cosh\frac{C}{2} + \cosh\frac{C(z-b)}{l}\left\{\sinh\frac{C}{2} + \frac{N_p{}^*C}{2}\cosh\frac{C}{2}\right\}\right]$$

$$+ (T_a - t_{r+1})\left[\sinh\frac{C(z-b)}{l} \sinh\frac{C}{2} + \cosh\frac{C(z-b)}{l}\left\{\cosh\frac{C}{2} + \frac{N_p{}^*C}{2}\sinh\frac{C}{2}\right\}\right]$$

$\ldots.(A.89)$

$$\left(\frac{\partial T}{\partial z}\right) = \left(\frac{\partial T}{\partial z}\right)_a \left[\cosh\frac{C(z-b)}{l} \cosh\frac{C}{2} + \sinh\frac{C(z-b)}{l}\left\{\sinh\frac{C}{2} + \frac{N_p{}^*C}{2}\cosh\frac{C}{2}\right\}\right]$$

$\ldots.(A.90)$

$$+ \frac{C}{l}(T_a - t_{r+1})\left[\cosh\frac{C(z-b)}{l} \sinh\frac{C}{2} + \sinh\frac{C(z-b)}{l}\left\{\cosh\frac{C}{2} + \frac{N_p{}^*C}{2}\sinh\frac{C}{2}\right\}\right]$$

$\ldots.(A.91)$

section z = c

$$T_c - t_{r+1} = \frac{l}{C}\left(\frac{\partial T}{\partial z}\right)_a \left[\sinh C + \frac{N_p{}^*C}{2}(\cosh C + 1)\right] \quad \ldots(A.92)$$

$$+ (T_a - t_{r+1})\left[\cosh C + \frac{N_p{}^*C}{2}\sinh C\right] \quad .$$

$$\left(\frac{\partial T}{\partial z}\right)_c = \left(\frac{\partial T}{\partial z}\right)_a \left[\cosh C + \frac{N_p{}^*C}{2}\sinh C\right] + (T_a - t_{r+1})\frac{C}{l}\left[\sinh C + \frac{N_p{}^*C}{2}(\cosh C - 1)\right]$$

$\ldots.(A.93)$

APPENDIX 8 HOT WIRE ANENOMETER SYSTEM

The anenometer probe consisted of .005 in. dia. nickel wire wound in a coil $\frac{3}{16}$ in. dia. and $\frac{1}{4}$ in. long. The ends of the coil were soldered to $\frac{3}{4}$ in. long sewing needles fixed into a cork attached to the end of a length of $\frac{1}{4}$ in. dia. screwed brass rod. The rod passed through a clearance hole in the centre of a 1 in. x 1 in. x $\frac{1}{2}$ in. brass block so that the probe could be fixed at any desired height relative to the block by means of lock nuts. The block could be slid along two parallel lengths of brass angle to any desired radial position relative to the bed axis. The lengths of angle were fixed to a wooden annulus which fitted over the outside of the bed container and could be rotated to any required angular position. In this way the probe could be placed at any required point across the bed cross section.

A 12 volt accumulator was connected in series with a fixed resistance, a variable resistance, the probe coil and an ammeter. The variable resistance was adjusted to give a constant current reading for the measurement of any required air flow past the coil. The voltage drop across the coil was measured on a potentiometer.

The anenometer was calibrated against the orifice plate readings by placing the probe in the vertical calming length pipe (Fig. 5.1).

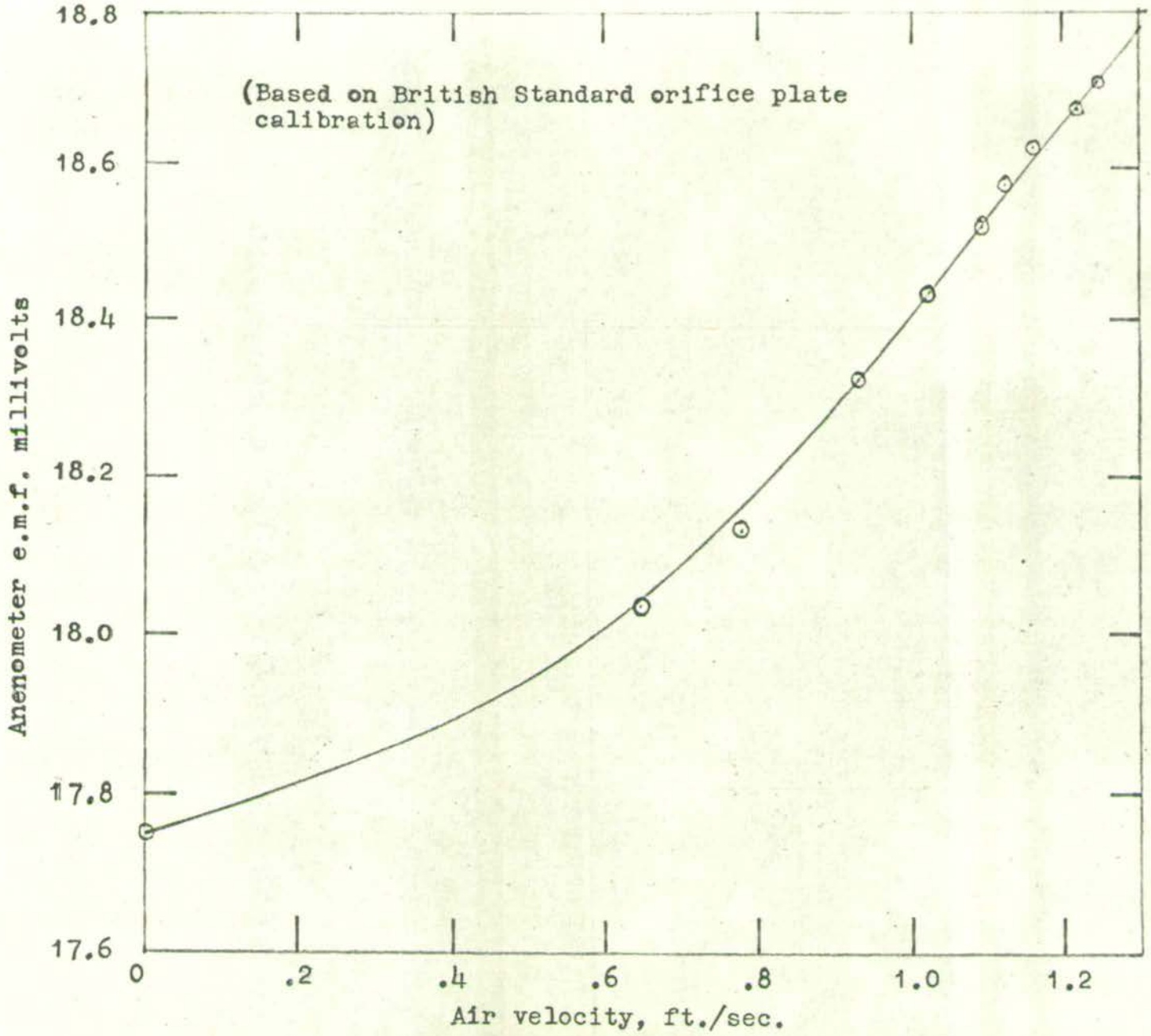

FIG.A.11 HOT WIRE ANENOMETER CALIBRATION CURVE

APPENDIX 9 MEASUREMENT OF THE THERMAL CONDUCTIVITY OF THE SOLID MATERIAL

(i) Method of measurement

The ball comparator method was used to determine the thermal conductivity of a sample of the fired alumina-silicate clay from which the particles were made. This method was chosen since it is simple, avoids heat loss problems and the equipment was readily available. The method was originally developed by Powell (Powell (1957, 1959, 1960); Clark and Powell (1962)).

(ii) Apparatus and Procedure

The thermal comparator consisted of two metal balls similarly mounted in a block of balsa wood, but one was at slightly lower level so that it touched any surface on which the block rested. After heating to a small fixed temperature excess the block was laid in contact with the test surface. Differentially conncected thermocouples attached to each ball measured the increased rate of cooling of the ball which made contact. The differential e.m.f. was observed ten seconds after contact was made and can be shown to be a function of thermal conductivity of the material on which the ball rests. The comparator was calibrated against materials of known conductivity.

(iii) Sample Preparation

A moist alumina-silicate clay sample was worked well to eliminate any air pockets and placed in a disc shaped mould, to form a disc of 2 in.dia. and of $\frac{1}{4}$ in. thickness. This was dried overnight at a temperature of 150°C and then fired in a furnace at approximately 1000°C. One surface of the disc was then ground smooth using fine carborundum powder on a lapping wheel.

(iv) Measurements (Gordon (1966))

Twenty five measurements were made at different points on the smooth surface of the disc at a room temperature of 20°C.

NOMENCLATURE

(Any consistent set of units may be used)

Upper case letters

A	area
$A_{\Delta ABC}$	area of spherical triangle ABC
$C, C_1, \ldots$	constants
C_{SB}	Stefan-Boltzmann constant = 0.1712×10^{-8} BTU/hr. ft.^{2} $^\circ R^4$.
C_λ	absorption coefficient by gas for radiation of wavelength λ
C^*	concentration
$C_{\overline{\varepsilon}^*}$	defines the position of the mean value of the local mean voidage, $\overline{\varepsilon}^*$, relative to the maximum and minimum limits (equation A.52).
D_H	diameter of spherical hole equivalent to average void volume
D_h	hydraulic diameter of a void
$(D_h)_{rms}$	root mean square value of D_h
D_T	diameter of a tube containing packing
$\mathscr{D}$	molecular diffusivity of fluid
E	eddy dispersion diffusivity
E_t	turbulent eddy dispersion diffusivity
E_z, E_r	eddy dispersion diffusivity in axial and radial directions respectively
F_n	fractional frequency of spheres with coordination number n.
F^*_{12}	view factor defined as the fraction of radiant energy leaving surface 1 which is intercepted by surface 2
G	gas mass flow rate
Gr	Grashof number

H, H_L	convection parameters for mixing cell and diffusion models (equations 4.111, 4.51b)
H_r, H_{rs}, H_{rg}	radiation heat transfer coefficient parameters, $h_r D_P / k_g$, $h_{rs} D_P / k_g$, $h_{rg} D_P / k_g$ respectively
I	intensity of radiation emission; I_B, from a black body; $I_{B,\lambda}$, $I_{\lambda,z}$, $I_{\lambda,0}$ at a wavelength λ from a black body, at an axial distance z and at z = 0 respectively.
J	J factor (equation 3.42); J_h for heat transfer; J_d for mass transger
K, K_L	conduction parameters for mixing cell and diffusion models (equations 4.110, 4.51a)
L	length of bed or distance between parallel plates
L	length of fluid flow path through the bed
M_0, M_1, M_2, M_3	zeroth, first, second and third moments respectively of a distribution
N	number
N_{PR}, N_n	number of pendular rings and contact points respectively in a unit cell
Nu	Nusselt number (equations 3.40)
N_{AV}	average number of spheres in a local shell
N_T	total number of spheres cut by an envelope of radius RD_P or by a plane crossectional cut
N_P^*	mixing cell model contact point resistance parameter (equation 4.112)
N_Q^*	mixing cell model axial heat flow parameter (equation 4.114)
$\overline{O}$	mixing cell model parameter (equation 4.108)
P	gas pressure
P^*	permeability of a packed bed

Pe, Pe_L	axial Peclet number based on particle diameter and bed length respectively (equations 2.10)
Pe_{rad}	radial Peclet number
Q	heat flow rate
Q'_{ar}, $Q'_{a(r+1)}$	intra-cell radiation heat flow rate (mechanism 6) to cells r and r+1 respectively
Q'_{br}, $Q'_{b(r+1)}$	inter-cell radiation heat flow rate (mechanism 5) to cells r and r+1 respectively
Q^*	heat flow rate per unit area; $Q^*_{\varepsilon_{A1}}$, $Q^*_{(\varepsilon_{A1}+\varepsilon_{A2})}$ through areas ε_{A1} and $\varepsilon_{A2}+\varepsilon_{A3}$ respectively
R	radius of a spherical envelope (in particle diameters) about a base sphere centre; R_1, R_2, R_3 are the inner limits of the first, second and third shell spheres respectively
R^*	radial distance from centre of tube
$\bar{R}, \bar{R}_0, \bar{R}_1 \ldots \bar{R}_m$	heat transfer resistances of bed, unit cell and m parallel cell paths respectively
Ra	Rayleigh number (equation 3.39)
Re	Reynolds number = $D_p G/\mu$
Re', Re''	modified Reynolds numbers (equations 2.9, 3.46 respectively)
Re^*	interstitial Reynolds number
S	particle surface area per unit bed volume
Sc	Schmidt number = $\mu/\rho\mathcal{D}$
T	solid particle temperature; T_o, T_r, T_{r+1}, T_m at the bed entrance, rth mixing cell, r+1 th mixing cell and bed exit respectively; T_a, T_b, T_c, T_z at z = a, b, c, z respectively
T_A	absolute solid temperature
T_0	reference temperature for a temperature dependent thermal conductivity

T^* dimensionless solid temperature = $\frac{T - T_m}{T_o - T_m}$, T_Z^* at axial position Z

$\bar{U}$ mixing cell model parameter (equation 4.109)

V fractional volume of a sphere cut by and enclosed by a spherical envelope of radius RD_P

V_H volume of a spherical hole equivalent to the average void volume

V_{PR} volume of a pendular ring

V' volume of a local spherical envelope of radius RD_P

W mixing cell parameter (equations 4.104, 4.105)

X ratio of a solid and gas thermal conductivities $= k_s / k_g$

X_{rs}, X_{rg} radiation parameters; $X_{rs} = h_{rs} D_P / k_g$ (mechanism 5), $X_{rg} = h_{rg} D_P / k_g$ (mechanism 6)

Y effective solid path thermal conductivity ratio with gas flow = k_{es} / k_g, k_e / k_g

Y' effective thermal conductivity ratio with gas flow = k'_{es} / k_g

Y_C effective conduction thermal conductivity ratio = k_{ec} / k_g

Y_C^* effective conduction thermal conductivity ratio under vacuum = k^*_{ec} / k_g

Y_O effective thermal conductivity ratio of stagnant bed = k_{eo} / k_g

Y_O^* effective thermal conductivity ratio of evacuated bed = k^*_{eo} / k_g

Y_r effective radiation thermal conductivity of stagnant bed = k_r / k_g

Y_{rad} radial effective thermal conductivity ratio

Z dimensionless axial distance = z/L

Lower case letters

a	radiation absorption cross section per unit bed volume
b	radiation scattering cross section per unit bed volume
c_p	gas specific heat at constant pressure
c_s	solid specific heat
e, e_g	solid and gas emissivities respectively
f_{x^*}	probability of a value x^* of a local property in a packed bed
f_A^*, f_T^*, f_S^*	fraction of incident radiation flux respectively absorbed, transmitted and scattered
g	gravitational acceleration
h	heat or mass transfer, solid-gas convection coefficient
h_l, h, h_p	local mean, bulk mean and point heat or mass transfer coefficients respectively
h_p	contact point heat transfer coefficient
h_v	heat or mass transfer, solid-gas convection coefficient per unit volume of bed
h_r, h_{rs}, h_{rg}	radiation heat transfer coefficients; h_{rs} for solid-gas series path; h_{rg} for gas parallel path across a void
h^*	centre to centre distance from second shell sphere to base sphere
i	forward radiation flux
j	backward radiation flux
k	thermal conductivity
k_e	effective thermal conductivity (based on bed area)
k_{ec}	effective conduction thermal conductivity (based on bed area)

k_{ec}^*	effective conduction thermal conductivity under vacuum (based on bed area)
k_{es}	effective solid path thermal conductivity (based on solid area, $1 - \varepsilon$)
k'_{es}	effective solid path thermal conductivity (based on bed area)
k_{eo}	effective thermal conductivity of stagnant bed (based on bed area)
k_{eo}^*	effective thermal conductivity of evacuated bed (based on bed area)
k_g	gas thermal conductivity
k_p	effective contact point conductivity (based on bed area)
k_r	effective radiation thermal conductivity (based on bed area)
$k_{\bar{o}}$	thermal conductivity at a temperature $T_{\bar{o}}$
k_{ov}	overall effective thermal conductivity (based on bed area)
l	mixing cell or stage length
m	number of mixing cells in the bed length
n	coordination number, the number of first shell spheres touching the base sphere
p	number of second shell spheres
p^*	bed permeability
q	centre-centre distance of two first shell spheres
r	number of mixing cells from bed inlet
r^*	radius of spherical shell
t	gas temperature; t_o, t_r, t_{r+1}, t_m, at bed entrance, r th mixing cell, r+1 th mixing cell, bed exit respectively
t^*	dimensionless gas temperature = $\frac{t - T_m}{T_o - T_m}$

v	interstitial velocity = v_0 / ε
v_0	superficial gas velocity based on empty tube cross-sectional area
w	thermal conductivity temperature coefficient
x^*	local structural or transport property in a packed bed; x^*_m, mean value thereof.
z	axial length along bed

Greek letters

α	gas fraction of unit cell length in series path
α^*	$= \alpha \varepsilon_{A2}$
α'	$= \frac{1}{2} - \beta^*$
β	number of particle diameters in unit cell length or layer spacing
β^*	distance from sphere centre to spherical envelope
ΔP	pressure drop across bed length
$\Delta T, \Delta\overline{\varepsilon}, \Delta x^*$	difference in temperature, local mean voidage and a local property respectively
δ	half width of local volume element
ε	bulk mean voidage
$\overline{\varepsilon}, \overline{\varepsilon}^*, \overline{\varepsilon}^*_n$	local mean voidage, average value of local mean voidage and average value for coordination number n (equation A.13) respectively
$\overline{\varepsilon}_w$	local mean wall voidage
ε_A	area fraction; ε_{A1}, ε_{A2}, ε_{A3}: unit cell area fractions for parallel gas, series gas-solid, and parallel solid paths respectively
ε', ε'_A	local voidage and local area fraction respectively
	volume coefficient of thermal expansion of gas
	thermal conductivity temperature function (equation A.69)

θ	angle of equilateral triangle formed by three adjacent first shell spheres
θ_n	polar angle between two contact points
θ_n^*	$= \frac{1}{2}(1 - \cos \theta_n)$
θ_P	angle of equivalent perfect solid-solid contact at a contact point (Fig. 4.2)
θ_{PR}	angle defining the volume of a pendular ring (Fig. 4.2)
Λ	roots of an equation
μ	viscosity of gas
π^3	third moment of a probability distribution
ρ	density of gas
ρ_s	density of solid
Σ	summation
σ	standard deviation of probability distribution; $\sigma_{\overline{\varepsilon}}$, for local mean voidage; $\sigma_{\overline{\varepsilon}_n}$ for local mean voidage with coordination number n; $\sigma_{\tau C}$ for residence time τC; σ_{x^*} for a local property x*
τ	time
Φ_A, Φ_B	relative heat flow parameters (equations 4.116, 4.116b)
$\emptyset D_P$	gas layer thickness in series path in a unit cell
$\emptyset^*$	angle subtended at centre of base sphere by two adjacent sphere centres
χ	tortuosity of bed $= L_\chi / L$
Ψ	function
ω	refractive index of solid relative to gas

Subscripts

a	upper limit
b	lower limit
br	brick
l	local mean
n	coordination number n
R	spherical envelope radius, R, about base sphere centre
rad	radial
z	axial direction

Adivarahan P., Kunii D., and Smith J.M. Soc. Petrol. Eng. Journal 2, 290, 1962.

Aerov M.E. Doctoral dissertation, Moscow University, 1951.

Aerov M.E. Intern. Chem. Eng. 3, 272, 1963.

Aerov M.E., Nikimina N.I., Trainina S.S. and Gusev N.V., Zh. Tek. Fiz. 29, 974, 1959.

Akehata T., and Sato K. Chem. Eng.(Japan) 22, 430, 1958.

Alder B.J., Frankel S.P., and Lewinson V.A. J. Chem. Phys. 23, 417, 1955.

Alder B.J., and Wainwright T.E. J. Chem. Phys. 27, 1208, 1957.

Anon. New Scientist 27, 143, 1965.

Argo W.B., and Smith J.M. Chem. Eng. Progress 49, 443, 1953.

Aris R. Chem. Eng. Science 10, 80, 1959.

Aris R., and Amundson N.R. A.I.Ch.E. Journal 3, 280, 1957.

Arthur J.R., Linnett J.W., Raynor E.J., and Sington E.P.C., Trans. Faraday Soc. 46, 270, 1950.

Asaad Y. Ph.D. thesis, University of California, 1955.

Baddour R.F., and Yoon C.Y. Chem. Eng. Progress Symposium Series 57, No. 32, 35, 1960.

Barker J.J. Ind. Eng. Chem. 57, No. 4, 43, 1965.

Bartell F.E., and Osterhof H.J. J. Phys. Chem. 32, 1553, 1928.

Baumeister E.B., and Bennett C.O., A.I.Ch.E. Journal 4, 69, 1958.

Benenati R.F., and Brosilow C.B. A.I.Ch.E. Journal 8, 359, 1962.

Bennett J.G., and Brown R.L. J.Inst.Fuel 13, 232, 1940.

Bernal J.D. Nature 183, 141, 1959.

Bernal J.D. Nature 185, 68, 1960.

Bernal J.D. Soviet Physics - Crystallography 7, 410, 1963.

Bernal J.D., Knight K.R., and Cherry I. Nature 202, 852, 1964.

Bernal J.D., Proc. Roy. Soc. (Lond.) A 280, 299, 1964.

Bernal J.D., and Mason J. Nature 188, 910, 1960. See also Furth R. Proc. Roy. Soc.(Edinb.) A76, 232, 1963-4.

Bernal J.D., Mason J., and Knight K.R., Nature 194, 959, 1962.

Bernard R.A., and Wilhelm R.H., Chem. Eng. Progress 46, 233, 1950.

Beveridge G.S.G. Ph.D. Thesis, Edinburgh University, 1960.

Beveridge G.S.G. "A Survey of Interphase Reaction and Exchange in Fixed and Moving Beds", University of Minnesota, 1962.

Beveridge G.S.G. in "Symposium on Chemical Engineering in the Metallurgical Industries", Inst. Chem. Eng., 1963.

Bischoff K.B. Chem. Eng. Science 16, 131, 1961.

Bischoff K.B. Canad. J. Chem. Eng. 40, 161, 1962.

Bischoff K.B., and Levenspiel O. Chem. Eng. Science 17, 245, 257, 1962.

Blum E.H., and Wilhelm in "Symposium on Mathematical Models in Chemical Engineering", Inst. Chem. Eng., 1965. also Blum E.H. Ph.D. dissertation, Princeton University, 1964.

Bonifaz C. Sc.D. Thesis, Massachusetts Inst. Techn., 1962.

Bosworth R.C.L. "Heat Transfer Phenomena", Pergamon Press, 1952.

Bradshaw R.D., and Bennett C.D. A.I.Ch.E. Journal 7, 48, 1961.

Brailsford A.D., and Major K.G. Brit. J. Appl. Phys. 15, 313, 1964.

Bretsznajder S., and Ziolkowski D. Bull. Acad. Polon. Sci. Ser. Sci. Chim. 7, 579, 1959. also Int. Chem. Eng. 6, 85, 1966.

Brinkman H.C. Appl. Sci. Res. A1, 27, 1947.

Brown G.G. et al "Unit Operations, 1951.

Brown R.L., and Hawksley P.G.W. Coal Research p.113, 1945.

Brown R.L. and Hawksley P.G.W. Nature 157, 585, 1945.

Brown R.L. and Hawksley P.G.W. Times Sc. Rev. p.6 Summer 1954.

Browning W.J., Hydronyl Ltd. Private Communication, 1964.

Bruggeman D.A.G. Ann. Physik. V. 24, 636, 1935.

Burgers H.C. Physik. Z. 20, 73, 1919.

Cairns E.J., and Prausnitz J.M. Ind. Eng. Chem. 51, 1441, 1959.

Cairns E.J., and Prausnitz J.M. Chem. Eng. Science 12, 20, 1960, also Prausnitz J.M. Ph.D. dissertation, Princeton University 1955.

Calderbank P.H., and Pogorski L.A. Tr. Inst. Chem. Eng. 35, 195, 1957.

Carberry J.J. A.I.Ch.E. Journal 4, 124, 1958.
Carberry J.J. A.I.Ch.E. Journal 6, 460, 1960.
Carberry J.J., and Bretton R.H. A.I.Ch.E. Journal 4, 367,1958.
Carman P.C. Tr. Inst. Chem. Eng. 15, 150, 1937.
Carman P.C. Tr. Inst. Chem. Eng. 16, 168, 1938.
Carman P.C. "Flow of Gases through Porous Media", Butterworths Scientific Publications, 1956.
Carslaw H.S., and Jaegar J.C. "Conduction of Heat in Solids" Oxford Univ. Press, 1948.
Chao R., and Hoelscher H.E. A.I.Ch.E. Journal 12, 271, 1966, also Chao R. Ph.D. dissertation, John Hopkins University, 1965.
Chechetkin A.V. "High Temperature Heat Carriers", 1957 translation, Pergamon Press, 1963.
Chen J.C., and Churchill S.W. A.I.Ch.E. Journal 9, 35,1963, also Ph.D. Thesis, University of Michigan, 1961.
Chiam J.T. Ph.D. Thesis, Manchester College of Technology,1962.
Cholette A., and Blanchet J. Can. J. Chem. Eng. 39, 192, 1961.
Cholette A., and Cloutier L. Can. J. Chem. Eng. 37, 105,1959.
Chukhanov Z.F. Int. J. Heat Mass Transfer 6, 691, 1963.
Clark W.T., and Powell R.W. J. Sci. Instruments 39, 545,1962.
Coberly C.A., and Marshall W.R. Chem. Eng. Progress 47, 141, 1951.
Collins M. B.S. Thesis, University of Delaware, 1957.
Converse A.O. A.I.Ch.E. Journal 6, 344, 1960.
Cornell D., and Katz D.L. Ind. Eng. Chem. 47, 1379, 1955.
Coulson J.M., and Richardson J.F. "Chemical Engineering", Vol. 2, p. 392, Pergamon Press, 1959.
Crider J.E., and Foss A.S. A.I.Ch.E.J. 11, 1012, 1965 also Univ. California Radiation Lab. Rept.(UCRL - 11757,1965)
Damkohler G. in "Der Chemie Ingenieur", Akademische Verlagsgesllschaft. m.b.H., 3, 441, 1937.
Danckwerts P.V. Chem. Eng. Science 2, 1, 1953.
Deans H.A. Soc. Petrol. Eng. Journal 3, , 1963.
Deans H.A., and Lapidus L. A.I.Ch.E. Journal 6, 656, 1960.

Deissler R.G., and Boegli J.S. Tr. A.S.M.E. 80, 1417, 1958.
Deissler R.G., and Eian C.S. Natl. Advisory Comm. Aeronaut. (RM E52C05, 1952)
Denton W.H. "Proc. General Discussion Heat Transfer" p. 370, 386, Inst. Mech. Eng., 1951.
Denton W.H. A.E.R.E. Report E/R 1095, 1957.
De Vries D.A. Mededel Landb. Hogesch. Wageningen 52, 1, 1952.
Dul'nev G.N., and Sigalova Z.V. Int. Chem. Eng. 5, 218,1965. also J. Eng. Phys.(USSR) 7, No. 10, 49, 1961.
Ebach E.R., and White R.R. A.I.Ch.E. Journal 4, 161, 1958.
Epstein N. Can.J.Chem.Eng. 36, 210, 1958.
Epstein N., and M.J. Young, Nature 196, 885, 1962.
Ergun S., Chem. Eng. Progress 48, 89, 1952.
Eucken A. Forsch. Gebiete Ing., B3, VDI - Forschungsheft, 353, 1932.
Fahien R.W., and Smith J.M. A.I.Ch.E. Journal 1, 28, 1955.
Fan L.T., and Ahn Y.K. Ind. Eng. Chem.(Proc.Des. and Dev.) 1, 190, 1962.
Fan L.T., and Bailie R. Chem. Eng. Sc. 13, 63, 1960.
Fatt I. Tr. A.I.M.M.E. 207, 144, 160, 164, 1956.
Fenech H. and Rohsenow W.M. Tr.A.S.M.E. 85C, 15, 1963.
Fesenmeier J.J. Ph.D. dissertation, Carnegie Inst. Tech.1965.
Fluendy M.A., and Smith E.B, Quart. Rev. 16, 241, 1962.
Fischer R.A., J.Agr.Sci. 16, 492, 1926.
Fowler J.L., and Hertel K.J. J.Appl. Phys. 11, 496, 1940.
Fricke H. Phys. Rev. 24, 575, 1924.
Fromm H. Optik 3, 137, 1948.
Galloway L.R., Komarnicky W., and Epstein N. Can.J.Chem. Eng. 35, 139, 1957.
Gamson B.W., Chem. Eng. Progress 47, 19, 1951.
Gay B., and Alcorn T.E., Chem. Eng. Science 17, 641, 1962.
Glaser H. Chem. Ing. Tech. 34, 468, 1962.
Glaser P.E. "Int. Dev. in Heat Transfer" part 4 p.829,1961.
Glassman I., and Bonilla C.F. Chem. Eng. Symposium Ser. 49, 153, 1953.
Godbee H.W., and Ziegler W.T. J.App.Phys. 37, 40, 56, 1966.

Gopalarathnam C.D., Hoelscher H.E., and Laddha G.S. A.I.Ch.E. Journal 7, 249, 1961.

Gordon R.D., Glasgow University, Private Communication, 1966.

Gorring R.L., and Churchill S.W., Chem. Eng. Progress 57, No. 7, 53, 1961.

Gottschlich C.F. A.I.Ch.E. Journal 9, 88, 1963.

Graton L.C., and Fraser H.J. J. Geology 43, 785, 1935.

Green D.W., Perry R.H., and Babcock R.E. A.I.Ch.E. Journal 10, 645, 1964.

Greenaway L.R., Chem. Eng. Science 10, 199, 1959.

Griffith J.S. Nature 196, 764, 1962.

Grootenhuis D., Mackworth R.C.A., and Saunders U.A. Proc. of General Discussion on Heat Transfer, Inst. Mech. Eng. p.363, 1951.

Gupta A.S., and Thodos G. A.I.Ch.E. Journal 9, 751, 1963.

Hadwiger H. Elemente der Math. 7, 97, 1952.

Haigh R. Morgan Refractories Ltd., Private Communication, 1965.

Hamaker H.C. Philips Research Reports 2, 55, 103, 112, 420, 1949.

Hamilton R.L., and Crosser O.K. Ind. Eng. Chem. (Fund) 1, 187, 1962.

Happel J. Ind. Eng. Chem. 41, 1161, 1949.

Happel J. and Brenner H. "Low Reynolds Number Hydrodynamics", Prentice Hall, 1965.

Harper J.C., and El Sahrigi A.F. Ind. Eng. Chem.(Fund.) 3, 319, 1964.

Harris C.C. Nature, 205, 353, 1965.

Haughey D.P., and Beveridge G.S.G. Chem. Eng. Science, to be published, 1966.

Heaslet M.A., and R.F. Warming Int. J. Heat Mass Transfer 8, 979, 1965.

Hiby J.W. in "Symposium on the Interaction between Fluids and Particles", Inst. Chem. Eng. p.312, 1962.

Hiby J.W., and Schummer P., to be published (referred to by Hiby (1962)).

Hill F.B., and Wilhelm R.H. A.I.Ch.E. Journal 5, 486, 1959, also Hill F.B. Ph.D. Thesis, Princeton University, 1958.

Hirai E. Chem. Eng.(Japan) 18, 528, 1954.
Hoelscher A.E. A.I.Ch.E. Journal 4, 300, 1958.
Hogendijk M.J. Philips Research Reports 18, 109, 1963.
Horsfield H.T. J. Soc. Chem. Ind. 53, 107T, 1934.
Horton C.W., and Rogers F.T. J.Appl. Phys. 16, 367, 1945.
Hottel H.C. Int. J. Heat Mass Transfer 5, 82, 559, 1962.
Howell J.R. Chem. Eng. Progress. Symposium Ser. 61,No. 59, 162, 1965.
Huang J.H., and Smith J.M. J. Chem. Eng. Data 8, 437, 1963.
Hudson D.R. J. Appl. Phys. 20, 154, 1949.
Hutchinson H.P., and Sutherland D.N. Nature 206, 1036, 1965.
Hulbert H.M. Ind. Eng. Chem. 36, 1012, 1944.
Huyten F.H., Van Beersum W., and Rijnders in Scott R.P.W. (Editor) "Gas Chromatography",Butterworths p.224, 1960.
Ikeda M., Nishimura y., and Kubota H. Chem. Eng.(Japan) 28, 350, 1964.
Jacques G.L., and Vermuelen T. University of California Report UCRL - 8029, 1957.
Jenkins F.A., and White H.E. "Fundamentals of Optics", McGraw-Hill, p.455, 1957.
Jeschar R. Archiv. Eisenhuttenwesen p.91, 1964.
Jones W.M., Mills D. Brit. J. Appl. Phys. 12, 172, 1961.
Kannuluick W.G., and Martin L.H. Proc. Roy. Soc.(London) A141, 144, 1933.
Kennard E.H. "Kinetic Theory of Gases", McGraw-Hill, 1938.
Kessler H.G. Chem. Ingr. Techn. 34, 163, 1962.
Kimura M. Chem. Eng.(Japan) 25, 742, 1961.
Kimura M. and Kaeda T. Chem. Eng.(Japan) 19, 397, 1955.
King P. Ph.D. Thesis, Manchester University, 1965.
Kingery W.D., Klein J.D., McQuarrie M.C. Trans. A.S.M.E. 80, 705, 1958.
Kinney S.P. U.S.Bur.Mines.Tech. Paper 442, 1929.
Kistler S.S. J. Phys. Chem. 39, 79, 1935.
Kistler S.S., and Caldwell A.G. Ind. Eng. Chem. 26, 658,1934.
Kitaura Y., and Tanaka H. J. Chem. Eng.(Japan) 28, 740, 1964.
Klinkenberg L.J. Bull. Geol. Soc. Amer. 62, 559, 1951.

Kolar V. Coll. Czech. Chem. Comm. 27, 2263, 1962.
Kramers H., and Alberda G. Chem. Eng. Science 2, 173,1953.
Kramers H., and Thoenes D. Chem. Eng. Science 8, 271, 1958.
Kunii D., and Smith J.M. A.I.Ch.E. Journal 6, 71, 1960.
Kunii D., and Smith J.M. A.I.Ch.E. Journal 7, 29, 1961.
Lamb D.E., and Wilhelm R.H. Ind. Eng. Chem.(Fund.) 2, 173, 1963, also Lamb D.E. Ph.D. dissertation, Princeton University, 1962.
Larkin B.K., and Churchill S.W. A.I.Ch.E. Journal 5, 467, 1959, also Larkin B.K. Ph.D. thesis, University of Michigan, 1957.
Latinen G.A. Ph.D. dissertation, Princeton University,1951.
Lebedev P.D., and Petrov-Denisov V.G. Int. J. Heat Mass Transfer 7, 1033, 1964.
Lenz F. Optik 11, 525, 1954.
Leva M., and Grummer M. Chem. Eng. Progress 43, 713, 1947.
Leva M. and Grummer M. Ind. Eng. Chem. 40, 415, 1948.
Levenspiel O. "Chemical Reaction Engineering", John Wiley,1962.
Levenspiel O. Can. J. Chem. Eng. 40, 113, 1962.
Levenspiel O. Chem. Eng. Science 17, 576, 1962.
Levenspiel O. in "Advances in Chemical Engineering", Vol. 4, Academic Press, 1963.
Levenspiel O., and Bischoff K.B., Ind. Eng. Chem. 51, 1431, 1959.
Levenspiel O., and Smith W.K., Chem. Eng. Sci. 6, 227,(1957).
Levenspiel O., and Bischoff K.B. (1962), see Bischoff K.B. and Levenspiel (1962).
Levine M.M., and Chernick J. Nature 208, 69, 1965.
Lichtenecker K. Physik. Z. 25, 169, 193, 1924.
Lichtenecker K. Physik. Z. 27, 115, 1926.
Liles A.W., and Geankoplis C.J. 6, 591, 1960.
McAdams W.H. "Heat Transmission" 3rd Ed. McGraw-Hill, 1954.
McConnachie J.T.L., and Thodos G. A.I.Ch.E. Journal 9, 60, 1963.
McGeary R.K., J. Amer. Ceramic Soc. 44, 513, 1961.
McHenry K.W., and Wilhelm R.H. A.I.Ch.E. Journal 3, 83,1957.

MacCrae J.C., and Gray W.A. Brit. J. Appl. Phys. 12, 164,1961.

Martin J.J., McCabe W.L., and Monrad C.C. Chem. Eng. Progress 47, 91, 1951, also Martin J.J. Sc.D. thesis, Carnegie Inst. Techn. 1948.

Marvin J.W. Amer. J. Botany 26, 280, 1939.

Masamune S., and Smith J.M. Ind. Eng. Chem.(Fund) 2, 136,1963.

Mason G., and Clark W. Nature 207, 512, 1965.

Matzke E.B. Amer. J. Botany 26, 288, 1939.

Maxwell J.C. "A Treatise on Electricity and Magnetism", Clarendon Press, 3rd Edition, Vol. 1, p.440.

Meek R.M.G. Natl. Eng. Lab., Glasgow, Report No. 54, 1962, also "Int. Dev. in Heat Transfer" p. 751, 1961.

Meissner H.P., Michaels A.S., and Kaiser K. Ind. Eng. Chem. (Proc. Des. and Dev.) 3, 202, 1964.

Metropolis N., Rosenbluth A.W., Rosenbluth M.N., and Teller A.H. J. Chem. Phys. 21, 1087, 1953.

Mickley H.S., Smith K.A., and Korchak E.I. Chem. Eng. Sci. 20, 237, 1965.

Morales M., Spin W.O., and Smith J.M. Ind. Eng. Chem. 43, 225, 1951.

Morrison H.L. J. Appl. Phys. 18, 849, 1947.

Morrison H.L., Rogers F.T., and Horton C.W. J. Appl. Phys. 20, 2027, 1949.

Mott R.A. "Some Aspects of Fluid Flow", Arnold p.242, 1951.

Nawaz M. Private Communication, 1966.

Nield M.A., and Ross A.A. Project Report, Dept. Chem. Eng., University of Edinburgh, 1966.

Oman A.O., and Watson K.M. Natl. Petroleum News 36, R795,1944.

Otake T., and Kunugita E. Chem. Eng.(Japan) 22, 144, 1958.

Ozisik N., Korsmeyer R.B., and Rhoden G.L. U.S. Atomic Energy Comm. CF-61-6-16, 1961.

Palmer N.K. Ph.D. thesis, Manchester University, 1960.

Parrish R.J. Nature 190, 800, 1961.

Pearson J.R.A. Chem. Eng. Science 6, 89, 1956.

Perkins T.K., and Johnston O.C. Soc. Petrol. Eng. Journal 3, 70, 1963, also supplement published with reprint.

Perry J.H., Editor "Chemical Engineers Handbook", 4th Edit. p. 3 - 197, 1963.

Pfeffer R. Ind. Eng. Chem.(Fund.) 3, 381, 1964.

Pfeffer R., and Happel J. A.I.Ch.E. Journal 10, 605, 1964.

Pirani M. J. Sci. Instruments 16, 372, 1939.

Polack J. Sc.D. thesis, Massachusetts Inst. Techn., 1948.

Powell R.W. J. Sci. Instruments 34, 485, 1957.

Powell R.W. Mem. Sci. Rev. Metall. 56, 181, 1959.

Powell R.W. Bull. Inst. Int. Froid, Annexe 1960-2, p.129.

Prager S. Chem. Eng. Science 18, 227, 1963.

Prausnitz J.M., and Wilhelm R.H. Ind. Eng. Chem. 49,978,1957.

Prushek R. Forsch. Gebiete Ing. 29, No. 1, p.11, No. 2 p.57, 1963.

Ranz W.E. Chem. Eng. Progress 48, 247, 1952.

Rayleigh Lord Phil. Mag. 34, 481, 1892.

Reid W.P. J. Math. Phys. 34, 95, 1955.

Rhoades R.G. Ph.D. thesis, Rensselaer Poytech. Inst., 1964.

Rhodes J.M., and Peebles F.N. A.I.Ch.E. Journal 11, 481,1965, also Rhodes J.M. Ph.D. thesis, University of Tennessee,1962.

Rice O.K. J. Chem. Phys. 12, 1, 1944.

Riemann G.H.M. Weber, "Die Partiellen Differential-Gleichunger der Mathematischen Physik", Band 1,p.474, F. Vieweg and Sohn, 1919.

Roblee L.H.S., Baird R.M., and Tierney J.W. A.I.Ch.E. Journal 4, 460, 1958.

Rogers F.T., and Morrison H.L. J.Appl. Phys. 21, 1177,1950.

Rose W.J. J.Appl. Phys. 29, 687, 1958.

Rosenbluth M.N., and Rosenbluth H.W. J. Chem. Phys. 22, 881, 1954.

Rotenburg A. J. Chem. Phys. 43, 4377, 1965.

Rosseland S. "Theoretical Astrophysics" Oxford Univ. Press,1936.

Round G.F., and Newton R. Nature 198, 747, 1963.

Rowe P.N., and Claxton K.T. Tr. Inst. Chem. Eng. 43,T321,1965.

Russel H. J. Amer. Ceramic Soc. 18, 1, 1935.

Rutgers R. Nature 193, 465, 1962.

Saffman P.G. J. Fluid Mech. 6, 321, 1959.

Saffman P.G. J. Fluid Mech. 7, 194, 1960.
ibid 8, 273, 1960.

Satterfield C.N., and Resnick H. Chem. Eng. Progress 50, 505. 1954.

Saunders O.A., and Ford H. J. Iron and Steel Inst. 141, 291, 1940.

Scarborough J.B. "Numerical Mathematical Analysis", 3rd Edit. Oxford Univ. Press, 1955.

Stephenson D.G., and Woodside W. Trans. A.S.M.E. 80, 1424, 1958.

Stewart W.E. Chem. Eng. Progress Symposium, Series 61, No. 58, p. 61, 1965.

Strickler H.S. Ind. Eng. Chem. 46, 828, 1954.

Sullivan R.R., and Herdel K.L. J. Appl. Phys. 11, 761,1940.

Supnik F. Trans. Amer. Math. Soc. 65, 19, 1949.

Snyder L.J., and Stewart W.F. A.I.Ch.E. Journal 12, 167,1966, also Snyder L.J. Ph.D. dissertation, University of Wisconsin, 1965.

Takeoka S., and Nishimura Y. Chem. Eng.(Japan) 27, 646, 1963.

Thadani M.C., and Peebles F.N. Ind. Eng. Chem., to be published 1966.

Thoenes D. Doctoral thesis, Delft University, 1957.

Thompson H.A., and Sogin H.H. J. Fluid Mech. 24, 451, 1966.

Topper L. Ind. Eng. Chem. 47, 1377, 1955.

Trambouze P. Rev. Inst. Franc. Petrole. 15, 1948, 1960.

Traugott S.C., and Wang K.C. Int. J. Heat Mass Transfer 7, 269, 1964.

Tsao G.T. Ind. Eng. Chem. 53, 395, 1961, also Ind. Eng. Chem.(Fund) 1, 223, 1962.

Turner G.A. Chem. Eng. Sci. 7, 156, 1958.

Turner G.A. Chem. Eng. Sci. 10, 14, 1959.

Usiskin C.M., and E.M. Sparrow, Int. J. Heat Mass Transfer 1, 28, 1960.

Van Cauwenberghe A.R. Chem. Eng. Science 21, 203, 1966.

Van der Held E.F.M. Appl. Sci. Res. A3, 237, 1952.

Van der Laan E.Th. Chem. Eng. Sci. 7, 187, 1958.

Van Loon W. Doctoral dissertation, Delft University, 1952.
Verman L.C., and Banerjee S. Nature 157, 584, 1946.
Verschoor J.D., and Greebler P. Trans. A.S.M.E. 74, 961, 1952.
Verschoor H., and Schuit G. Appl. Sci. Res. A2, 97, 1952.
Vidoni C.M. U.S. Atomic Energy Comm. UCRL-14264, 1965.
Viskanta R. Appl. Sci. Res. A13, 291, 1964.
Viskanta R. Trans. A.S.M.E. 87C, 143, 1965.
Viskanta R., and Grosh R.J. "Int. Developments in Heat Transfer" Part 1V,A.S.M.E., P.820, 1961.
Viskanta R., and Grosh R.J. Trans. A.S.M.E. 84C, 63, 1962.
Viskanta R., and Grosh R.J., Int. J. Heat Mass Transfer 5, 729, 1962.
Viskanta R., and Grosh R.J. Appl. Mech. Revs. 17, 91, 1964.
Voice E.W., and Wild R. Journal Iron and Steel Inst. 183, 404, 1956.
Wadell H. J. Geology 43, 276, 1935.
Wadsworth J. Nat. Res. Council Canada, Report MT-41, 1960, also "Int. Dev. in Heat Transfer", A.S.M.E., p.760,1961.
Warren J.E., and Messmer J.H. Ind. Eng. Chem.(Fund.) 1, 223, 1962.
Webb J. Nature 177, 989, 1956.
Wehner J.F., and Wilhelm R.H. Chem. Eng. Science 6, 89,1956.
Weiner M.M., and Edwards D.K. Proc. Heat Transfer and Fluid Mechanics Inst. p. 16, 1963.
Weisman J. A.I. Ch. E. Journal 1, 342, 1965.
Wentz C.A., and Thodos G. " " " " 9, 81, 1963.
Westman A.E.R., and Hugill H.R. J. Amer. Ceramic Soc. 13, 767, 1930.
Wilhelm R.H. Chem. Eng. Progress 49, 150, 1953.
Wilhelm R.H. Pure and Applied Chem. 5, 403, 1962.
Wilhelm R.H., Johnson W.C., Wynkoop R., and Collier D.W. Chem. Eng. Progress 44, 105, 1948.
Willhite G.P., Kunii D., and Smith J.M. A.I.Ch.E. Journal 8, 340, 1962.
Williamson J.E., Bazaire K.E., and Geankoplis C.J. Ind. Eng. Chem. (Fund.) 2, 126, 1963.

Wilson E.J., and Geankoplis C.J. Ind. Eng. Chem.(Fund.) 5, 9, 1966.

Wise M.E. Philips Research Reports 7, 321, 1952.

Wise M.E. Philips Research Reports 15, 101, 1960.

Wohlbier H., and Reisner W. Chem. Ing. Tech. 34, 603,1962.

Wologdine S., and Queneau A.L. Chem. Met. Eng. 7, 383, 433, 1909.

Wood W.W., and Jacobson J.O. J.Phys.Chem. 27, 1207, 1957.

Wood W.W., and Parker F.R. J.Phys.Chem. 21, 720,1957.

Woodside W. Can.J.Phys. 36, 815, 1958.

Woodside W., and Messmer J.H. J.Appl.Phys. 32, 1688, 1699, 1961.

Yerazunis S., Cornell S.W., and B. Wintner, Nature 207, 835, 1965.

Yagi S., and Kunii D. A.I.Ch.E. Journal 3, 373, 1957.

Yagi S., Kunii D., and Wakao N. A.I.Ch.E. Journal 6, 543,1960.

Yeh G.C. J. Chem. Eng. Data 6, 526, 1961.

Yoshida F., Ramaswami D., and Hougen O.A. A.I.Ch.E. Journal 8, 5, 1962, see also Bird R.B., Stewart W.E., and Lightfoot E.N. "Transport Phenomena", John Wiley, p. 411, 1960.

Zenz F.A., and Othmer D.F. "Fluidization and Fluid-Particle Systems", Reinhold, 1960.

Zhavoronkov N.M. Zh. Khim. Fiz. No.1, 1944.

ACKNOWLEDGEMENTS

The author wishes to thank the following:

Dr. G.S.G. Beveridge, who supervised this research, for his encouragement and sympathetic guidance;

Mr. C. McLeod and the workshop staff for their cooperation;

Hydronyl Ltd. for supplying the packing material;

Mr. R. Gordon, Glasgow University, for making the solid thermal conductivity measurement;

Miss Edwina Inch for her patient typing of a difficult manuscript;

Meat Industry Research Institute of New Zealand (Inc.) for the provision of a Research Fellowship.